**UNIVERSIDADE DE LISBOA**

**INSTITUTO SUPERIOR TÉCNICO**

# Concentration of small-volume samples by centrifugal and tangential flow nanofiltration

**Carlos Duarte da Silva Completo**

**Supervisor: Doctor Vitor Manuel Geraldes Fernandes**

**Co-Supervisor: Doctor Viriato Sérgio de Almeida Semião**

**Thesis approved in public session to obtain the PhD Degree in Chemical Engineering**

**Jury final classification: Pass with Distinction and Honour**

**2018**

**UNIVERSIDADE DE LISBOA**

**INSTITUTO SUPERIOR TÉCNICO**

# Concentration of small-volume samples by centrifugal and tangential flow nanofiltration

**Carlos Duarte da Silva Completo**

**Supervisor: Doctor Vitor Manuel Geraldes Fernandes**

**Co-Supervisor: Doctor Viriato Sérgio de Almeida Semião**

**Thesis approved in public session to obtain the PhD Degree in Chemical Engineering**

**Jury final classification: Pass with Distinction and Honour**

**Jury**

**Chairperson:**

Doctor Francisco Manuel da Silva Lemos, Instituto Superior Técnico da Universidade de Lisboa

**Members of the Committee:**

Doctor Bart Van der Bruggen, Faculty of Engineering, KU Leuven

Doctor Maria Norberta Neves Correia de Pinho, Instituto Superior Técnico da Universidade de Lisboa

Doctor João Paulo Serejo Goulão Crespo, Faculdade de Ciências e Tecnologia da Universidade Nova de Lisboa

Doctor Duarte Miguel de França Teixeira dos Prazeres, Instituto Superior Técnico da Universidade de Lisboa

Doctor Vitor Manuel Geraldes Fernandes, Instituto Superior Técnico da Universidade de Lisboa

**Funding Institutions:** Fundação para a Ciência e a Tecnologia (SFRH/BD/87326/2012)

**2018**

# Abstract

This thesis aims at studying adequate techniques to concentrate low molecular weight (MW) solutes (MW < 1000 g/mol) in small-volume liquid samples (less than 100 mL). This is a theme of interest for biological and chemical applications like sample concentration for the detection of drugs and toxins in body fluids and in environmental specimens. The main objective of the present work is to develop techniques and devices capable of performing the sample concentration in a cheap, replicable and easy way, based on pressure-driven membrane processes, such that concentration factors (CF) above 10 are obtained.

Three main subjects were focused in this work: 1) the use of microfluidic tangential flow filtration (micro-TFF); 2) the development of a hybrid computational / semi-empirical method to predict nanofiltration (NF) performance; 3) the assessment of centrifugal nanofiltration (CNF) performance. To prove the feasibility of these techniques, and discard fouling effects, only binary aqueous solutions of small inorganic salts and neutral organic molecules were used. Concentration of samples with two osmotic pressures were tested (0.6 bar and 2.6 bar), while the applied transmembrane pressure varied between 7 and 42 bar.

Both micro-TFF and CNF result in appreciable concentration factors (CF between 15 and 22) when applied to the samples with the lowest osmotic pressure. For the samples with highest osmotic pressure, lower concentration factors are obtained (CF between 5 and 10). In these scenarios, CNF provides better concentration performance due to its self-cleaning mechanism that disrupts the concentration polarization (CP) layer, while in micro-TFF the CP layer is stable, which decreases the permeate flux and the permeate quality.

The CP phenomenon can be minimized in micro-TFF devices using improved channel or spacer designs. To speed up the selection of the best designs, the hybrid method developed herein can be used, since its estimations for the NF performance deviates less than 10 % from the results obtained from the full CFD simulation of the permeation process. The validation of the momentum and mass transport models, used for the CFD simulations, was performed by comparing the numerical results against the corresponding experimental ones obtained with micro-PIV and holographic interferometry.

Similarly, the CNF performance can also be improved by optimizing the filtration chamber geometry of the centrifugal device. It was verified that the obtained CF value depends on both the height of the filtration chamber, $h$, and the angle between the centrifugal force and the membrane surface, $\beta$. For the range of tested values of these two parameters ($h$ from 0.1 mm to 2.4 mm; and $\beta$ from -10º to +10º) the optimal values were $h$ = 0.2 mm and $\beta$ = -10º. These results suggest that $h$ should be high enough to permit efficient mixing of the liquid inside the

filtration chamber, but also small enough to minimize the volume of the filtration chamber. At the same time, the $\beta$ angle should be as negative as possible provided that the normal to the membrane surface points radially outwards.

Overall, the aim to develop methods for the concentration of small samples of low MW solutes by pressure-driven membrane processes was accomplished and CNF proved to be the most efficient one.

# Resumo

A presente tese estuda técnicas adequadas para a concentração de solutos de baixo peso molecular (inferior a 1000 g/mol) em amostras líquidas de pequeno volume (menos de 100 mL). Este é um tema relevante para aplicações biológicas e químicas, como a concentração de amostras para a detecção de drogas e toxinas em fluidos corporais e em amostras ambientais. O principal objetivo do presente trabalho é desenvolver técnicas e dispositivos capazes de efectuar a concentração das amostras de forma fácil, reprodutível e a baixo custo, com base em processos de separação por membranas com pressão como força motriz, de modo a que sejam obtidos factores de concentração (FC) acima de 10.

O trabalho foca-se em três temas principais: 1) o uso de filtração de escoamento tangencial à micro-escala (micro-TFF); 2) o desenvolvimento de um método híbrido computacional / semi-empírico para prever o desempenho da nanofiltração (NF); 3) a avaliação do desempenho da nanofiltração centrífuga (CNF). Por forma a provar a viabilidade destas técnicas, e ao mesmo tempo descartar os efeitos de *fouling*, apenas foram utilizadas soluções aquosas binárias de sais inorgânicos e moléculas orgânicas neutras de baixo peso molecular. Para cada soluto foram utilizadas soluções com duas pressões osmóticas diferentes (0,6 bar e 2,6 bar), enquanto a pressão transmembranar aplicada variou entre 7 e 42 bar.

Quando aplicadas à concentração das amostras com a pressão osmótica mais baixa, tanto a técnica micro-TFF como a CNF resultam em factores de concentração apreciáveis (FC entre 15 e 22). No entanto, nos casos em que são concentradas as amostras com maior pressão osmótica, são obtidos factores de concentração mais baixos (FC entre 5 e 10). Nestes cenários, a técnica CNF proporciona um melhor desempenho na concentração da amostra devido ao mecanismo de auto-limpeza que desestabiliza a camada de polarização de concentração (PC), ao contrário do que acontece na concentração por micro-TFF (a camada de PC não é desestabilizada), originando menor fluxo de permeado e menor qualidade do permeado.

Em dispositivos de micro-TFF, o fenómeno de polarização da concentração pode ser minimizado utilizando canais ou espaçadores projectados para o efeito. Por forma a agilizar o processo de seleção dos melhores canais e espaçadores, o método híbrido desenvolvido nesta tese pode ser usado, uma vez que o desvio das estimativas do desempenho da nanofiltração obtido pelo método híbrido é inferior a 10% face aos resultados obtidos pela simulação computacional do processo. A validação dos modelos de transporte de quantidade de movimento e massa, utilizados nas simulações numéricas, foi realizada comparando os resultados obtidos por estas com os correspondentes resultados experimentais obtidos com micro-PIV e interferometria holográfica.

O desempenho dos dispositivos de CNF também pode ser melhorado através da optimização da geometria da câmara de filtração do dispositivo centrífugo. Verificou-se que o valor do factor de concentração depende da altura da câmara de filtração, $h$ e do ângulo entre a força centrífuga e a superfície da membrana, $\beta$. Na gama de valores testados destes dois parâmetros ($h$ de 0,1 mm a 2,4 mm e $\beta$ de -10º a + 10º), os valores óptimos foram $h$ = 0,2 mm e $\beta$ = -10º. Estes resultados sugerem que $h$ deve ser suficientemente elevado para permitir uma mistura eficiente do líquido dentro da câmara de filtração mas também suficientemente baixo para que o volume da câmara seja pequeno. Simultaneamente, o ângulo $\beta$ deve ser o mais negativo possível desde que a normal à superfície da membrana aponte radialmente na direcção positiva.

Em resumo, o objetivo de desenvolver métodos para a concentração de solutos de baixo PM em amostras líquidas de pequeno volume através de processos de separação por membranas com pressão como força motriz foi realizado com sucesso, sendo a técnica CNF aquela apresentou melhor desempenho.

# Keywords

Concentration by nanofiltration
Centrifugal nanofiltration
Microscale tangential flow filtration
Hybrid computational / semi-empirical method
Micro-PIV
Holographic interferometry

# Palavras-chave

Concentração por nanofiltração
Nanofiltração centrífuga
Filtração por escoamento tangencial à microescala
Método híbrido computacional / semi-empírico
Micro-PIV
Interferometria holográfica

# Aknowledgments

I would like to express my sincere gratitude to my supervisors Professor Vitor Geraldes and Professor Viriato Semião for the opportunity, guidance and encouragement throughout the thesis period.

I am indebted to Fundação para a Ciência e a Tecnologia for funding my PhD scholarship (SFRH/BD/87326/2012).

I am grateful to Professor Marília Mateus for authorizing the centrifugal filtration work in the centrifuge of the Bioengineering Department. I am also grateful to Professor Miguel Rodrigues for access to the HPLC pump used in the micro-TFF experiments and to Professor Maria de Lurdes Serrano for access to the differential refractometer.

I would like to acknowledge Jorge Pinheiro for the manufacture of the CNF device, to Pedro Rego for his assistance in the 3D-printing process of the rotor adaptors, and to the FabLab Lisboa for access to the laser cutting machine.

Last, but always first, I would like to thank my family for all their love and support.

# List of chapters

# Table of contents

# List of figures

# List of tables

# List of nomenclature

The parameters expressed in this list are presented in SI units (including some derived units), but in the main text other common units may be used for convenience. The derived units used in this list are $C$ (coulomb), $J$ (joule), $Pa$ (pascal), $rad$ (radians) and $V$ (volt).

Latin letters

| | |
|---|---|
| $a$ | fitting parameter of $Sh$ empirical correlation, equation (2-17), $[dimensionless]$ |
| $a$ | slope of the linear relationship between $n$ and $w$, equation (4-9), $[m^3/kg]$ |
| $a$ | semi-major radius of an ellipse, Figure 5-11, $[m]$ |
| $a$ | parameter to estimate $\Delta p$ in rectangular cross-section channels, equation (C-1), $[dimensionless]$ |
| $A_{c.i}$ | surface area of the cell $i$ of the CFD domain, in the $x$-direction, equation (4-21), $[m^2]$ |
| $A_{eff}$ | effective cross-section area of the channel, $[m^2]$ |
| $A_m$ | surface area of the membrane, equations (2-1) and (2-5), $[m^2]$ |
| $A_{m.i}$ | surface area of the membrane that makes part of the cell $i$ of the CFD domain, equation (4-22), $[m^2]$ |
| $b$ | fitting parameter of $Sh$ empirical correlation, equation (2-17), $[dimensionless]$ |
| $b$ | semi-major radius of an ellipse, Figure 5-11, $[m]$ |
| $b(\rho)$ | friction parameter, equation (2-39), $[dimensionless]$ |
| $B$ | solute permeability, equation (2-30), $[m/s]$ |
| $c$ | solute concentration, $[kg/m^3]$ |
| $c$ | fitting parameter of $Sh$ empirical correlations, equation (2-17), $[dimensionless]$ |
| $c$ | location of the centre of an ellipse, Figure 5-11, $[m]$ |
| $c_b$ | solute concentration in the bulk of the feed side, $[kg/m^3]$ |
| $c_c$ | solute concentration in the concentrate, $[kg/m^3]$ |
| $c_f$ | solute concentration in the feed, $[kg/m^3]$ |
| $c_i$ | concentration of the solute $i$ in the membrane pore, equation (2-44), $[mol/m^3]$ |
| $c_{i,p}$ | concentration of the solute $i$ in the permeate, equation (2-44), $[mol/m^3]$ |

| | |
|---|---|
| $c_m$ | solute concentration at the membrane surface of the feed side, $[kg/m^3]$ |
| $c_p$ | solute concentration in the permeate, $[kg/m^3]$ |
| $CF$ | concentration factor, equation (2-46), $[dimensionless]$ |
| $d_f$ | diameter of filament or of rib, $[m]$ |
| $d_h$ | hydraulic diameter of the channel, equation (2-23), [m] |
| $D$ | flexural rigidity, equation (5-2), $[Pa \cdot m^3]$ |
| $D_{AB}$ | diffusion coefficient of the solute $A$ in the solvent $B$, $[m^2/s]$ |
| $D_{AM}$ | diffusion coefficient of the solute $A$ in the membrane, equation (2-30), $[m^2/s]$ |
| $D_i^{\infty}$ | diffusion coefficient of the ion $i$ at infinite dilution, equation (2-44), $[m^2/s]$ |
| $D_{sw}$ | diffusion coefficient of the solute in bulk solution, $[m^2/s]$ |
| $D_{sm}(\rho)$ | diffusion coefficient of the solute in membrane pore, $[m^2/s]$ |
| $D_{wM}$ | diffusion coefficient of the solvent in the membrane, equation (2-29), $[m^2/s]$ |
| $E$ | Young's modulus, equation (5-2), $[Pa]$ |
| $F$ | Faraday constant, equation (2-44), $[96487\ C/mol]$ |
| $F$ | parameter in the Spiegler-Kedem model, equation (2-37), $[dimensionless]$ |
| $h$ | height of the channel, $[m]$ |
| $h_r$ | height of the square rib, Figure 4-11, $[m]$ |
| $H$ | hindrance factor of diffusion, equation (2-43), $[dimensionless]$ |
| $j_A$ | mass flux of solute $A$, $[kg/(m^2 \cdot s)]$ |
| $j_s$ | mass flux of solute that permeates through the membrane, $[kg/(m^2 \cdot s)]$ |
| $j_{s,c}$ | convective mass flux of solute, Figure 2-4, $[kg/(m^2 \cdot s)]$ |
| $j_{s,d}$ | diffusive mass flux of solute, Figure 2-4, $[kg/(m^2 \cdot s)]$ |
| $J_i$ | molar flux of ion $i$ that permeates through the membrane, $[mol/(m^2 \cdot s)]$ |
| $J_s$ | molar flux of solute that permeates through the membrane, $[mol/(m^2 \cdot s)]$ |
| $J_v$ | volumetric permeate flux, $[m/s]$ |
| $J_{vm}$ | molar permeate flux, $[mol/(m^2 \cdot s)]$ |
| $J_{v,0}$ | volumetric permeate flux that occurs at $t$ = 0 (without CP effects), Figure 3-9, $[m/s]$ |
| $J_w$ | volumetric pure water permeate flux, equation (2-1), $[m/s]$ |
| $J_{w,34bar}$ | volumetric pure water permeate flux when using the 34 bar BPV, $[m/s]$ |
| $J_{w,42bar}$ | volumetric pure water permeate flux at $\bar{p}_0$ = 42 bar, $[m/s]$ |
| $J_{w.p}$ | volumetric pure water permeate flux at pressure $p$, $[m/s]$ |
| $k_0$ | mass transfer coefficient of the non-suction mass transfer process, equation (4-23), $[m/s]$ |
| $k_1$ | transport parameter for the diffusivity of water in the membrane, equation |

(2-33), $[m/(Pa \cdot s)]$

$k_2$ transport parameters for the flow of water inside the pores of the membrane, equation (2-33), $[m/(Pa \cdot s)]$

$k_3$ transport parameter for the diffusivity of the solute in the membrane, equation (2-34), $[m/s]$

$k_4$ transport parameters for the flow of solute inside the pores of the membrane, equation (2-34), $[m/(Pa \cdot s)]$

$k_c$ mass transfer coefficient, equations (2-15) and (2-16), $[m/s]$

$k_{c,0}$ mass transfer coefficient of non-suction processes, equation (4-23), $[m/s]$

$K_A$ partition coefficient of the solute, equation (2-30), $[dimensionless]$

$K_{i,c}$ hindrance factor for the convection of an ion, equation (2-44), $[dimensionless]$

$K_{i,d}$ hindrance factor for the diffusion of an ion, equation (2-44), $[dimensionless]$

$K_w$ partition coefficient of the solvent, equation (2-29), $[dimensionless]$

$l_f$ distance between two consecutive filaments, $[m]$

$l_{f1}$ distance between two consecutive filaments of the bottom layer of a mesh, Figure 4-6, $[m]$

$l_{f2}$ distance between two consecutive filaments of the top layer of a mesh, Figure 4-6, $[m]$

$l_p$ length of the membrane pore, $[m]$

$l_r$ distance between two consecutive ribs, Figure 4-11, $[m]$

$L$ length of the channel, $[m]$

$L_c$ characteristic length, equations (2-16) and (2-21), $[m]$

$L_d$ length of the membrane or of the impermeable-dissolving wall, Figure 4-11, $[m]$

$L_e$ entrance length, equation (4-7), $[m]$

$L_o$ path length of the light beam through the medium, equations (4-1) and (4-9), $[m]$

$L_p$ hydraulic permeability, equation (2-2), $[m/(s \cdot Pa)]$

$L_r$ length of the square rib, Figure 4-11, $[m]$

$m$ mass of a fluid element, Figure 2-5, $[kg]$

$M_{max}$ maximum bending stress, equation (5-3), $[Pa]$

$n$ refractive index, $[dimensionless]$

$p$ pressure, $[Pa]$

$\bar{p}_0$ average pressure at the membrane surface at the initial instant of the filtration cycle, equation (5-4), $[Pa]$

| | |
|---|---|
| $p_{eff,m}$ | effective pressure at the membrane surface in the feed side, $p_{eff,m} = p_m - \pi_m$, $[Pa]$ |
| $p_{eff,p}$ | effective pressure at the membrane surface in the permeate side, $p_{eff,m} = p_p + \pi_p$, $[Pa]$ |
| $p_m$ | pressure of the liquid at the membrane surface (feed side), $[Pa]$ |
| $p_{max}$ | maximum applied pressure, $[Pa]$ |
| $p_p$ | pressure of the liquid at the membrane surface (permeate side), often referred as pressure of the permeate, $[Pa]$ |
| $P_w$ | hydraulic permeability of the membrane, equation (2-4), $[m]$ |
| $P_s$ | solute permeability, equation (2-36), $[m/s]$ |
| $Pe_p$ | Péclet number used in steric pore model, equation (2-43), $[dimensionless]$ |
| $q$ | uniform load on a circular clamped plate, equation (5-1), $[Pa]$ |
| $Q$ | volumetric flow rate, $[m^3/s]$ |
| $Q_{max}$ | maximum volumetric pure water flow rate that can cross the membrane for a given $A_m$, $Q$ and $\Delta p_m$, $[m^3/s]$ |
| $Q_p$ | volumetric flow rate set up on the panel of the pump, $[m^3/s]$ |
| $Q_v$ | volumetric permeate flow rate, equation (2-5), $[m^3/s]$ |
| $Q_w$ | volumetric pure water flow rate, equation (2-1), $[m^3/s]$ |
| $Q^{in}$ | volumetric flow rate in the entrance of a channel section, Figure 4-12, $[m^3/s]$ |
| $Q^{out}$ | volumetric flow rate in the exit of a channel section, Figure 4-12, $[m^3/s]$ |
| $r$ | radial position, $[m]$ |
| $r_1$ | radial position of the innermost extremity of the neck channel, Figure 5-7b, $[m]$ |
| $r_1'$ | radial position of the air-liquid meniscus in the sample chamber at initial time instant of the filtration cycle, Figure 5-7b, $[m]$ |
| $r_2$ | radial position of the outermost extremity of the neck channel, Figure 5-7b, $[m]$ |
| $r_2'$ | radial position of the outermost extremity of the filtration chamber, Figure 5-7b, $[m]$ |
| $r_{max}$ | radial position of the outermost extremity of the rotor bucket, $[m]$ |
| $r_p$ | radius of membrane pore, $[m]$ |
| $r_p$ | radius of the circular clamped plate, equation (5-1), $[m]$ |
| $r_p$ | Stokes' radius of a molecule, $[m]$ |
| $R_a$ | apparent rejection, equation (2-6), $[dimensionless]$ |
| $R_g$ | gas constant, $[8.314\ (kg \cdot m^2)/(K \cdot s^2)]$ |
| $R_i$ | intrinsic rejection, equation (2-7), $[dimensionless]$ |
| $R_m$ | intrinsic resistance to water filtration of a membrane, equation (2-3), $[m^{-1}]$ |

| | |
|---|---|
| $R_o$ | observable rejection, the same as $R_a$, $[dimensionless]$ |
| $R^2$ | coefficient of determination, [dimensionless] |
| $Re$ | Reynolds number, equation (2-21) |
| $Re_{dh}$ | Reynolds number based on $d_h$ and $U_{eff}$, equation (2-23) , $[dimensionless]$ |
| $Re_h$ | Reynolds number based on $h$ and $U_0$, equation (2-22), $[dimensionless]$ |
| $Sc$ | Schmidt number, equation (2-24), $[dimensionless]$ |
| $Sh$ | Sherwood number, equation (2-16), $[dimensionless]$ |
| $Sh_0$ | Sherwood number for the non-suction mass transfer process, $[dimensionless]$ |
| $t$ | time, $[s]$ |
| $t$ | thickness of the circular clamped plate, equation (5-2), $[m]$ |
| $t_{ss}$ | necessary time to reach steady-state in a TFF process, $[s]$ |
| $T$ | temperature, [K] |
| $U$ | average velocity, $[m/s]$ |
| $\boldsymbol{U}$ | velocity vector, $[m/s]$ |
| $U_0$ | constant plug flow velocity at the entrance of the channel, equation (2-22), $[m/s]$ |
| $U_c$ | characteristic velocity of the liquid, equations (2-16) and (2-21), $[m/s]$ |
| $U_{eff}$ | effective velocity of the liquid, equation (2-23), $[m/s]$ |
| $U_{max}$ | maximum velocity of the liquid in a channel, equation (2-9), $[m/s]$ |
| $U_{wall}$ | velocity of the liquid at the surface of impermeable walls, Figure 4-11, $[m/s]$ |
| $U_x$ | $x$-component of $\boldsymbol{U}$, $[m/s]$ |
| $\boldsymbol{U_{xz}}$ | two-dimensional velocity vector with $x$- and $z$- components of $\boldsymbol{U}$, $[m/s]$ |
| $U_y$ | $y$-component of $\boldsymbol{U}$, $[m/s]$ |
| $U_z$ | $z$-component of $\boldsymbol{U}$, $[m/s]$ |
| $V_p$ | velocity of the permeate inside the membrane pore, equation (2-41), $[m/s]$ |
| $V_w$ | molar volume of the solvent, equation (2-29), $[m^3]$ |
| $w$ | solute mass fraction, $[dimensionless]$ |
| $w_b$ | solute mass fraction in the bulk of the feed side, $[dimensionless]$ |
| $w_{bLN,sec}$ | logarithmic mean of solute bulk mass fraction in a section of the channel, equation (4-20), $[dimensionless]$ |
| $w_b^{in}$ | solute bulk mass fraction in the entrance of a section of the channel, equation (4-21), $[dimensionless]$ |
| $w_b^{out}$ | solute bulk mass fraction in the exit of a section of the channel, calculated similarly to $w_b^{in}$, $[dimensionless]$ |
| $w_{c,i}$ | solute mass fraction in the cell $i$ of the CFD domain, $[dimensionless]$ |

| | |
|---|---|
| $w_f$ | solute mass fraction in the feed, $[dimensionless]$ |
| $w_m$ | solute mass fraction at the membrane surface in the feed side, $[dimensionless]$ |
| $w_{m,sec}$ | average solute mass fraction at the membrane surface in a section of the channel, equation (4-22), $[dimensionless]$ |
| $w_{m,i}$ | solute mass fraction at the membrane surface of the cell $i$ of the CFD domain, equation (4-22), $[dimensionless]$ |
| $w_m^{in}$ | solute mass fraction at the membrane surface in the entrance of a section of the channel, Figure 4-12, $[dimensionless]$ |
| $w_m^{out}$ | solute mass fraction at the membrane surface in the exit of a section of the channel, Figure 4-12, $[dimensionless]$ |
| $w_{max}$ | maximum deflection of a circular clamped plate, equation (5-1), $[m]$ |
| $w_p$ | solute mass fraction at the membrane surface in the permeate side, or average solute mass fraction in the permeate, $[dimensionless]$ |
| $w$(z) | solute mass fraction along the channel height, $[dimensionless]$ |
| $W$ | width of the channel, $[m]$ |
| $W$ | hindrance factor of convection, equation (2-43), $[dimensionless]$ |
| $W_r$ | width of the square rib, $[m]$ |
| $x$ | spatial coordinate, $[m]$ |
| $x'$ | spatial coordinate in the $x$-direction with origin at the middle location of a circular transverse rib, Figures 4-15 and 4-16, $[m]$ |
| $X_{sw}$ | friction constant between the solute and the solvent, $[(J \cdot s)/(m^2 \cdot mol)]$ |
| $y$ | spatial coordinate, $[m]$ |
| $z$ | spatial coordinate, $[m]$ |
| $z_{1f}$ | distance from the first fringe to the membrane surface, $[m]$ |
| $z_i$ | charge of the ion $i$, equation (2-44), $[dimensionless]$ |

Greek letters

| | |
|---|---|
| $\alpha$ | characteristic angle of the centrifuge rotor, $[rad]$ |
| $\alpha(\rho)$ | dimensionless velocity in membrane pore, equation (2-38), $[dimensionless]$ |
| $\beta$ | angle between the centrifugal force and the membrane surface, $[rad]$ |
| $\Gamma$ | concentration polarization modulus, equations (2-10) and (4-2), $[dimensionless]$ |
| $\delta_D$ | thickness of the concentration boundary layer, $[m]$ |
| $\delta_m$ | thickness of the membrane, $[m]$ |

| | |
|---|---|
| $\delta_M$ | thickness of the momentum boundary layer, $[m]$ |
| $\Delta c_A$ | characteristic concentration difference of solute $A$, $[kg/m^3]$ |
| $\Delta n$ | difference of refractive index between two consecutive fringes in an interferogram, equation (4-1), $[dimensionless]$ |
| $\Delta n_{mb}$ | difference of refractive index between the liquids on the membrane and in the bulk, $[dimensionless]$ |
| $\Delta p$ | pressure drop between two locations, $[Pa]$ |
| $\Delta p_{eff}$ | effective pressure difference between the feed and permeate sides of the membrane, $\Delta p_{eff} = p_m - p_p$, $[Pa]$ |
| $\Delta p_m$ | transmembrane pressure, $[Pa]$ |
| $\Delta t$ | time interval, $[s]$ |
| $\Delta w$ | difference of $w$ between consecutive fringes, equation (4-9), $[dimensionless]$ |
| $\Delta w_{LNwb}$ | logarithmic mean difference of $w$ between the membrane surface and the bulk solution at the inlet and outlet of each section, equation (4-24), $[dimensionless]$ |
| $\Delta \pi$ | difference between two osmotic pressures, $[Pa]$ |
| $\Delta \pi_m$ | difference between the osmotic pressure through the membrane, $[Pa]$ |
| $\varepsilon$ | porosity of the medium, $[dimensionless]$ |
| $\varepsilon$ | tolerance criterion to stop an algorithm, Figure 4-13, $[dimensionless]$ |
| $\theta$ | flow attack angle, $[rad]$ |
| $\theta_1$ | flow attack angle between bulk flow and the filaments of the bottom layer of a mesh, Figure 4-6, $[rad]$ |
| $\theta_2$ | flow attack angle between bulk flow and the filaments of the bottom layer of a mesh, Figure 4-6, $[rad]$ |
| $\lambda$ | wavelength of the light, equations (4-1) and (4-9), $[m]$ |
| $\lambda$ | sieving factor, $\lambda = r_s/r_p$, $[dimensionless]$ |
| $\mu$ | dynamic viscosity, $[kg/(m \cdot s)]$ |
| $\mu_w$ | dynamic viscosity of liquid water, $[kg/(m \cdot s)]$ |
| $\nu$ | kinematic viscosity, $[m/s]$ |
| $\nu$ | Poisson's ratio, equation (5-2), $[dimensionless]$ |
| $\xi$ | zeta potential, $[V]$ |
| $\Xi$ | generalized mass transfer correction factor, equations (2-19), (4-3) and (4-5), $[dimensionless]$ |
| $\pi_f$ | osmotic pressure of the liquid in the feed, $[Pa]$ |
| $\pi_m$ | osmotic pressure of the liquid at the membrane surface (feed side), $[Pa]$ |
| $\pi_p$ | osmotic pressure of the liquid at the membrane surface (permeate side), often |

| | |
|---|---|
| | referred as osmotic pressure of the permeate, $[Pa]$ |
| $\rho$ | density, $[kg/m^3]$ |
| $\rho$ | dimensionless radial distance in membrane pore, $[dimensionless]$ |
| $\rho_m$ | density of the liquid at the membrane surface in the feed side, $[kg/m^3]$ |
| $\rho_p$ | density of the liquid at the membrane surface in the permeate side, $[kg/m^3]$ |
| $\sigma$ | reflection coefficient, equation (2-35), $[dimensionless]$ |
| $\varphi$ | electrical potential within the membrane pore, equation (2-44), $[V]$ |
| $\Phi(\rho)$ | dimensionless potential accounting all the surface forces, equation (2-39), $[dimensionless]$ |
| $\phi$ | ratio between $Pe$ number and $Sh_0$, equation (4-4), $[dimensionless]$ |
| $\psi$ | angle between bottom and top filaments in a two-layer mesh, Figure 4-6, $[rad]$ |
| $\omega$ | angular velocity, $[rad/s]$ |

Other symbols

| | |
|---|---|
| d$x$ | elemental $x$ |
| $\partial$ | partial derivative |
| $\nabla$ | gradient |
| $\nabla^2$ | divergence |
| $\bar{x}$ | average of $x$ |

# List of acronyms

| | |
|---|---|
| 2D | two-dimensional |
| 3D | three-dimensional |
| AFM | atomic force microscopy |
| ATR-FTIR | attenuated total reflection coupled to Fourier transform infrared spectroscopy |
| BPV | back-pressure valve |
| BSA | bovine serum albumin |
| CCD | charge-coupled device |
| CNF | centrifugal nanofiltration |
| CP | concentration polarization |
| CPU | central processing unit |
| CUF | centrifugal ultrafiltration |
| DHI | digital holographic interferometry |
| DNA | deoxyribonucleic acid |
| ENP | extended Nernst-Planck equation |
| HI | holography interferometry |
| LDV | laser Doppler velocimetry |
| LOC | lab-on-a-chip |
| MD-SF-PF | modified surface force - pore flow |
| MEMS | microelectromechanical systems |
| MF | microfiltration |
| MRV | magnetic resonance velocimetry |
| MW | molecular weight |
| MWCO | molecular weight cut-off |
| NF | nanofiltration |
| PDMS | polydimethylsiloxane |
| PIV | particle imaging velocimetry |
| RBS | Rutherford backscattering spectroscopy |
| RCF | relative centrifugal force |
| RO | reverse osmosis |
| RPM | rotations per minute |
| SEM | scanning electron microscopy |
| SEM-EDS | SEM coupled to energy dispersive x-ray spectroscopy |
| SHM | starred-herringbone micromixer |

| | |
|---|---|
| SIV | scalar image velocimetry |
| SWMM | spiral wound membrane modules |
| TFC | thin-film composite |
| TFF | tangential flow filtration |
| TFN | thin-film nanocomposite |
| TMP | transmembrane pressure |
| UF | ultrafiltration |
| XPS | x-ray photoelectron spectroscopy |
| μTAS | micro total analysis systems |

# 1 Introduction

## 1.1 Thesis overview

The main scope of the present thesis is the development of pressure-driven membrane filtration techniques[1] capable to concentrate low molecular weight (MW) solutes present in small-volume liquid samples. This is a niche of application not yet covered by any kind of technology in the membrane field. Conversely, for the scenarios where it is intended to concentrate large MW solutes or large sample volumes, one can use diverse well-established techniques (Mulder 1996; Baker 2004). These techniques differ in the installation size but function based on using slit or hollow fiber filtration channels (for medium-to-high amounts of liquid) and on using batch stirred cells or centrifugal filtration devices (when the objective is that the membrane retains particulate matter or large solutes present in small samples). In Figure 1-1 the ranges of application of such common techniques are shown and it is also evidenced the niche requiring significant developments, i.e. for the separation of small-volume samples of low MW solutes, which is precisely the focus of the present thesis.

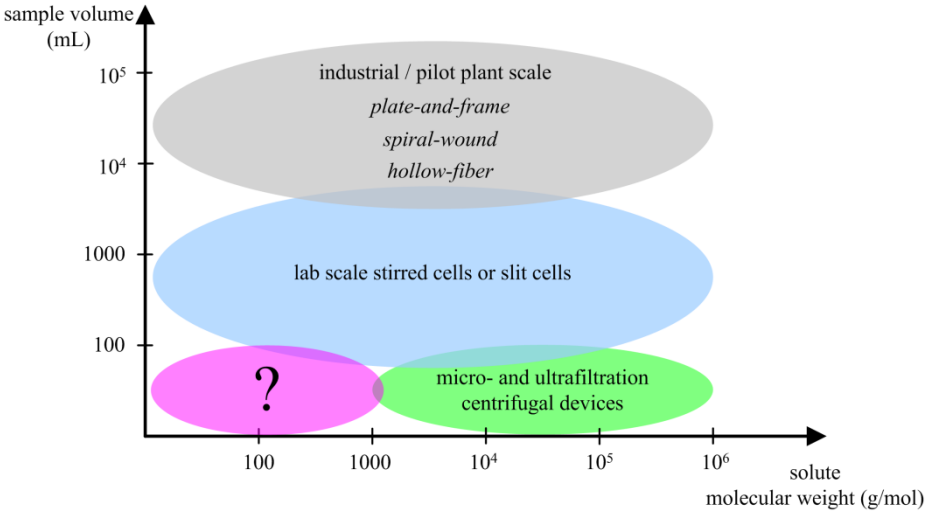


Figure 1-1 – The niche for the separation processes of small-volume samples of low molecular weight solutes.

Despite being a small niche in terms of molecular weight (MW lower than 1000 g/mol) and sample volume (less than 100 mL), the identified gap possesses a high potential interest both for scientific research and for commercial applications. Examples of practical application

[1] Pressure-driven membrane filtration is a group of well-established techniques used to separate liquid solutions into two or more fractions. A more detailed description of these techniques will be given ahead in section 2.1.1.

are the concentration, for further analysis, of small compounds present in body fluids or in the environment. However, there is no currently available technique or device capable of concentrating small samples of low MW solutes in a cheap and fast way. Small solutes can be fractionated by chromatographic techniques, but to do so highly qualified personnel and expensive equipment is needed. Thus, the existence of devices working based on membrane processes that can fulfill the concentration purposes has clearly an interesting economic viability.

It is for that particular small niche that it is intended to develop filtration devices capable of achieving high concentration factors[2]. The two filtration techniques that can be seen as the most obvious candidates to reach such objective are: tangential flow filtration (TFF) and centrifugal filtration[3]. Therefore, these two techniques will be studied and evaluated extensively in order to assess their potentials and limitations.

As said before, it is intended that the developed concentration devices are based on pressure-driven membrane processes. However, these separation processes are affected by concentration polarization (CP) and fouling phenomena[4], leading to flux decline and a decrease in the quality of solute separation. Therefore, the developed devices should tackle these issues, especially because the filtration resistance increases with the osmotic pressure of the solution, and this increases both as the MW of the solute decreases and its concentration increases. Thus, to be considered efficient, a filtration device must be capable of minimizing CP and fouling phenomena.

For sample volumes above 100 mL, filtration can be easily performed with stirred or TFF filtration cells since there are convenient methods to handle the liquids and, at the same time, mitigate CP and fouling effects. Some of these methods will be described in Chapter 2 aiming their application in small-volume filtration processes.

For sample volumes lower than 100 mL, which is the sample range of interest in this work, if one is interested in obtaining high concentration factors, the stirred and TFF cells might be unsuitable. The use of dead-end stirred cells would result in filtration almost to dryness leading to the inefficiency of the stirring mechanism and the consequent increase of CP and fouling. On the other hand, TFF also poses some issues. First, reaching high concentration factor is equivalent to obtain high feed recovery which practically turns the TFF system into a dead-end filtration one. Second, while for stirred cells there is no net macroscopic liquid movement, as the cell is hydrostatically pressurized by compressed gases, for TFF processes a

[2] As it will be defined later in section 2.3.1 the concentration factor is the ratio between the solute concentration in the concentrate and in the sample (or feed).

[3] Centrifugal filtration technique refers to a pressure-driven membrane filtration technique that uses centrifugal force as the mean to both pressurize the system and mitigate flux decline phenomena that arise due to concentration polarization (CP) and fouling.

[4] Concentration polarization phenomenon is one of the limiting causes of filtration efficiency. Since the membrane is a selective barrier, the solute concentration and, subsequently, the osmotic pressure near the membrane surface increases leading to a reduction of both the permeate flux and the permeate quality. A more detailed description of CP phenomenon can be found in section 2.1.4.

pump to impel the liquid flow is usually necessary. Since pumps only work properly if primed with liquid, this means that some amount of sample will be left unfiltered. Moreover, depending on the design of the hydraulic system, retention volumes, which are always present, can be significant when dealing with small-volume samples. This amount of sample inappropriately processed would have an intolerable cost when dealing with unique samples or with high value substances. Although TFF presents all these issues, it is the most straightforward technique to be used and, for that reason, its performance will be evaluated.

The use of nanofiltration membrane integrated in microfluidic TFF devices may be an option to concentrate low MW solutes in small-volume samples (Kaufman et al. 2012; Wardrip & Arnusch 2016). However, most of the published studies on this technique deal only with nanofiltration at low concentration factors, while in the only work where a high concentration factor (above 10) was reached the sample was very diluted (Kaufman et al. 2012). Therefore, in this work, it will be assessed the capability of TFF to perform the desired solute concentration but at higher concentration factors than done before by other authors. Thus, not only the potential of concentration by microscale TFF will be evaluated but also its results will serve as benchmark to compare with the centrifugal filtration results obtained thereafter. A comprehensive literature review on the application of nanofiltration at microscale is presented in Chapter 3.

Another option to concentrate low MW solutes in small-volume samples is centrifugal filtration, which is commonly used nowadays to filter particulate or colloidal mater and solutions containing solutes with MW above 1000 g/mol. Examples of practical applications include the concentration, or separation, of cells (Wunderlich et al. 2016) and cell particulates (Yang et al. 2015), viruses (Hata et al. 2014; Ahmed et al. 2015), DNA chains (Zhou et al. 2008; Borujeni & Zydney 2012) and proteins (Zhloba & Subbotina 2014; Tang et al. 2015). Therefore, the use of similar centrifugal devices to filter solutions of solutes with MW below 1000 g/mol would appear to be straightforward, just by replacing the currently used micro- and ultrafiltration membranes by others with tighter structure. However, that strategy would not work due to several reasons, including the need to apply high pressure and its fast decrease as the filtration proceeds. In fact, an important part of the present work was devoted to study the limitations of the current centrifugal devices and to devise a strategy to overcome them. A detailed description of the available commercial devices and on the developed centrifugal device is one of the subjects of Chapter 5.

The apparent little interest in the development of efficient centrifugal filtration devices adequate to filter low MW solutes, shown by the major players, should not be due to the lack of applicability of such product. In fact, in the last decades, a new interest on the research on some substances of low MW has emerged, as are the cases of finding disease biomarkers and the detection and quantification of toxic compounds in the environment or in body fluids. Thus,

there are several active research areas where the liquid samples are separated into "light" and "heavy" fractions using centrifugal filtration using ultrafiltration membranes. The application of tighter membranes would allow extra separation stages of the "light" fraction and, thus, a deeper insight into their molecular distribution.

There are several application fields where centrifugal filtration is already applied to separate small from large size molecules; however, only ultrafiltration membranes are currently used. Thus, depending on the molecular cut-off of the membrane applied in the centrifugal ultrafiltration (CUF) devices, the low MW solutes may be recovered in the permeate which is analysed without any further concentration. For instance, in the life sciences field, a continuous effort is being done to relate the presence of small molecules in body fluids, or changes in their concentration, with the occurrence of diseases, i.e. the detection of biomarkers. These can include peptides[5] which are generated from protein synthesis and lysis (Lai et al. 2015). Since in pathological conditions the metabolism may be changed, altering the peptidome profile, peptides have been used as biomarkers for hepatic cancer (Orvisky et al. 2006), colon cancer (Greening et al. 2013) and other diseases (Bateson et al. 2011). In a related area, screening drugs in biological fluids is another area where such separation would be relevant since the MW of many of those compounds is smaller than 1000 g/mol (Zhang et al. 2012). In the environmental field, more restrictive laws and with the environmental concerns in the public eye, chemical industries tend to pay more attention to monitoring their potential harmful activities. Examples include the determination of uranium in contaminated soils (Graham et al. 2011) and the impact of mine drainage on the metallic ions dissolved in groundwater (Chamier et al. 2015), but other applications can be developed based on the fact that tighter membranes, like nanofiltration membranes, retain common drugs (Ge et al. 2017) and toxic compounds dissolved in water (Sorin et al. 2004; Z. Liu et al. 2012). Another field concerns to those who work in the chemical/biological synthesis of very tiny amounts of high value products. In all these scenarios, the existence of a simple, cheap and reliable technique to perform the concentration and/or fractionation of small-volume samples would be of great significance.

It is within this scope that the present thesis is inserted. The main subject of this thesis is to develop the concept, study the feasibility, and materialize innovative devices to concentrate small-volume liquid samples containing low molecular weight solutes.[6] Although it is intended that such devices may concentrate any kind of solution, in the experiments run in the present work only binary water-solute solutions were used. The use of synthetic binary solutions of low

[5] A peptide is a polymeric chain of amino acids monomers (usually less than 50). In human genome there are 20 different amino acids and their MW range varies between 75 g/mol (for glycin) and 204 g/mol (for tryptophan). A protein is a group of one or more peptides, arranged in a biologically functional way.

[6] Herein, small-volume samples refer to solutions with a volume too small to be processed efficiently by commonly used pressure-driven filtration devices. Low molecular weight solutes refer to substances with MW lower than 1000 g/mol.

MW solutes has two advantages. First, binary solutions permit the assessment of nanofiltration efficiency more easily than if complex solutions were used, because these may present intricate relationships between permeation performance and solution composition. Second, using synthetic solutions, scaling and fouling issues are minimized and one can focus only on CP effects.

As mentioned above, the use of centrifugal filtration devices similar to those utilized for large MW solutes and/or particulate matter might emerge as a sound approach. However, and despite the fact that centrifugal force enhances the permeation process by mitigating the concentration polarization and fouling effects even for low MW salts, as reported in several works of other authors (Andeen 1981; Eid & Andeen 1983; Bergen et al. 2000; Fyles & Lycon 2000; Bergen et al. 2003), the simple replacement of coarser membranes by tighter ones (nanofiltration or reverse osmosis membranes) is not enough. Therefore, a more efficient centrifugal device is developed in this work and, in parallel, the potential of a micro-TFF system is assessed, both aiming the concentration of low MW solutes in small-volume samples.

In pressure-driven membrane filtration, the osmotic pressure of the liquid sample plays an important role in the process performance. For the same membrane area, the flux of liquid passing through the membrane is inversely proportional to the solution concentration. Moreover, the osmotic pressure increases as the MW of the solute decreases. Thus, solutions containing low MW solutes are very difficult to filter, when compared to solutions of high MW solutes with the same concentration. While the latter solutions are easily filtered at low pressure, high pressure is needed to filter the former. As it will be seen later, the pressure generated by the centrifugal force on the liquid is proportional to the liquid head and to the angular velocity of the centrifugal filtration device. Using common lab scale centrifuges, and common filtration cartridges, pressure up to 5 – 20 bar (depending on the equipment) can be achieved at the initial instants of the filtration process, which is enough to filter particulate matter or solutions of high MW solutes (usually less than 2 bar is needed). However, current centrifugal filtration devices are not suitable to filter solutions of high osmotic pressure (low MW solutes) not only because they need higher pressure (usually in the range between 10 and 50 bar) but also because that due to their design, the pressure on the liquid drops sharply along the filtration cycle. This fact turns the filtration even harder, as the filtration cycle proceeds and the solution becomes more concentrated. Thus, to filter this type of solutions, using a centrifugal technique, one needs to develop devices capable of reaching the necessary pressure and maintain it during the most part of the filtration cycle.

The previous discussion evidences the reasons why an important part of the present work is devoted to the design and operation of a centrifugal filtration device suitable to perform the filtration of small-volume samples of low MW solutes or of high osmotic pressure. Due to the MW range focused in this work (MW < 1000 g/mol), the technique and device developed herein

are named centrifugal nanofiltration (CNF), as opposed to the already existent centrifugal ultrafiltration (CUF) for higher MW solutes. Nonetheless, one should not restrict the fields of application of the developed device, since it should also be able to filter low osmotic pressure solutions that are commonly processed by CUF devices.

Succinctly, the developed centrifugal filtration device is made up of a cylindrical tube where a membrane separates the concentrate from the permeate liquids. The sample is placed in the sample chamber inside the device, the device is made to rotate around a rotation axis in a centrifuge, and the filtration proceeds due to the pressure created by the centrifugal force. Using the selected design for the CNF device, the upstream of the membrane consists of three chambers: the sample chamber (where most of the sample is placed); the filtration chamber (where the filtration occurs) and the concentrate chamber (where the concentrated liquid is accumulated). The downstream of the membrane consists of the permeate chamber (where the liquid that passed through the membrane is collected). In the development of the CNF device the following points were addressed: a) assessment of its use to filter small-volume samples of low MW solutes producing clear permeate liquids; b) obtainment of high concentration factors for the concentrated liquids; c) study of the impact of the height of the filtration chamber on the filtration performance (heights from 0.1 mm to 2.4 mm were tested); d) study of the impact of the angle between the centrifugal force and the membrane surface on the filtration performance (angles between -10° and +10° were tested).

TFF and CNF were the two selected techniques to be assessed in this work. It was observed that the use of the TFF microdevice results in fair solute concentration, even though it consists in a simple open slit channel with a height of 0.25 mm where none of the methodologies to mitigate concentration polarization were applied. To enhance further the TFF performance more efficient channel geometries and/or the use of static mixers is necessary. The evaluation of such improved devices can be done experimentally or by CFD simulations, but both these two techniques are very time and/or money consuming. Therefore to fasten the development of innovative microscale filtration devices a hybrid computational / semi-empirical method was developed (Chapter 4), which is herein called as hybrid method.

The developed hybrid method speeds up the prediction of the nanofiltration data (like the permeate flux and the solute concentration data) by correlating the mass transfer coefficient for non-suction[7] mass transfer processes with the corresponding permeation ones. In the developed hybrid method, the mass transfer coefficient for the non-suction process is determined by computational simulation of the flow in impermeable-dissolving wall channels, while making use of a correction factor, developed by other authors (Geraldes & Afonso 2006), the mass

[7] As non-suction processes are meant those mass transfer processes in which a membrane is not used. Examples of non-suction mass transfer processes are impermeable-dissolving wall and electrode processes.

transfer coefficient for the permeation process is obtained from the former. Hence, provided that the mass transfer coefficient of the non-suction process is known in advance, the filtration performance can be obtained easily using a simple algorithm that couples the equations quantifying the filtration system. The mass transfer coefficients of non-suction processes can be obtained using pre-determined semi-empirical correlations[8] or, if they are unavailable, by simulating the non-suction processes by CFD, which is faster than computing the full permeation process model. Therefore, the developed hybrid method strategy paves the way for the efficient simulation of complex 3D geometries and may be used for finding optimal feed spacer geometries.

The hybrid method was validated by comparing the predicted values of permeate flux and solute concentration with the corresponding results of CFD simulations for the same nanofiltration processes. For the hybrid model calculations, the mass transfer coefficients of non-suction processes were determined by CFD, using a impermeable-dissolving wall model, while the CFD simulations of the nanofiltration processes were validated by experimental data obtained using the holographic interferometry (HI) technique. Since the hybrid method is intended to be used for the development of channels and static mixers at microscale, where the Reynolds number is usually small, the validity of the hybrid method was checked for Reynolds numbers in the range between 0.8 and 10 for flows in open and ribbed channels. Nevertheless, HI experiments were performed up to Reynolds number of 125. Due to limitations of the HI technique, the slit channel used to study of the CP phenomenon had a height of 2 mm. In addition, the momentum transfer in the CFD model was validated comparing the velocity fields obtained numerically with those acquired by micro-PIV experiments.

The HI technique permits to assess the solute concentration field in two-dimensional flows and it was used to monitor the parameters that influence the concentration polarization phenomenon including: the flow rate, the transmembrane pressure, the solute concentration, the geometry of the channel and the time. A comprehensive literature review on the application of micro-PIV and of holographic interferometry is presented in Chapter 4. In this same chapter, a review on the main conclusions on the hydrodynamics and mass transfer of flows inside slit channels filled with static mixers is shown.

Both tangential flow and centrifugal filtration are pressure-driven membrane filtration processes. As such, the fundaments of membrane science and technology are presented prior to their study (Chapter 2). Since these processes are affected by CP and fouling phenomena, the methods for their mitigation are discussed and this will be used as reasoning for the selection of the centrifugal filtration as technique under study. Although all the CP mitigation methods

[8] The semi-empirical correlations are usually in the form of the Sherwood number as function of the domain geometry, of the Reynolds number and of the Schmidt number. The formal definitions of these three dimensionless numbers are shown in section 2.2.1

considered in the literature were studied, only the ones with evident potential for small scale application were subject to a more in-depth description in the present thesis. In addition, since this work only deals with nanofiltration of binary water-solute solutions, fouling phenomena may be neglected and one can focus only on the CP effect.

This dissertation shows that CNF is an efficient and reliable method to concentrate small-volume samples of binary aqueous solutions of low MW solutes. Although TFF and CNF have identical concentration efficiency for dilute solutions, the TFF performance decreases faster than the one of CNF as the sample concentration increases. In fact, for medium sample concentration (corresponding to an osmotic pressure of 2.6 bar) the concentration factor obtained using CNF were higher than those obtained using TFF, for similar applied pressures. It was also verified that the height of the filtration chamber of the CNF device and the angle between the centrifugal force and the membrane surface play significant roles in the filtration performance. The best results were obtained for filtration chamber heights between 0.2 mm and 0.6 mm and when the membrane surface was oriented such that the centrifugal force dragged the most concentrated fluid elements away from it.

The results obtained in this thesis shows that it is feasible to concentrate small-volume solutions (with medium-to-high osmotic pressure) using pressure-driven membrane processes. However, to reach concentration factors higher than 10 the concentration polarization phenomenon should be mitigated. Despite only binary aqueous solutions have been used in this work, the CNF technique looks to be the most promising one to be used in a consistent way for the concentration or fractionation of multicomponent solutions, which should be subject of future studies, especially after optimization of the membrane orientation relative to the centrifugal force vector.

## 1.2 Thesis structure

This thesis is structured in seven chapters and a brief description of their content is given below.

The present Chapter 1 makes an overview of the thesis, presents the reasoning for the selected theme and the significance that its output can have on the development of the techniques to concentrate small-volume samples. In this chapter it is also presented all the work performed during the thesis, the structure of the thesis document and the publications already published, or to be published in a near future, that have arisen as outcome of the thesis.

In Chapter 2 (Fundaments of pressure-driven membrane processes) are discussed the basic concepts of membrane science and technology, especially those related with pressure-driven membrane processes. Special focus is given to the techniques and methodologies used to

characterize membranes, to quantify filtration performance and mass transport, and to the methods that can be used to mitigate the CP phenomenon.

In Chapter 3 (Tangential flow nanofiltration of small-volume samples of low molecular weight solute solutions) it is described, analysed and discussed the performance of the micro-TFF cell. A brief literature review on the work of other authors related with nanofiltration at microscale is presented. The experimental work in this chapter included the characterization of the used membranes in terms of their permeability and solute rejection performance, the verification that CP effects exist in TFF processes, and the evaluation of the concentration by micro-TFF of low MW solutes in small-volume samples.

Chapter 4 (Development of a hybrid computational / semi-empirical method to predict NF performance and its validation by experimental visualization) has several capstones. The main purpose of the chapter is to demonstrate that it is possible to use the developed hybrid method to predict the nanofiltration data in processes conducted at low Reynolds numbers inside channels filled with static mixers. Subsequently, the hybrid method can be used to evaluate and optimize innovative channel designs for their use in micro-TFF systems. However, to validate the hybrid method, the models used for the CFD simulations had to be validated before. That was accomplished comparing the results of particular CFD simulations with the experimental data obtained by micro-PIV and by holographic interferometry techniques. After the validation of the CFD models, the simulation results are then used both to assess the mass transport periodicity of the nanofiltration process and to compare it with the results of the hybrid algorithm. In this chapter, a brief literature review on the works of other authors related with micro-PIV, holographic interferometry and with flows inside channels with transversal or mesh spacers is also presented.

The developed CNF device and its performance are described, analysed and discussed in Chapter 5 (Centrifugal nanofiltration of small-volume samples of low molecular weight solutes). The first experimental part of the chapter is devoted to validate the concept of nanofiltration by centrifugation showing that it produces clean permeates. The focus of the second experimental part of this chapter is the effect, on the filtration performance, of the height of the filtration chamber and of the angle between the centrifugal force and the membrane surface. For the development of the CNF device, a comprehensive literature review was made considering not only papers from scientific journals but also using the many disclosed patents that cover the subject.

In Chapter 6 (Comparison between centrifugal and tangential flow nanofiltration) it is made a comparison between the two methods used for the concentration of small-volume samples containing low MW solute (micro-TFF and CNF) in terms of their benefits and limitations.

Chapter 7 (Conclusions and future work) summarizes the principal findings and conclusions of the thesis and presents possible directions to prospective work. The latter should include, among others, the further development of the CNF and micro-TFF devices and their application to fraction multicomponent solutions.

In addition to the main chapters of the thesis, six appendices archive information not suited to be included in the previous chapters, or that would defocus the discussion from the main issues. The properties of aqueous solution used in this work are summarized in Appendix A, while Appendix B shows the calibration curves used for quantitative analysis of the binary solutions. Additional information on the setup of the micro-TFF system is shown in Appendix C. In Appendix D it is shown the development of the concentration boundary conditions used in CFD. Appendix E shows the specifications of the centrifuge and centrifuge rotors. Finally, in Appendix F are summarized the main experimental procedures.

## 1.3 List of publications arising from this thesis

**Papers published in peer-reviewed journals**

C. Completo, V. Geraldes, V. Semião, *Rheological and dynamical characterization of blood analogue flows in a slit*, International Journal of Heat and Fluid Flow, 46, 17-28 (2014)

C. Completo, V. Semião, V. Geraldes; *Efficient CFD-based method for designing cross-flow nanofiltration small devices*, Journal of Membrane Science, 500, 190-202 (2016).

C. Completo, V. Geraldes, V. Semião, M. Mateus, M. Rodrigues; *Centrifugal nanofiltration for small-volume samples*, Journal of Membrane Science, 540, 411-421 (2017).

*Papers to be prepared and submitted to peer-reviewed journals*

It is intended to publish a paper with the main outcomes from chapters 3, 5 and 6, especially those related with the comparison between the TFF and the CNF methodologies to concentrate small-volume samples containing low molecular weight substances. It is worth to mention that none of the information present in chapters 3 and 6 was published in the previous papers.

**Patent applications**

V. Geraldes, V. Semião, M. Rodrigues, C. Completo; *Dispositivo de filtração centrífuga e método para concentração de misturas líquidas*, Pedido de Patente de Invenção Nacional nº 109932, Boletim da Propriedade Industrial, 163/2018 (to be published in 24/08/2018). Patent application with priority date of 24/02/2017.

**Posters in conferences**

C. Completo; *Development of centrifugal nanofiltration for efficient concentration of small samples*, PhD Open Days, Lisboa, Portugal, (2016).

C. Completo, V. Semião, V. Geraldes; *Effective methods for nanofiltration of small volume samples*, Encontro Ciência'16, Lisboa, Portugal, (2016).

C. Completo, V. Semião, V. Geraldes; *Concentration of small volume samples using Centrifugal Nanofilttration*, Encontro Ciência'17, Lisboa, Portugal (2017).

# 2 Fundaments of pressure-driven membrane processes

The first two sections of this chapter present the fundamental concepts of pressure-driven membrane processes and the classical models of mass transport through the membrane. The last section examines methods usually used to reduce concentration polarization in order to, subsequently, select the most appropriate ones to concentrate small-volume samples of low MW solutes.

## 2.1 General concepts

Membrane filtration processes refer to the separation of substances present in a feed stream by means of a membrane (Mulder 1996; Baker 2004). Thus, a membrane is any selective barrier to the transport of substances through it. Since the membrane is selective, the transport through it is more effective for some substances contained in the feed than for others, resulting in the fractionation of the feed stream into a permeate stream (the fraction that crosses the membrane) and a concentrate stream (the fraction that is retained by the membrane). However, for mass transport to take place a driving force must be applied.

Although different types of driving forces have been used in membrane processes, in this work the focus is put only in pressure-driven membrane processes, i.e. processes where the driving force is a pressure difference between both sides of a membrane: the so-called transmembrane pressure, TMP or $\Delta p_m$.

### 2.1.1 Pressure-driven membrane processes

Pressure-driven membrane processes can be categorized into four main groups [9]: microfiltration (MF), ultrafiltration (UF), nanofiltration (NF) and reverse osmosis (RO). No sharp distinction can be made between these four operations since all of them perform the same process: part of the solvent and of some of the solutes permeate through the membrane, while other solutes are retained in the feed side. However, MF/UF/NF and RO processes are commonly distinguished in terms of the size range of the solutes, or dispersed particles, that the membrane retains, as depicted in Figure 2-1.

Microfiltration separates fine particles from liquid suspensions using symmetric or asymmetric porous membranes. Due to the large pore diameter of MF membranes (from 0.1 µm

[9] Gas-gas and gas-liquid separations can also be performed by pressure-driven membrane process but these processes are not covered here.

to 10 μm) the filtration is based on the size exclusion principle and the applied $\Delta p_m$ is small (usually in the range from 0.1 bar to 2 bar).

Ultrafiltration is another low-pressure process ($\Delta p_m$ in the range from 1 bar to 10 bar) that also separates compounds and colloids by the size exclusion principle. Given that the pore diameter of UF asymmetric membranes lies in the range between 1 nm to 100 nm, these membranes retain from medium-to-large solutes (MW > 2000 g/mol) to small particulate matter (like small virus or cell debris).

Nanofiltration separates small molecules or bivalent ions (MW from 200 g/mol to 2000 g/mol) from the solvent using thin-film composite (TFC) membranes with characteristic pore diameter lower than 2 nm. Due to the very small pore diameter of the membrane, the mass transport in NF is explained both by the sieving effect and by a solution-diffusion mechanism, which states that the solvent and solutes in the feed side dissolve into the membrane material and diffuse through it. To maintain a satisfactory permeate flux, $\Delta p_m$ between 10 bar and 25 bar are necessary.

Finally, in reverse osmosis even smaller substances (like monovalent $Na^+$ and $Cl^-$ ions) are retained by the membrane. To keep salt rejection higher than 99%, the pore diameter of the used asymmetric TFC membranes should be smaller than 0.6 nm (Lee et al. 2011) and, therefore, the permeation also occurs by the above-mentioned solution-diffusion mechanism. In RO processes, $\Delta p_m$ lies usually between 20 bar and 100 bar due to the substantial osmotic pressure of small salt solutions.

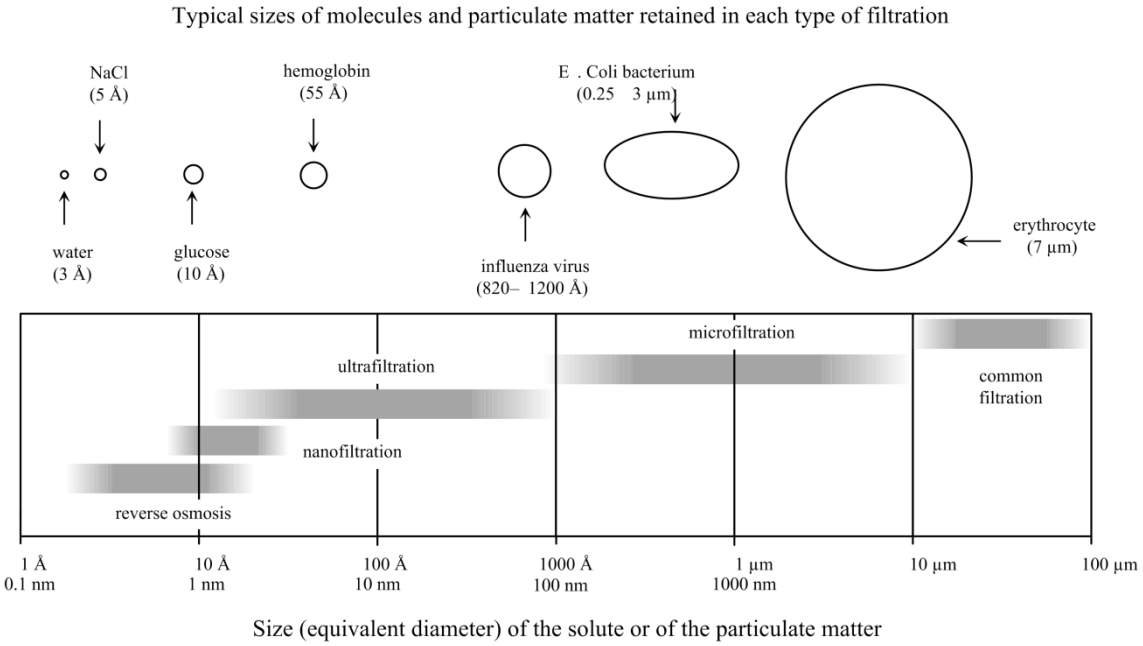


Figure 2-1 – Comparison between the typical size of molecules, or of particulate matter, versus the typical membrane pore diameter and identification of the range of each pressure-driven membrane process. The sizes of molecules and particulate matter are not at scale.

### 2.1.2 Polymeric membranes for pressure-driven membrane processes

Membranes for pressure-driven processes are grouped in terms of their constituting materials and morphologic structure.

Regarding their constituting materials, membranes can be polymeric, ceramic or metallic. Ceramic and metallic membranes are more stable than polymeric ones since they support higher physical and chemical stresses (Kim et al. 2005; Grein et al. 2013; Ambrosi et al. 2014; Xie et al. 2015; Das et al. 2016; Dickhout et al. 2016). In addition, ceramic and metallic membranes are more durable, less prone to fouling, have narrower pore size distribution and exhibit almost no swelling by solvents. However, these membranes have as major disadvantage their cost (usually at least 4 times more expensive than polymeric membranes). Other limitations are their heavier weight, brittleness, and lower capability for physical and chemical surface modification. Due to their lower cost and fair properties, the vast majority of pressure-driven membrane processes use polymeric membranes.

Regarding their morphologic structure, polymeric membranes can be described as symmetric or asymmetric, as sketched in Figure 2-2. The structure of symmetric membranes is uniform in the whole volume of the membrane. Symmetric membranes can be dense or porous, while the asymmetric ones can be integrally skinned membranes or composite membranes.

Integrally skinned membranes are made of a single material and the structure through the membrane is differentiated during the manufacturing process, usually resulting in a 0.1 µm to 1 µm thin dense layer over a 100 µm to 200 µm porous layer. Composite membranes are made of several layers of, possibly, different materials.

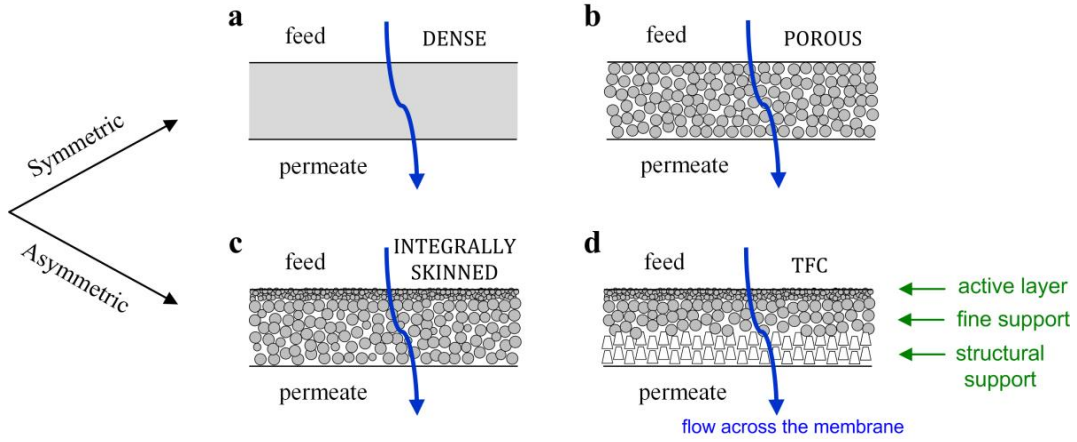


Figure 2-2 – Sketches of the four common membrane structures: a) symmetric dense membrane; b) symmetric porous membrane; c) asymmetric integrally skinned porous membrane; d) thin-film composite membrane.

Since the flux through the membrane is inversely proportional to the thickness of the membrane, the most successful commercial membranes are those made of a thin selective layer

supported on a coarser structure. This is the case of the integrally skinned membranes, as those based on the Loeb-Sourirajan method (Loeb & Sourirajan 1963), and of the thin-film composite (TFC) membranes, as those based on the Cadotte method (Cadotte et al. 1980). The selective layer of the latter type has a very small thickness, between 20 nm and 200 nm (J. Wang, Dlamini, et al. 2014). Although the support layers below the selective layer are usually considered as non-significant for mass transport, recent research has shown that the porosity and the pore size of such support layers may contribute the enhance or lessen the membrane performance (J. Wang, Dlamini, et al. 2014).

The Loeb-Sourirajan method is a phase inversion process where a solution of a polymer is cast on a support and immersed in a semi-miscible non-solvent bath (Guillen et al. 2011). The solvent exchange between the two phases makes the polymer precipitate and form the membrane. Different membrane properties can be obtained by selecting appropriately the polymer, the solvents and by tuning the operating parameters (temperature, time of contact, etc). An interesting brief historical resume about the development of the Loeb-Sourirajan method is described by the author itself (Loeb 1981).

Thin-film composite membranes are obtained by the Cadotte method consisting of the deposition of a very thin, and selective, membrane over a support by interfacial polymerization. Succinctly, a coarser support is soaked in a pre-polymer solution and then immersed in a solution containing the reactive agent (Buonomenna 2013). On the interface of the solutions, the polymerization reaction takes place resulting in a very thin membrane over the initial coarser support. Varying the reacting substances, and operating parameters, membranes with different properties are obtained.

Since the present work is not focused on membrane synthesis, further details on membrane production can be found in the many reviews on the subject (Petersen 1993; Lalia et al. 2013; Paul & Jons 2016).

More recently, thin-film nanocomposite (TFN) membranes, or mixed-matrix membranes, have been developed, where nanoparticles of organic or inorganic materials (graphene, carbon nanotubes, zeolites, oxide particles, etc.) are incorporated into the membrane structure to improve its properties (Kim & Bruggen 2010; Buonomenna 2013; Daer et al. 2015; Goh et al. 2015; Giwa et al. 2016).

Another type of composite membranes is that where functional layers are coated or grafted on the membrane surface.

### 2.1.3 Membrane characterization

Membrane properties influence the interaction between solvent, solutes and the membrane itself. Therefore, to predict adequately the performance of a specific membrane, its properties must be well characterized. The characterization of membranes can be divided into three groups: performance, morphological and physical/chemical/biological characterization. The main parameters and techniques used for membrane characterization are described in the following sub-sections.

**Performance characterization**

The performance of a pressure-driven membrane is usually quantified by two types of parameters: hydraulic permeability and solute permeability.

Hydraulic permeability

Hydraulic permeability is related to the amount of solvent that passes through a membrane per unit of area and per unit of time. When the feed is pure water, the pure water permeate flux, $J_w$, is given by

$$J_w = \frac{Q_w}{A_m} \tag{2-1}$$

where $Q_w$ is the volumetric pure water flow rate and $A_m$ is the membrane surface area. Since it is the pressure gradient between both sides of the membrane that makes the water flow through the membrane, then, the water flux increases with the increase of the transmembrane pressure. The hydrodynamic permeability of a membrane, $L_p$, gives the increment of the pure water permeate flux per unit of transmembrane pressure

$$L_p = \frac{J_w}{\Delta p_m} \tag{2-2}$$

In addition, the hydrodynamic permeability is also used to determine the resistance of new and clean membranes to water permeation, $R_m$

$$L_p = \frac{1}{\mu_w R_m} \tag{2-3}$$

where $\mu_w$ is the dynamic viscosity of water (or of the solvent). It is also common to express this hydraulic resistance of the membrane as the inverse of its permeability, $P_w$, according to

$$R_m = \frac{1}{P_w} \tag{2-4}$$

The concept of hydraulic permeability can be seen as an intrinsic property of pristine membranes. Despite some authors claim that $L_p$ decreases at high transmembrane pressure due to membrane compaction (McGovern et al. 2015), for practical operating conditions the $L_p$ value decrease as result of fouling processes and not of membrane compaction (Rudie et al. 1985).

If the feed is a solution then the permeate flux through the membrane, $J_v$, is

$$J_v = \frac{Q_v}{A_m} \tag{2-5}$$

where $Q_v$ is now the volumetric permeate flow rate. The permeate flux, $J_v$, is not an intrinsic property of the membrane since it depends on the solutes and on their concentration.

Solute permeability

To have a glimpse on the membrane selectivity, model solutions of tracer solutes are used to determine their retention. The retention of a solute by the membrane is expressed by a rejection coefficient. Two types of rejection coefficient exist. The most simple to be determined is the apparent rejection coefficient of the membrane, $R_a$, defined as

$$R_a = \frac{c_f - c_p}{c_f} = 1 - \frac{c_p}{c_f} \tag{2-6}$$

where $c_f$ and $c_p$ are the solute concentrations in the feed stream and in the permeate stream respectively. The apparent rejection coefficient is also known as observable rejection, $R_o$. However, the solute transport through the membrane (and, thus, $c_p$ and $R_a$) depends on operating parameters. To avoid this effect, it is also common to use the intrinsic rejection coefficient of the membrane, $R_i$, defined as

$$R_i = \frac{c_m - c_p}{c_m} = 1 - \frac{c_p}{c_m} \tag{2-7}$$

where $c_m$ is the solute concentration at the membrane surface. Using the film theory (section 2.2.1), $R_a$ and $R_i$ are related by

$$ln\left(\frac{1-R_a}{R_a}\right) = ln\left(\frac{1-R_i}{R_i}\right) + \frac{J_v}{k_c} \quad (2\text{-}8)$$

where $k_c$ is the mass transfer coefficient in the concentration boundary layer over the membrane. Thus, $R_i$ and $k_c$ are obtained plotting the experimental data of $R_a$ versus $J_v$.

**Morphological characterization**

The most common parameters used to describe the morphology of membranes are: its pore size (and its distribution), its molecular weight cut-off, its surface roughness and its internal structure. These parameters can be determined using several complementary techniques referred below.

The pore size and its distribution are usually determined directly by scanning electron microscopy (SEM) (Bogner et al. 2007) and atomic force microscopy (AFM) (Johnson & Hilal 2015) techniques. There are also indirect techniques to determine the pore size of a membrane, such as: gas adsorption-desorption on the membrane surface (T. Wang et al. 2013), calorimetric analysis of the liquid-solid phase change on pores (Iza et al. 2000), vapor condensation inside pores (Zeidler et al. 2014), vapor-pressure depression of a wetting liquid on pores (Akhondi et al. 2014), or displacement of fluids on pores (Reichelt 1991; Calvo et al. 2011; Fan et al. 2016). Alternatively, the pore size can be estimated using empirical correlations between the radius of the smallest molecule retained by the membrane and its molecular weight (Calvo et al. 2011). For this approach, the molecules are assumed as rigid spheres with MW equal to the molecular weight cut-off of the membrane.

The molecular weight cut-off (MWCO) of a membrane is, by definition, the minimum molecular weight of a solute with an intrinsic retention of 90 % (Causserand & Aimar 2010; Xu et al. 2017). Therefore, the MWCO can be seen as an alternative way to characterize the pore size of a membrane. The MWCO of a membrane is determined experimentally by plotting the retention as function of MW for a series of solutes with different molecular weights.

The roughness of the membrane surface can be determined by AFM and by white light interferometry (Wyart et al. 2014). Information on the membrane porosity and internal structure can be obtained by small-angle neutron scattering (Hu et al. 2011), small-angle x-ray scattering (Hu et al. 2011), x-ray tomography (Lee et al. 2017), positron annihilation spectroscopy (Fujioka et al. 2015), and ellipsometry of angle resolved scattering (Wyart et al. 2008).

**Physical, chemical and biological characterization**

The chemical composition and physical properties of membranes influence their permeation performance by affecting the hydrophilicity and the electrical charge of the membrane. In addition, biological characterization of membranes should be performed to assess their antifouling and biocompatibility properties.

The elemental composition of the membrane surface can be obtained using x-ray photoelectron spectroscopy (XPS) (Guillen et al. 2011), SEM coupled with energy dispersive x-ray spectroscopy (SEM-EDS) (Newbury & Ritchie 2013) and Rutherford backscattering spectroscopy (RBS) (Cahill et al. 2008). An interesting comparison between these three methods was recently performed by Gorzalski and colleagues (Gorzalski et al. 2017) showing that they are complementary: XPS has the smallest depth of analysis of 10 nm, but can detect trace elements; SEM-EDS has the largest depth of analysis (few microns) but is not suitable to detect trace elements, and RBS has an intermediate depth of analysis (ca. 2 μm).

Specific functional groups can be detected and quantified using attenuated total reflection with Fourier transform infrared spectroscopy (ATR-FTIR) (Andanson & Baiker 2010; Zaera 2012). ATR-FTIR scans the material into to a depth ranging from few hundred nanometers to a few micrometers (Tang et al. 2009), depending on the used wavelength. A complementary technique to assess the chemical bonds in a material is Raman spectroscopy (Khulbe & Matsuura 2000). In addition, Raman spectroscopy is also used to evaluate the crystallinity of polymers (Wesełucha-Birczyńska et al. 2015). However, for crystallinity studies, the most used technique is x-ray diffraction (Khulbe et al. 2000; Li et al. 2011).

The filtration performance depends not only on the membrane properties but also on the solutions that the membrane contacts. Examples are the change of the zeta-potential or the change of the contact angle between the membrane surface and the solution when the solution changes.

Membrane surfaces can be electrically charged depending on the membrane material, on the pH of the solution and on compounds present in the solution, resulting in distinct permeation performances (Childress & Elimelech 2000). On such conditions, a double electrical layer between the charged surface and counter ions is formed and an electrical potential exists between the membrane and the solution. Since the actual interfacial electrical potential is not easily measurable, an approximation is made where it is considered the potential between the membrane and the shear layer: the zeta-potential. The streaming potential technique is usually used to measure the zeta-potential and it consists of making a solution to flow inside a channel and measure the generated potential differential between the inlet and the outlet of the channel (Elimelech et al. 1994).

The contact angle is another parameter that is commonly used to characterize membranes. When a solid is placed in contact simultaneously with a liquid and a gas, several interfaces are formed. The contact angle is defined as the angle between the solid-liquid and liquid-gas interfaces, measured in the counter-clockwise direction (Chau 2009). Thus, the contact angle is a measure of the wettability and of the hydrophobic/hydrophilic nature of system membrane-solution. The contact angle depends on the surface tension of the interfaces and, ultimately, on the properties of the solid, liquid and gas. However, one must be aware that even when the system is the same, differences in the measured contact angle can arise. As an illustrative example, for the interaction between water and the NF90 membrane the contact angle values found in the literature varies between 42° and 68° (Gryta et al. 2012), which is a very wide range in terms of contact angle for the same system. The main reason for these discrepancies lies, probably, on the different pre-conditioning of the membrane and measurement conditions

Current membrane research is focused on the development of antifouling and biocompatible membranes. One of the most difficult types of fouling to control is biofouling, which is the growth of films of microorganisms on the membrane surface. Thus, new membranes should have antimicrobial properties. To assess the antimicrobial properties of membranes, assays are performed where the membrane is incubated with model microorganisms. After incubation, the number of colonies, or their growth inhibition is visually inspected (Sile-Yuksel et al. 2014; Xu et al. 2015; J. Li et al. 2016). In many cases, the antimicrobial behaviour of the membrane is due to the presence and release of metal complexes or metal ions from metal nanoparticles. Therefore, it is important to evaluate the release of such substances in order to, not only assess the durability of antimicrobial properties, but also verify that they are not present and released at toxic levels into the environment (Xu et al. 2015; J. Li et al. 2016; Panico et al. 2016). The compatibility of the membrane to be used with body fluids is usually assessed by simple protein and platelet adhesion assays (Xiang et al. 2013; Zheng et al. 2016) or, sometimes, by more complex cytotoxicity, thrombogenicity and haemolytic potential studies (Elbarbary & El-Sawy 2016).

### 2.1.4 Concentration polarization and fouling

Membrane processes are usually operated at constant transmembrane pressure or at constant permeate flux (Guo et al. 2012). Solutes or particulate matter in the feed stream make the permeate flux to decline over time, in constant pressure processes, or to demand higher transmembrane pressure, in constant flux processes. The term “flux decline” is used interchangeably hereafter both for flux decline in constant pressure processes and for the

necessity to increase the applied pressure in constant permeate flux processes. Three phenomena are responsible for the permeate flux decline: concentration polarization, scaling and fouling.

Concentration polarization (CP) is the phenomenon that makes the solute or particulate matter concentration to be higher in the membrane vicinity than in the bulk solution (Sherwood et al. 1965; Sablani et al. 2001). This occurs in membrane processes due to the selectivity of the membrane. The CP phenomenon is depicted in Figure 2-3, considering a TFF process in a straight open channel with a membrane in the bottom surface.

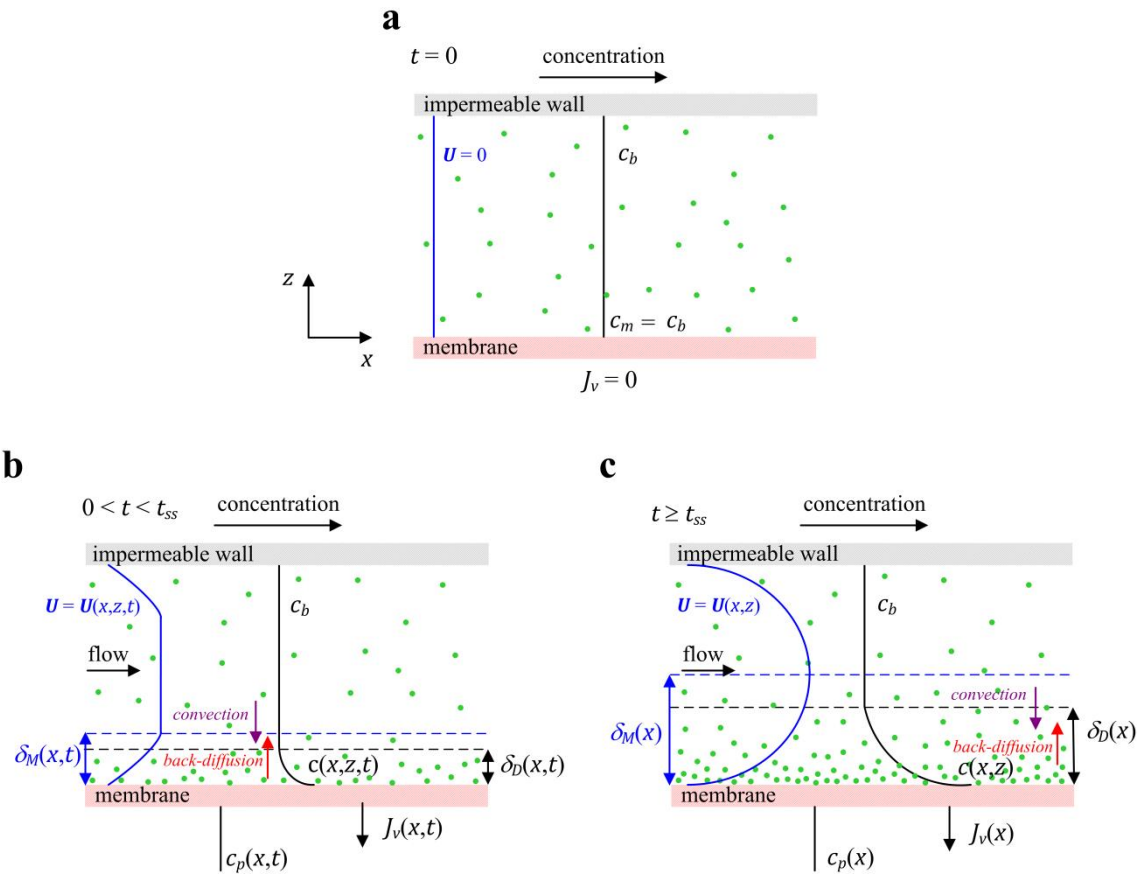


Figure 2-3 – Concentration polarization phenomenon in a TFF process: a) prior to the application of pressure the solute the concentration is $c_b$ in the whole volume; b) applying pressure permeation occurs and concentration/velocity profiles develop; c) after some time ($t_{ss}$) steady-state is reached. Green dots represent solute molecules.

Prior to the filtration ($t \leq 0$) no permeation occurs and the solute concentration is the same in the whole volume (Figure 2-3a). When pressure is applied, the bulk solution starts to flow, the filtration begins and a convective flow occurs from the bulk solution towards the membrane (Figure 2-3b). Since the solvent passes through the membrane more easily than the solutes, part of the solute is retained upstream the membrane and its concentration increases in that region. The increase of the solute concentration near the membrane results in a back-diffusion process of the solute from the membrane region back to the bulk of the solution. These

three phenomena result in a solute concentration gradient along the $z$-direction (the direction normal to the membrane surface).

The region, in the $z$-direction, where a solute concentration gradient exists is called concentration boundary layer and it has a thickness $\delta_D$. Solute concentration gradient in the $x$-direction (the main direction of the flow) may also occur due to convection, diffusion and permeation, but for the understanding of the CP phenomenon this gradient is usually not considered due to its much smaller value. For non-suction mass transfer processes or when the feed recovery small, the $\delta_D$ value in open channels depends of the longitudinal location from the point where the mass transport begins, $x$, of the height of the channel, $h$, of the diffusion coefficient of solute in the solvent, $D_{AB}$, and of the velocity of the liquid (M. Li et al. 2016) and can be estimated by

$$\delta_D = 1.475 \left(\frac{xhD_{AB}}{2U_{max}}\right)^{1/3} \tag{2-9}$$

where $U_{max}$ is the maximum velocity of the liquid in the channel. For open channels with rectangular cross-section and very high width-to-height ratio, $U_{max} = \frac{3}{2}U_0$, where $U_0$ is the average velocity of the liquid at the channel entrance.

Similarly, due to the no-slip condition, the fluid velocity, $\boldsymbol{U}$, also has a gradient in the $z$-direction inside the momentum boundary layer, which has a thickness of $\delta_M$. In impermeable channels, the velocity of the liquid would develop to a constant parabolic profile, in the $z$-direction; however, due to the continuous loss of liquid, by permeation, the average velocity decreases along the channel and its shape can change.

For TFF processes the concentration and velocity profiles develop over time until a steady-state is reached, at $t = t_{ss}$, as depicted in Figure 2-3c. For dead-end processes, no steady-state is achieved.

The magnitude of the concentration polarization phenomena is expressed by the concentration polarization modulus, $\Gamma$, which is defined as (Geraldes & Afonso 2006)

$$\Gamma = \frac{c_m - c_b}{c_b} \tag{2-10}$$

where $c_b$ is the solute concentration in the bulk solution.

The CP phenomenon decreases the permeate flux, which can be explained by the increase of the osmotic pressure at the surface of the membrane when dense NF and RO processes are used. As it will be seen later, for these scenarios, the permeate flux is inversely proportional to the difference of the osmotic pressure between the feed and permeate sides of the membrane.

In addition, the rise of the solute concentration at the membrane surface enlarges the driving force for the solute diffusion through the membrane. This results in a higher $c_p$ and lower apparent solute rejection. Thus, for NF and RO processes, $c_p$ and $R_a$ are influenced by concentration polarization that, in turn, depends on the operating conditions (transmembrane pressure, feed flow rate, etc). It is for this reason that the characterization of membranes in terms of its intrinsic rejection coefficient is preferable.

For MF and UF processes, the small size solutes pass easily through the membrane pores and the large molecules that are retained do not cause significant osmotic pressure at low-to-medium concentration. Thus, the permeate flux decline in MF and UF processes is due to other mechanisms, which can also occur in NF and RO, including: adsorption of molecules inside the pore and on the membrane surface, gel layer formation, scaling, cake layer deposition and biofouling. These processes are generically named as fouling. As referred before, since in the present work only binary solutions of small MW solutes were used, fouling effects were neglected. Further description of fouling mechanisms can be found elsewhere (Shirazi et al. 2010; Chellam & Cogan 2011; Guo et al. 2012; Iritani 2013).

## 2.2 Mass transport models for membrane processes

Mass transport in membrane processes can be grouped according to the domain where the phenomenon occurs. For monophasic solutions without particulate matter, and discarding fouling and cake formation, the mass transport in the feed channel is usually described using the film theory model (Murthy & Gupta 1997). Several models exist to quantify the solute transport through the active layer of the membrane, the most adequate one for each application being dependent of the type of the membrane and of the feed solution (J. Wang, Dlamini, et al. 2014). Recently, models to account the impact of the membrane support layer were disclosed, since it may influence the permeate transport by creating preferential flow paths in the membrane active layer (J. Wang, Dlamini, et al. 2014). Similarly, the flow conditions inside the permeate channel can affect the permeate flux and, thus, the solute concentration in the feed side; however, these effects are usually taken into account only when one intends to simulate the whole filtration device or filtration plant, and when high pressure drop can occur on the permeate channel. Since the permeate channel is usually filled with fine meshes, the flow in this channels can be described by porous medium flow models (Kostoglou & Karabelas 2013).

Given the fact that in this work the used permeation devices are small, the effect of the pressure drop in the permeate channel can be discarded. Therefore, in the next sub-sections, only the models for the mass transport in the feed side and in the membrane active layer are considered.

### 2.2.1 Mass transport in the liquid adjacent to the membrane

**Film theory model**

The mass transport in the liquid adjacent to the membrane surface can be modelled using the film theory (Murthy & Gupta 1997). For the film theory model, it is assumed that the resistance to the transport phenomena (momentum, heat and mass) occur in thin layers adjacent to the solid surface where the flow regime is laminar. It is assumed that these layers have constant thickness along the channel length, but their thicknesses may be different for each transport phenomenon.

Regarding mass transport, the concentration boundary layer is, in fact, the concentration polarization layer. Thus, in this layer, the solute concentration profile develops between $c = c_m$ at $z = 0$ and $c = c_b$ at $z = \delta_D$, as depicted in Figure 2-4.

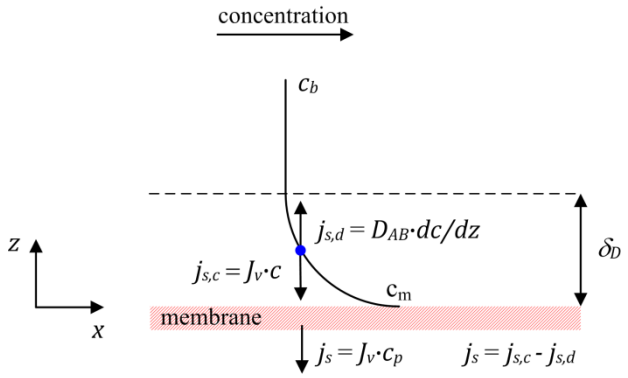


Figure 2-4 – Unidimensional solute transport towards a semi-permeable wall.

On the other hand, assuming that the mass transfer of the solute is unidimensional, the solute transport in the concentration boundary layer consists of a convective solute mass flux towards the membrane, $j_{s,c}$, and in a diffusive solute mass flux in the opposite direction, $j_{s,d}$. Thus, the net solute flux, in the film layer, is equal to the solute mass flux into the permeate, $j_s$,

$$j_s = j_{s,c} - j_{s,d} = J_v c_p \tag{2-11}$$

and the global solute balance can be approximated by

$$J_v c_p = J_v c - D_{AB} \frac{dc}{dz} \tag{2-12}$$

Equation (2-12) can be solved between $z = 0$ and $z = \delta_D$ using as boundary condition equation (2-13)

$c = c_b$, for $z = \delta_D$ (2-13)

resulting in

$$\frac{c_m - c_p}{c_b - c_p} = exp\left(\frac{J_v}{D_{AB}/\delta_D}\right) = exp\left(\frac{J_v}{k_c}\right) \quad (2\text{-}14)$$

Therefore, the film theory can be used to determine $c_m$ and $\Gamma$, provided that $\delta_D$ or the mass transfer coefficient, $k_c$, are known since by this theory $k_c = D_{AB}/\delta_D$.

**Mass transfer coefficient**

Generically, the mass transfer coefficient, $k_c$, is a proportional constant between a solute flux, $j_A$, and a characteristic concentration difference of the solute $A$, $\Delta c_A$, defined as (de Pinho & Prazeres 2008)

$$j_A = k_c \cdot \Delta c_A \quad (2\text{-}15)$$

The mass transfer coefficient $k_c$ for the mass transfer process can be seen as the analogous heat transfer coefficient for the heat transfer process. Thus, while the heat transfer coefficient is made dimensionless using the Nusselt number, the mass transfer coefficient is made dimensionless using the Sherwood number, $Sh$, defined as

$$Sh = \frac{k_c \cdot L_c}{D_{AB}} \quad (2\text{-}16)$$

where $L_c$ is the characteristic length of the system. Thus, the Sherwood number can be interpreted as the ratio between the global mass transfer and the mass transfer due to diffusion. The mass transfer coefficient can be predicted from empirical correlations obtained for non-suction processes or for permeation processes.

As a first approximation, $k_c$ can be estimated using empirical correlations (Gekas & Hallstrom 1987; van den Berg et al. 1989) of the form

$$Sh = aRe^b Sc^c \quad (2\text{-}17)$$

where $a$, $b$ and $c$ are fitting parameters, $Re$ is the Reynolds number and $Sc$ is the Schmidt number. For developed laminar flows in open slit channels, the Graetz-Lévêque equation is commonly used,

$$Sh = 1.86\left(Re_{dh} \cdot Sc \cdot \frac{d_h}{L}\right)^{\frac{1}{3}} \tag{2-18}$$

where $Re_{dh}$ is the Reynolds number based on the hydraulic diameter of the channel, $d_h$, and $L$ is the length of the channel. However, the use of empirical correlations has two main drawbacks: first, the used correlation must be appropriate for the flow regime and device geometry; second, the available correlations were usually obtained for non-suction processes.

The mass transfer coefficient can also be determined coupling experimental permeation data (permeate flux and solute rejection) with both the film theory model and with one of the mass transport models for the solute transport across the membrane (see section 2.2.2). Using the osmotic pressure model one can calculate $k_c$ from a single permeation run (Sutzkover et al. 2000; Qiu & Davies 2015; Xie & Gray 2016). The use of the solution-diffusion model can lead to the velocity variation method or to the flux variation method (Nakao & Kimura 1980; van den Berg et al. 1989; Bouchoux et al. 2005; Morão et al. 2008; Drazevic et al. 2014), both requiring the linearization and fitting of the experimental data of a series of permeation runs. The Spiegler-Kedem model can also be applied and uses non-linear parameter estimation to determine the $k_c$ value (Murthy & Gupta 1997; Murthy & Gupta 1999).

For the permeation in open flat channels, a more sound approach is to use the methodology proposed by Geraldes and Afonso (Geraldes & Afonso 2006), which estimates the mass transfer coefficient for the permeation process from the corresponding one for the non-suction mass transfer coefficient using the correction factor, $\Xi$, as defined by

$$\Xi = \frac{Sh}{Sh_0} = \phi + (1 + 0.26\phi^{1.4})^{-1.7} \tag{2-19}$$

where $Sh_0$ is the Sherwood number for the corresponding non-suction process. The parameter $\phi$ of the previous equation is defined as the $J_v/k_{c,0}$ ratio, where $k_{c,0}$ is the mass transfer coefficient of the corresponding non-suction mass transfer process. The permeate flux can be determined experimentally or estimated by an appropriate model for the mass transport through the membrane (section 2.2.2). Subsequently, the solute concentration at the membrane surface can be determined, since the concentration polarization modulus, $\Gamma$, defined in equation (2-10), is simultaneously given by

$$\Gamma = \frac{c_m - c_b}{c_b} = \frac{R_i}{\frac{\Xi}{\phi} - R_i} = \frac{R_a}{\frac{\Xi}{\phi} - 1} \tag{2-20}$$

Therefore, using the Geraldes and Afonso's methodology, the mass transport coefficient of the permeation process can be determined if one knows in advance the mass transport coefficient of the corresponding non-suction process and the solute rejection of the membrane. Despite the fact that Geraldes and Afonso's methodology can be used at any nanofiltration and reverse osmosis scenarios, the authors have found that its application is only relevant when $\phi >$ 1, since for $\phi \leq 1$ the $k_c$ value determined using the film theory is an adequate estimate (Geraldes & Afonso 2006). This methodology was successfully applied on membrane filtration processes using plate-and-frame and ribbed-wall geometries (Morão et al. 2008; Completo et al. 2016). Further details on this methodology for the correction of $k_c$ can be found in section 4.4.5.

In equation (2-17) the Reynolds number, $Re$, is given by

$$Re = \frac{\rho U_c L_c}{\mu} \tag{2-21}$$

where $\rho$, $\mu$ and $U_c$ are the density, the viscosity and a characteristic velocity of the liquid, respectively. As characteristic length the hydraulic diameter, $d_h$, is commonly used or, in some cases, the height of the channel, $h$, (Fimbres-Weihs & Wiley 2010). If $Re$ is defined based on $h$ then the following equation is used

$$Re_h = \frac{\rho U_0 h}{\mu} \tag{2-22}$$

where $U_0$ is the average liquid velocity at channel inlet, while if the Reynolds number is defined based on $d_h$ then it is used the following expression

$$Re_{dh} = \frac{\rho U_{eff} d_h}{\mu} \tag{2-23}$$

where $U_{eff}$ is the effective velocity calculated based on the volumetric flow rate and on the effective cross-section area, $A_{eff}$, which in turn is function of the channel porosity, $\varepsilon$.

The Schmidt number, $Sc$, is the ratio between the momentum and mass transport diffusivities and reflects the relative ease of molecular momentum and mass transfer (Bird et al. 2007)

$$Sc = \frac{\mu/\rho}{D_{AB}} \quad (2\text{-}24)$$

### 2.2.2 Mass transport through the membrane

The mass transport of solvent and solutes across the membrane can be modelled by a multitude of models. Phenomenological models treat the membrane as a black box and give no information on the flow and separation mechanisms. Conversely, mechanistic models are based on mass transport mechanisms, which give a better insight on the physics of the process.

**Osmotic pressure model**

The phenomenological osmotic pressure model uses a Darcy-like equation to relate the solvent flux with the effective pressure difference, $\Delta p_{eff}$, between both sides of the membrane (Elimelech & Bhattacharjee 1998)

$$J_v = L_p \Delta p_{eff} \quad (2\text{-}25)$$

The effective pressure difference, $\Delta p_{eff}$, is the pressure-driven force between both sides of the membrane, so one must account for both the applied pressure and the osmotic pressure. Considering the active side of the membrane as side $m$ and the permeate side of the membrane as side $p$, then $p_{eff,m} = p_m - \pi_m$ and $p_{eff,p} = p_p - \pi_p$, where $p_m$ and $\pi_m$ are the applied pressure and the osmotic pressure of the liquid at the membrane surface of the feed side, while $p_p$ and $\pi_p$ are the applied pressure and the osmotic pressure of the liquid at the membrane surface of the permeate side. Then, the osmotic model of equation (2-25) is in fact

$$J_v = L_p(\Delta p_m - \Delta \pi_m) \quad (2\text{-}26)$$

where

$$\Delta p_m = p_m - p_p \quad (2\text{-}27)$$

and

$$\Delta \pi_m = \pi_m - \pi_p \quad (2\text{-}28)$$

**Solution-diffusion model**

The solution-diffusion model is suitable to be used with membranes with dense active layers, so it is widely applied to model the mass transport through NF and RO membranes.

The solution-diffusion model is based on the following assumptions (Wijmans & Baker 1995; Jonsson & Macedonio 2010; J. Wang, Dlamini, et al. 2014): the membrane is non-porous and homogeneous; the solvent and the solutes dissolve into the membrane according to their individual partition coefficients; the diffusion of the substances through the membrane occurs according to their individual concentration gradients and diffusion coefficients; and the pressure inside the membrane is equal to the one in the feed side.

The solvent flux is determined using an equation similar to the one of the osmotic pressure model, but the solution-diffusion model allows for a deeper insight of the process by relating the hydraulic permeability of the membrane, $L_p$, with physical and chemical properties of the membrane and of the solvent, namely the thickness of the membrane, $\delta_m$, the feed-membrane partition coefficient of the solvent, $K_w$, the diffusion coefficient of the solvent in the membrane, $D_{wM}$, and its molar volume, $V_w$. Thus, $J_v$ is given by

$$J_v = L_p(\Delta p_m - \Delta\pi_m) = \frac{K_w D_{wM} V_w}{\delta_m R_g T}(\Delta p_m - \Delta\pi_m) \tag{2-29}$$

while the solute flux is given by

$$j_s = J_w c_p = B\left(c_m - c_p\right) = \frac{K_A D_{AM}}{\delta_m}\left(c_m - c_p\right) \tag{2-30}$$

where $B$ is the solute permeability, $K_A$ is its partition coefficient between the feed and the membrane, and $D_{AM}$ is the diffusion coefficient of the solute in the membrane. Considering equations (2-30) and (2-7) one obtains

$$R_i = \frac{J_w}{J_w + B} \tag{2-31}$$

This equation shows that, admitting $B$ constant, the solute rejection decreases as the permeate flux decreases. Thus, since the solute flux is independent of $\Delta p_m$ but the solvent flux increses with $\Delta p_m$, the solute rejection increases with the transmembrane pressure. Moreover, when the difference between $\Delta p_m$ and $\Delta\pi$ decreases, the solute rejection drops sharply, in spite of the small magnitude of CP for those scenarios.

Solute-diffusion model is usually coupled with the film theory to obtain the solute permeability, $B$, and mass transfer coefficients from experimental permeation data (Murthy & Gupta 1997; Murthy & Gupta 1999) using

$$ln\left(\frac{1-R_a}{R_a}\right) = ln\left(\frac{B}{J_v}\right) + \frac{J_v}{k_c} \quad (2\text{-}32)$$

which is equivalent to equation (2-8) applied to determine the membrane MWCO.

**Solution-diffusion-imperfection model**

The solution-diffusion-imperfection model (Sherwood et al. 1967) assumes that, although most of the membrane is dense and homogeneous, some imperfections or pores exist on the membrane surface. These surface imperfections permit that both solvent and solutes flow through the membrane without changing the solute concentration. Thus, equations (2-29) and (2-30) are corrected to account for the contribution of the flow through the imperfections by adding an extra term similar to the Darcy's equation

$$J_v = k_1(\Delta p_m - \Delta\pi_m) + k_2\Delta p_m \quad (2\text{-}33)$$

$$j_s = k_3(c_m - c_p) + k_4\Delta p_m c_m \quad (2\text{-}34)$$

where $k_1$ and $k_3$ are transport parameters for the diffusivity of water and solute in the membrane, and $k_2$ and $k_4$ are transport parameters for the flow of water and solute inside the pores of the membrane.

Since this model assumes that a portion of the permeate has crossed the membrane without changing its solute concentration ($R_i$ = 0 in the imperfection pores), then the global solute rejection is smaller than the unity. At the limit, when the flux through the imperfection pores is negligible the solute-diffusion-imperfection model shortens to the solute-diffusion model described before.

**Spiegler-Kedem model**

The phenomenological Spiegler-Kedem model is based on irreversible thermodynamics concepts and provides a simple framework to describe solute transport in NF and RO membranes (Soltanieh & Gill 1981; J. Wang, Dlamini, et al. 2014). The separation process is characterized by two parameters: the solute permeability, $P_s$, and the reflection coefficient, $\sigma$.

The value of $\sigma$ varies between 0 and 1, corresponding 1 to complete solute rejection and 0 to no rejection. The solvent flux is given by

$$J_v = L_p(\Delta p_m - \sigma \Delta \pi_m) \tag{2-35}$$

while for binary solutions, the solute flux is determined by

$$j_s = P_s \delta_m \frac{dc}{dz} + (1 - \sigma) c J_w \tag{2-36}$$

where $z$ is the direction normal to the membrane surface. The intrinsic solute rejection coefficient of the membrane can be estimated by

$$R_i = \sigma \left( \frac{1 - F}{1 - \sigma F} \right) \tag{2-37}$$

where $F$ = exp(- $J_v(1 - \sigma)/P_s$).

The Spiegler-Kedem model is usually coupled with the film theory model, after integration of equation (2-36) to obtain $\sigma$, $P_s$, and the permeation mass transfer coefficient from experimental data (Murthy & Gupta 1997; Murthy & Gupta 1999).

**Pore flow models**

Although NF and RO membranes are considered dense, the actual structure of polymeric membranes consists of a matrix of solid material and void spaces. Therefore, the mass transport through NF/RO membranes can be modelled using a transport model that consider the membrane as a solid material with pores (J. Wang, Dlamini, et al. 2014).

Pore models are based on the balance of applied and frictional forces inside pores. Herein it will be considered only the modified surface force – pore flow model (MD-SF-PF) and the steric pore flow model. Details on other pore models are available elsewhere (Mehdizadeh 1990; Jonsson & Macedonio 2010; J. Wang, Dlamini, et al. 2014).

In the MD-SF-PF model (J. Wang, Dlamini, et al. 2014) it is assumed that: the flow through the membrane is made via cylindrical pores; the transport of solvent is described by viscous flow; the transport of solute is due to convection and diffusion; mass transport is driven by the sum of several forces including interaction forces, friction forces and chemical potential. Making a force balance in a radial element inside the pore of radius $r_p$ and integrating in the

whole pore length $l_p$ results in the molar permeate and solute fluxes, $J_{vm}$ and $J_{sm}$, (Mehdizadeh & Dickson 1989)

$$J_{vm} = 2\left(\frac{R_g T}{l_p X_{sw}}\right)\int_0^1 \alpha(\rho)d\rho \tag{2-38}$$

$$J_s = 2\left(\frac{1}{l_p X_{sw}}\right)\int_0^{1-\lambda} \frac{\alpha(\rho)}{b(\rho)}\left(\pi_m + \frac{\pi_m - \pi_p}{e^{\alpha(\rho)} - 1}\right) e^{\Phi(\rho)}\rho d\rho \tag{2-39}$$

where $\rho$ is the dimensionless radial distance, $\alpha(\rho)$ is the dimensionless velocity profile inside the pore, $\lambda$ is the sieving factor ($\lambda = r_s/r_p$, being $r_s$ the solute Stokes radius), $b(\rho)$ is the friction parameter (i.e., $b(\rho) = D_{sw}/D_{sm}(\rho)$, being $D_{sw}$ and $D_{sm}(\rho)$ the solute diffusion coefficients in bulk solution and in the pore, respectively), $\Phi(\rho)$ is the potential accounting all the surface forces and $X_{sw}$ is the friction constant between solute and water. In most cases there is good agreement between experimental and MD-SF-PF model results. However, MD-SF-PF needs to be solved by complex numerical algorithms or using the Monte Carlo simulations.

The steric pore model is based on force balances to a molecule flowing inside a membrane pore (Deen 1987). The permeate flux is given by (Rosa 1995)

$$J_v = \varepsilon \bar{V}_p \tag{2-40}$$

where $\varepsilon$ is the porosity of the membrane and $\bar{V}_p$ is the average permeate velocity inside the pore. $\bar{V}_p$ can be estimated applying the Hagen-Poiseuille equation

$$\bar{V}_p = \frac{r_p^2 \Delta p}{8\mu l_p} \tag{2-41}$$

In the steric pore model, the solute flux is given by

$$j_s = \varepsilon \bar{V}_p W \frac{c_m e^{Pe_p} - c_p}{e^{Pe_p} - 1} \tag{2-42}$$

where $Pe_p$ is the Peclet number defined as

$$Pe_p = \frac{W l_p \bar{V}_p}{H D_{sw}} \tag{2-43}$$

In equations (2-42) and (2-43), $W$ and $H$ are the convection and diffusion hindrance factors, respectively, which can be estimated as function of $\lambda$.

**Electrokinetic models**

For electrolytic solutions and admitting that the concentration and concentration gradient of the solutes are very small, the molar flux of the solute $i$ through the membrane, $J_i$, can be estimated using the extended Nernst-Plank equation (ENP), which accounts for solute diffusion, convection and electro-migration in the membrane pore

$$J_i = J_w c_{i,p} = -K_{i,d} D_i^{\infty} \frac{dc_i}{dx} + K_{i,c} c_i J_w - \frac{z_i c_i K_{i,d} D_i^{\infty} F}{R_g T} \frac{d\varphi}{dx} \quad (2\text{-}44)$$

where $c_i$ and $c_{i,p}$ are the concentration of the solute $i$ in the pore and in the permeate, $K_{i,d}$ and $K_{i,c}$ are the diffusive and convective hindrance factors, respectively, $D_i^{\infty}$ is the diffusion coefficient of the solute $i$ at infinite dilution, $z_i$ is the charge of the ion $i$, $F$ is the Faraday constant and $\varphi$ is the electrical potential within the membrane pore caused by the membrane charge. Since it is difficult to determine $\varphi$, that parameter is usually replaced by the zeta potential, $\xi$, of the membrane, as discussed in section 2.1.3. Admitting that $\varphi$ (or $\xi$) is constant along the pore and that there is electro-neutrality on the membrane, then, the solute concentration gradient is given by

$$\frac{dc_i}{dx} = \frac{J_w}{K_{i,d} D_i^{\infty}} \left(K_{i,c} c_i - c_{i,p}\right) - \frac{z_i c_i J_w}{\sum z_i^2 c_i} \sum \frac{z_i}{K_{i,d} D_i^{\infty}} \left(K_{i,c} c_i - c_{i,p}\right) \quad (2\text{-}45)$$

Using appropriate models for the hindrance factors one can obtain the solute flux and permeate concentration by solving equations (2-44) and (2-45) (Bhattacharjee et al. 2001).

## 2.3 Efficient methods to perform solute concentration

### 2.3.1 The problem

In the present work, it is intended to develop methods to concentrate low MW solutes at least up to concentration factors, $CF$, of 10, $CF$ being the ratio between the solute concentration in the concentrate, $c_c$, and in the feed, $c_f$

$$CF = \frac{c_c}{c_f} \tag{2-46}$$

Alternatively, a volumetric concentration factor may also be defined as the ratio between the sample volume and the concentrate volume. However, in this text, all the experimental $CF$ values will be shown as defined in (2-46).

Concentration factors of similar magnitude to that intended to be achieved in this work were obtained before by other authors (Kaufman et al. 2012) performing tangential flow filtration in a straight open microchannel, but for very diluted solutions ($\pi_f \approx 0.05$ bar) of a specific peptide (MW = 895 g/mol), while in this work it is intended to concentrate solutions with higher osmotic pressure ($\pi_f \approx 0.6$ bar and 2.6 bar). In the above-mentioned work where TFF was used to concentrate small samples (Kaufman et al. 2012), the authors noticed that CP phenomenon occurred in the used straight open channel. Nevertheless, at least in some conditions, TFF filtration produces relatively high $CF$ values. For that reason, TFF will also be used in this work to assess its capability to obtain high CF in the concentration of higher osmotic pressure solutions, despite the expected CP phenomenon and consequent permeate flux decline. Thus, to increase the performance of the concentration process, potential methods to maximize the permeate flux and permeate quality are herein assessed.

Permeate flux is proportional to the effective pressure difference between feed side and the permeate side of the membrane, as defined by most of the mass transport models used for dense membranes – see equation (2-26), (2-29) and (2-35). Thus, to maintain the permeate flux as high as possible, the solute concentration at the membrane surface (in the feed side) should be kept as low as possible. This means that the CP layer formed during the permeation should be disrupted and efficiently mixed with the bulk liquid.

In the remainder of this section, potential methodologies to accomplish efficient CP disruption and, consequently, to improve the concentration process will be described, including the application of static mixers, pulsatile and oscillatory flows, gas sparging, centrifugal filtration and ultrasounds. As it will be made clear, all these methods result in the formation of flow instabilities that disrupt the CP layer.

Despite the fact that none of these methods were used before to concentrate low MW solutes in small-volume samples, there is no evident limitation to their use in small scale devices. As it will be referred in Chapter 3, NF membranes were used by other authors in microdevices, but only for standard tangential flow filtration, i.e. without the application of any of the CP disruptive methods. In terms of the use of RO membranes to process small-volume samples no works were found.

It is also worth to mention that many other methods exist to enhance permeation performance at macroscale but their application to deal with small volumes or small devices is

not straightforward. These include dynamic filtration, retrofiltration, filtration aided by the addition of solid particles or by application of electrical and magnetic fields (W. Zhang et al. 2015).

Dynamic filtration consists of filtration processes where rotating cylinders (Shah et al. 2006; Cheryan 1998; Jaffrin 2012), rotation disks (Jaffrin 2008; Ding & Jaffrin 2014) or vibrating plates (Jaffrin 2008; Gomaa & Rao 2011) are used. The scale down of rotating devices would make the rotation speed insufficient to obtain the aimed pressure. At the same time, the small moving parts would pose mechanical and leakage problems.

Standard retrofiltration (Hilal et al. 2005) is not suited for NF and RO membranes because it would cause membrane delamination (Ramon et al. 2013). For NF and RO processes, osmotic backwashing can be used (Qin et al. 2010), by which a solution with high osmotic pressure is injected into the feed stream. This makes part of the solvent in the CP layer to move towards the bulk with the consequent CP disruption. However, the use of osmotic backwashing may not be compatible with the feeds and it also implies further separation steps.

Similarly, solid particulate matter can increase the mixing between the CP layer and the bulk solution (van der Waal et al. 1977; Boer et al. 1980; Rios et al. 1987; Mikulasek & Filandrova 1995; Noordman et al. 2002; Noordman et al. 2003; Scott & Lobato 2004) but it would also require further separation steps downstream to recover the solid particles and to purify the concentrate. Moreover, the continuous scouring on the membrane surface by the solid particles can damage the membrane.

The use of electric (Rios et al. 1988; Agana et al. 2012; Dudchenko et al. 2014; Liang et al. 2014; Wei et al. 2015) and magnetic (Li et al. 2007; Zin et al. 2016; Rouina et al. 2016) fields increases the permeation performance in MF and UF processes, but its study for NF and RO is scarce (Liang et al. 2014). Electric fields alter the movement of charged particles and their orientation, while magnetic fields induce changes on the growth and on the structure of scale crystals. However, the main concern with these methods is that there is not enough knowledge on their long-term effect on the membrane structure.

Methods as the sample pre-treatment (physical and chemical treatments) (Wakeman & Williams 2002; Huang & Schwab 2009; W. Zhang et al. 2015; Zhao & Yu 2015), the optimization of operating filtration parameters (flow rate, temperature, pH, etc.) (W. Zhang et al. 2015) and the modification of the membrane surface (coating, grafting, etc.) (Kang & Cao 2012; W. Zhang et al. 2015; Zhao & Yu 2015; A. Lee et al. 2016) will not be discussed here.

In the text below the considered methodologies for the CP mitigation are described.

### 2.3.2 Mitigation of concentration polarization

**Static mixers**

The introduction of static mixers inside feed channels changes the flow hydrodynamics and can lead to mass transfer enhancement. In the literature, static mixers are also called spacers or turbulence promoters, although in many cases the flow is laminar. In practical applications, the flow is not really fully turbulent, but the "turbulence" term refers to flow conditions where weak oscillations in the flow structure or strong instabilities (like vortices) are generated (Schwinge et al. 2002c; Alexiadis et al. 2007). There are several types of static mixers, including: filaments/wires/ribs, baffles, helical screws, and many kinds of meshes (Hilal et al. 2005).

The reasoning for the use of static mixers is to promote liquid mixing between the CP layer and the bulk solution. The smaller magnitude of the CP phenomenon results from two effects. First, static mixers turn the channels narrower, which increases the shear stress, at least at the spacers sections, for the same flow rate. Second, static mixers promote flow separation and vortex-like structures that enhance the mixing of the solution, as verified experimentally (Kang & Chang 1982; Almeida et al. 2010) and by CFD simulations (Fimbres-Weihs et al. 2006; Lau et al. 2009).

It was also verified that the Reynolds number at which the unsteady flow appears, the critical Reynolds number, is much lower than the threshold for the turbulent regime (Ahmad & Lau 2006; Almeida et al. 2010). The critical $Re$ at which flow unsteadiness begins depends on the geometric parameters like the height of the channel, the shape and dimensions of the static mixer, and the distance between repeating units of the static mixers. Since static mixers alter the flow hydrodynamics, they enhance the permeation performance (Da Costa et al. 1991; Gao et al. 2013). More details on these phenomena are described in the section 4.2.3.

Since in this work it is intended to concentrate small-volume samples, a possible choice is to process the sample inside microchannels with static mixers. However, up to now, no work was disclosed reporting the use of static mixers in NF and RO processes at microscale and only straight open microchannels were used for nanofiltration (Rundel et al. 2007; Kolfschoten et al. 2011; Kaufman et al. 2012; Kaufman et al. 2014; Wardrip & Arnusch 2016).

To disrupt the CP layer at microscale a possible option is to use passive chaotic micromixers (Nguyen & Wu 2005; Hessel et al. 2005; Capretto et al. 2011; Kumar et al. 2011), which stretch, fold and split flows into directions transversal to the original flow, resulting in higher contact areas between the fluid elements. Transversal ribs or ladder meshes are unable to produce such tridimensional flows. Slanted ridges inside straight (Stroock et al. 2002) or curved channels (Islami & Khezerloo 2017) produce some degree of mixing, but the best mixing

performance is obtained when using non-aligned slanted ridges as the starred-herringbone micromixer (SHM) (Stroock et al. 2002).

The mixing length of the SHM is two orders of magnitude lower than that for an open channel. For the specific scenario of mixing two distinct inlet streams at $Re$ = 0.01, complete mixing was obtained after 3 cm from the channel entrance in the SHM, while for an open channel it would take from 1 m to 10 m (Stroock et al. 2002), depending on the Reynolds number. Several geometrical parameters influence the mixing performance in SHM channels, including the asymmetry in each set of ridges, the number of ridges in each set of ridges and the ridge-to-channel height ratio.

Although the mixing performance in microchannels (like the SHM) usually refers to the capability of the channel to efficiently mix two or more distinct streams in impermeable channels, it can also be seen as a fair criterion for CP disruption.

In the present work the permeation and concentration performance at microscale was performed only in open microchannels and, therefore, the application of static mixers was not studied. However, a hybrid method to predict nanofiltration data (permeate flux and concentration polarization modulus) based on mass transfer coefficients of non-suction processes was developed and validated (Chapter 4). This hybrid method can be very handy for the development of microchannels with integrated membranes, including those with static mixers.

**Pulsatile flows and oscillatory flows**

In pulsatile and oscillatory flows the instantaneous velocity is time-dependent. A distinction between pulsatile flow and oscillatory flow must be made. Both involve periodic pressure and flow rate variations, but while for the former flow pulses are superimposed over a steady flow rate basis, for the latter the fluid oscillates forward and backward without a net forward (or backward) flow (Blanpain-Avet et al. 1999).

The enhancement of mass transfer can be explained by changes in flow hydrodynamics when compared with a steady state scenario. First, in pulsatile flow, the Richardson's annular effect occurs (Winzeler & Belfort 1993), where velocity overshoots near the surface wall are present. This leads to very high wall shear stress when compared to those typical of parabolic velocity profile flows obtained for steady state conditions of laminar Newtonian fluids inside open channels. Furthermore, if the velocity amplitude of the pulse is higher than the average steady velocity, a temporary flow reversal may occur (Bode et al. 2007).

The increase in mass transfer efficiency using pulsatile and oscillatory flows was verified by many authors for MF (Blanpain-Avet et al. 1999; Olayiwola & Walzel 2009), UF (Abel 1997) and RO (Kennedy et al. 1974), and enhancements up to 150%, depending on the process, were

obtained. The performance enhancement is dependent on the frequency, on the amplitude of the pulse and on the Reynolds number (Rodrigues et al. 2015; Zaki et al. 2011). In fact, it was found that the mass transfer coefficient, measured using the limiting current technique, increases with the first two mentioned parameters, while little increase was obtained in turbulent flows.

**Gas sparging**

Mass transfer enhancement and, thus, lower CP can be obtained using gas sparging, a method where a gas (usually air) is injected into the feed generating flow instabilities and increasing the shear stress in the membrane vicinity (Cui et al. 2003; Wibisono et al. 2014). Gas sparging has been successfully applied in many MF, UF, NF and RO processes and in all common membrane geometries.

In a stationary liquid, the rising gas bubbles can have distinct shapes, from spherical and ellipsoidal blobs to wobbling and skirted caps (Cui et al. 2003). The shape of the gas bubbles depends on the properties of the liquid and of the gas, and on the size of the bubble.

In the case of flows inside tubes and channels other bubble patterns exist and, besides the above-mentioned factors, such patterns depend also on the gas-to-liquid flow rate ratio and on the module orientation (Cui et al. 2003; Wibisono et al. 2014). Usually, the processes are operated at conditions leading to bubble and slug flows. Although bubble flows promote larger local mixing, slug flows produce higher permeation enhancement. While slug flows increase the shear stress in the liquid layer near the membrane and generate vortex shedding (Ghosh & Cui 1999), the bubbles of the bubble flow move preferentially towards the middle of the channel, leading to a smaller mixing effect near the membrane surface.

Similarly to that described for static mixers, there is no evidence of using gas sparging with permeation processes at microscale; however, air-liquid flows are very common in microfluidics. For channels with large width-to-height aspect ratios, the flow patterns depend on the gas-to-liquid ratio (Chinnov et al. 2016) and are similar to those at macroscale flows. It was also verified that the application of gas sparging in microchannels delays cell adhesion and can remove cells attached to walls (Khodaparast et al. 2017). Therefore, it is very plausible that gas sparging can be very efficient to minimize the CP phenomena at microscale.

**Centrifugal filtration**

The centrifugal filtration technique consists of making the filtration device, or the section where the filtration occurs (the membrane region), to rotate around an axis, the axis of rotation. The use of centrifugal filtration presents two major advantages: external pumping is not needed (since the pressure is generated by the rotation of the system itself) and, at optimized

configurations, there is a self-cleaning mechanism which drags heavier fluid elements away from the membrane.

Although pressure can be applied to the feed, the rotation of the system generates hydraulic pressure itself. Consider the fluid element of mass $m$ depicted in Figure 2-5a. The pressure generated by the centrifugal force can be determined at any radial location taking in to consideration the fluid properties and the angular velocity, $\omega$. According to the Newton's second law, the equation of motion, the elemental pressure, $dp$, exerted on the fluid element of elemental mass, $dm$, located at the radial position $r$ is given by

$$dp = \rho\omega^2 r \cdot dr \tag{2-47}$$

Thus, the pressure difference, $\Delta p$, between two points, at distinct radial locations, $r_1$ and $r_2$, connected by a fluid is given by

$$\Delta p = \int_{r_1}^{r_2} dp = \int_{r_1}^{r_2} \rho\omega^2 r \cdot dr \tag{2-48}$$

Considering that the fluid has constant density and that the angular velocity is constant, then

$$\Delta p = \frac{1}{2}\rho\omega^2(r_2^2 - r_1^2) \tag{2-49}$$

Therefore, for the scenarios with constant fluid density, equation (2-49) is usually enough to calculate the pressure difference between points $r_1$ and $r_2$; otherwise equation (2-48) should be used. Likewise, equations (2-48) and (2-49) can be used to estimate the gauge pressure at the radial location $r_2$, if one admits that the interface air/liquid is at radial location $r_1$ and the generated pressure by the column of air (from the axis of rotation up to $r_1$) is negligible, when compared with the pressure generated by the liquid.

The self-cleaning mechanism observed on centrifugal filtration is caused by centrifugal and Coriolis forces, which are depicted in Figure 2-5b. In physical terms, both centrifugal and Coriolis forces are apparent forces that only appear in rotating frames of reference.

The centrifugal force always acts in the radial direction (away from the axis of rotation) and is given by (Leung & Ren 2013)

$$d\vec{F}_{centrifugal} = -dm \cdot \vec{\omega} \times (\vec{\omega} \times \vec{r}) \tag{2-50}$$

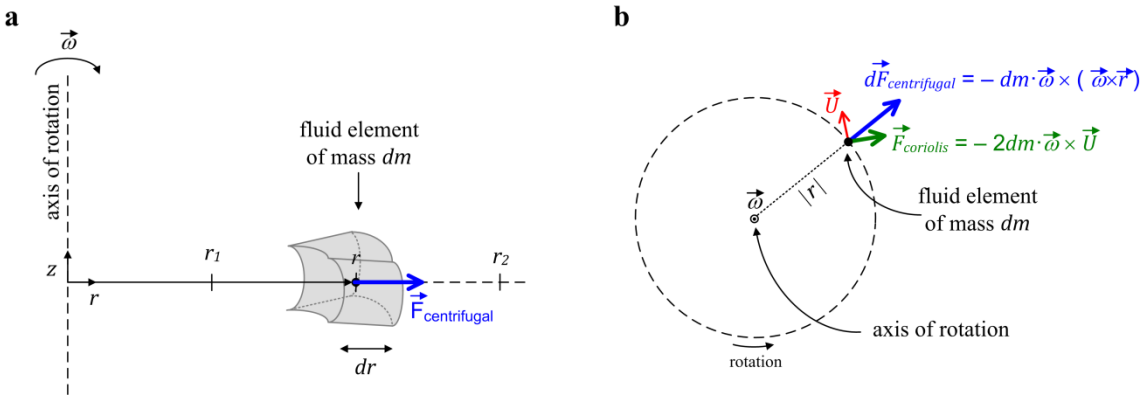


Figure 2-5 – Fundaments of centrifugal filtration: a) lateral view of a fluid element spinning around an axis of rotation; b) top view of a fluid element spinning around an axis of rotation. The centrifugal force (blue vector) points always in the radial direction. The direction of the Coriolis force (green vector) is function of the fluid velocity vector (red vector). Herein, the velocity vector $\vec{U}$ was chosen arbitrarily.

Since the centrifugal force is directly proportional the mass of the fluid element, then, the force exerted on heavier fluid elements are larger than that acting on lighter fluid elements. Thus, heavier fluid elements tend to be dragged in the radial direction. Since heavier fluid elements usually correspond to the more concentrated ones, this means that the most concentrated fluid elements are pulled away from the axis of rotation.

The effect of the centrifugal force on the permeation can be seen as similar to the effect of the gravitational force but at a greater extent. In fact, it is well known that gravity can influence the filtration process due to natural convection (Hendricks et al. 1972; Fernández-Sempere et al. 2007; Fernández-Sempere et al. 2012), and that is the reason why most of the single membrane studies are performed with the membrane placed on the bottom wall of the filtration devices, to avoid natural convection. However, the magnitude of the centrifugal force generated by centrifuges is much higher than that of the gravitational force. A common parameter used to compare these two forces, and to compare the applied force in different centrifugal experiments is given by the relative centrifugal force, $RCF$, also known as "g" force (Wilson & Poole 2009)

$$RCF = \frac{centrifugal\ force}{gravitational\ force} = \frac{r\omega^2}{g} = \frac{r(2\pi \cdot RPM)^2}{60g} \approx 0.00112r(RPM)^2 \qquad (2\text{-}51)$$

where $g$ is the acceleration of gravity and $RPM$ is the rotational speed given in rotations per minute.

Simultaneously, secondary flows are also induced by the Coriolis force, given by (Leung & Ren 2013)

$$d\vec{F}_{coriolis} = -2 \cdot dm \cdot \vec{\omega} \times \vec{U} \qquad (2\text{-}52)$$

The distinctive feature of the Coriolis force is that its relative direction changes as the velocity vector of the fluid element, $\vec{U}$, varies. The effect of the Coriolis force on the mixing of liquids in T-channels and in chambers was studied by several authors using lab-on-CD[10] devices (La et al. 2013; Leung & Ren 2013; Leung & Ren 2014; Ren & Leung 2013). Ren and colleagues (Ren & Leung 2013) have found that the Coriolis force promotes the mixing between two fluids in impermeable milli- and micro-chambers due to secondary toroidal flows. Since the geometry of the filtration chamber of the CNF device developed in this thesis is similar to those used by Ren and colleagues, then, it is expected that the Coriolis force also influences the performance of centrifugal filtration.

Centrifugal filtration is ubiquitously used to filter small-volume samples containing particulate and colloidal matter and solutions with macromolecules. There are commercial MF and UF batch devices for centrifugal filtration available from several suppliers (EMD Millipore Corporation 2015; Sartorius GmbH 2017; Corning Incorporated 2010; Thermo Fisher Scientific Incorporated 2017; Pall Corporation 2010; Orbital Biosciences 2017). In fact, the term centrifugal ultrafiltration (CUF) is nowadays well established. Briefly, a sample (between 0.5 and 100 mL) is placed inside the device, made to spin, and at the end of the filtration cycle the concentrate and permeate are collected. More details and examples on CUF devices can be found in section 5.2.2.

Conversely, few works were developed dealing with NF and RO processes. Nevertheless, it was found that centrifugal filtration is efficient to mitigate the CP (Andeen 1981; Bergen et al. 2000) and fouling (Eid & Andeen 1983; Fyles & Lycon 2000) effects in RO processes. Unlike commercial CUF devices, the studies about the enhancement of RO performance by centrifugal filtration were performed feeding continuously samples to hollow fibers (Andeen 1981; Eid & Andeen 1983), flat plates (Bergen et al. 2000; Fyles & Lycon 2000) and spiral wound membrane modules (Bergen et al. 2003). More importantly, it was verified that the orientation of the membrane, in relation to the centrifugal force, plays an important role on the filtration performance (Bergen et al. 1997; Bergen et al. 2000; Fyles & Lycon 2000). When the centrifugal force points away from the active side of the membrane, there is an enhancement of the filtration performance; but if the centrifugal force points towards the active surface of the membrane the filtration performance decreases. The effects of the Coriolis force was studied numerically showing that it also plays an important role in the filtration performance. Similarly to the effect of the centrifugal force, the filtration performance is enhanced if the Coriolis force points away from the active membrane surface (Pharoah et al. 2000).

[10] In a lab-on-CD device the microchannels where the liquids flow are built on the surface of a CD-like device that will spin around its axis (Madou et al. 2006). CD means “compact disc”.

**Ultrasounds**

Ultrasounds are mechanical vibrations, with frequencies ranging from kHz to MHz, that are superimposed to the hydraulic pressure generating sequences of compression and rarefaction cycles in the media (Kyllönen et al. 2005; Muthukumaran et al. 2006). The use of ultrasounds can result in four mechanisms that promote secondary flows and, thus, disruption of CP and fouling layers, including acoustic streaming, microstreaming, microjets and microstreamers (Lamminen 2004), which are depicted in Figure 2-6.

The secondary flows of acoustic streaming result from the absorption of the acoustic energy, causing a bulk liquid movement towards and from the membrane surface, as depicted in Figure 2-6a. Under certain conditions, the liquid is unable to absorb the decompression energy and bubbles are formed by acoustic cavitation. If not reabsorbed, the bubble size oscillates in the following compression and decompression acoustic cycles, until it collapses. This oscillation creates secondary flows with high shear stresses in the vicinity of the bubble, a process called microstreaming, as depicted in Figure 2-6b. In some conditions, the bubble collapses. Usually, the time lapse of bubble collapse is less than 10 μs generating high local pressure and high-temperature spots. If the bubble collapse takes place near the membrane, it produces a non-symmetrical fluid inrush, resulting in microjets towards the membrane surface, as depicted in Figure 2-6c. Microstreamers are groups of bubbles formed at nucleation sites that move to different locations on the membrane surface where they coalesce or collapse, as depicted in Figure 2-6d.

The efficiency of ultrasounds to enhance permeation performance depends on several ultrasonic and non-ultrasonic factors (Z. Wang et al. 2014; Tao & Sun 2015). The frequency, power and duration of the acoustic waves, the orientation and distance of the ultrasound source are common ultrasonic factors, while the composition, concentration, temperature and pressure of the feed are seen as non-ultrasonic factors.

Ultrasound frequency has a fundamental role in the magnitude of the enhancement of the filtration performance (Cai et al. 2010). It was found that lower frequencies, in the range 20 – 50 kHz, result in a larger increase of permeate flux when compared with higher frequencies, because, despite the smaller number of collapses, the bubbles are usually bigger and collapse more violently. The increase of permeation flux also increases with ultrasound power, but only up to a certain critical power threshold, beyond which cavitational activity diminishes. The easiness of bubble formation, movement and collapsing energy depends on the fluid temperature, pressure, viscosity and surface tension. In addition, the presence of particulate matter hinders acoustic propagation, leading to a reduction of the ultrasonic effect.

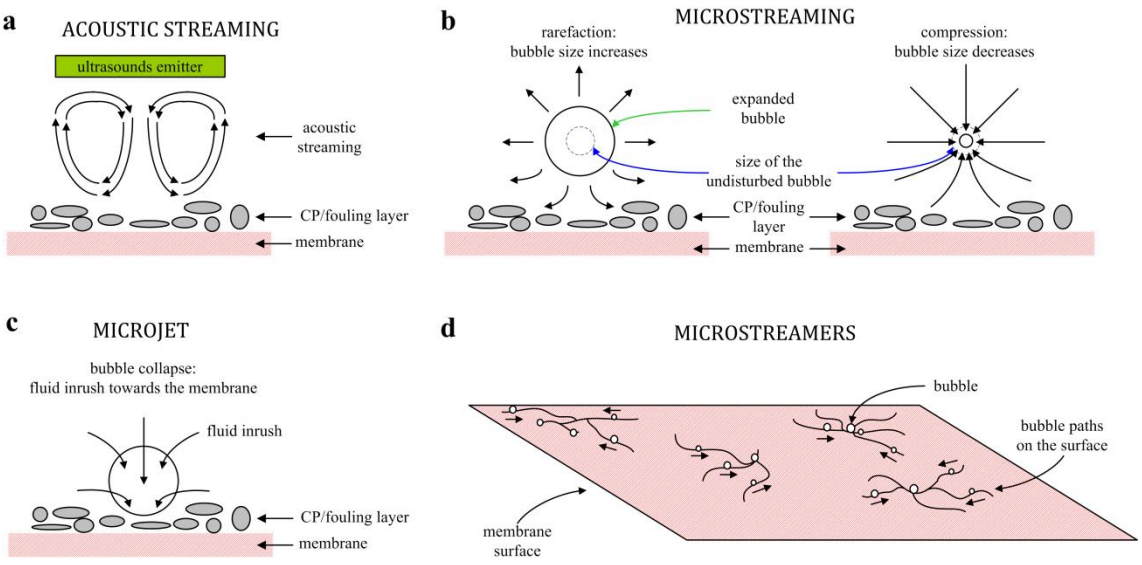


Figure 2-6 – Mechanisms of secondary flow formation by ultrasounds: a) acoustic streaming; b) microstreaming; c) microjects; d) formation of microstreamers. Figure adapted from (Kyllönen et al. 2005).

An important issue when applying ultrasounds in membrane processes is whether the membrane will withstand the mechanical and chemical stresses caused by bubble collapse. Although some studies have been made, they are still insufficient for a comprehensive understanding of the membrane material limitations (Kallioinen & Mänttäri 2011).

The feed pressure has a huge impact on the cavitation threshold. As one increases the pressure it becomes harder, for the same acoustic energy, to obtain bubble cavitation. This is probably the reason why the majority of the ultrasounds studies are related to MF and UF processes (Muthukumaran et al. 2006; Ahmad et al. 2012) and only two studies using NF/RO membranes were published (Feng et al. 2006; Patel & Nath 2013), although both of them were performed at low pressures, 1 bar and 4.9 bar, respectively.

The use of ultrasounds to mitigate CP and fouling looks a promising method to be adopted. However, further studies are needed on the effect of ultrasounds on long-term membrane resistance and on its implementation at high-pressure processes.

## 2.4 Conclusion

The fundaments of membrane science and of pressure-driven membrane separation processes were described in this chapter. In these processes, concentration polarization and fouling phenomena cause the decline of the flux and quality of the permeate. In addition, since the objective of the present thesis is to concentrate low MW solutes in small-volume samples, any decrease in flux and solute rejection leads to larger filtration cycles and lower concentration factors. Therefore, it is important to apply methods to minimize the CP and fouling phenomena.

At macroscale processes, several methods can be used and, usually, they rely on one of the following principles: pre-treatment of the feed to remove foulants or to change its fouling potential; change of flow hydrodynamics to increase shear stress or to generate flow instabilities; modification of membrane properties to enhance its antifouling behaviour; cleaning of the membrane.

Since it is intended to concentrate small-volume samples, the filtration cycles are short (usually not more than a couple of hours). Therefore, membrane cleaning methods are irrelevant here since, if needed, they will be done before and not during the filtration cycle. Pre-treatment of the sample is an obvious step and it is not considered here too. Membrane synthesis and membrane modification are cutting edge fields in membrane research; however, they are not the focus of the present work, which is centered in obtaining efficient concentration methods by improving the hydrodynamics of the permeation process.

From the several methods described in the literature to improve liquid mixing, by an adequate management of flow hydrodynamics, centrifugal filtration was selected as the method to be studied (in addition to standard tangential flow filtration). Centrifugal filtration is free of many of the limitations presented by other methods, namely: it does not need external pumping; it does not need tubing, so the problem of unfiltered liquids does not exist; it does not need complex flow control; it does not need subsequent steps for purification of the concentrate and permeate streams; and there is evidence that appreciable solute rejection can be obtained be at high feed pressure. In addition, if well designed, the centrifugal filtration has a membrane self-cleaning mechanism that disrupts the CP layer.

Therefore, centrifugal filtration looks like the most appropriate technique to accomplish the objective of the present thesis (to concentrate small-volume samples of low MW solutes) and it will be thoroughly assessed later in Chapter 5, while in the next chapter it will be tested how well TFF performs the same task.

# 3 Tangential flow nanofiltration of small-volume samples of low molecular weight solute solutions

## 3.1 Introduction

The main aim of the present thesis is to develop techniques capable of concentrate small-volume samples of solutions containing low MW solutes, obtaining fairly high concentration factors ($CF$ > 10). As highlighted in Chapter 1, none of the currently available pressure-driven membrane techniques is adequate for such task, since they are only suited to process large volumes or high MW solutes. From the study, performed in Chapter 2, on the techniques used to mitigate flux decline, centrifugal filtration comes out as a promising one since it can reduce the concentration polarization phenomena common in the NF and RO processes. However, one must not discard the use of tangential flow filtration (TFF) to accomplish the same objective, since it has already been used to concentrate samples by nanofiltration at mesoscale (Minhalma et al. 2007), where $CF$ = 5 was obtained, and at microscale (Kaufman et al. 2012), where $CF$ = 10 was obtained for dilute solutions. Therefore, the work developed in this chapter has two objectives: evaluate the potential of TFF as a concentration technique for small samples, even without applying any mitigation method for the CP phenomenon, and to gather nanofiltration data that will be used later, in Chapter 6, as means of comparison with centrifugal nanofiltration (CNF) results, obtained in Chapter 5.

Since the sample volumes to be processed are small (less than 10 mL), the TFF system must present specific characteristics that may be universal and applicable to alternative technologies, namely the height of the filtration chamber and the ratio between the sample volume and membrane area. The compliance with these two requirements makes the TFF filtration cell, developed herein, a device with physical dimensions in the microfluidics range and, for that reason, it is named as micro-TFF cell.

Several works and literature reviews deal with the application of membrane processes at microscale, but the vast majority of the used devices are applied to filter particulate matter or very large molecules, like DNA chains and proteins, or simply used as medium for cellular growth (de Jong et al. 2006; Chen & Shen 2017). The works dealing with the application of NF membranes to microfluidics are very scarce and will be covered in the following literature review section. No works were found about the application of reverse osmosis at microscale.

The potential of the micro-TFF device to concentrate samples was evaluated by filtering binary model solutions at several flow and pressure conditions. Low concentration efficiency was expected since none of the CP mitigation techniques was used on the device. However, in

some conditions, the micro-TFF device was surprisingly efficient, particularly when solutions of low osmotic pressure were filtered at high transmembrane pressure. In those scenarios, the obtained concentration factor can be higher than 10. Although only clean model solutions were tested, the results show that micro-TFF filtration should be taken into account when selecting a technique to concentrate small-volume samples with osmotic pressures lower than a few bars.

The confirmation that micro-TFF is capable of concentrating small molecules by nanofiltration paves the way for future development of small microfluidic cartridges where the sample is injected and, at the end of the filtration cycle, the concentrate remains inside the device for further analysis or processing.

## 3.2 Literature review

Microfluidics, the use and study of flows at microscale, dates back at least to the 1970's, when the first microscale flow system was developed (Terry et al. 1979) but it was only in the 1990's that a boost in the interest on microscale flows emerged grounded on the development of both analytical and of microfabrication techniques (Whitesides 2006). The development of chemical and biological analysis has allowed the increase of the accuracy, precision and sensibility of the analytical techniques (Liu et al. 2010). In turn, the use of techniques developed for the fabrication of microelectromechanical systems (MEMS) permitted the manufacture of fluidic devices capable of processing tiny volumes (few microliters) (Judy 2001). These innovative microdevices that could manipulate very small volumes of liquid flows were commonly named as micro total analysis systems (μTAS) and later as lab-on-a-chip (LOC) devices (Reyes et al. 2002).

The application of lab-on-a-chip devices presents several advantages over traditional methods for synthesis and analysis of fluids: smaller sample volumes, fewer reagent consumption and waste production, lower manufacture costs, and surface properties can be exploited due to high surface-to-volume ratio. Thus, overtime LOC devices have been applied for several purposes: cooling in electronics (Erickson & Li 2004), chemical and environmental analysis (Ohno et al. 2008; Jang et al. 2011), protein and DNA analysis (Beebe et al. 2002; Das & Chakraborty 2009); cell analysis (Andersson & van den Berg 2003; Bhagat et al. 2010) and health monitoring point-of-care systems (Gervais et al. 2011; Gubala et al. 2012). Like at macroscale, to achieve a fully operational microfluidic system, the microscale device should include a series of components that can handle the fluid samples in the proper manner. Depending on their function, these components are usually grouped in vessels, micropumps (Laser & Santiago 2004; Zhang et al. 2007; Luo et al. 2009; Nabavi 2009), micromixers (Nguyen & Wu 2005; Lim et al. 2010), microvalves (Oh & Ahn 2006; Zhang et al. 2007),

microreactors (Doku et al. 2005), microseparators (Lim et al. 2010) and microsensors (Nguyen 1997; Bashir 2004).

Despite the study of membrane processes and its integration at microscale has increased in the last few years (de Jong et al. 2006; Chen & Shen 2017), membrane application at microscale is usually limited to processes working at very low pressure (as those where large particulate matter or large molecules are separated by sieving – microfiltration or ultrafiltration – and those related with gas exchange through the membranes – like pervaporation or membrane distillation). The reason for this is threefold. First, the used laboratory devices made by rapid prototyping are fragile, they cannot withstand medium-to-high pressure, and leakage can occur just by applying a few tenths of bar for a short period of time. Second, the membranes that are produced in situ are not adequate for high-pressure processes. Third, the application of commercial membranes presents issues related to the bonding of the membrane to the microfluidic device itself. Although there are some examples of microfluidic devices that can withstand large pressure, up to a few hundreds of bar (Benito-López et al. 2008; Verboom 2009; Luther & Braeuer 2012), they are usually made of metal, glass or silicon capillaries and are not developed for membrane processes. Therefore, the integration of membranes into microfluidic devices is not a trivial task, especially for high-pressure processes.

Most of microfluidic devices used in research are manufactured by rapid prototyping using soft lithographic techniques (Xia & Whitesides 1998). The commonly used material is polydimethylsiloxane (PDMS), which, for single layer channels, is cast over a mold and let to cure, resulting in a semi-rigid piece with the shape of the desired channel (McDonald & Whitesides 2002; Berthier et al. 2012). The channel is then closed by fixing the PDMS piece to a glass slice. Rapid prototyping using PDMS presents some advantages, as the transparency of the material (allowing the visualization of the flows or of the deposition of particles in the channel), and the easy replicability of the channels from the same mold. Besides the above-mentioned issues related to rapid prototyping devices (fragility and difficult integration of membranes), there are also two extra problems caused by the use of PDMS. The elasticity of PDMS limits its utilization at high-pressure processes since the deformation of the channel wall may result in a different channel cross-section than the designed one. Moreover, PDMS is permeable to gases and swells and deforms in contact with some solvents. Despite these limitations, PDMS channels are profusely used for low-pressure processes.

Recently, PDMS channels were integrated with a commercial UF membranes for the visualization of membrane fouling (Di et al. 2017). In that work, the deposition of 0.4 μm latex particles on the membrane surface was observed. However, it must be emphasized that no real ultrafiltration was performed, and the work was limited to the study of the deposition of the particles on the membrane surface.

Due to the limitations posed by the use of PDMS channels at high operating pressures, all experimental works studying the integration and application of NF membranes in microfluidic devices have used channels manufactured with rigid plastics. The first microfluidic devices where NF membranes were manufactured by machining, using computer controlled mills, but the recent developments in 3D-printing technology allowed the manufacture of similar devices faster and at a competitive cost (J. Lee et al. 2016; Zhang et al. 2017). Nevertheless, currently, 3D-printing still has some limitations, mainly related to its low resolution and the narrow variety of materials, which can be inadequate for certain purposes. Other possible manufacture processes of microchannels are: embossing, mold injection and laser ablation (Fiorini & Chiu 2005).

In Table 3-1 all the experimental works published up to date related to the application of NF membranes in microfluidic devices are summarized. The microfluidic devices used in those works were manufactured by machining or by 3D-printing.

The first work referring the application of NF membrane to a microfluidic device was performed by to Rundel and colleagues (Rundel et al. 2007), who studied the retention of a poly(amidoamine) dendrimer dissolved in an organic solvent using a microfluidic device with a 100 μm height channel. Although the MW of the selected dendrimer is higher than 400 Da and the used membrane has a MWCO of 220 Da the dendrimer rejection was only 55 %. Another problem that those authors had to face was that leakage occurred at medium-to-high pressures and, for that reason, they limited the microfluidic experiments to a maximum pressure of 1.4 bar.

The microdevice developed by Kaufman and colleges (Kaufman et al. 2012) withstood a higher pressure value (4 bar). These authors studied experimentally and numerically the nanofiltration of aqueous solutions of $MgSO_4$ and of a selected peptide (MW = 897 Da) in channels with 50 μm and 250 μm of height. Although the feed and permeate channels were straight, they were shifted in order to prevent membrane deformation. However, the authors considered that once the permeate passed through the membrane the hydraulic resistance of the membrane support layer was insignificant and, thus, the permeate flowed easily into the permeate channel.

Two remarking conclusions are enunciated in Kaufman's work. First, it was shown that for the same liquid bulk velocity the CP effect is mitigated as the channel height decreases, which was verified by the higher $MgSO_4$ rejection for the thinner channel and by the solute concentration fields obtained by CFD simulations. On the other hand, it was verified that adsorption of the solute on the channel walls, or on the membrane itself, may lead to significant loss of mass in microfluidic devices, which is an issue that must be addressed when designing microchannels or selecting membranes. The authors have proposed the use of surface modification techniques to obtain walls less prone to solute adsorption. The same microfluidic device was later used in a work where it was studied the nanofiltration, at 16 bar,

Table 3-1 – Previous studies on the use of NF membranes at microscale.

| Authors (year) | $h$ (μm) | $W$ (μm) | $L$ (cm) | $A$ (mm$^2$) | $p_{max}$ (bar) | $Re$ | Membrane | Cell material | Manufacture process | Notes |
|---|---|---|---|---|---|---|---|---|---|---|
| Rundel *et al.* (2007) | 100 | n.a. | n.a. | 400 | 1.4 | n.a. | Starmem 122 (MWCO = 220 Da) | PET | channel manufactured by milling; membrane fixed by laser transmission welding; cell tightened with screws | Nanofiltration of PANAM G-0.5 (MW = 404 Da) diluted in methanol solution containing methyl acrylate |
| Kolfschoten *et al.* (2011) | 50 - 200 | 500 | 8.06 | 40.3[†] | not pressurized | 0.5 – 6 [†] | SelRo MPF34 (MWCO = 200 Da [§]) SelRO MPF36 (MWCO = 1000 Da [§]) NADIR NP010 NADIR NP030 | PVC | channel manufactured by milling; cell tightened with screws | Diffusion of glucose (MW = 180 Da), sucrose (MW = 342 Da) and raffinose (MW = 504 Da) from the aqueous quaternary solution to the pure water stream |
| Kaufman *et al.* (2012) | 50 - 250 | 500 | 3 | 15[†] | 4 | 3 - 37 [†] | NF270 | PMMA | channel manufactured by milling; cell tightened with screws | Nanofiltration of aqueous solutions of $MgSO_4$ (MW = 120 Da) and of a peptide (MW = 897 Da) |
| Kaufman *et al.* (2014) | 200 | 500 | 3 | 15[†] | 16 | n.a. | NF270 and NTR-7450 | the same cell as Kaufman (2012) | channel manufactured by milling; cell tightened with screws | Nanofiltration of NaCl aqueous solutions using biomimetic lipid membranes adsorbed on commercial membranes |
| Haas *et al.* (2015) | 100 | 1400 | 3 | 42[†] | 4 | 4 | NF200 | Veroclear + Tangoblackplus | channel manufactured by 3D-printing; cell tightened with screws | Effect of the adsorption of two different lipids on the fouling caused by bacteria |
| Wardrip *et al.* (2016) | 200 | 1000 | 3 | 30[†] | 4 | 56[†] | UF and NF membranes | n.a. | channel manufactured by 3D-printing; cell tightened with screws | Nanofiltration of $MgSO_4$ (MW = 120 Da) and ultrafiltration of BSA (MW = 66.5 kDa) |

n.a.: not available; [†] estimated from the data given in the paper; [§] data from the manufacturer of the membrane

of NaCl aqueous solutions through commercial membranes covered with biomimetic lipid layers (Kaufman et al. 2014).

While the works of Rundel *et al.* and of Kaufman *et al.* reported the use of microchannels manufactured by milling, other two more recent works mention the application of NF membranes to microfluidics with devices built by 3D-printing. The bulk of the 3D-printed microfluidic device of Haas and colleagues (Haas et al. 2015) was made of Veroclear™ plastic, while a thin 50 μm layer of Tangoblackplus™ rubber was coated on the surfaces to be in contact with the membrane to prevent liquid leakage. Both these two plastics are proprietary materials and their properties can be found elsewhere (Stratasys Limited 2017). This device was used to study the effect of different lipid layers (glycosphingolipids or lipopolysaccharide) deposited on the membrane surface on the adsorption and fouling phenomena of a specific group of bacteria. Monitoring the permeate flux over time and visualizing the bacteria attachment on the membrane surface, it was found that depending on which lipid layer was deposited, the attachment of the bacteria is reversible or irreversible. A similar microfluidic device was 3D-printed by Wardrip and colleagues (Wardrip & Arnusch 2016) to compare the flux decline caused by NaCl, $MgSO_4$ and BSA solutions. The maximum applied pressure in these 3D-printed microfluidic devices was 4 bar.

Additionally, Kolfschoten and colleagues (Kolfschoten et al. 2011) reported the use of a NF membrane to a non-pressurized microfluidic device consisting in two co-current streams, one of pure water and the other of an aqueous solution containing glucose, sucrose and raffinose. The separation occurs due to different diffusivities of each solute. Despite some interesting results, like the confirmation that the rejection and selectivity depend on the flow rate and on the height of the channel (channels with height between 50 μm and 200 μm were tested), this process is more similar to dialysis than to common pressure-driven processes. There are also microfluidic devices with the objective of removing small volatile molecules but, instead of using pressure-driven processes, membrane distillation (Yang et al. 2017) or pervaporation (Berger et al. 2014; Zhang et al. 2016; Ziemecka et al. 2017) techniques are used.

The above-mentioned works show that it is possible to perform NF at microscale by integrating commercial NF membranes into microfluidic devices. However, in those works, the recovery of permeate was always low and, for that reason, the concentration factor is small. The exception is the work of Kaufman and colleagues where $CF$ values near or above 10 were obtained. However, the maximum peptide feed concentration, used by Kaufman and colleagues, was 1.8 g/L, which corresponds to an osmotic pressure of 0.05 bar. This is a rather diluted solution that may not resemble actual solutions obtained from body fluids, from environmental or industrial samples.

The purpose of this part of the present work is to evaluate the performance of micro-TFF nanofiltration as a process to concentrate small-volume samples of liquids containing low

molecular weight solutes at concentrations corresponding to osmotic pressures of 0.6 bar and 2.6 bar. In addition, the obtained results will be used for comparison purposes (Chapter 6) against the ones obtained by CNF of similar model solutions (Chapter 5).

## 3.3 Tangential flow nanofiltration system for small-volume samples

In the following sub-sections, the designs of the micro-TFF nanofiltration system (section 3.3.1) and of the micro-TFF nanofiltration cell (section 3.3.2) are shown.

### 3.3.1 Micro-TFF nanofiltration system

A sketch of the micro-TFF nanofiltration system is shown in Figure 3-1. Not all the depicted elements are mandatory to perform a nanofiltration run. The basic experimental setup consists of: a micro-TFF nanofiltration cell (1); a pump (2) that delivers the liquid sample from a sample reservoir (3) to the cell; a permeate reservoir (4); a concentrate reservoir (7); and a back pressure valve (5) that imposes the pressure in the system. As it will be seen later, the pressure in the system can differ from the nominal pressure of the back-pressure valve (BPV). Additionally, the setup of the micro-TFF nanofiltration system can also include: pressure sensors (8, 9, 10), used to measure the gauge or differential pressures; a micro-metering valve (6), used to tune the feed pressure; and a signal acquisition system to acquire, process, display and store pressure data, comprised of an electronic circuit (11), an acquisition board (12) and a computer (13).

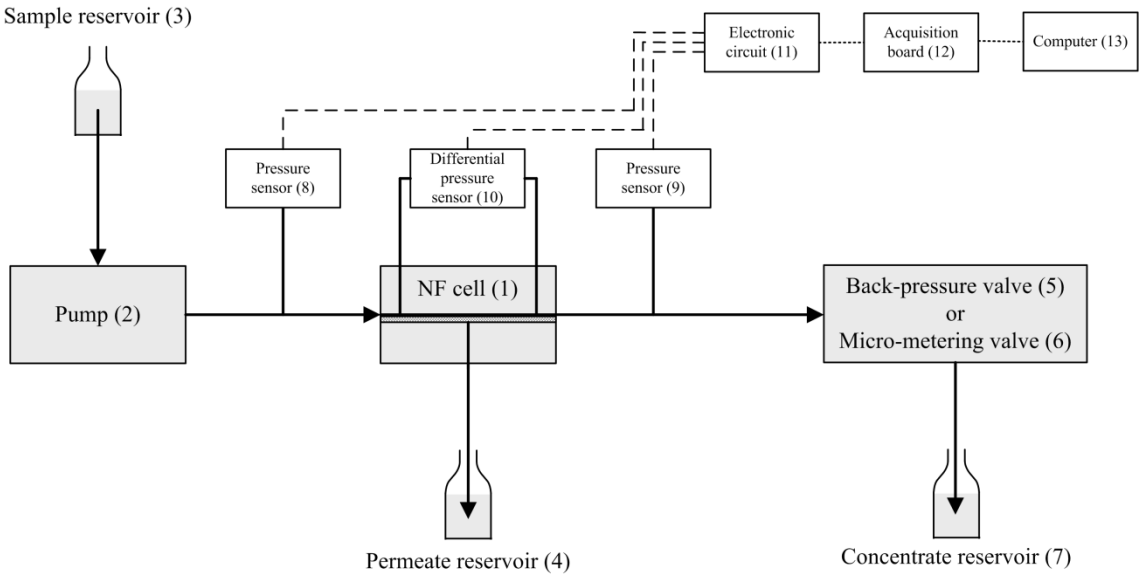


Figure 3-1 – Sketch of the micro-TFF nanofiltration system used for the nanofiltration of small-volume samples.

All the experiments where nanofiltration data was collected used the basic setup of the micro-TFF system. The setup for the experiments using gauge pressure sensors is shown in Figure 3-2. Although the connections to plug a differential sensor exist, the differential sensor itself is not present, to avoid its damage by the pressure generated by the back-pressure valve. The electronic circuit was used in pressure drop measurement experiments in order to amplify the output signal of the pressure sensors, as shown in Figure 3-3.

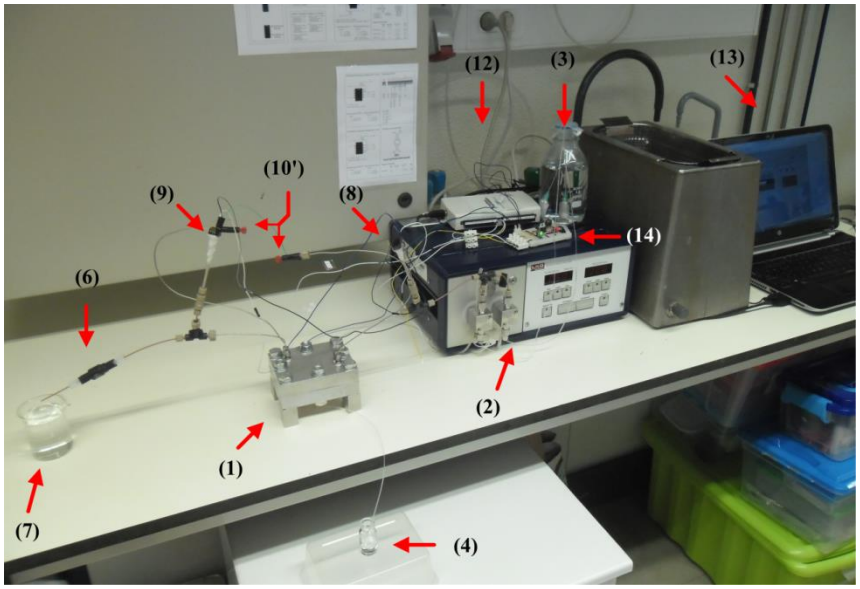


Figure 3-2 – Experimental setup used for the nanofiltration of small-volume samples: micro-TFF cell (1); HPLC pump (2); sample reservoir (3); permeate reservoir (4); back-pressure valve (6); concentrate reservoir (7); gauge pressure sensors (8) and (9); connections to differential pressure sensor (10'); acquisition board (12); computer (13); power source for the pressure sensors (14).

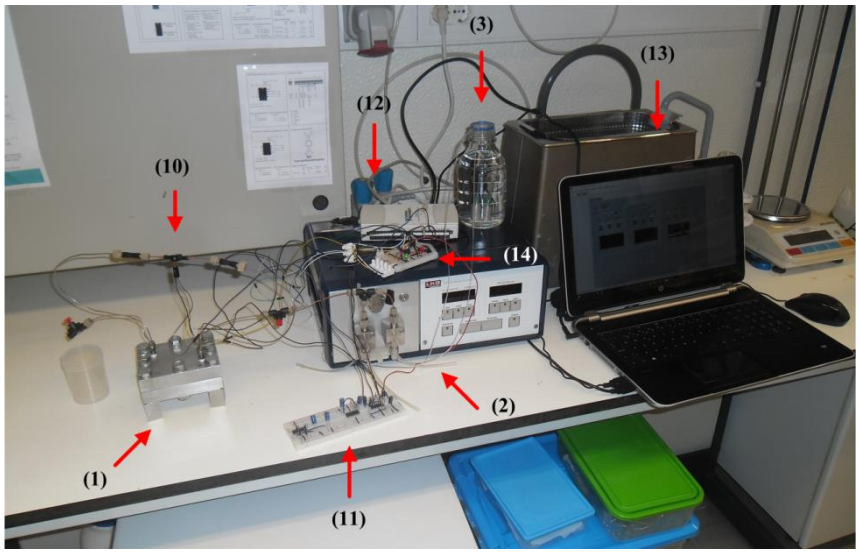


Figure 3-3 – Experimental setup used to measure the pressure drop of water flows inside impermeable channels: micro-TFF cell (1); HPLC pump (2); differential pressure sensor (10); electronic circuit for signal processing (11); acquisition board (12); computer (13); power source for pressure sensor (14).

The equipment, used to build the micro-TFF nanofiltration are described below. The micro-TFF cell (1) was designed specifically for this work and was built in stainless steel. Further details on the design of the nanofiltration cell are described in section 3.3.2. The liquid samples were driven by a dual-piston HPLC pump (model 2150, LKB, Sweden), while the system was pressurized using one of three back-pressure valves (models P-763 / P-764 / P-765, Idex, USA). These three valves pressurize the system to 7 bar (100 psi), 17 bar (250 psi) and 34 bar (500 psi), respectively. Alternatively, the pressure can also be adjusted using a micro-metering (model P-446, Idex, USA).

The selected gauge and differential pressure sensors, the models 40PC500G2A and 24PCEFA1D / 26PCAFA6D / 26PCCFA6D (Honeywell, USA) respond linearly to the pressure in their pressure range. To gather the pressure-to-voltage signal it was used a USB-6211 acquisition board (USB-6211, National Instruments, USA) which has an input voltage in the range 0 – 10 V.

The above-mentioned pieces of equipment of the hydraulic system were connected by standard 1/16'' stainless steel and PEEK tubing, connectors, unions and t-junctions supplied by Idex (USA). Finally, the sample, permeate and concentrate reservoirs were glass flasks.

Prior to the nanofiltration experiments, several verification/calibration procedures were performed. These include: a) verification of the actual flow rate given by the HPLC pump versus the flow rate set up on its front panel; b) calibration of pressure sensors; c) design and set up of the electronic circuit to process the pressure-to-voltage signal given by the pressure sensors; d) programming of the software to acquire and store pressure data. The descriptions of these validation procedures are available in Appendix C.

### 3.3.2 Micro-TFF nanofiltration cell

In TFF processes, high concentrations factors are only achieved if the amount of concentrate is a tiny portion of the feed. For small inlet flow rates, if $CF$ is very high, the concentrate flow rate is so low that, in practical terms, the filtration turns almost into a dead-end process. Accordingly, since it is intended to nanofilter small-volume samples, high $CF$ in dead-end filtration will be obtained only if the ratio of volume of sample / volume of the filtration chamber is very high. This confines the design of this cell to a very small volume of the filtration chamber.

The micro-TFF nanofiltration cell was, in fact, a rectangular slit channel constituted by a chamber separating the surfaces of two plates. Inside this chamber, a membrane was placed to divide the slit chamber into a filtration chamber and a permeate chamber. The height of the filtration chamber, $h$, was by design 0.25 mm.

Sketches of the micro-TFF nanofiltration cell are shown in Figure 3-4. Figure 3-4a shows the side view of the micro-TFF cell when assembled. The slots of both the top plate (1) and bottom plate (2) are separated by a membrane (3), forming the filtration chamber (4) and the permeate chamber (5). The feed solution enters and exits the filtration chamber by inlet / outlet channels (6) in the top plate, whereas the permeate exits the cell through the permeate channel (7) in the bottom plate. The inlet / outlet channels (6) in the top plate are connected to the main hydraulic system by standard connectors (8) (model SS-100-1-1, Swagelok, USA). To facilitate the permeate handling, a plastic tube is attached to the permeate channel (7). The assembly is kept steady by tightening standard M10 screws and nuts, inserted in the respective holes (9). Four stainless steel supports (10) maintain the bottom plate two centimeters above the ground level.

Top views of the top and bottom plates (looking at faces with the slots) are depicted in Figure 3-4b and in Figure 3-4c, respectively. Each of the top and bottom plates, and thus the micro-TFF nanofiltration cell, has a length of 110 mm and a width of 90 mm. The slots, which form the filtration and the permeate chambers, correspond to the areas located in the interior of the red lines in the figures. These slots have a length of 66 mm, a width of 50 mm and exhibit round corners. In the top plate, there are four holes (6) that can be used as connectors to inlet/outlet streams or as ports for pressure sensors. In the bottom plate, the permeate channel (7) is placed at the middle of the chamber. Eight holes (9) allow the insertion of M10 screws that are tightened to keep the assembly steady and to prevent leakage by pressing two O-rings (11) and (12) between the two plates.

Each of the slots on the top and bottom plates has an area of 32.9 $cm^2$. Different active membrane areas can be obtained by fitting flat plastic pieces, of 0.25 mm thickness, into the slot of the top plate, with the intended channel shape. Figure 3-5 shows the design of the channel used in this work for nanofiltration experiments. In this figure, the green area corresponds to the plastic piece that defines the channel and the white area the channel itself. The distance from the inlet to the outlet ports is 6.9 mm and the width of the channel, $W$, is 10 mm. Near the inlet and outlet ports the channel has a round shape to ease liquid distribution. Other channel shapes can be used. For pressure drop measurements, in addition to the channel with $W$ = 10 mm, channels with $W$ = 3.3 mm and $W$ = 1 mm were also used.

To facilitate the comparison of the nanofiltration performance obtained by both the micro-TFF and CNF techniques, the target value for the ratio between the sample volume and the membrane area was set to 1.4 $mL/cm^2$. In addition, to permit reasonable permeate flow rates, the used filtration channel (Figure 3-5) had a membrane area of 6.9 $cm^2$, resulting in a sample volume to be processed of 9.6 mL.

The plastic pieces that define the channels were cut with the intended shapes by laser cutting (Mercury III, GCC, Taiwan). In these channel designs hole (1) is the inlet, hole (2) is the

outlet, while holes (3) and (4) are used as ports for the differential pressure sensors. To ensure that the actual active membrane area is the designed one, a very thin layer of silicone is spread on the surface of the plastic sheet that will be in contact with the membrane. At the same time, this silicone layer prevents leakage, as Wardip and colleagues did when they coated their 3D-printed device with a thin rubber layer (Wardrip & Arnusch 2016).

Below the membrane, the permeate chamber was filled with a piece of standard permeate side mesh cut from a commercial spiral wound membrane module, in order to give mechanical support to the membrane and at the same time produce low resistance to the flow of the permeate.

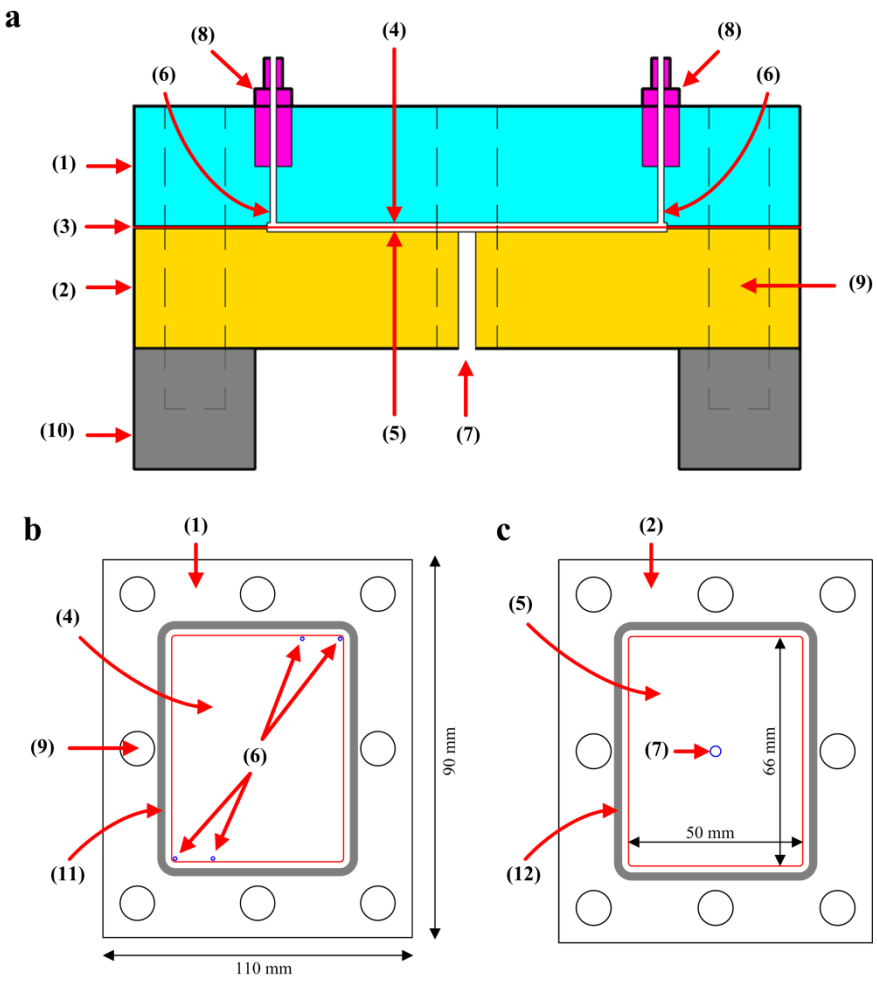


Figure 3-4 – Sketches of the micro-TFF cell: a) side view of the assembly including the top plate (1), the bottom plate (2), the membrane (3), the filtration chamber (4), the permeate chamber (5), the inlet/outlet channels (6), the permeate channel (7), the inlet/outlet connector (8), the holes to insert the screws (9), and the cell supports (10); b) bottom view of the top plate, showing the location of the upper O-ring (11); c) top view of the bottom plate, showing the location of the lower O-ring (12).

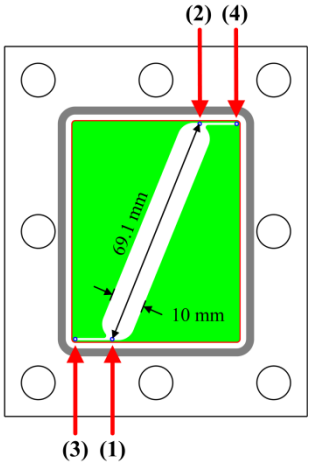


Figure 3-5 – Sketch of the channel used for nanofiltration experiments in the micro-TFF cell. The four holes in the top plate serve as liquid inlet (1), liquid outlet (2), and ports for the high pressure and low pressure sides of the differential pressure sensor: (3) and (4) respectively.

## 3.4 Experimental part

### 3.4.1 Experimental setup

The nanofiltration experiments presented in this section were performed using the micro-TFF nanofiltration system designed and described in section 3.3.

### 3.4.2 Materials

The binary solute-water solutions used in this part of the work were prepared by mixing deionized water with the corresponding solutes. The deionized water was generated in a Milli-Q system (EMD Millipore, USA) and its conductivity was always lower than 2 $\mu$S/cm. The following solutes were used: sodium chloride (NaCl) of reagent grade (BDH Prolabo, Belgium), magnesium chloride hexahydrate ($MgCl_2.6H_2O$) of analysis grade (Merck, Germany), magnesium sulfate heptahydrate ($MgSO_4.7H_2O$) of analysis grade (Merck, Germany), sodium sulfate anhydrous ($Na_2SO4$) of reagent grade (Scharlau, Spain), potassium sulfate ($K_2SO_4$) of reagent grade (Scharlau, Spain), D(-)-Fructose (hereafter designated as fructose) of extra pure grade (Scharlau, Spain), D(+)-Sucrose (hereafter designated as sucrose) of analysis grade (Panreac, Spain) and polyethylene glycol (hereafter designated as PEG-1000) of synthesis grade with a weight average molecular weight of 1000 g/mol (Merck, Germany).

Two nanofiltration membranes were tested: the NFX membrane manufactured by Synder Filtration (Synder Filtration Incorporated n.d.) and the NF90 membrane manufactured by Dow (Dow Chemical Company n.d. a). To obtain a membrane sample, first a good portion of pristine membrane was selected, and then it was cut, including the holes for the screws. A good portion

of membrane was defined as a section of membrane that when back lit did not show bright spots, which usually indicates damaged areas of the membrane. When assembling the micro-TFF nanofiltration cell, a filter paper (Whatman 40, Whatman, England) was placed under the membrane to give mechanical support. Prior to run any experiment, the membranes were compacted by a dual cycle of deionized water permeation: one hour using the 17 bar back-pressure valve followed by another hour using the 34 bar back-pressure valve.

### 3.4.3 Methods

The experiments performed in this chapter are divided into two groups. In the first group of experiments (pressure measurement experiments), the pressure drop was measured for water flows inside channels with impermeable walls and, then, the actual transmembrane pressures in permeation and non-permeation conditions were compared with the nominal values of the back-pressure valves. The pressure drop inside impermeable channels was measured for the channel designs with $W$ = 1 mm, 3.33 mm and 10 mm. In the second group of experiments (nanofiltration experiments), the used membranes were characterized by measuring their hydraulic permeability and solute rejection, and, finally, the potential of the micro-TFF technique to concentrate small-volume samples by nanofiltration was assessed. Since the sample was impelled by the HPLC pump the maximum flow rate was limited to $Q_p$ = 5 mL/min ($Re_h \approx 8$). Both pressure drop and nanofiltration experiments were performed at room temperature, which varied in the range of 20 °C ± 3 °C.

Pressure drop measurements inside the channel were done to evaluate their significance in relation to the transmembrane pressure and they were performed by replacing the membrane by an impermeable plastic sheet. The measurement of the actual pressure inside the channel, when back-pressure valves pressurize the system, was performed to evaluate whether the flow rate and the solution influenced the pressure in the system.

The measurement of the hydraulic permeability and of the solute rejections, at low feed recovery, had two purposes: the $L_p$ value characterize the membranes, while the $R_a$ values at low water recovery serve as benchmark for comparison with the results obtained in the concentration experiments, both using micro-TFF and CNF techniques. NFX is a relatively new membrane, which is not very well characterized in the literature. Conversely, the NF90 nanofiltration performance is profusely described in the literature and their results will be used as means of comparison with the NFX ones. The solute rejection experiments were performed using a single concentration for each of the solutes referred in section 3.4.2, those that the osmotic pressure of the feed, $\pi_f$, is 1.6 bar. Thus, the selected solute concentrations (in their

anhydrous form) are those shown in Table 3-2. The flow rate was set to 5 mL/min and it was used the 17 bar BPV.

Table 3-2 – Selected solute concentrations to be used in solute rejection measurements.

| | solute | | | | | | | |
|---|---|---|---|---|---|---|---|---|
| | NaCl | $MgCl_2$ | $MgSO_4$ | $Na_2SO_4$ | $K_2SO_4$ | fructose | sucrose | PEG-1000 |
| $c$ (g/L) | 2.0 | 2.4 | 7.2 | 4.0 | 5.2 | 11.4 | 21.5 | 50.9 |

For the experiments performed to concentrate small-volume samples only three solutes were used ($K_2SO_4$, fructose and sucrose) but at two distinct concentrations expressed in Table 3-3, which correspond to $\pi_f$ = 0.6 bar and $\pi_f$ = 2.6 bar [11]. The experiments have proceed during the estimated time to inject 9.6 mL from the sample reservoir, according to Table 3-4. The effects of the flow rate ($Q_p$ in the range from 0.1 to 5 mL/min) and of the applied pressure were studied.

At the lowest feed flow rate, the concentrate remaining inside the filtration chamber after the filtration cycle was also collected. The reason for this is the very small amount of concentrate stream produced at such low flow rates. However, as it will be seen later, there is a discrepancy between the solute concentration values of the concentrate stream and those of the liquid remaining inside the filtration chamber.

Detailed procedures of the experimental methods are described in Appendix F.

Table 3-3 – Selected solute concentrations to be used in the micro-TFF nanofiltration experiments for the concentration of small-volume samples.

| | Solute | | |
|---|---|---|---|
| | $K_2SO_4$ | Fructose | Sucrose |
| $c$ (g/L) for $\pi$ = 0.6 bar | 2 | - | 7.7 |
| $c$ (g/L) for $\pi$ = 2.6 bar | 8 | 19 | 30.7 |

Table 3-4 – Necessary time duration to process 9.6 mL of sample using the adopted micro-TFF device.

| | $Q_p$ (mL/min) | | | | | | | | |
|---|---|---|---|---|---|---|---|---|---|
| | 0.10 | 0.25 | 0.50 | 0.75 | 1.00 | 2.00 | 3.00 | 4.00 | 5.00 |
| time | 98 min 35 s | 39 min 26 s | 19 min 43 s | 13 min 09 s | 9 min 52 s | 4 min 56 s | 3 min 17 s | 2 min 28 s | 1 min 58 s s |

### 3.4.4 Chemical analysis

In this part of the work, the samples consisted of model solutions of salts (NaCl, $MgCl_2$, $MgSO_4$, Na2SO4 and $K_2SO_4$) and of neutral molecules (fructose, sucrose and PEG-1000).

[11] Fructose solution concentration was only evaluated for $\pi_f$ = 2.6 bar.

While the samples and liquids resulting from the nanofiltration of salt solutions were analysed by conductometry, those resulting from the nanofiltration of the neutral molecules were analysed by differential refractometry.

To measure salt concentrations, it was used a GLP32 conductivity meter (Crison, Spain), calibrated with standard 0.01 M and 0.1 M KCl solutions (Crison, Spain). The conductivity of the salt solution under analysis was converted to salt concentration using calibration curves. Each of the calibration curves (one for each salt) was obtained measuring the conductivity of known concentration solutions (of that salt) and are available in Appendix B.

Similarly, the output signal of the used DD-5 differential refractometer (Atago, Japan) is a numerical value proportional to the concentration difference between the solution under analysis and a reference liquid. Deionized water (with conductivity lower than 2 μS/cm) was used as reference liquid. Calibration curves used to convert the refractometer output signal to solute concentration were obtained gathering the output signal as function of the solute concentration of known solutions (Appendix B).

## 3.5 Results and discussion

The results of this part of the work are presented in four sub-sections. First, the data of pressure drop measurements for water flows inside three different open and straight microchannels are shown and compared to the predicted ones (section 3.5.1). In this section, it will also be demonstrated that when the system is pressurized with a back-pressure valve, the transmembrane pressure depends on the feed flow rate and on the feed solution itself. Thereafter, the determination of the hydraulic permeability and of the model solutes rejections are used to characterize the NFX and NF90 membranes (section 3.5.2). Although the micro-TFF cell does not have optical accesses for flow visualization, the flux decline and CP effects were verified by evaluating the time evolution of the permeate flux and comparing the experimental steady-state permeate fluxes with the ones estimated by the osmotic pressure model (section 3.5.3). Finally, the capability of micro-TFF technique to concentrate small-volume samples of high osmotic pressure solutions up to high $CF$ values was assessed (section 3.5.4).

### 3.5.1 Characterization of the flow hydrodynamics: pressure drop and transmembrane pressure inside the micro-TFF cell

The micro-TFF nanofiltration cell exhibits dimensions within the precision tolerance of the manufacturing machine. Based on measurements performed after manufacturing the micro-

TFF cell, it is reasonable to claim that the filtration chamber has a height of 250 µm ± 20 µm and that the actual channels widths are slightly larger than the designed ones, as expressed in Table 3-5.

Table 3-5 – Design and actual width of the channels used in the micro-TFF cell for pressure drop measurements

| channel | design width (mm) | actual width (mm) |
|---|---|---|
| 1 mm width channel | 1.0 | 1.2 |
| 3.3 mm width channel | 3.3 | 3.4 |
| 10 mm width channel | 10.0 | 10.3 |

The measured and estimated pressure drops of water flows, for the three used impermeable channels (Table 3-5), are shown in Figure 3-6. The results show that there is a good agreement between experimental and estimate data. For the same channel, the pressure drop increases linearly with the flow rate (typical of the laminar regime), while it increases as the channel width diminishes (for the same channel height). The estimated pressure drop was determined for open channels with rectangular cross-section using the empiric equation (C-1), defined in Appendix C.

For the channels used in micro-TFF nanofiltration experiments, the pressure drop along their length is insignificant (less than 0.1 bar), in the used flow rate range, when compared with the applied pressure (from 7 to 34 bar).

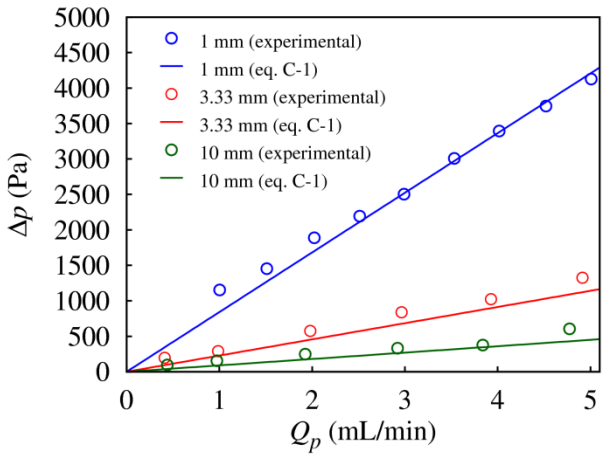


Figure 3-6 – Pressure drop of water flows inside impermeable channels.

The pressure in the hydraulic system is generated by using back-pressure valves. Each BPV is characterized by its nominal pressure, which, in theory, is the pressure upstream the valve. Moreover, the BPV valve should allow the passage of liquid only when the pressure in the system reaches its nominal pressure. However, the actual pressure in the system depends, not only on the BPV valve but also on the feed flow rate, on the permeability of the membrane, on the membrane area and on the sample itself. Figure 3-7 shows that, for each back-pressure

valve, the relationship between the applied pressure and the outlet flow rate is similar for distinct operatory conditions. The applied pressure increases with the concentrate flow rate, reaching a plateau equal to the nominal pressure of BPVs for flow rates higher than 1 mL/min. Therefore, this characteristic behaviour of the used back-pressure valves is more relevant in the range of small flow rates, which were the most efficient conditions to perform the sample concentration by micro-TFF.

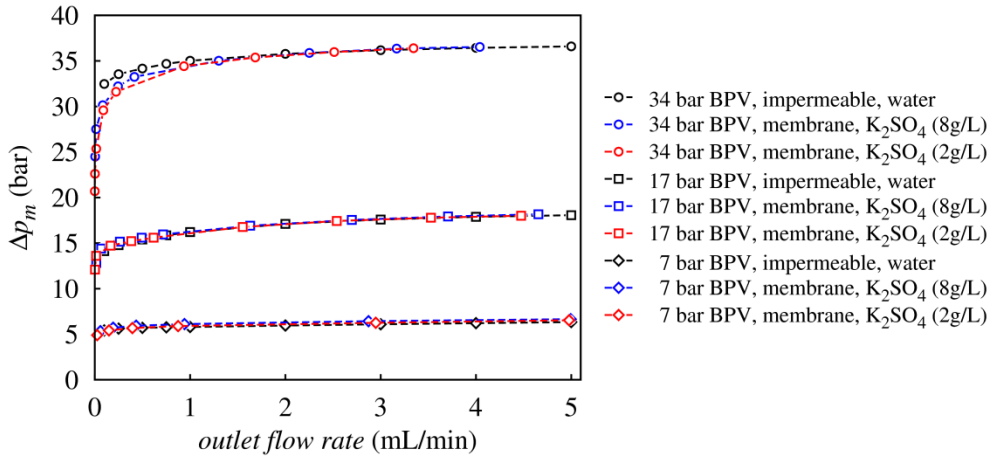


Figure 3-7 – Effect of outlet flow rate on the transmembrane pressure when using different back-pressure valves. All the measurements were performed using the 10 mm width channel and the used membrane was the NFX membrane.

### 3.5.2 Characterization of the used membranes: permeability and solute rejection

The NFX membrane was characterized in terms of the hydraulic permeability and solute rejection because this membrane was also selected to perform most of CNF experiments (Chapter 5). In addition, solute rejection data of small inorganic salts are scarce for the NFX membrane; so, NF90 membrane characterization was set as a benchmark for the results obtained for the NFX membrane.

For transmembrane pressure between 6 bar and 40 bar, the obtained $L_p$ values for the NFX and NF90 membranes were 6.1 $Lm^{-2}h^{-1}bar^{-1}$ and 3.2 $Lm^{-2}h^{-1}bar^{-1}$, respectively. The larger $L_p$ value for the NFX membrane suggests that it has a coarser structure than NF90 membrane. These $L_p$ values are compared, in Table 3-6 and Table 3-7, with the corresponding ones obtained from other authors' works. Although these values are in accordance with the typical $L_p$ values for NF membranes, which vary in the range 1.4 – 12 $Lm^{-2}h^{-1}bar^{-1}$ (Mulder 1996), a large variability of $L_p$ occurs for the same membrane type. Despite this fact may be irrelevant for TFF processes, for centrifugal filtration applications, this issue causes undesirable distinct concentration performance obtained by similar CNF devices. In addition, at extreme conditions, mechanical failure of the centrifuge rotor can occur due to an imbalance of the mass centres of

the CNF devices. Therefore, when using centrifugal filtration techniques, the membranes of the devices placed at opposite locations in the rotor bucket should have the same hydraulic permeability.

Table 3-6 – Hydraulic permeability of the NFX membrane determined, or referred, by various authors.

| Reference | $L_p$ ($L \cdot m^{-2} h^{-1} bar^{-1}$) | $\Delta p_m$ (bar) | $T$ (°C) | Area of membrane ($cm^2$) |
|---|---|---|---|---|
| This work | 6.1 | 6 – 40 | 20 ± 3 | 6.9 |
| supplier[a] | 6.8 – 8.0 | 7.5 | 25 | † |
| (J. Wang, Wei, et al. 2014) | 5.7 | 0 – 15 | 25 | 3300 |
| (Temido 2015) | 3.0 | 0 – 20 | 25 | 360 |
| (Long & Wang 2015) | 10.8 | 3.5 | † | 17.5 |
| (Yu et al. 2017) | 20 | † | † | † |

[a] (D'Costa 2018) † data not available.

Table 3-7 – Hydraulic permeability of the NF90 membrane determined, or referred, by various authors.

| Reference | $L_p$ ($L \cdot m^{-2} h^{-1} bar^{-1}$) | $\Delta p_m$ (bar) | $T$ (°C) | Area of membrane ($cm^2$) |
|---|---|---|---|---|
| this work | 3.2 | 0 – 36 | 20 ± 3 | 6.9 |
| (Krieg et al. 2004) | 3.6 | 5 – 20 | † | 44 |
| (Artuğ et al. 2007) | 13 | 3 – 13 | 20 | 274 |
| (Teixeira et al. 2009) | 7.0 | 10 – 20 | 25 | 51.4 |
| (Fernández et al. 2011) | 4.6‡ | 10 – 40 | † | 13.9 |
| (Luo et al. 2011) | 10.5 | 0 – 12 | 25 | 4.52 |
| (Nicolini et al. 2016) | 4.7 | 5 – 20 | 23 | 28 |

† data not available. ‡ the linear fitting of the data has a positive intercept.

Although the hydraulic permeability is an important parameter to characterize membranes, the effective membrane performance must be assessed performing the filtration with solutions. Model solutes for nanofiltration membranes are usually small inorganic salts and small organic molecules, all of them with molecular weight below 1000 g/mol. In the present work, inorganic salts with MW up to 174 g/mol and organic molecules with MW between 180 and 1000 g/mol were used. Despite NFX and NF90 membranes are, according to their manufacturers, suitable for nanofiltration, they present distinct filtration behaviour.

A summary of the results obtained for the solute rejection experiments of both NFX and NF90 membranes is shown in Table 3-8. The experiments were conducted according to the methodology described in section 3.4.3. From the obtained data, it is clear that the NF90 membrane has a more efficient blocking power than the NFX one, which results from a denser membrane structure or from the more negative electrical charge of the membrane surface. Both

NF90 and NFX are polyamide membranes, which at neutral pH present negative zeta-potential (Artuğ et al. 2007; Tang et al. 2007; D'Costa 2018).

The obtained apparent rejection, $R_a$, is higher for all the solutes when using the NF90 membrane. However, while for some solutes the $R_a$ values differ between membranes just by tenths of percentage points, for other solutes the differences are more significant.

For instance, the $R_a$ value for the 2 g/L NaCl solution is 87 % when using the NF90 membrane but drops abruptly to 19 % when using the NFX membrane, which is much smaller than the value specified by the manufacturer: 40 % (Synder Filtration Incorporated n.d). However, while the manufacturer has measured the solute rejection at 7.6 bar, in this work it was measured at 17.2 bar. By the solution-diffusion theory it is expected that the rejection increases with the increase of the permeate flux, as suggested by equation (2-31). However, as it will be shown later, despite rising $\Delta p_m$ can lead to higher permeate flux, in the case of NaCl solutions it results in lower rejection due to the inability of the NFX membrane to retain the ions when the intrinsic rejection is already low, i.e. when the membrane is unable to perform efficient separation of the solute.

Similar observations are observed for the $MgCl_2$ and fructose solutions. The $R_a$ value for the $MgCl_2$ solution is almost 99 % when using the NF90 membrane, but only 68 % when using the NFX membrane. The $R_a$ value for the fructose solution is above 99 % when using the NF90 membrane, but of only 73 % when using the NFX membrane.

Table 3-8 – Experimental solute rejections, permeate flux and concentration factor, for the NFX and NF90 membranes, obtained at $Re_h \approx 8$ and $T = 20 \pm 3$ °C, using the 17 bar back-pressure valve.

| | | | Membrane | | | | | |
|---|---|---|---|---|---|---|---|---|
| | | | NFX | | | NF90 | | |
| solute | MW (g/mol) | $c$ (g/L) | $R_a \times 100$ | $\bar{J}_v / \bar{J}_w$ | $CF$ | $R_a \times 100$ | $\bar{J}_v / \bar{J}_w$ | $CF$ |
| NaCl | 58.4 | 2.0 | 18.6 | 0.97 | 1.12 | 86.6 | 0.86 | 1.08 |
| $MgCl_2$ | 95.2 | 2.4 | 68.7 | 0.48 | 1.06 | 98.9 | 0.62 | 1.15 |
| $MgSO_4$ | 120.4 | 7.2 | 99.1 | 0.25 | 1.08 | 99.7 | 0.46 | 1.13 |
| $Na_2SO_4$ | 142.0 | 4.0 | 98.9 | 0.38 | 1.06 | 99.5 | 0.57 | 1.14 |
| $K_2SO_4$ | 174.3 | 5.2 | 99.1 | 0.39 | 1.05 | 99.4 | 0.80 | 1.07 |
| Fructose | 180.2 | 11.4 | 73.2 | 0.50 | 1.09 | 99.5 | 0.75 | 1.07 |
| Sucrose | 342.3 | 21.5 | 99.5 | 0.39 | 1.07 | 99.8 | 0.68 | 1.06 |
| PEG-1000 | 1000 | 50.9 | 99.4 | 0.30 | 1.02 | 99.8 | 0.33 | 1.03 |

Also interesting, when using the NFX membrane, is the fact that although fructose has higher MW than $MgSO_4$, $Na_2SO_4$ and $K_2SO_4$ salts, its rejection is lower: 73 % for fructose and above 98 % for those salts. This behaviour shows that nanofiltration is governed not only by a

size exclusion process but also by electrical repulsions. Since fructose is a neutral molecule the surface charge of the membrane is less significant for its retention and, therefore, one can assume that pores are larger in NFX membrane than in NF90 membrane ($R_a$ of 73 % and 99 % for NFX and NF90 membranes, respectively). On the other hand, the NFX membrane was able to retain salts with lower MW than that of fructose which means that the NFX membrane has a very appreciable surface electrical charge. In fact, at pH = 7, the zeta-potentials of these two membranes are ca. -30 mV for the NF90 (Artuğ et al. 2007; Tang et al. 2007) and -80 mV for the NFX (D'Costa 2018).

The solute rejections obtained in this work for both NFX and NF90 membranes (Table 3-8) are in accordance with the solute rejection values obtained by other authors. Few works were published on the NFX nanofiltration performance and none of them uses small salts as model solutes. NFX was mainly applied to nanofilter inorganic complexes with MW above 300 g/mol, resulting in $R_a$ values always above 97 %, as can be seen in Table 3-9. For the NF90 membrane there are plenty of data in the literature, both for salts and for organic molecules, some of which is presented in Table 3-10.

As an illustrative example, one can compare the $R_a$ values obtained in this work for the nanofiltration of sucrose (MW = 342 g/mol) solution against that obtained by Hang and colleagues (Hang et al. 2015) for the nanofiltration of difructose anhydrous (MW = 324 g/mol) solution. In both works, the $R_a$ values were above 98.5 % and larger solute rejection was observed when using the NF90 membrane. In another example, now just for the NF90 membrane and for organic molecules with equal MW (180.2 g/mol), the solute rejection for the fructose ($R_a$ = 99.5 %) obtained in this work is very similar to that of glucose ($R_a$ = 99.1 – 99.8 %) obtained by other authors (Artuğ et al. 2007; Rodrigues et al. 2010). Similar results were also verified for the used small inorganic salts.

The effect of the pressure on the nanofiltration performance is shown in Figure 3-8, for the NFX membrane. The two most interesting aspects of the pressure influence is the reduction of both the rejection $R_a$ and of the permeate flux ratio $\bar{J}_v/\bar{J}_w$ as the pressure increases.

The magnitude of the $R_a$ reduction depends on the ability of the membrane to block the solute molecule and, thus, the rejection of smaller solutes drops more sharply with pressure. This behaviour can be verified in Figure 3-8a comparing the rejections of the two neutral solutes of different sizes: fructose (smaller molecule) and sucrose (larger molecule). For the same pressure variation, i.e. performing the nanofiltration with the 17 bar or with the 34 bar back-pressure valves, the rejection of fructose dropped from 73 % to 69 %, while the rejection of sucrose has a minimal decrease from 99.5 % to 99.3 %. This same behaviour has already been seen for the very low NaCl rejection obtained when using the NFX membrane: 19 % at 17 bar versus 40 % at 7.6 bar, as expressed in Table 3-9.

Table 3-9 – Data on the solute rejection of the NFX membrane determined, or referred, by various authors. For detailed information on the composition of the feed solutions look at the respective literature source.

| Feed | MW (g/mol) | $c_f$ (g/L) | $\Delta p_m$ (bar) | $t$ (°C) | $U$ (cm/s) | $R_a \times 100$ | Reference |
|---|---|---|---|---|---|---|---|
| NaCl | 58.4 | 2 | 17.2 | 20 | 3.3 | 19 | this work |
| | | 2 | 7.6 | 25 | † | 40 | supplier [a] |
| fermentation broth from lactic acid production | NaL[b]: 112.1 | NaL[b]: 116.1<br>protein: 4.4<br>$Ca^{2+}$: 1.02<br>$Mg^{2+}$: 0.80 | 20 | 30 | † | 20% NaL [b]<br>99% protein<br>88% $Ca^{2+}$<br>95% $Mg^{2+}$ | (K. Wang et al. 2013) |
| $MgSO_4$ | 120.4 | 2.4 | 17.2 | 20 | 3.3 | 99.1 | this work |
| | | 2 | 7.6 | 25 | † | 99 | supplier [a] |
| Norfloxacin | 319.3 | $2\times10^{-4}$ | 2 | 20 | 35 | > 98 | (Liu et al. 2014) |
| difructose anhydrous | 324 | 76 | 1 | 50 | [c] | 98.7 | (Hang et al. 2015) |
| Ofloxacin | 361.4 | $2\times10^{-4}$ | 2 | 20 | 35 | > 98 | (Liu et al. 2014) |
| Ferric-lactate complex | ≈ 495 | 25 – 50 | 8 | † | † | 97.0 – 99.5 | (Yu et al. 2017) |
| Azithromycin | 749.0 | $2\times10^{-4}$ | 2 | 20 | 35 | > 99 | (Liu et al. 2014) |
| Roxithromycin | 837.0 | $2\times10^{-4}$ | 2 | 20 | 35 | > 99 | (Liu et al. 2014) |
| wastewater from Spiramycin production | Spiramycin: 843.1 | TOC [d]: 0.03<br>COD [e]: 0.10<br>$Na^+$: 1.05<br>$Ca^{2+}$: 0.25<br>$Cl^-$: 2.00<br>$SO_4^{2-}$: 0.08 | 10 | † | † | TOC [d]: 99.3<br>COD [e]: 91.8<br>$Na^+$:23.9<br>$Ca^{2+}$: 91.6<br>$Cl^-$: 39.5<br>$SO_4^{2-}$: 97.2 | (J. Wang, Wei, et al. 2014) |

† not available. [a] supplier: (Synder Filtration Incorporated, n.d). [b] sodium lactate. [c] dead-end. [d] TOC: total organic carbon. [e] COD: chemical oxygen demand.

The most plausible justification for the decrease of the rejection with pressure is the incapacity of the membrane to efficiently retain the solute that is dragged by the water flow through the membrane. This occurs when the size of neutral solutes is lower than the membrane pore size, as is the case of fructose. In this scenario, increasing the pressure results in an increase of the permeate flux and, thus, of the relative importance of the convective transport in comparison to the diffusive transport through the membrane. At the same time, the increase of the permeate flux increases the concentration at the membrane surface. Therefore, very highly concentrated fluid elements are dragged across the membrane and the rejection drops. This phenomenon becomes less significant as the solute retention by the membrane rises and, therefore, the sucrose rejection remained nearly unchanged.

A proof of the direct relationship between the applied pressure and concentration polarization can be seen by the variation of both $\bar{J}_v$ and $\bar{J}_v/\bar{J}_w$, as depicted in Figure 3-8b.

Despite the $\bar{J}_v$ increases with the applied pressure, the ratio $\bar{J}_v/\bar{J}_w$ decreases, showing that higher osmotic pressure near the membrane and, thus, concentration polarization exists. This same behaviour, i.e. the increase of the solute concentration near the membrane, will also be verified in Chapter 4 by visualizing the solute concentration field by holographic interferometry.

Table 3-10 – Data on the solute rejection of the NF90 membrane, determined, or referred, by various authors. For detailed information on the composition of the feed solutions look at the respective literature source.

| Solute | MW (g/mol) | $c$ (g/L) | $\Delta p_m$ (bar) | $T$ (°C) | $U$ (cm/s) | recovery (%) | $R_a \times 100$ | Reference |
|---|---|---|---|---|---|---|---|---|
| NaCl | 58.4 | 2.0 | 17.2 | 20 ± 3 | 3.3 | 8 | 87 | this work |
| | | 2.0 | 15.5 | 25 | † | 15 | 85 – 95 | supplier [a] |
| | | 20 ppm $Cl^-$ | 20 | [b] | [c] | † | 92 | (Krieg et al. 2004) |
| | | 1.46 | 5 – 20 | 23 | † | † | ≈ 93 | (Nicolini et al. 2016) |
| | | 0.175 – 6 | 10 | 20 | 110 | † | 87 – 95 | (Artuğ et al. 2007) |
| | | 1 – 10 | 6 | 22 | † | † | 85 – 92 | (Hilal et al. 2015) |
| $MgCl_2$ | 95.2 | 2.4 | 17.2 | 20 ± 3 | 3.3 | 15 | 98.9 | this work |
| | | 16 | 35 | † | † | † | 96.6 | (Altaee et al. 2016) |
| $MgSO_4$ | 120.4 | 7.2 | 17.2 | 20 ± 3 | 3.3 | 13 | 99.7 | this work |
| | | 2.0 | 4.8 | 25 | † | 15 | > 97 | supplier [a] |
| | | 3.0 | 5 – 20 | 23 | † | † | ≈ 98.5 | (Nicolini et al. 2016) |
| | | 0.4 – 14 | 10 | 20 | 110 | † | 96.8 – 97.4 | (Artuğ et al. 2007) |
| | | 33 | 35 | † | † | † | 99.8 | (Altaee et al. 2016) |
| $Na_2SO_4$ | 142.0 | 4.0 | 17.2 | 20 ± 3 | 3.3 | 14 | 99.5 | this work |
| | | 20 ppm $SO_4^{2+}$ | 20 | [a] | [c] | † | 93 | (Krieg et al. 2004) |
| | | 3.55 | 5 – 20 | 23 | † | † | ≈ 99.2 | (Nicolini et al. 2016) |
| | | 0.4 – 15 | 10 | 20 | 110 | † | 97.7 – 98.1 | (Artuğ et al. 2007) |
| | | 1 – 10 | 6 | 22 | † | † | 99.1 – 99.7 | (Hilal et al. 2015) |
| | | † | 10 – 60 | 22 ± 2 | 90.5 | † | 99.4 – 99.8 | (Rodrigues et al. 2010) |
| $K_2SO_4$ | 174.3 | 5.2 | 17.2 | 20 ± 3 | 3.3 | 7 | 99.4 | this work |
| | | 4.36 | 5 – 20 | 23 | † | † | ≈ 97.8 | (Nicolini et al. 2016) |
| Fructose | 180.2 | 11.4 | 17.2 | 20 ± 3 | 3.3 | 7 | 99.5 | this work |
| Glucose | 180.2 | 0.43 | 3 – 10 | 20 | 110 | † | 99.1 – 99.3 | (Artuğ et al. 2007) |
| | | † | 10 – 60 | 22 ± 2 | 90.5 | † | 99.3 – 99.8 | (Rodrigues et al. 2010) |
| difructose anhydrous | 324 | 76 | 1 | 50 | [c] | † | 99.1 | (Hang et al. 2015) |
| Sucrose | 342.3 | 21.5 | 17.2 | 20 ± 3 | 3.3 | 6 | 99.8 | this work |
| | | 0.43 | 3 – 10 | 20 | 110 | † | 97.9 – 99.3 | (Artuğ et al. 2007) |
| | | † | 10 – 60 | 22 ± 2 | 90.5 | † | 99.4 – 99.9 | (Rodrigues et al. 2010) |

† not available. [a] referred in (Hilal et al. 2015). [b] room temperature. [c] dead-end.

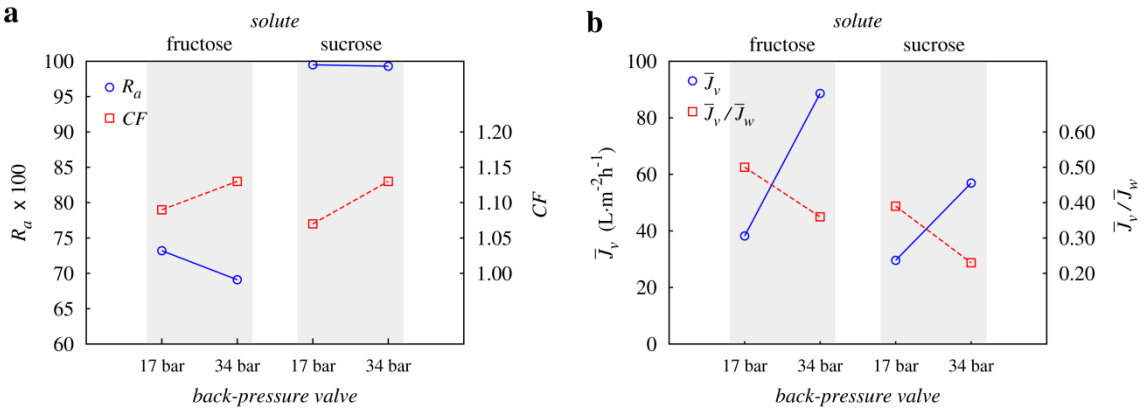


Figure 3-8 – Effect of the applied pressure (17 bar and 34 bar backpressure valves) on the solute rejection, permeate flux and concentration factor, for the nanofiltration of fructose and sucrose aqueous solutions ($c_f$ = 11.4 g/L and $c_f$ = 21.5 g/L, respectively) using a NFX membrane, at $T$ = 20 ± 3 °C and $Q_p$ = 5.00 mL/min ($Re_h \approx 8$).

### 3.5.3 Concentration polarization effects

Concentration polarization phenomenon will be studied in detail in Chapter 4 by the holographic interferometry technique for the nanofiltration of $K_2SO_4$ solutions using a different TFF cell with optical access windows. Since the micro-TFF cell used in the present chapter does not allow for optical access, visualization by HI technique is not possible. Hence, the alternative way is to monitor the temporal evolution of the permeate flux, and compare the experimental and predicted data for the permeate flux at steady-state conditions.

The permeate flux decline was measured during the time period of one hour after the beginning of the nanofiltration process of 8 g/L $K_2SO_4$ solution and of a 30.7 g/L sucrose solution. In these experiments, the system was pressurized using the 34 bar back pressure valve and two different flow rates were imposed ($Q_p$ = 5.00 mL/min and $Q_p$ = 0.25 mL/min). The temporal evolution of the permeate fluxes, under such conditions, is shown in Figure 3-9. Figure 3-9a shows the results for $Q_p$ = 5.00 mL/min, while Figure 3-9b shows the results for $Q_p$ = 0.25 mL/min, which correspond to $Re_h \approx 8$ and $Re_h \approx 0.4$, respectively. In these figures the open symbols refer to experimental data, whereas the solid points, at $t$ = 0 min, were calculated using the osmotic pressure model expression, equation (2-26), and represent the predicted permeate flux that would occur without CP effects, $J_{v,0}$. The dashed line is given by the permeate flux of pure water, while the solid lines represent the fittings to the sets of values including the experimental data and $J_{v,0}$.

Two distinct behaviours can be inferred from Figure 3-9a and Figure 3-9b. If the inlet flow rate is much higher than the maximum flow rate that can cross the membrane, $Q_{max}$, for the same applied pressure, then the magnitude of the permeate flux decline is large. First, let us define $Q_{max}$ as the minimum value between $Q_p$ and product of $J_w$ by the membrane area. That is the case of the data depicted in Figure 3-9a: $Q_p$ = 5.00 mL/min and $Q_{max}$ = 1.3 mL/min.

Conversely, for the data of Figure 3-9b both $Q_p$ and $Q_{max}$ are equal to 0.25 mL/min resulting in a small reduction of permeate flux along the time.

Steady-state appears to be reached in ca. 10 min, since after that time instant the reduction of the permeate flux is small, as can be seen in Figure 3-9a. Therefore, for experiments where the nanofiltration process has to be considered at steady-state, a minimum of 10-minute filtration cycle had to be conducted prior to collect permeate and/or concentrate streams. These were the cases of the experiments performed to measure the apparent rejection of model solutes, which results were already presented in the previous section 3.5.2. In addition, as it will be seen later, in Chapter 4, the necessary time period of 10 minutes to reach steady-state will be corroborated by interferogram analysis, providing that $Re_h \geq 5$.

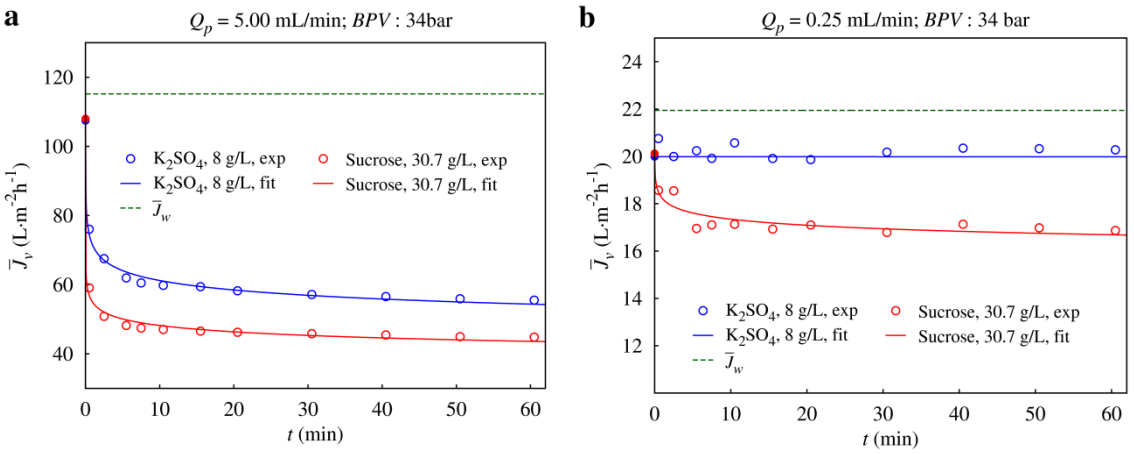


Figure 3-9 – Temporal evolution of the permeate flux for the nanofiltration of $K_2SO_4$ and sucrose solutions ($c_f$ = 8 g/L and $c_f$ = 30.7 g/L, respectively) using the 34 bar BPV for: a) $Q_p$ = 5.00 mL/min; b) $Q_p$ = 0.25 mL/min.

For all the used model solutes, the experimental permeate flux at steady-state, i.e. determined at $t$ = 10 min (Table 3-8) was compared with the one predicted by the osmotic pressure model, decomposing in equation (2-26) the $L_p$ factor by $1/\mu R_m$, as defined in equation (2-3). Herein, the permeate flux is replaced by the ratio between the permeate flux itself and the pure water permeate flux, $\bar{J}_v/\bar{J}_w$. If the obtained permeate flux predictions are in good agreement with the experimental ones, then, one can suppose that no concentration polarization occurs. Conversely, if the predictions do not match the experimental results, then, one is probably facing concentration polarization phenomenon. In addition, the osmotic pressure model uses as parameter the value of water viscosity, $\mu_w$. However, other authors suggest to use the viscosity of the feed stream (Rodrigues et al. 2010).

In Figure 3-10 four types of $\bar{J}_v/\bar{J}_w$ ratios are shown. In addition to the experimental $\bar{J}_v/\bar{J}_w$ ratios (black bars), three other distinct $\bar{J}_v/\bar{J}_w$ ratios were calculated using the osmotic pressure model. The $\bar{J}_{vc,fw}/\bar{J}_w$ ratios (blue bars) were calculated considering that there was no

concentration polarization and that the solute rejection is 100 %. In this scenario $\pi_m = \pi_f$, $\pi_p$ = 0 and $\mu = \mu_w$. To calculate $\bar{J}_{vc,mw}/\bar{J}_w$ ratios (red bars), polarization concentration was assumed and $\pi_m$ was determined based on the solute concentration at the membrane surface, $c_m$, which was estimated according to the methodology described in Appendix F. The osmotic pressure on the permeate was calculated as function of its solute concentration. Finally, the $\bar{J}_{vc,mm}/\bar{J}_w$ ratios (orange bars) was calculated as the $\bar{J}_{vc,mw}/\bar{J}_w$ ratios but it was used the viscosity of the liquid near the membrane ($\mu = \mu_m$).

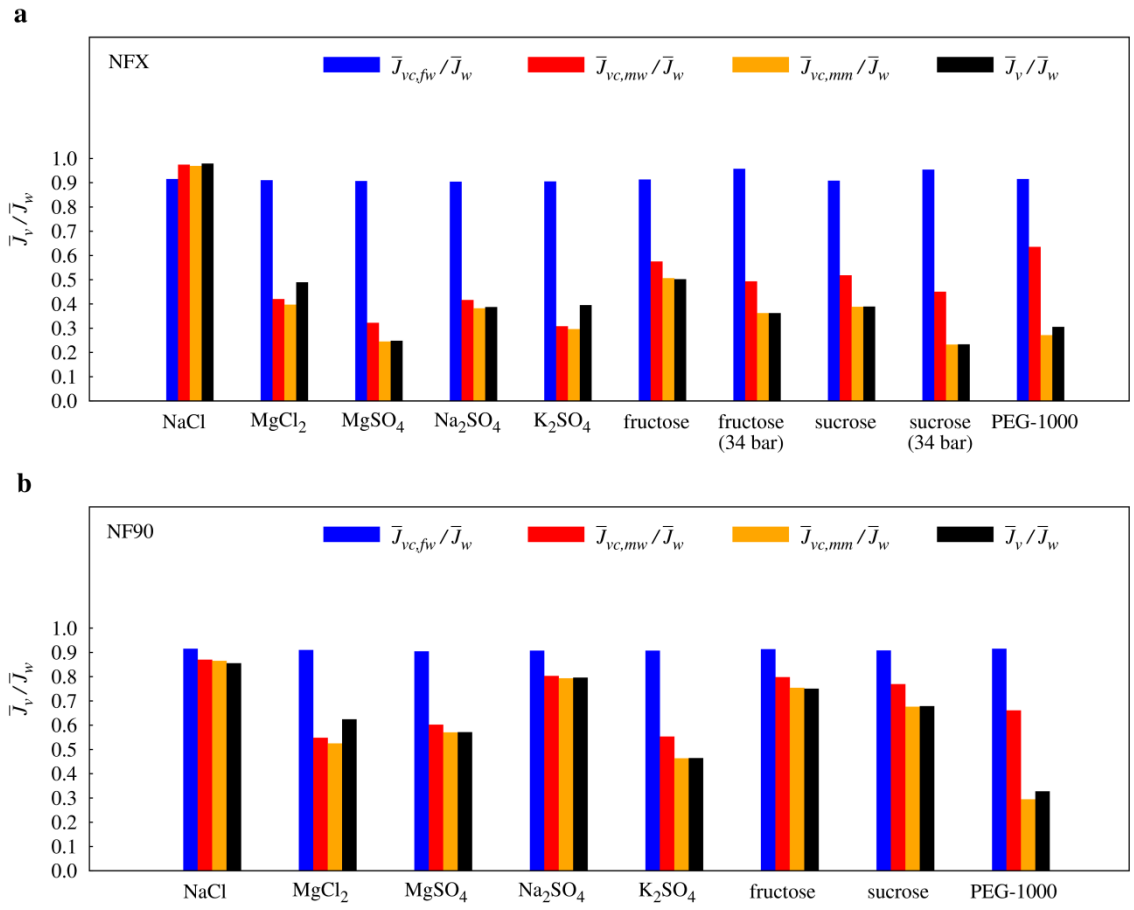


Figure 3-10 – Comparison of experimental permeate flux to pure water flux ratio ($\bar{J}_v/\bar{J}_w$) and the corresponding values predicted by the osmotic pressure model. Nanofiltration was performed at $Re_h \approx 8$ and $T = 20 \pm 3$ °C. Unless stated, the 17 bar backpressure valve was used. Solute concentrations of the feed solutions and the definitions of each permeate flux ratios are referred in the text. Data refers to: a) NFX membrane; b) NF90 membrane.

With the exception of the NaCl nanofiltration, there is a significant difference between experimental permeate fluxes and the predicted ones based on the feed concentration, i.e. the $\bar{J}_{vc,fw}/\bar{J}_w$ ratio (blue bars), which indicates that concentration polarization occurs at a great extent near the membrane surface. Better accordance is obtained, as expected, applying the osmotic pressure model based on solute concentration at the membrane surface (red and yellow bars). In addition, while for salt solutions it is almost indifferent to use water or solution viscosities to calculate the permeate flux (since their viscosity vary little with solute

concentration), for fructose, sucrose and PEG-1000 better matches occur using the viscosity of the solution near the membrane. Therefore, when predicting the permeate flux using the osmotic pressure model, the viscosity of the solution must be incorporated in the model if its viscosity is much higher than that of water. This fact will be used later (in Chapter 5) when comparing the experimental and predicted permeate fluxes for the CNF process.

### 3.5.4 Concentration of small-volume samples

First of all, one must recognize that the experimental results proved that it is possible to concentrate small-volume samples, of binary aqueous solutions of low MW solutes, using the micro-TFF nanofiltration system developed in this work. However, high concentration factors can only be achieved when the Reynolds number is so small that the TFF filtration process degenerates into a dead-end filtration process. Since, none of the concentration polarization mitigation methodologies, described in section 2.3.2, was adopted to be used in conjunction with the micro-TFF nanofiltration system, it is expected that high CP effects exist. Nevertheless, under certain circumstances, high concentration factors up to ca. 20 were achieved, in particular for low feed concentrations and small flow rates.

The previous reasoning lies in the evaluation of the data obtained for the micro-TFF nanofiltration processes of aqueous solutions of $K_2SO_4$, fructose and sucrose. The nanofiltration of those solutions was performed in accordance with the method described in section 3.4.3. Briefly, the permeate, the concentrate and/or the liquid remaining in the filtration chamber were collected after the injection of 9.6 mL of the solution under study at a particular flow rate ($Q_p$ ranging from 0.10 mL/min to 5.00 mL/min) while applying pressure with one of the three available back-pressure valves (7 bar, 17 bar and 34 bar). Two different concentrations were used for each of the $K_2SO_4$ and sucrose solution: 2.0 g/L and 8.0 g/L, for $K_2SO_4$, and 7.7 g/L and 30.7 g/L for sucrose, which osmotic pressures correspond to $\pi$ = 0.6 bar and had $\pi$ = 2.6 bar, respectively. For fructose, it was used a single concentration (19.0 g/L) which osmotic pressure corresponds to $\pi$ = 2.6 bar. Also, for fructose, the whole range of flow rate was covered only in the 34 bar experiments (for the 7 bar and 17 bar BPVs, the fructose solution experiments were performed only for $Q_p$ = 5.00 mL/min).

It should be mentioned that the $CF$ magnitude depends on the collection station. In the present work there were two possible station locations: a) at the exit of the BPV valve, being collected over the whole filtration cycle; b) at filtration chamber in the end of the filtration cycle, i.e. the liquid remaining inside the filtration chamber. As far as the concentrate remaining in the filtration chamber is concerned, its collection was performed only for very low feed flow rates, leading to very high feed recovery (above 90%).

The comparison of the concentration factor determined for the concentrate stream and for the concentrate remaining inside the filtration chamber, for a selected scenario – nanofiltration of $K_2SO_4$ aqueous solutions ($c_f$ = 2 g/L) using the NFX membrane and the 34 bar BPV – is shown in Figure 3-11 as function of the measured feed flow rate, $Q$, i.e. the sum of the concentrate and permeate flow rates. It is clear that the $CF$ of the concentrate remaining in the filtration chamber is higher than the $CF$ of the concentrate stream (at the outlet of the BPV). Two factors may contribute to this.

First, the liquid collected from the concentrate stream may have some amount of untreated feed that fills the tubing going from the micro-TFF cell to the BPV valve, resulting in a drop in the measured concentration. The maximum volume of liquid entrapped is ca. 0.9 mL (0.2 mL in the tubing, 0.1 mL in the BPV, and 0.1 mL in each of the port connectors). Since in each experiment 9.6 mL of sample was injected, the maximum entrapped volume represents 9 % of the feed. In the experiments where the liquid remaining inside the filtration channel was collected, some amount of the liquid inside the port connectors was removed after the filtration cycle to minimize dilution effects. Thus, this first factor should not be very significant when low feed recovery occurs, but it is important in high feed recovery experiments, which are the ones where high $CF$ values are obtained. The second factor leading to the difference in the obtained $CF$ is the liquid velocity profile inside the filtration chamber.

When the feed recovery is low, the permeate flux is at least an order of magnitude smaller than the average bulk velocity, resulting in velocity profiles similar to those occurring in flows within impermeable walls slit channels. In these scenarios velocity profiles are parabolic (Completo et al. 2014) with the apex at the middle height of the channel. Thus, the fluid elements that flow to the outlet port in low recovery processes are mainly those with larger velocity. Since the CP layer is located in the vicinity of the membrane, where the velocity is lower, the most concentrate fluid elements have a larger residence time inside the filtration chamber. For this reason, the $CF$ value of the concentrate stream is lower than that of the liquid inside of the filtration chamber. However, one should be aware that, for the presently applied $Re_h$, the feed recovery can attain very high values leading to a deformation of the parabolic velocity profile manifested through the deviation of its apex. Moreover, the average solute concentration inside the filtration chamber is volumetric, i.e. all the fluid elements count to the average equally. On the other hand, to calculate the average solute concentration in the concentrate stream one should integrate the product of the concentration profile with the velocity profile, at the extremity of the channel, over the channel height, which results in lower solute concentration due to the lower velocity near the walls, and particularly near the membrane where the concentration is higher. Therefore solute concentrations inside the filtration chamber must be higher than those in the concentrate stream, which is accordance with the data of the Figure 3-11.

The drop in the $CF$ value observed in Figure 3-11 for the lower feed flow rate ($Q_p$ = 0.10 mL/min) have distinct explanations. For the concentrate stream, the $CF$ value decreases due to high feed recovery which leads to a small amount of volume collected in the concentrate stream. Thus, the unfiltered solution inside the tubing masks the final $CF$ value. On the other hand, the $CF$ decrease for the liquid collected from the filtration chamber can be explained by the reduction of the $R_a$ value (from 96.2 % to 92.7 %). The drop in the $R_a$ is due to the inability of the used NF membrane to effectively retain small solutes near its MWCO. This behaviour was already shown in Figure 3-8, where it was compared the $R_a$ decrease for fructose and sucrose. However, this same behaviour may be practical for sample fractionation. Therefore, to ensure that the solute of interest remains in the filtration chamber, the used membrane should be wisely selected. For the specific presented cases, the concentration of $K_2SO_4$ and of fructose, that would imply the use of tighter membranes than the NFX one.

The data shown in Figure 3-11 refers only to particular conditions of solute concentration and applied pressure, but it was verified that the $CF$ value for the concentrate stream is consistently lower than that for the liquid inside the filtration chamber. However, for the other permeation experiments, the liquid inside the filtration chamber was collected only for the experiments of smallest $Q_p$ or when the amount of concentrate stream was tiny. The data points of such measurements will be marked with solid symbols in the following figures.

For solutes with MW > MWCO, the $CF$ value increases as the inlet flow rate decreases. However, as Figure 3-11 shows, it is possible to obtain appreciable concentration ($CF$ > 10) for inlet flow rates between 0.25 mL/min and 0.50 mL/min, provided the sample concentration is low. Therefore, micro-TFF can be used to effectively concentrate diluted samples in relatively small filtration cycles. To obtain larger $CF$ values smaller flow rates may be needed.

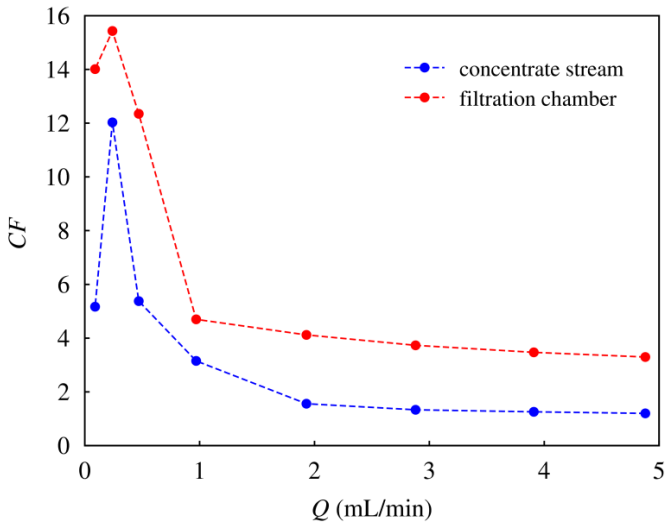


Figure 3-11 – Comparison between the concentration factor values determined for the liquid collected from the concentrate stream and the liquid remaining inside the filtration chamber (at the end of the filtration cycle). The data refer to the nanofiltration of $K_2SO_4$ aqueous solutions ($c_f$ = 2 g/L) using the NFX membrane and the 34 bar BPV.

Representative nanofiltration performance data, as function of the feed flow rate, obtained for the concentration of sucrose, $K_2SO_4$ and fructose aqueous solutions are shown in Figures 3-12, 3-13 and 3-14, respectively. It should be mentioned that although the presented data covers only some of the operating conditions, similar results were obtained for the remaining operating conditions (different solute concentrations as specified in Table 3-3), the differences being only the magnitude and the sharpness of the curves plotted in the charts.

As the inlet flow rate, $Q$, decreases, the feed recovery increases because $Q$ approaches the maximum pure water permeate flow rate for that particular applied pressure, $Q_{max}$ (defined in section 3.5.3). Feed recovery should get closer to 100 % for any $Q$ lower than $Q_{max}$, for the same membrane and pressure. However, two factors contribute to feed recovery lower that 100 % even when $Q < Q_{max}$. First, the presence of solute and the concentration polarization effect reduces the permeate flux. Second, the actual pressure in the system decreases as $Q$ diminishes (as discussed in section 3.5.1) and, for that reason, $Q_{max}$ also drops which makes the system to depart from the conditions of full feed recovery. In fact, feed recovery rates near 100% only occur at very low $Q$ and for the highest applied pressure (figures "a").

Very high feed recovery results in relatively large $CF$ values (figures "b") but at the expense of a decrease of solute rejection (figures "a"). As expected, with basis on the solution diffusion model, the rejection decreases as the permeate flux decreases (figures "c"). The reduction of $Q$ and, therefore, the increase of the feed recovery leads to an increase of both the solute concentration in the concentrate (as already verified by the increase of $CF$) and the solute concentration at the membrane surface, $c_m$, in the feed side (figures "d"). This justifies the reduction of the permeate flux by the increase of the osmotic pressure near the membrane. The $c_m$ values were determined by using the methodology described in in Appendix F.

Consider the $\bar{J}_v/\bar{J}_{w,34bar}$ and the $\bar{J}_v/\bar{J}_{w,p}$ ratios. The $\bar{J}_v/\bar{J}_{w,p}$ ratio corresponds to the ratio between the permeate flux, $\bar{J}_v$, using the BPV with nominal pressure $p$ and the pure water permete flux obtained using the same BPV, $\bar{J}_{w,p}$, whereas the $\bar{J}_v/\bar{J}_{w,34bar}$ ratio corresponds to the ratio between the permeate flux at $p$ and the pure water permeate flux obtained using the 34 bar BPV, $\bar{J}_{w,34bar}$. Then, one can verify that the permeate flux depends on the feed pressure, and it increases as the pressure in the systems increases, which can be verified by the $\bar{J}_v/\bar{J}_{w,34bar}$ ratios (figures "e"). For the same BPV valve, the permeate flux decreases as $Q$ decreases due to two factors. First, as $Q$ decreases, its value will eventually drop below $Q_{max}$. However, the pressure in the system also drops (as seen in section 3.5.1) leading to a higher decrease in the permeate flux. In addition, lowering $Q$ results in higher concentration inside the filtration chamber (figures "d") and, therefore, an increase in the osmotic pressure and a subsequent drop of the permeate flux. The CP effect becomes less significant as the applied pressure decreases, resulting in higher $\bar{J}_v/\bar{J}_{w,p}$ ratios (i.e. the permeate fluxes become closer to

the pure water permeate flux for the same pressure) as can be confirmed comparing the $\bar{J}_v/\bar{J}_{w,p}$ ratios for the 7 bar, 17 bar and 34 bar BPV valves (figures "f").

Comparing now the results for the different tested solutions, it is possible to withdraw further conclusions. The magnitude of $CF$ increases when $\pi_f$ decreases (compare Figures 3-12b and 3-13b, for $\pi_f$ = 0.6 bar and $\pi_f$ = 2.6 bar, respectively). For neutral molecules, the $R_a$ value diminishes as the MW of the solute decreases (compare Figures 3-12b and 3-14b, for sucrose and fructose, respectively). Moreover $R_a$ decreases more sharply as $Q$ decreases. In fact, while for sucrose solutions the $R_a$ is always above 95 % (despite the little decrease for the lowest $Q$ values), the $R_a$ value for the fructose solutions decreases sharply from more than 60 %, at $Q \approx$ 5 mL/min, to less than 30 %, at $Q \approx$ 0.1 mL/min.

As before, the experiments have shown that the electrical charge of the membrane plays an important role in the solute separation. Thus, applying the same BPV pressure (34 bar), while in the nanofiltration of the fructose solution the $R_a$ droped from 60 % to less than 30 % (Figure 3-14a), for the same conditions the $R_a$ drop was much smaller for the corresponding $K_2SO_4$ solution: from 99 % to 92 % (Figure 3-13a). In addition, the magnitude of the decrease of the solute rejection becomes bigger as the applied pressure increases, as can be seen in Figures 3-12a and 3-13a.

All the results obtained for the concentration of small-volume samples, including the ones not shown herein, demonstrate that the higher $CF$ values were obtained when the feed flow rate is as low as possible (unless $R_a$ drops at a great extent). The performance of the micro-TFF at the smallest flow rate ($Q_p$ = 0.10 mL/min $\approx Re_h$ = 0.2) is summarized in Figure 3-15, in terms of $CF$, $R_a$ and feed recovery, as a function of the applied BPV. From the charts in this figure the same conclusions are obtained as before: $CF$ increases as the applied pressure increases; $CF$ decreases as $\pi_f$ increases; $CF$ increases with the MW of the solute due to higher $R_a$; $R_a$ decreases with the applied pressure; and the feed recovery increases with the increase of the the applied pressure.

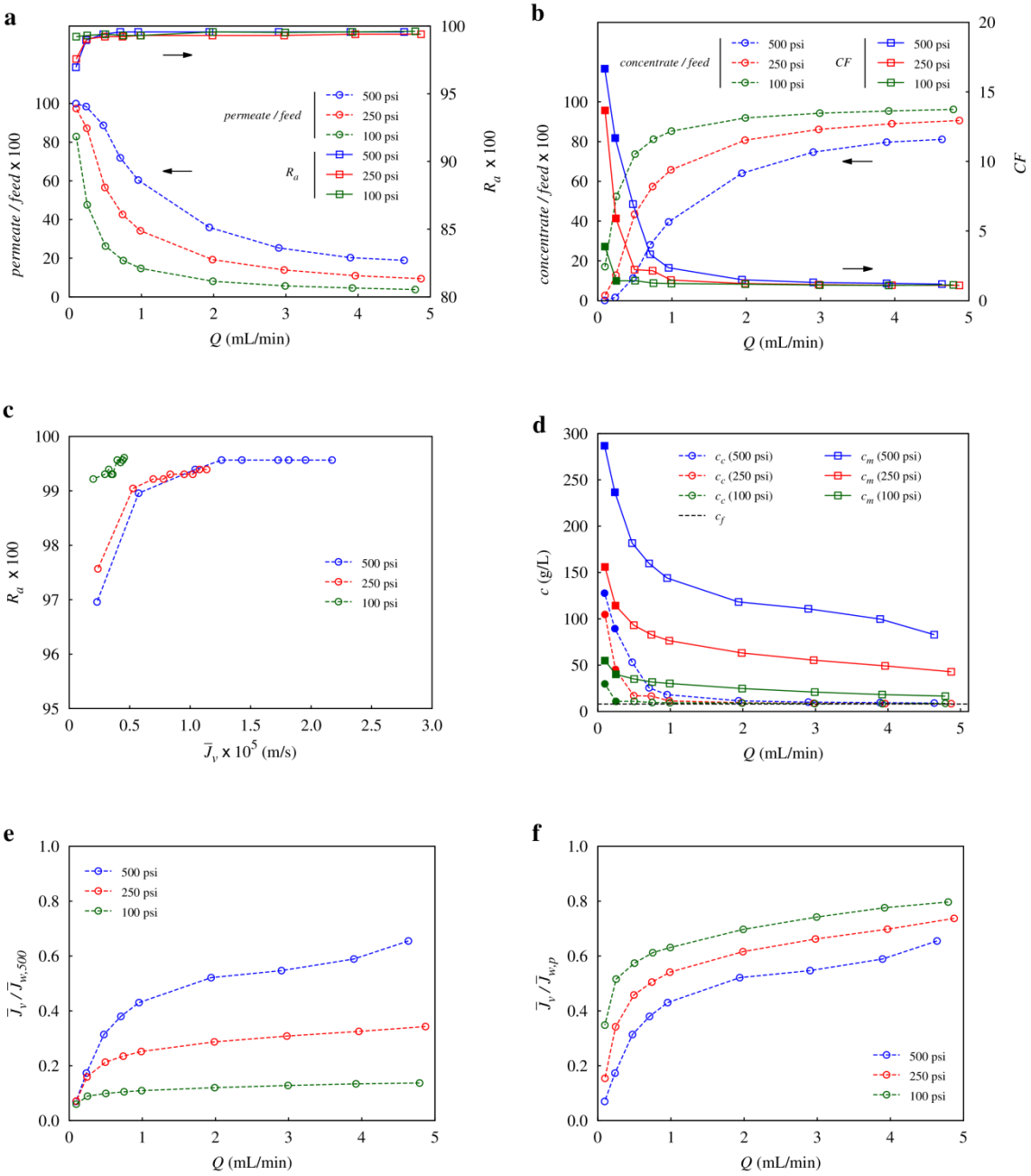


Figure 3-12 – Permeation data of the nanofiltration of the sucrose aqueous solution ($c_f$ = 7.7 g/L) using the NF90 membrane and three back-pressure valves (7 bar, 17 bar and 34 bar) at $T$ = 20 ± 3 °C and distinct inlet flow rates $Q$: a) permeate-to-feed ratio, or feed recovery, and apparent rejection; b) concentrate-to-feed ratio and concentration factor; c) apparent rejection versus permeate flux; d) solute concentration in the concentrate and at the membrane surface; e) ratio between the permeate flux and the water flux using the 34 bar BPV; f) ratio between the permeate flux and the water flux at each pressure. Solid symbols mean that the value was obtained from the liquid remaining inside the filtration chamber at the end of the filtration cycle.

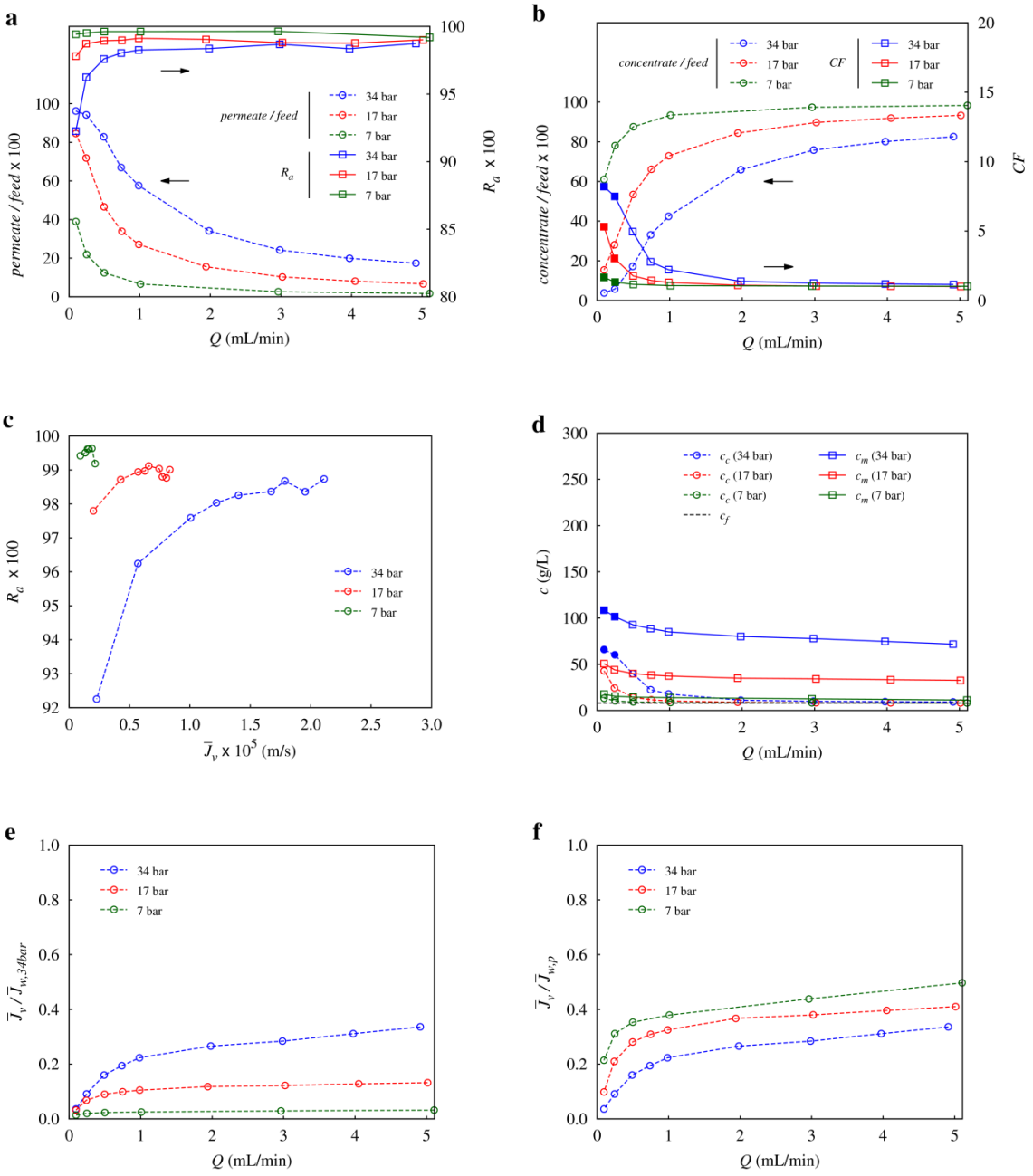


Figure 3-13 – Permeation data of the nanofiltration of the $K_2SO_4$ aqueous solution ($c_f$ = 8 g/L) using the NFX membrane and three back-pressure valves (7 bar, 17 bar and 34 bar) at $T$ = 20 ± 3 °C and distinct inlet flow rates $Q$: a) permeate-to-feed ratio, or feed recovery, and apparent rejection; b) concentrate-to-feed ratio and concentration factor; c) apparent rejection versus permeate flux; d) solute concentration in the concentrate and at the membrane surface; e) ratio between the permeate flux and the water flux using the 34 bar BPV; f) ratio between the permeate flux and the water flux at each pressure. Solid symbols mean that the value was obtained from the liquid remaining inside the filtration chamber at the end of the filtration cycle.

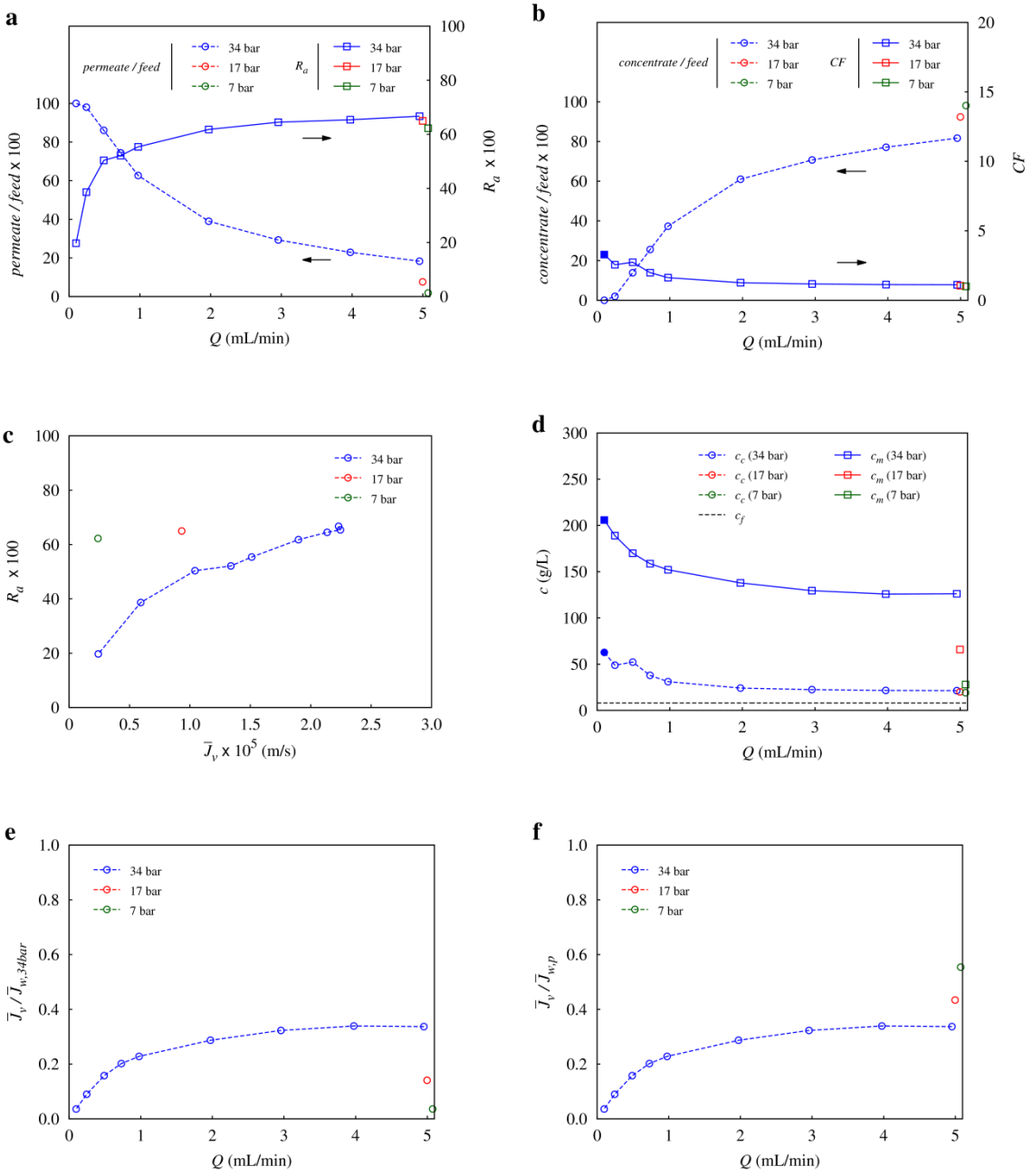


Figure 3-14 – Permeation data of the nanofiltration of the fructose aqueous solution ($c_f$ = 19 g/L) using the NFX membrane and three back-pressure valves (7 bar, 17 bar and 34 bar) at $T$ = 20 ± 3 °C and distinct inlet flow rates $Q$: a) permeate-to-feed ratio, or feed recovery, and apparent rejection; b) concentrate-to-feed ratio and concentration factor; c) apparent rejection versus permeate flux; d) solute concentration in the concentrate and at the membrane surface; e) ratio between the permeate flux and the water flux using the 34 bar BPV; f) ratio between the permeate flux and the water flux at each pressure. Solid symbols mean that the value was obtained from the liquid remaining inside the filtration chamber at the end of the filtration cycle.

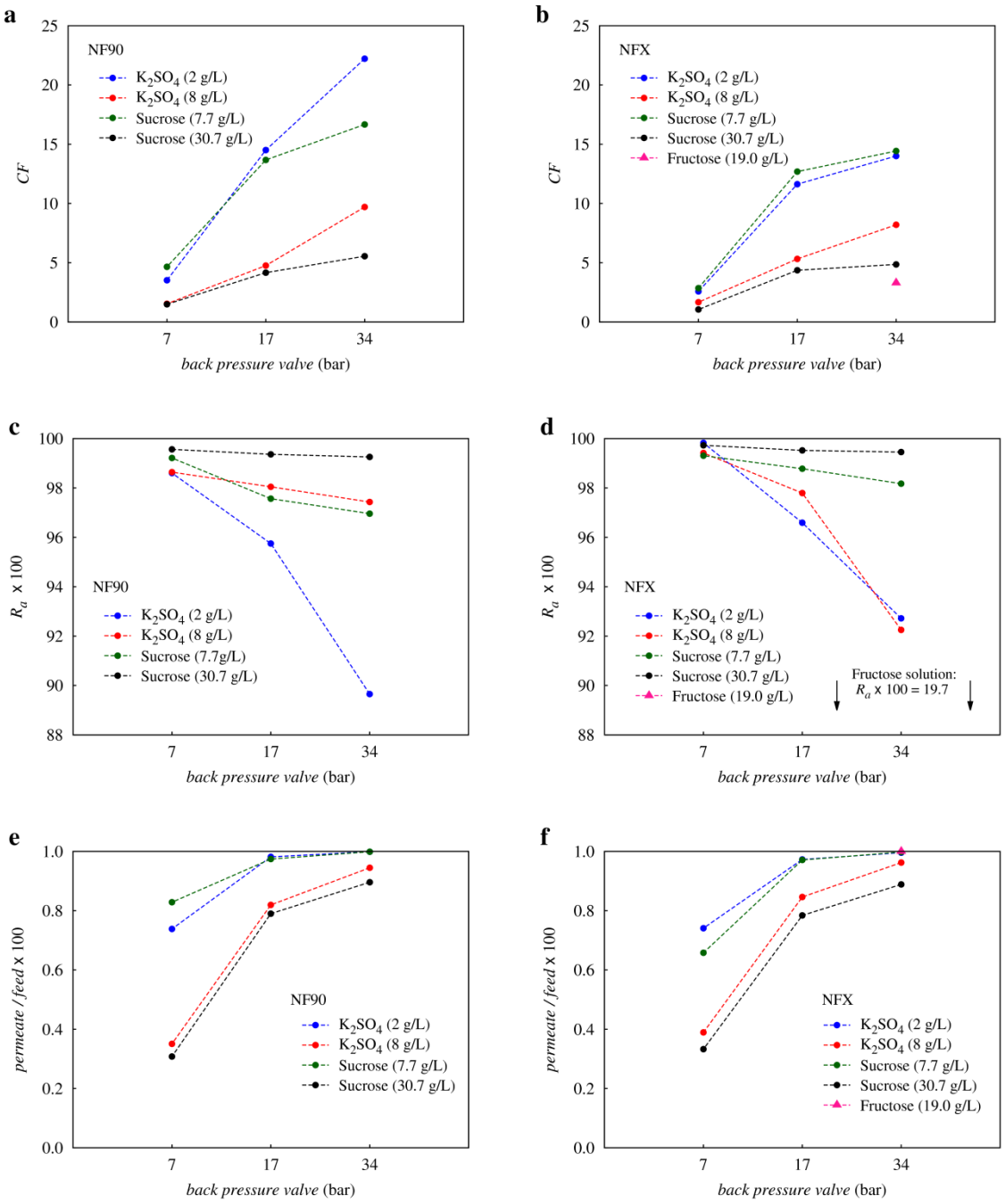


Figure 3-15 – Summary of the obtained data ($CF$, $R_a$ and $permeate/feed$ flow rate ratio) for the concentration by micro-TFF nanofiltration of $K_2SO_4$, fructose and sucrose solutions ($\pi_f$ = 0.6 bar and $\pi_f$ = 2.6 bar) for $Q_p$ = 0.10 mL/min. The only fructose solution tested had $\pi_f$ = 2.6 bar and was concentrated using the NFX membrane.

## 3.6 Conclusion

Tangential flow filtration is commonly used to concentrate liquid samples. However, as discussed in Chapter 1, TFF is seldom used to separate and concentrate small-volume samples containing low MW solutes. The main reason for this lies in the difficulty to incorporate

membranes in mini- and microdevices. A small number of researchers were able to do it but the maximum feed pressure in their works was 16 bar.

In this work, it was assessed the viability of a micro-TFF device to concentrate small-volume samples (9.6 mL) of model binary solutions ($\pi_f$ = 0.6 bar and 2.6 bar). Transmembrane pressures up to ca. 34 bar were applied to permeate the solutions using NFX and NF90 membranes. $K_2SO_4$, fructose and sucrose were used as model solutes. Despite the fact that the concentration process was performed using only an open thin slit ($h$ = 0.25 mm), relatively high concentration factors were obtained. For instance, it was possible to concentrate a $K_2SO_4$ solution from 2 g/L ($\pi_f$ = 0.6 bar) up to ca. 45 g/L ($CF \approx 22$) using the 34 bar back-pressure valve to pressurize the system. However, such high $CF$ values are obtained only when very low feed flow rates are applied, which practically turns the TFF process into a dead-end one. High $CF$ values are more difficult to achieve as the osmotic pressure of the sample increases. For instance, the concentration of a $K_2SO_4$ solution with $\pi_f$ = 2.6 bar resulted in a $CF$ lower than 10. Even worse results are obtained if the solutes are inefficiently retained by the membranes, as was the case of fructose. In addition, and although $R_a$ increases with the decrease of the applied pressure, very small $CF$ values are obtained for low pressure because feed recovery is low, even at the smallest applied inlet flow rate, $Q_p$.

The used micro-TFF cell system was pressurized using several back-pressure valves of different nominal pressure. However, it must be underlined that the actual feed pressure, for the same valve, decreases as the $Q_p$ rate decreases and increases as $\pi_f$ increases. This is due to the permeation process, the maximum pressure for a valve being achieved when the walls are impermeable. For a given back-pressure valve, the actual pressure is function of the permeate flux and, consequently, of the feed osmotic pressure.

Data about the NFX membrane is very scarce in the literature, especially as far as the solute rejection for salts is concerned. For this reason, the NFX membrane was characterized both in terms of its hydraulic permeability and its solute rejection to several salts and neutral molecules. The same characteristics were determined for the NF90 membrane and used as benchmarks. The NFX membrane presents higher hydraulic permeability but the solute rejections are lower than those of the NF90 membrane. The results suggest that the NFX membrane has a larger pore size and a large electrical surface charge.

From the several topics covered in the present chapter the most important outcome that should be emphasized is the fact that it is possible to concentrate small-volume samples by nanofiltration using micro-TFF. However, using this technique high concentration factor values are only obtained when the feed flow rate is so low that the process degenerates into dead-end. Although $CF$ values above 10 can be achieved by micro-TFF when processing diluted solutions, more efficient methods are necessary for concentrated solutions.

Some issues should be addressed to increase the performance of micro-TFF devices. One of the difficulties is the withdrawing process of the concentrated liquid that remains in the filtration chamber after the filtration cycle, since it was verified that this liquid presents higher $CF$ than the concentrate stream itself. Despite the fact that in this work a HPLC pump was used to pressurize the system, the pressure can be also generated by compressed air. Although the sample concentration can be done in multiple passages, recycling the concentrate stream to the feed, to use micro-TFF devices in a disposable way, it is preferable to concentrate the samples in a single passage. Therefore, the performance of such filtration channels must be optimized.

A possible option is to use channels and spacers designed to enhance flow hydrodynamics and, thus, increase the mass transfer. Although direct experimentation will not be done in the present thesis, a hybrid algorithm that can be used to calculate the nanofiltration performance in such innovative devices is developed in Chapter 4. Another alternative to enhance concentration efficiency is by using the centrifugal filtration technique. To date, no efficient centrifugal filtration device was developed to nanofilter small-volume samples. Therefore, in Chapter 5 it will be designed and proved the capability of the herein developed CNF device to concentrate such samples. The efficiency of micro-TFF technique applied in the present chapter will be compared with the corresponding CNF one later in Chapter 6.

# 4 Development of a hybrid computational / semi-empirical method to predict NF performance and its validation by experimental visualization

## 4.1 Introduction

In the previous chapter, it was shown that tangential flow filtration at microscale, micro-TFF, is capable of concentrating solutions of small solutes (MW < 1000 g/mol). However, some limitations of the micro-TFF technique were identified which are related to the concentration polarization (CP). To mitigate CP phenomenon and, thus, increase permeate quality and reduce the filtration time, several methods can possibly be used, as already discussed in section 2.3.2. In the last decades, special focus has been given to those methods that create flow instabilities.

Static mixers increase permeate flux, disrupting the CP layer, and are commonly used in pressure-driven membrane processes at meso- and macroscale. Consequently, their use at the microscale can be convenient, but studies on this subject are scarce. It is also known that non-aligned grooved walls in impermeable microchannels increase liquid mixing (Stroock et al. 2002). This suggests that the use of static mixers, or grooved walls, can enhance permeation performance at microscale. Therefore, the integration of static mixers in microchannels should be taken into account as a method to increase the micro-TFF effectiveness for solute concentration.

Two complementary methods to develop filtration devices are usually applied: trial-and-error experimental testing and computational fluid dynamics (CFD) simulation. Despite having their own benefits, experimental testing is usually expensive and tedious, while CFD can be very demanding in terms of time and computational requirements, which rises as the geometric and model complexity increases. Thus, more flexible methods are urged to obtain estimates for the performance of nanofiltration processes, especially at microscale.

In this part of the work a hybrid computational / semi-empirical method was developed to predict nanofiltration performance, i.e. permeate flux and CP modulus. The hybrid method consists of forecasting nanofiltration data (permeate flux and solute concentration) using an algorithm to solve the equations that quantify the system. One of these equations is the one defining the mass transfer correction factor which relates the actual and the non-suction mass transfer coefficients (Geraldes & Afonso 2006), as seen previously in section 2.2.1. The predictions of the hybrid method were validated comparing them with the corresponding ones obtained from numerical simulations of the permeation process. The momentum and mass transfer models used in the CFD simulations were validated by experimental data obtained by

micro-particle image velocimetry (micro-PIV) and holographic interferometry (HI). The validated model was then used to simulate the permeation in different channel geometries and assess whether spatial periodicity is attained in terms of the mass transfer. This information is fundamental to justify the use of cyclic conditions when simulating mass transfer in a single unit cell representative of the developed flow.

The work developed in this chapter is composed of five parts, to which an initial review on the addressed subjects is included. In the first part of the work, the differences between the flow structure of flows inside impermeable open channels and channels filled with transversal ribs are evaluated using μPIV and CFD. The second part is devoted to visualize the development of CP layer in a nanofiltration process using HI, assessing the influence of several operating parameters, including: time, feed flow rate, applied pressure, solute concentration and channel geometry. In the third part, the experimental solute concentration profiles (and patterns), obtained by HI, will be used to validate the mathematical model applied in the CFD computations performed to simulate the nanofiltration process. Then, in the fourth part, the effect of different two-dimensional channel geometries on the permeation efficiency will be assessed. This will be performed by analysing the results of CFD simulations conducted for longer channels than that used for CP experimental visualization. Finally, CFD simulations will also be used to verify whether nanofiltration data can be predicted by applying a hybrid method based on the Geraldes and Afonso's methodology, which determines the mass transfer coefficient for the permeation process from those of non-suction processes.

The results obtained in this chapter, including the knowledge of the parameters affecting CP, the recognition that periodicity occurs in nanofiltration processes, and the possibility of using the expedite hybrid method to predict nanofiltration data, pave the way for the use of efficient and less demanding computational schemes for the development of microfluidic nanofiltration devices.

## 4.2 Literature review

### 4.2.1 Flow visualization

The visualization of flow hydrodynamics is relevant to assess the degree of fluid mixing responsible for the disruption of the concentration polarization layer. Although there are several techniques for visualization of fluid flows (Freymuth 1993), the number of studies dealing with filtration processes is small. Most of the authors simulate permeation conditions using impermeable channels, admitting that permeate flow rate is several orders lower than feed flow

rate and, therefore, the existence of a semi-permeable wall does not influence the hydrodynamics of the flow.

The most simple flow visualization technique is the injection of dye or tracer particles in the channel and the observation of the flow patterns. Dye/tracer injection is not entirely non-invasive and it is not possible to obtain velocimetry data. However, dye injection is very useful for a first insight on the flow structures and it was used by several authors to evaluate the influence on the flow of static mixers placed inside channel (Broussous et al. 2000; Geraldes et al. 2002a; Almeida et al. 2010).

To obtain flow velocimetry data several techniques can be applied. Some techniques are single-point as, for instance, hot-wire anemometry (Comte-Bellot 1976), laser Doppler velocimetry (LDV) (Charrett et al. 2012) and the use of shear stress sensors (Du et al. 2017). Other techniques permit the visualization of flows in two-dimensional fields as, for instance, particle imaging velocimetry (PIV) (Adrian 1991) and scalar image velocimetry (SIV) (Sinton 2004). The LDV, PIV and SIV techniques require optical access to the interior of the channel. For opaque channels, one can use non-optical techniques like magnetic resonance velocimetry (MRV) (Elkins & Alley 2007) and x-ray velocimetry (Dubsky et al. 2012), which produce also 2D flow fields. In fact, MRV was already used to evaluate the flow velocity inside a commercial SWMM (Graf von der Schulenburg et al. 2008).

Hot-wire anemometry and the use of shear stress sensors are very intrusive techniques, leading to flow disturbance. Although current LDV equipment can produce 2D maps of the flow, the technique principle is based on the measurement of the velocity in a single point. Therefore, LDV is not suitable for velocity mapping with high temporal resolution. SIV is a wide group of techniques in which velocity data is obtained solving the transport equation and admitting that the spatial and temporal derivatives of the transported scalar (usually concentration) can be estimated by correlating acquired images of the flow. However, SIV techniques are not usually considered when studying filtration processes. On the other hand, for research purposes, laboratorial devices can be made transparent, so the use of MRV or x-ray velocimetry is unnecessary. In addition, despite powerful, these two techniques are extremely expensive, needs extra safety cautions and qualified personnel. For all these reasons, PIV is the most commonly used technique to evaluate the flow structure in channels simulating permeation conditions.

In PIV technique images of the flow are captured at very close time instants. These images are divided into small individual areas and, in each area, a velocity vector will be generated using correlation algorithms. These algorithms correlate the images obtained at the two time instants in order to obtain the most probable displacement of the particles in each area and, thus, the velocity vector.

While some authors used PIV techniques to study the flows using impermeable open slits (Completo et al. 2014) or impermeable channels filled with static mixers (Gimmelshtein &

Semiat 2005; Willems et al. 2010; Mojab et al. 2014; Bucs et al. 2015; Haidari et al. 2016) to mimic the flow in pressure-driven membrane processes, other used the technique to obtain velocimetry data in devices with real membranes but for other membrane processes: membrane bioreactors (H. Zhang et al. 2015), rotating cylinders (Yang et al. 2006; Figueredo-Cardero et al. 2012) and forward osmosis (Liu et al. 2015). In addition, it was also studied the external flow to a submerged impermeable fiber bundle miming hollow fibers (Yeo et al. 2006).

**PIV and micro-PIV techniques for flow visualization**

Micro-particle image velocimetry (micro-PIV) is a technique used for flow visualization and velocimetry measurements in microfluidics and it was the selected technique for those purposes in this work. Micro-PIV is derived from the PIV technique used at macroscale. PIV technique was developed in the beginning of 1980's (Adrian 2005; Raffel et al. 2007) and its measuring principle is based on the classical definition of velocity (displacement divided by time) as depicted in Figure 4-1. Briefly, images of the flow, seeded with tracer particles, are acquired at different time instants, the images are divided in to small interrogation areas, and the displacement patterns of the particles in each interrogation area are converted into velocity vectors by applying mathematical correlation algorithms.

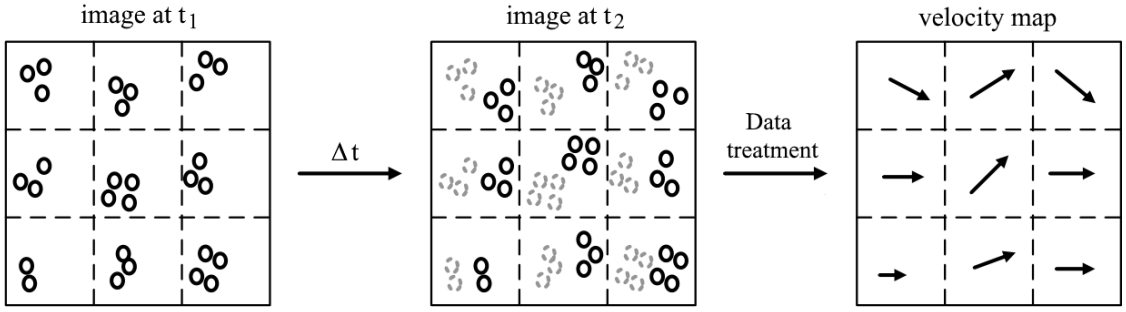


Figure 4-1 – Fundamentals of PIV and micro-PIV techniques.

The main distinction between conventional PIV and micro-PIV systems lies in their optical and lighting systems. As sketched in Figure 4-2, the optical system of PIV creates a light sheet which thickness constitutes the focal depth of the image, but for micro-PIV the thickness of the laser sheet would be too thick (Lee & Kim 2009); so, the focal depth in micro-PIV is defined by the characteristics of the microscope objective.

Santiago and colleagues (Santiago et al. 1998) used micro-PIV for the first time in 1998 to visualize water flow around a 30 μm cylinder. Thereafter, authors have used micro-PIV to map the velocity field of flows inside channels (Wang & Wang 2009; Zerai et al. 2005), achieving good agreement between experimental and numerical results at the centre of the channel. Performing micro-PIV measurement at distinct focal planes, 3D flow profiles can be

reconstructed (Silva et al. 2008; Han & Wang 2012; Completo et al. 2014). In the previous referred works the flows were maintained in steady state but many works were performed in unsteady conditions (Sheen et al. 2007; Sun et al. 2011).

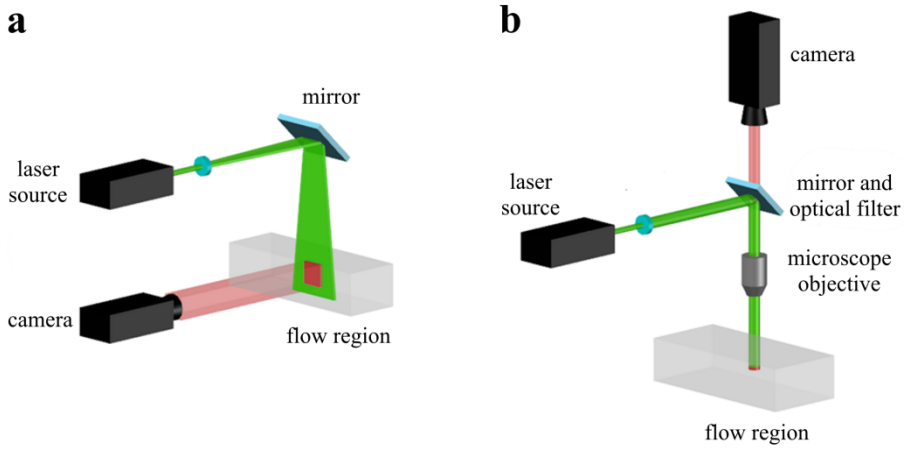


Figure 4-2 – Comparison between the basic setups of: a) PIV; b) micro-PIV.

Micro-PIV has also been used to study the features of more complex flows, like the flow structure near liquid-liquid and air-liquid interfaces (King et al. 2007; Malsch et al. 2008; Sarrazin et al. 2006; Steijn et al. 2007), the flow structure of counter-current streams (Shinohara et al. 2004) and the mixing process of liquid streams in T- and Y-channels (Hoffmann et al. 2006).

Although conventional micro-PIV uses laser illumination and is seeded by fluorescent tracer particles, the technique approach can be used in different setups. The use of particulate matter already presents in the medium is very common in biological fluids. For instance, red blood cells are usually used as tracers in blood flows; however, this results in low spatial resolution (Chayer et al. 2012) and in deviation up to 50 % of the actual velocity field (Poelma et al. 2012; Pitts & Fenech 2013).

The main limitation to apply PIV techniques to the study of flows in pressure-driven membrane processes is the fact that tracer particles can deposit on the surfaces and change the flow in the membrane vicinity. For this reason, in all the studies where PIV was adopted to visualize flows inside channels filled with spacers only impermeable walls were used (Gimmelshtein & Semiat 2005; Willems et al. 2010; Mojab et al. 2014; Haidari et al. 2016). However, in these works only conventional PIV was used (and not micro-PIV). Nevertheless, the above-mentioned literature shows that PIV techniques are well-accepted techniques in the research community. Recent advances in micro-PIV can be found elsewhere (Lee & Kim 2009; Lindken et al. 2009).

### 4.2.2 Visualization of the concentration polarization layer

Concentration polarization influences the performance of permeation processes. Therefore, the factors that affect the CP phenomenon should be investigated. In Chapter 3, the CP phenomenon was evaluated using global parameters like permeate fluxes and solute rejections. However, to have a better insight on the CP effects it is important to assess how the concentration boundary layer develops both in time and space, and how it is affected by operating conditions. Thus, suitable methods should be used to provide complementary data to that obtained by global parameters, preferably using non-invasive, in-situ, and real-time techniques. The gathered data can then be used to evaluate permeation performance, to build and improve transport models and to validate the predictions given by CFD simulations.

Comprehensive reviews on the techniques to obtain information about concentration polarization and flow characteristics are available elsewhere (V. Chen et al. 2004; J. Chen et al. 2004; Li et al. 2017). Since in this work only model binary water-solute solutions were used, the fouling phenomena are not studied. For this reason, the experimental techniques to monitor fouling development are not considered here.

#### Visualization of the solute concentration field

There are several techniques to experimentally assess the solute concentration field. Herein it will be succinctly described the techniques that can monitor the concentration polarization in real-time and that have been applied to membrane processes.

Shadowgraph, schlieren and refractometry are imaging techniques that rely on the bending of the light rays due to refractive index gradients. Assuming that solute concentration is proportional to the refractive index, then from light bending measurements, it is possible to infer the concentration field in the medium.

The simpler technique is shadowgraph and, in principle, it does not need any optical component except a light source and a recording plane onto which the shadow of the varying refractive index field is projected. Shadows are generated because light rays are deflected by the refractive index gradient of the fluid. Thus, the position on the recording plane where the undeflected ray would arrive (in the undisturbed environment) becomes darker (in the disturbed environment). At the same time, the position where the deflected ray arrives appears brighter than before.

Shadowgraph technique was used to observe concentration fields in the ultrafiltration of BSA solutions in a dead-end cell (Vilker et al. 1981) and to show that buoyancy effects occur when a membrane is placed on the top wall of channels (Hendricks et al. 1972).

The concept of schlieren technique is similar to shadowgraph: the light rays bend due to the refractive index gradient. However, in schlieren technique, part of the resulting light field is blocked by placing a knife-edge between the object and the image plane. The light rays that pass the knife-edge produce bright areas in the image plane, while the areas corresponding to the light rays that were blocked get darker. This results in very visual images that can be interpreted qualitatively.

Quantitative information from schlieren images is possible but calibration is needed, which can be difficult to obtain. For instance, solute concentration profiles near surfaces were determined for electrochemical processes (Cooper 1958) and for ion-exchange membrane processes (Tanaka 1991). In a more recent work, schlieren images were calibrated to obtain quantitative data for the mixing process in a microfluidic T-channel (Sun et al. 2015). The current advances in schlieren and shadowgraph techniques can be found elsewhere (Settles & Hargather 2017).

Refractometry is used to obtain quantitative data of the concentration field. In this technique, a laser light beam that passes through a sample bents and the light deflection is measured in a light position detector. However, since refractometry is a single-point technique, it is not possible to obtain the solute concentration field in a precise time instant. Nevertheless, refractometry was already used to obtain the solute concentration profile in a dead-end cell for the ultrafiltration of hyaluronic acid solutions (Gowman & Ethier 1997b; Gowman & Ethier 1997a).

The fundaments of interferometry are also related to the bending of light rays due to the refractive index gradient. However, while in schlieren, shadowgraph and refractometric techniques the light passes only through the object of study, in interferometry the light is split in two beams that cross the object of study and a reference object.

Distinct light paths of the light occur in the reference and object of study if they present different conditions from one another[12], which causes phase shifting of the light emerging from the objects. If the two light beams are then detected on the same focal plane, the phase shifting results in interferences (or fringes) due to the superposition of the light beams (Naylor 2003).

The advantage of the interferometry technique is that quantitative data on the solute concentration field can be easily obtained from the interferograms. Unlike schlieren, shadowgraph and refractometric techniques, interferometry has been profusely used to study the CP phenomenon in membrane processes.

Electronic diode array microscopy technique is an optical technique in which the quantitative data on the solute concentration is obtained by measuring the intensity of light that hits a sensor (McDonogh et al. 1995). If the solute absorbs light, the detected light intensity will

[12] For instance, the solute concentration in the reference object may be uniform, while concentration gradients may exist in the object of study.

be inversely proportional to its concentration and, thus, the concentration field can be reconstructed. Although this technique looks to be practical, it does not take into account the light bending phenomena. In addition, it is inappropriate to evaluate samples with particulate matter that blocks the incident light.

Radio isotope labeling, or scintigraphic technique, allows quantifying the amount of labeled solute present in the CP layers (McDonogh et al. 1990). However, this technique only quantifies global amounts of the solute, without obtaining concentrations profiles.

Pressure information can also be useful to quantify of CP phenomena. Theoretical studies have shown that a CP layer produces a pressure gradient normal to the membrane surface which contrasts with the pressure zero-gradient in the scenarios of flows without the CP effect in open straight channels. Thus, measuring the pressure drop along the normal direction of the membrane surface one can assess the presence of the CP layer (Zhang & Ethier 2001). However, the insertion of pressure sensors can disturb the flow (J. Chen et al. 2004).

Microprobes to measure the conductivity (Liu & Williams 1970) or the capacitance (Cobry et al. 2011) of salt solutions may also be used, but they have the same issue of disturbing the flow.

From the above-mentioned techniques, interferometry seems to be the one that best suits the objective of study the concentration polarization phenomena since: it is a non-invasive technique, so it keeps the flow undisturbed; it is a real-time and in-situ technique that permits to obtain instantaneous two-dimensional interferograms; it is easy to obtain quantitative solute concentration data from the acquired interferograms. Therefore, interferometry, in particular holography interferometry, was the technique selected to visualize and quantify the concentration polarization phenomena in nanofiltration experiments and it will be described in more detail in the following.

**Interferometry and holographic interferometry**

Interferometry is a technique used to map the distribution of the refractive index, $n$, in the medium under study. Thus, it can be used for the visualization of concentration polarization in membrane processes, provided that the solute concentration is proportional to the refractive index. Holographic interferometry can be seen as a branch of the wide set of interferometric techniques.

Despite the complex mathematical and physical descriptions of interferometry, the reasoning of interferometric techniques is rather simple and relies on the superposition principle of light waves. As explained by the wave theory of light (Hecht 1998), the superposition of light waves can intensify the amplitude of the combined light wave if the original ones are in phase, or it can make the amplitude to vanish if they are out of phase. These changes in the light

amplitude are called interferences or fringes. Thus, when the combined electromagnetic field produced by out-of-phase monochromatic light beams is observed, for instance projecting it in the plane of focus, bright and dark zones appear, which corresponds to the zones with intensified or vanished amplitudes.

Although interferometry can be used for several purposes, herein the focus is only on its use to obtain the concentration distribution of a solute in a solution. The two most common types of interferometers are the Michelson and the Mach-Zehnder interferometers. In the Michelson-type interferometers (Zhang et al. 1988; Ikram & Hussain 1999), depicted in Figure 4-3a, a laser light is split into two beams by a beam splitter, both being then deflected back by optical mirrors to the beam splitter and then to the detector. If in one of the optical paths there is a reference object (which can be simply air) and in the other path a different object is placed, a phase shift of the light wave occurs and, thus, interferences in the focused superposed light appear. The same principle is used in the Mach-Zehnder-type interferometer (Zhang et al. 1989; Naylor 2003): the separation of a light beam in a reference beam and an object beam. However, in the Mach-Zehnder interferometers two beam splitters, rather than one, are used, as depicted in Figure 4-3b. Mach-Zehnder-type interferometers are commonly used in fluid flow studies (especially in aerodynamics). It should be mentioned that for the sake of simplicity, in the sketches of the interferometers presented in Figure 4-3 many of the optical components (lenses, optical filters, etc.) are not shown.

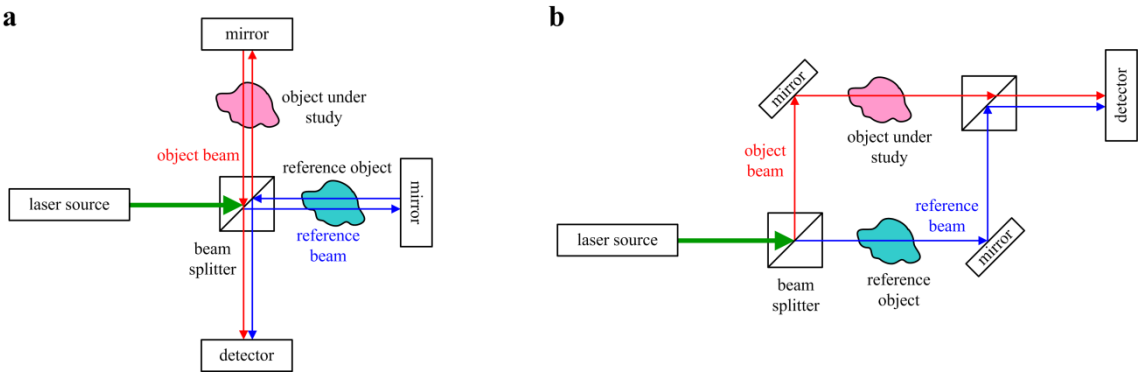


Figure 4-3 – Basic schemes of: a) Michelson interferometer; b) Mach-Zehnder interferometer.

Apparatus of classical interferometry, like the Michelson and Mach-Zehnder interferometers, must be equipped with optical components of high quality; otherwise high distortions and inaccurate results are obtained. For instance, to measure concentration profiles in a filtration process, two identical cells with optical accesses of high-quality glass must be used (one to be placed in the reference light path and the other on the object light path). In addition, the beam splitters, the mirrors and all the other surfaces designed to be flat must comply with such requirement to at least $1/20^{th}$ of the light wavelength. This makes classical interferometry equipment quite expensive.

Interferometry has been used by many authors, since the 1950's, to determine the concentration distribution of solutes in mass transfer processes. For instance, Ibl and Müller (Ibl & Muller 1955) and O'Brien (O'Brien 1966) have studied the natural convection of solutes at the vicinity of electrode surfaces in electrochemical processes, while Forgacs and colleagues (Forgacs et al. 1975) and Clifton and Sanchez (Clifton & Sanchez 1979) have measured the solute concentration near ion-exchange membranes in electrodialysis processes. The first reference to the physical meaning of the fringes was described by Bollenbeck and Ramirez (Bollenbeck & Ramirez 1974), in their study on the diffusion of water-sucrose solution through a membrane. According to those authors, a fringe shift in the interferograms corresponds to an optical path difference equivalent to a wavelength between the reference and the object under study. If light bending is not considered, the change of the refractive index between two consecutive fringes, $\Delta n$, is then given by

$$\Delta n = \frac{\lambda}{L_o} \tag{4-1}$$

where $\lambda$ is the wavelength of the light and $L_o$ is the geometrical path length through the medium under study. A similar expression was also used by Min and Notter (Min & Notter 1976), who admitted that the light bending was non-significant in their work (the study of the diffusion of aqueous ethyl alcohol through cellophane membranes) due to the small thickness of the cell channel. The first work where the CP layer was studied in a pressurized membrane process was probably the one of Johnson (Johnson 1974). In that study, a Mach-Zehnder interferometer was used to quantify the salt concentration profile in the vicinity of a RO membrane in order to verify the effect of natural convection when the membrane was placed vertically. Later, Mahlab and colleagues (Mahlab et al. 1978; Mahlab et al. 1980) compared the experimental interferograms, acquired for the RO process of NaCl aqueous solutions, with the corresponding artificial interferograms obtained by solving the ray equation. Solving this equation is particularly important when the gradient of the refractive index is high because the light rays bend in the direction of that gradient which causes loss of information. The CP layer relaxation due to the depressurization in ultrafiltration and the corresponding decrease of the number of fringes with time were studied by Clifton and Sanchez (Clifton & Sanchez 1979) using holographic interferometry.

The use of holographic interferometry (HI) has permitted to drop sharply the cost of interferometric systems for the study of the CP phenomenon. The reason for the lower costs of HI, when compared with the classical systems, is the fact that HI does not require optical components of very high quality (Naylor 2003). The optical walls of the object under study may be made of commercial grade glass. Moreover, using the HI technique, the reference object is

replaced by a hologram that defines the reference state of the object under study. The reference beam that would be obtained in classical interferometry, by passing the light through a reference object, is regenerated in HI by hitting the hologram with a light beam similar to that which has produced the hologram. Therefore, the reference hologram already includes the optical aberrations of the object path, which allows for cheaper optical components. A basic sketch of a holographic interferometry system is depicted in Figure 4-4.

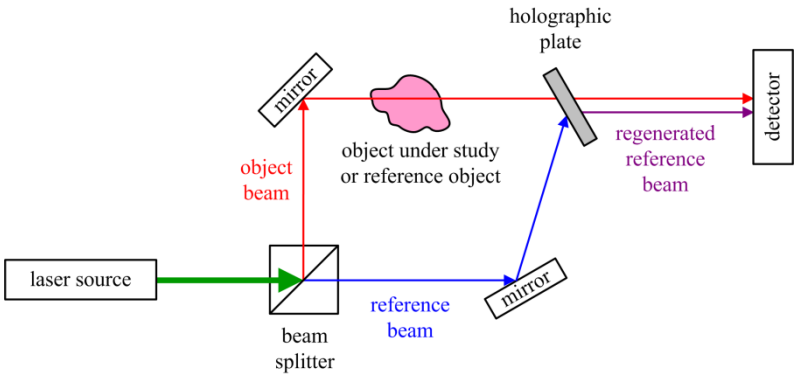


Figure 4-4 – Basic scheme of a holographic interferometer.

Briefly, the first step in HI is to record in the holographic plate the reference state of the object under study, which in membrane filtration processes corresponds to record the permeation channel filled with liquid (usually pure water or the solution to be treated). Thereafter, the reference liquid is replaced by the solution to be studied, the system is pressurized, the object beam will interfere with the reconstructed beam from the hologram, and the interferograms are acquired by a detector device, usually a CCD camera.

According to the work of Ruíz-Beviá (Ruiz-Bevia et al. 1985) from 1985, the HI technique has been used since the late 1960's to study several mass transfer phenomena that, up to that date, included electrochemical processes, electrophoresis, electrodialysis and the determination of mass diffusion coefficients. Therefore, there was a gap of almost 20 years without applying HI to monitor the CP effect in pressurized membrane modules, namely between the works of Clifton and Sanchez (Clifton & Sanchez 1979) (dated from 1979) and of Fernandez-Torres and colleagues (Fernández-Torres et al. 1998) (dated from 1998), both dealing with ultrafiltration processes.

Since 1998 there was a new interest in studying UF, NF and RO processes using holographic interferometry. First, it was shown that natural convection, or buoyancy, plays an important role in unstirred dead-end filtration. When the membrane is placed on the bottom wall of the filtration channel the CP layer is stable. However, when the membrane is placed vertically or on the top wall of the filtration channel, the CP layer is disrupted by the gravitational force effects. In fact, descending jets of concentrated fluid elements were

visualized in UF and RO processes when membranes were placed on the top surface of the channel (Fernández-Sempere et al. 2007; Fernández-Sempere et al. 2012). The formation of such jets is in accordance with the ones visualized before by Hendricks and colleagues (Hendricks et al. 1972) using the shadowgraph technique. The importance of the gravity force on mass transfer has already been studied by interferometry by Dworecki and colleagues (Slezak et al. 1985; Dworecki & Wasik 1997), who studied the effect of placing the solution with higher density above or below the membrane; however, such studies refer to non-pressurized membrane processes.

Interesting is the fact that, in some UF processes, the interferograms acquired after cell depressurization suggest different mechanisms for the CP and fouling. For instance, for BSA ultrafiltration in an unstirred dead-end cell, the interferograms show that the number of fringes stabilizes after some time (Fernández-Torres et al. 1998). This looks questionable considering that it is an unsteady process. In addition, after depressurization of the UF cell, the layer with fringes expands from the membrane but the fringes number decrease with time. This means that the concentration gradient decreases after the depressurization of the cell. Moreover, small aggregates fall from the vertical membrane. These three facts suggest that for BSA ultrafiltration a cake layer with constant concentration is continuously formed near the membrane. However, for the UF process of polyethylene glycol (MW = 10000 g/mol) the depressurization results in an increase in the number of fringes (Fernández-Sempere et al. 2009). This suggests that a large amount of solute was adsorbed in the membrane during the filtration, which was then desorbed increasing the concentration above the membrane. The same kind of depressurization experiments was performed for reverse osmosis of $KNO_3$ aqueous solutions (Fernández-Sempere et al. 2008). The stabilization of the number of fringes in dead-end processes after a certain period of time is again somehow non-intuitive (Fernández-Sempere et al. 2004; Fernández-Sempere et al. 2006) but it is explained by the reduction of the membrane rejection (Fernández-Sempere et al. 2006), which in the limit will tend to zero.

The visualization of the CP development in tangential flow filtration was also performed (Fernández-Sempere et al. 2010; Rodrigues et al. 2013; Salcedo-Díaz et al. 2014; Completo et al. 2016). For the same feed solute concentration and applied pressure, the Reynolds number correlates with the detected number of fringes and permeate flux: increasing $Re$ the number of fringes decreases and the permeate flux increases (Fernández-Sempere et al. 2010). On the other hand, the development of the CP layer along the length of the channel was observed by Salcedo-Díaz and colleagues (Salcedo-Díaz et al. 2014), who built a RO cell with four optical accesses at different distances from the entrance of the filtration channel. That way, the authors were able to visually conclude that for a low average velocity ($Re$ = 13) the number of fringes, and thus the solute concentration, at the membrane surface increases along the majority of the channel length. For higher flow average velocities ($Re$ = 38 and $Re$ = 111) the number of fringes stabilizes after

a certain entrance length. In all their experiments, the number of fringes detected in the optical access closer to the channel outlet has decreased, which was justified by local flow instabilities close to the exit.

All the above-mentioned studies employing HI used open channels, i.e. channels without any kind of static mixers to generate flow instabilities and to disrupt the CP layer. In a recent paper that came out from the work performed during the present thesis, the nanofiltration of $K_2SO_4$ aqueous solutions inside a channel with the membrane on the bottom wall and with ribs placed on the top wall was visualized (Completo et al. 2016).

As mentioned above, the light rays bend in the direction of the gradient of the refractive index and, under such circumstances, equation (4-1) is no longer valid. To overcome this limitation, Rodrigues and colleagues (Rodrigues et al. 2013) presented an algorithm to correct the light deflection effect by minimizing the difference between the non-corrected experimental profile, given by equation (4-1), and the theoretical profile obtained by solving the ray tracing equation. Even though, the application of such correction algorithm can be avoided if the ratio $\Delta n_{mb}/\delta_D$, i.e. the ratio between the difference of the refractive index of the solution at the membrane surface and of the solution at the bulk, $\Delta n_{mb}$, and thickness of the CP layer, is smaller than 1 $m^{-1}$.

In some of the above-mentioned works (Fernández-Sempere et al. 2010; Fernández-Sempere et al. 2012; Salcedo-Díaz et al. 2014) a variant of the HI technique named as digital holographic interferometry (DHI) was used. This technique differs from the traditional HI technique by the fact that the image of the object under study in its reference state is saved in a computer file, instead of being stored in a holographic plate. Then, the images of the object under study are acquired and numerical computations reconstruct the interferograms. This kind of digital techniques has the advantage of avoiding the time-consuming and intricate steps of recording and photo developing the hologram on the holographic plate.

The experimental data obtained using the micro-PIV and HI techniques will be used to validate the applied CFD model for the simulation of nanofiltration in two-dimensional ribbed channels. In addition, the influence of several operating parameters on the development of the CP phenomenon is also evaluated.

### 4.2.3 Experimental and numerical studies on flows in channels with static mixers

Mass transfer processes performed inside open channels suffer from the CP and fouling phenomena. As referred in section 2.3.2, these effects can be mitigated using static mixers inside the channels in order to disrupt the CP layer, increase the mixing within the fluid and, thus, enhance the performance of the filtration process. Up to the 1990's most of the studies

were performed gathering global flow data like the pressure drop along the channel and by determining the integral concentration of the permeate and concentrate streams. Although rudimentary, these techniques can be used to determine global mass transfer coefficients, as described in section 2.2.1. In the last two or three decades, the boost in computational capacity and electronics made possible the development of powerful techniques to study the flow inside channels with spacers, both numerically and experimentally.

There are several types of static mixers that can be used in research work and in commercial applications. If the static mixer consists of ribs or filaments of simple geometry placed transversely inside the channel then the resulting flow is usually considered two-dimensional (2D). Static mixers of complex geometry or consisting of meshes produce three-dimensional (3D) flows. Moreover, some of the studies focus only on the flow hydrodynamics, while others couple this with the characterization of the mass transfer process. In addition, while some works report only experimental work, others report only numerical simulations. However, the current trend is to use both the experimental and computational works since they are complementary. Figure 4-5 depicts the type of research that authors usually do when studying flows of liquids inside channels with static mixers.

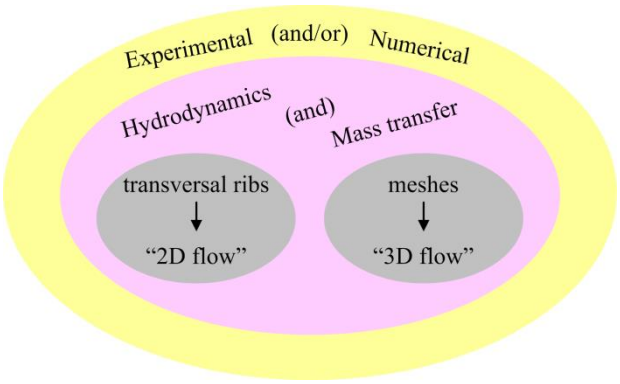


Figure 4-5 – Types of research work on liquid flow inside channels with static mixers.

**Studies on 2D flows**

When using static mixers, the flows inside channels with transverse ribs are the easiest ones to be visualized experimentally. In addition, the computational effort required to simulate numerically the flow in two-dimensions is much less than the corresponding one for three-dimensional flows. For this reason, the study of 2D flows was the first one to be assessed by researchers.

Two-dimensional flows using transversal ribs with several geometries and configurations have been studied. In experimental works, the ribs are usually of square (Fischl et al. 1985; Completo et al. 2016), rectangular (Kang & Chang 1982) or circular (Geraldes et al. 2002a;

Almeida et al. 2010) cross-section, since they can be easily manufactured with those geometries. The ribs can be placed along the channel in three typical configurations: cavity, zigzag and submerged (Karabelas et al. 2015). In the cavity configuration, all the ribs are placed in contact with a single wall (which can be the wall where the mass transfer occurs, or the opposing one). In the zigzag configuration, the ribs are placed alternately in both opposing walls. The submerged configuration consists in placing the ribs in the middle of the channel and, thus, not in contact with the walls.

The use of dye injection technique allowed verifying that the flow hydrodynamics is changed by the presence of the static mixers (Kang & Chang 1982). Flow instabilities and, thus, CP disruption occur at Reynolds numbers much lower than the typical value for open channels ($Re \approx 2000$). At low $Re$ the flow is laminar, but above a critical $Re$ instabilities occur. However, it was found that the flow cannot be described solely by the Reynolds number as other parameters influence the transition from the laminar regime to the unstable one, such as the size of the ribs, $d_f$, and the distance between consecutive ribs, $l_f$. Usually these parameters are defined by their ratios to the channel height , $h$, namely $d_f/h$ and $l_f/h$. For the submerged configuration it is also necessary to define the distance between the rib and one of the walls (Feron & Solt 1991).

The effect of increasing $d_f$ (or $d_f/h$) is to increase locally the shear stress and, thus, the mass transfer. Depending on the flow regime and specific geometries of spacer filaments, different conclusions about the influence of the ratio $l_f/h$ on the critical $Re$ were obtained by different authors. Based on the flow instabilities visualized by dye injection (Geraldes et al. 2002a) or on the change of slope of the friction coefficient as a function of $Re$ (Almeida et al. 2010), those authors claimed that the critical $Re$ decreases as $l_f/h$ increases for flows with cavity configuration. Other authors observed by flow visualization (Feron & Solt 1991) and, more recently, by computational simulations (Alexiadis et al. 2007) that the critical $Re$ increases as $l_f/h$ increases. This discrepancy is probably due to differences in the filaments geometries or flow regimes.

One of the advantages of CFD simulations is that one can obtain local information on hydrodynamics and mass transfer phenomena, with spatial resolution down to the domain grid refinement. Moreover, if the flow is unsteady, CFD simulation also allows obtaining the time evolution of the flow, but at the expense of longer simulations. However, CFD simulations also present some drawbacks, being the major one the dependence of the output on the adopted models and assumptions. In particular, geometrical and modelling simplifications were done in the early stages of CFD calculations due to memory and CPU constraints.

Over the time, the increase in computational power and in algorithm improvements allowed researchers to simulate mass transfer processes closer to the real processes. Even

though, in many of the published work, some or all of the following assumptions were used: a) impermeable walls due to non-significant permeation rate and constant concentration at the wall surface where permeation occurs (Schwinge et al. 2002b; Fimbres-Weihs et al. 2006); b) constant permeate flux (Geraldes et al. 2002b); c) film theory model (Ahmad et al. 2005; Ahmad & Lau 2006). More sophisticated models introduce the concentration gradient at the membrane surface, obtained by the solute mass balance, as boundary condition (Geraldes et al. 2004; Song & Ma 2005; Ma & Song 2006; Subramani et al. 2006; Wardeh & Morvan 2008; Wardeh & Morvan 2009; Amokrane et al. 2015). In addition, to minimize the computation effort, some of the works have used periodic boundary conditions to simulate the flow and mass transfer in a region considered as representative of the whole domain (Kang & Chang 1982; Geraldes et al. 2002a; Geraldes et al. 2004). The authors justify this assumption based on the periodicity of the hydrodynamics and heat transfer occurring in flows inside channels filled with repetitive static mixers. However, there is no evidence that the same occurs in membranes processes, especially those with high feed recovery. Nevertheless, many of the fundamental studies were obtained simulating only the flow hydrodynamics (Cao et al. 2001; Schwinge et al. 2002b; Schwinge et al. 2002a; Koutsou et al. 2004; Alexiadis et al. 2007; Sousa et al. 2014). Moreover, in addition to the square and cylindrical filaments used in experimental works on 2D flows, CFD simulations were also performed using triangular (Ahmad et al. 2005; Ahmad & Lau 2006) and elliptical (Sousa et al. 2014) filaments.

At low $Re$, i.e. in the steady laminar regime, 2D flows in channels filled with transverse filaments promote the appearance of recirculation zones upstream and downstream the filaments (Schwinge et al. 2002c). The size of the recirculation zone downstream the filament depends mainly on the $Re$ and for low $l_f/h$ it can span over the entire interfilament distance. As mentioned before, above a critical $Re$ the flow becomes unsteady, first by forming oscillations of the velocity field and then due to vortex shedding (Schwinge et al. 2002a; Schwinge et al. 2003; Ahmad & Lau 2006; Alexiadis et al. 2007). Most of the previous authors (Feron & Solt 1991; Schwinge et al. 2002b; Ma & Song 2006; Wardeh & Morvan 2008; Amokrane et al. 2015) have suggested that the zigzag configuration is the best option to be used in membrane processes with 2D flows, since it provides larger mass transfer rates, despite the slightly higher pressure drop. The main concern with the use of the zigzag configuration is the appearance of regions with high concentration in the vicinity of the filament due to the presence of recirculation zones (Subramani et al. 2006). These high concentration spots can trigger the fouling phenomena.

For cavity and zigzag configurations, mass transfer is enhanced with the decrease of the $l_f/h$ down to a certain value, below which the mass transfer decreases (Schwinge et al. 2002b). Opposingly, for the submerged configuration, mass transfer increases monotonically as $l_f/h$

decreases. However, pressure drop increases for all the configurations as $l_f/h$ decreases. Although the optimal $l_f/h$ depends on the feed properties, e.g. the salinity of the solution, it is commonly accepted that the optimal $l_f/h$ value is between 3 and 5 for transversal filaments in 2D flows (Ma & Song 2006). For steady laminar flows, the regions with higher mass transfer coefficients are those experiencing higher shear stresses or local flow directed towards the membrane surface (as the reattachment points) (Fimbres-Weihs et al. 2006). For unsteady flows, the vortex shedding near the membrane surface disrupts the CP layer resulting in the enhancement of mass transfer (Fimbres-Weihs et al. 2006; Amokrane et al. 2015) at those regions.

In terms of the filament geometry, it was shown that the use of triangular filaments adjacent to the membrane results in lower CP magnitude; however, above a certain $Re$ threshold, triangular filaments result in larger pressure drop and, for that reason, circular filaments are preferable (Ahmad & Lau 2006). On the other hand, when the filaments are placed at the wall opposite to the membrane the shape of the filaments has no noticeable influence on the mass transfer performance (Ma & Song 2006).

One of the advantages of the lower computational demand for 2D simulations is the possibility of simulating the flow in the whole channel length. It was found that, for medium-to-high $Re$, flow hydrodynamics periodicity is obtained after 6 filament sections (Schwinge et al. 2003; Alexiadis et al. 2007). It must be emphasized that the flow periodicity refers only to hydrodynamics, since the works where this issue was studied the mass transfer phenomenon was disregarded.

**Studies on 3D flows**

When the channel is filled with meshes, the flow hydrodynamics gets more complex and, usually, it cannot be predicted by 2D simulations. Meshes of superposed filaments (woven or non-woven) are commonly used to generate 3D flows and, thus, enhance liquid mixing and CP and fouling control. In addition to the parameters that describe 2D flows ($Re$, $l_f/h$ and $d_f/h$), for 3D flows, it is also necessary to define the flow attack angle, $\theta$, and the angle between the filaments, $\psi$. The vast majority of the studies on flow and mass transfer phenomena inside channels filled with meshes refer to the use of non-woven meshes.

A typical two-layer non-woven mesh with cylindrical filaments is depicted in Figure 4-6, where the top filaments are placed over the bottom ones. Conversely, in woven meshes, the filaments are interlaced (Li, W. Meindersma, et al. 2002). The angle between the top and bottom filaments is $\psi$. Special care must be taken when comparing works of different authors since they often use different definitions for the flow attack angle. One of the possibilities is to define $\theta$ as

the angle between the bulk velocity and the bottom (or top) filaments. Alternatively, and as depicted in Figure 4-6, the flow attack angle may be defined as the angle between the perpendicular to the bulk flow velocity and the bottom and top filaments, $\theta_1$ and $\theta_2$, respectively. In the same figure, the distances between two consecutive bottom and top filaments are given as $l_{f1}$ and $l_{f2}$, respectively. Usually $\theta_1 = \theta_2 = \theta$ and $l_{f1} = l_{f2} = l_f$. Similarly, in many cases, the thickness of the top and bottom filaments are the same and defined as $d_f$. If $\theta_1 = 0°$ and $\theta_2 = 90°$, or vice-versa, the mesh is called as ladder-type, while if $\theta_1 = \theta_2$ the mesh is of diamond-type. Researchers are mainly focused in analysing the effect of $Re$, $\theta$, $\psi$, $l_f/h$ and $d_f/h$ on the mass transfer performance.

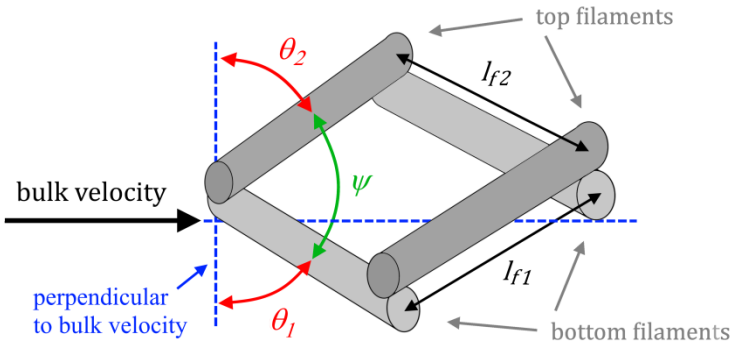


Figure 4-6 – Definitions of the flow attack angles, $\theta_1$ and $\theta_2$, of the angle between filaments, $\psi$, and of the distance between consecutive filaments, $l_{f1}$ and $l_{f2}$, in a non-woven mesh.

In the early studies of flows inside channels filled with meshes, only global parameters were obtained. In addition to the global mass transfer coefficient, the pressure drop along the channel was measured. It was found that the global pressure drop in spacer-filled flat channels is similar to the one obtained when using commercial spiral wound membrane modules (SWMM) (Schock & Miquel 1987). Over the time, this fact has justified the use of the flat channel geometries to simulate the flow in actual curved SWMM. Although this similitude has been accepted by some authors, based on CFD simulations (Ranade & Kumar 2006b), others claim that the curvature of SWMM causes distinct shear stress on the two membrane surfaces of each feed channel, when using filaments with equal diameter, which can pose problems to fouling management (Li & Tung 2008a). To tackle this issue, the use of filaments with different diameter was proposed (Y. Li et al. 2009). In this scenario, the filaments with larger diameter should be placed on the surface with larger curvature (i.e. the surface that corresponds to the internal leaf of the SWMM envelope).

For ladder-type meshes, the flow hydrodynamics is similar to the 2D flow described before, since the longitudinal filaments have no significant influence on the flow distribution (Santos et al. 2007). Thus, the flow in ladder-type meshes presents transversal recirculation zones, flow oscillations and vortex shedding, depending on the flow regime, $l_f/h$, and $d_f/h$ (Li,

W. Meindersma, et al. 2002; Santos et al. 2007). On the other hand, for diamond-type meshes, the flow presents two distinct behaviours. If the $Re$ is small, $l_f/h$ is large and $\theta$ is small, then, the liquid flows through the diamond mesh with a zigzag path, as observed both experimentally, by bubbling gas into the liquid flow (Da Costa et al. 1994), and numerically, by CFD simulations (Shakaib et al. 2007; Shakaib et al. 2009). Conversely, if the $Re$ is medium-to-high, and $\theta$ value is large, then the liquid flows through the diamond mesh parallel to the filaments, as observed both experimentally, by using dye injection technique (Feron & Solt 1991), and numerically, by CFD simulations (Shakaib et al. 2009). More recently, the PIV technique was used to visualize and quantify the flow field in diamond meshes (Willems et al. 2010; Mojab et al. 2014; Bucs et al. 2015; Haidari et al. 2016). It was concluded that for $Re$ in the range 150 – 250, the liquid flow inside the channel filled with diamond mesh ($\theta$ = 45°, $\psi$ = 90°) is divided into two streams, both flowing parallel to the mesh filaments: one flowing aligned with the top filament and the other aligned with the bottom filament. However, this flow structure only occurs if the mesh is well tightened and fills entirely the channel; otherwise preferential flow paths exist. In fact, it was verified by PIV visualization that liquid flows through the free space between the mesh and the channel walls (Gimmelshtein & Semiat 2005) when the thickness of the mesh is less than the height of the channel. While PIV gives only information on the flow velocity vectors, mass transfer performance can be assessed by obtaining permeate fluxes and/or solute concentrations in membrane processes (Schock & Miquel 1987; Da Costa et al. 1991; Da Costa & Fane 1994; Da Costa et al. 1994; Schwinge et al. 2004) or by using the limiting current technique for general mass transfer processes (Li et al. 2004; Li et al. 2005; Rodrigues et al. 2012).

As for 2D flows, the performance of different mesh geometries can be assessed by performing CFD simulations. The main issue with 3D simulations is the requirement of very high computational effort if one intends to simulate the flow in the whole channel. Because of that, only in the most recent works have the flows been simulated in areas of the channel containing several repeating cells (Saeed et al. 2012; Saeed et al. 2015; Mojab et al. 2014; M. Li et al. 2016; Kavianipour et al. 2017), while in the most earlier works the simulations were carried on single cells representing a repetitive unit along the channel. The exception was the work of Karode and Kumar (Karode & Kumar 2001), who predicted the flow hydrodynamics in a domain with 10×3 cells, but at the expense of very poor spatial resolution. Using a single cell, periodic boundary conditions are used to couple the cell inlet and outlet (Fimbres-Weihs & Wiley 2010; Keir & Jegatheesan 2014), making possible to predict the flow structures and mass transfer in small computer clusters or desktop personal computers. Considering that one is dealing with two-layer non-woven meshes, and supposing that the diameters of the filaments are the same in the top and bottom layers, then the repetitive cell can be chosen arbitrarily. However,

in the case of filaments of different dimensions, it was shown that the selection of distinct repetitive cells results in a different distribution of velocity and shear stress (Li & Tung 2008a).

Similarly to 2D flow simulations, some authors have performed 3D simulations only for the flow hydrodynamics (Karode & Kumar 2001; Dendukuri et al. 2005; Ranade & Kumar 2006a; Ranade & Kumar 2006b; Koutsou et al. 2007; Shakaib et al. 2007; Li & Tung 2008b; Li & Tung 2008a; Y. Li et al. 2009; Saeed et al. 2012; Mojab et al. 2014; Haaksman et al. 2017). Other works report the study of mass transfer phenomenon considering only impermeable-dissolving wall with constant solute concentration at the surface of interest (Li, W. Meindersma, et al. 2002; Li, G. Meindersma, et al. 2002; Fimbres-Weihs & Wiley 2007; Santos et al. 2007; Koutsou et al. 2009; Shakaib et al. 2009; Saeed et al. 2015; Kavianipour et al. 2017). Only a few works used more realistic models considering permeation (Lau et al. 2009; Gu et al. 2017).

Most of the CFD simulations were performed for non-woven meshes with cylindrical filaments. In any case, other not so intuitive filament shapes were also used, such as those possessing concave squared and concave rectangular cross-sections (Dendukuri et al. 2005). More recently, domains representing woven meshes were also used (Kavianipour et al. 2017; Gu et al. 2017). However, commercial meshes differ from those conceptual designs usually used in CFD simulations[13] and such approach yields discrepancies between numerical and experimental data. In a very interesting work, x-ray computerized tomography was used to reconstruct a domain with real non-woven meshes (Haaksman et al. 2017). Those domains were then used to study the flow hydrodynamics, resulting in a better agreement between numerical and experimental data than that obtained when using meshes of cylindrical filaments.

For impermeable channels, the hydrodynamics of the flow in channels filled with meshes becomes stabilized after the feed passes over 2 to 4 repeating units of the mesh (Shakaib et al. 2009; Saeed et al. 2012), but the flow structure, shear stress and pressure drop depend on the mesh geometry and on its alignment with the bulk flow (Saeed et al. 2012). Similarly, the mass transfer performance also depends on the same parameters (Saeed et al. 2015). For ladder meshes, it was found that the optimal mesh spacing, given by the ratio $l_f/h$, is 4 (Li, W. Meindersma, et al. 2002; Saeed et al. 2015), which is the same value as for 2D flows as discussed above. In addition, for steady laminar regime, the flows in channels filled with ladder meshes present the same type of recirculation regions as do 2D flows. For that reason, a first approach to the momentum and mass transport resulting from the flow over ladder meshes can be simulated by 2D CFD (Shakaib et al. 2007), at least for low $Re$. However, for diamond meshes the, flow hydrodynamics is completely distinct and results in better liquid mixing. Thus, in this geometry, the entrance length is small, as was verified by the stabilization of the mass

[13] Note that filaments of commercial non-woven meshes present non-uniform cross-section, being thicker in the region of the intersection between bottom and top filaments.

transfer coefficient in electrochemical processes after just two unit cells of the mesh, even for low Reynolds numbers (Rodrigues et al. 2012).

Although the amount of work already done in the field, there is not yet a comprehensive study on the optimization of $l_f/h$, $\theta$ and $\psi$ for diamond meshes. The critical $Re$ depends on the attack angle $\theta$, while the average shear stress is the same on the bottom and top surfaces for flat channels only if the diameters, the attack angle, and the spacing of the filaments are the same for both layers of filaments (Shakaib et al. 2007). The mass transfer increases as the mesh spacing $l_f/h$ decreases (Koutsou et al. 2009), at least down to a certain threshold. For $l_f/h$ = 4 the optimal performance was obtained using $\theta$ = 30° and $\psi$ = 120° (Li, W. Meindersma, et al. 2002; Lau et al. 2009). In fact, an increase of mass transfer is obtained as $\psi$ increases (Koutsou et al. 2009; Gu et al. 2017). When comparing directly ladder and diamond geometries some contradictory results are claimed by different authors: while some say that ladder meshes produce higher permeate flux (Da Costa & Fane 1994) others say that diamond meshes result in better mass transfer (Shakaib et al. 2009; Rodrigues et al. 2012). In terms of the comparison between woven and non-woven meshes, the former outperform the latter ones, despite an increase of pressure drop (Gu et al. 2017).

The general feeling that pops up from the other author's works is that 3D static mixers are much more efficient than the 2D counterparts. However, the development of new and more efficient 3D channel and spacer designs is computational very demanding. Moreover, entrance effects are not captured when cyclic conditions are applied, masking the actual performance of the device. Therefore, more efficient methods that can be used to estimate nanofiltration in the whole length of the channel are urged. A possible method is to use the hybrid method that is developed later in the section 4.4.5 and that applies the methodology proposed by Geraldes and Afonso (Geraldes & Afonso 2006) described in the following section.

### 4.2.4 Prediction of NF performance using the mass transfer correction factor

Despite the unparalleled increase of computational power in the last decades, together with the progress of numerical algorithms, it is still nowadays unfeasible or very time consuming to solve numerically the system of equations that model the permeation process, especially if the spatial discretization is very detailed. Moreover, if one intends to predict permeation data for similar geometries and conditions where a few parameters changes, the full simulation has to be performed again. To avoid this issue, Geraldes and Afonso (Geraldes & Afonso 2006) have developed a methodology to predict permeation data from mass transfer coefficients obtained from non-suction processes. Non-suction processes are surface mass transfer processes not involving semi-permeable walls and include those like dissolving-wall

processes or electrochemical processes. Geraldes and Afonso (Geraldes & Afonso 2006) have found that there is a correlation relating the CP modulus, $\Gamma$, the solute rejection ($R_i$ or $R_a$), the $\phi$ ratio and the correction factor $\Xi$, given by

$$\Gamma = \frac{R_i}{\frac{\Xi}{\phi} - R_i} = \frac{R_a}{\frac{\Xi}{\phi} - 1} \tag{4-2}$$

The correction factor $\Xi$

$$\Xi = \frac{Sh}{Sh_0} \tag{4-3}$$

relates the Sherwood numbers of the permeation process, $Sh$, with the corresponding one of the non-suction process, $Sh_0$, whereas $\phi$ is the ratio between the permeate flux and the mass transfer coefficient of the non-suction process, $J_v$ and $k_{c,0}$, respectively

$$\phi = \frac{J_v}{k_{c,0}} \tag{4-4}$$

Fitting CFD results for NF/RO membrane processes, Geraldes and Afonso (Geraldes & Afonso 2006) have found the following correlation that can be used for any $\phi$

$$\Xi = \phi + (1 + 0.26\phi^{1.4})^{-1.7} \tag{4-5}$$

In addition to equation (4-2), the CP modulus is also defined by

$$\Gamma = \frac{c_m - c_b}{c_b} \tag{2-10}$$

as described in section 2.1.4, or by

$$\Gamma = \frac{w_m - w_b}{w_b} \tag{4-6}$$

if the liquid density is constant. Since $\Gamma$ must obey simultaneously equations (4-2) and (4-6), one can predict the values for $J_v$ and $c_m$ (or $w_m$) providing some input parameters, including the solute rejection and the mass transfer coefficient for the non-suction process.

After the work of Geraldes and Afonso (Geraldes & Afonso 2006), the mass-transfer correction methodology was used, by other authors, for NF processes consisting of permeation in open channels and flows at medium-to-large $Re$ (Morão et al. 2008; Shah et al. 2012). Therefore, it is important to assess if the use of the Geraldes and Afonso's methodology remains valid for NF processes performed at low $Re$ in channels with spacers (Completo et al. 2016). This issue is addressed in the current chapter. In addition, if the $\Xi$ correlation is still valid in such scenarios, then, it can be applied in expedite algorithms to predict nanofiltration performance in innovative devices. With this purpose, a hybrid computational / semi-empirical method is developed in section 4.4.5, and used and validated in section 4.5.5 for the permeation in ribbed channels. Prior to that, to check that the used CFD model describe well the permeation process its validation is done using micro-PIV and HI experimental data.

## 4.3 Experimental part

The experimental work performed for this chapter refers to the visualization of both the flow inside impermeable channels and of the CP phenomenon in the nanofiltration of $K_2SO_4$ aqueous solutions. For the former, micro-PIV technique was applied to obtain the velocity fields of water flows in open channel and in channels filled with transverse circular ribs. For the latter, the HI technique was used to study of the influence that several operating conditions (time, feed concentration, flow rate, applied pressure, and geometry of the channel) have on the extent of the CP phenomenon.

### 4.3.1 Experimental setup for flow measurement by micro-PIV

The experimental setup used for velocimetry analysis of flows is composed by a hydraulic system, which drives the liquid through tubing into and out from an impermeable slit channel, and by a micro-PIV system that acquires images of the flow and calculates the corresponding velocity fields. Sketches of these individual systems are displayed in Figure 4-7a and Figure 4-7b. A picture of the actual main components is shown in Figure 4-7c.

**Hydraulic system**

The liquid was driven from a one litre reservoir by a peristaltic pump (LAV 200, Dosiper, Spain), while two manual valves controlled the flow rate, which value was acquired using a flowmeter (SCAU-010A, Elab, Portugal) and an acquisition board (USB-6008, National

Instruments, USA) that sent the data to the Labview software. The inherent flow pulses were dampened by a deformable rubber pipe with clamps.

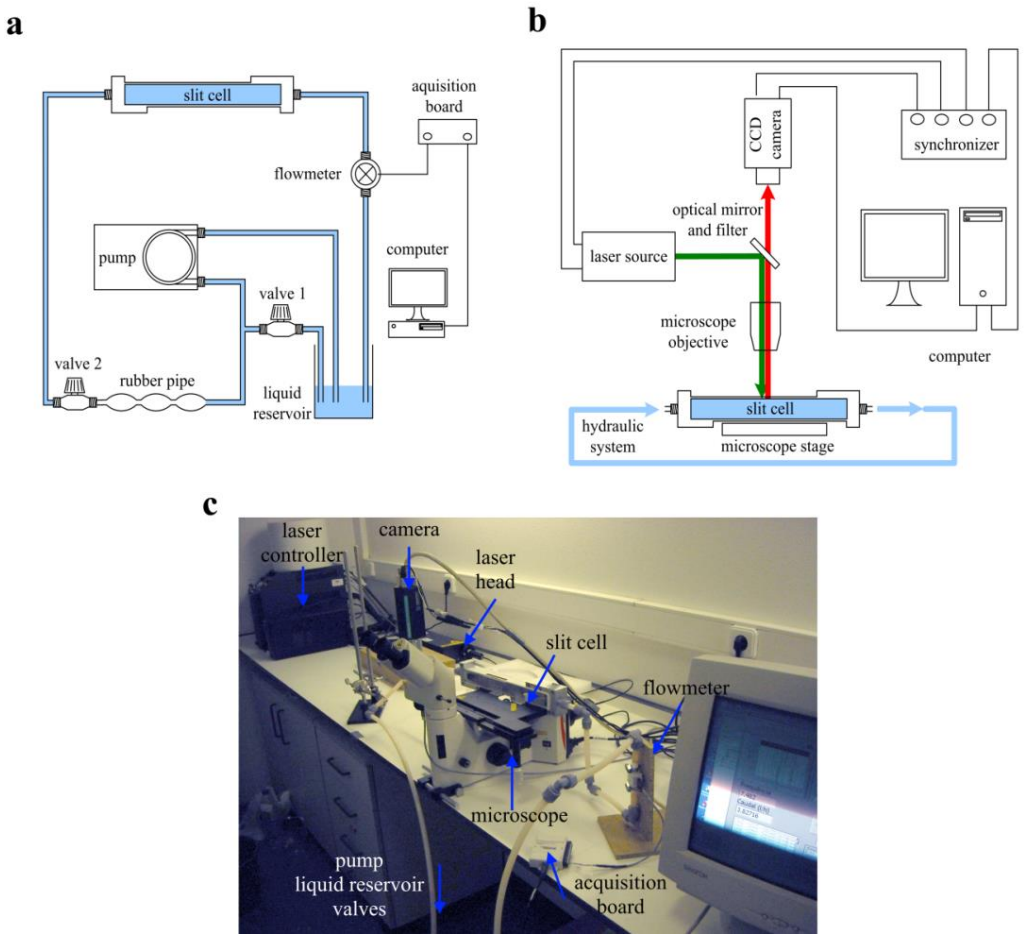


Figure 4-7 – Experimental setup used for flow measurement by micro-PIV: a) hydraulic system; b) micro-PIV system; c) main components of the setup. Adapted from (Completo et al. 2014).

**Micro-PIV system**

The used micro-PIV hardware was comprised six main components: a pulsed Nd:YAG laser source (Solo II-15, New Wave Research, USA); an inverted microscope (DM ILM, Leica Microsystems, Germany); an optical filter (Y3 cube filter, Leica Microsystems, Germany); a charge coupled device (CCD) camera (Flowsense 2M, Dantec, Denmark); a synchronizer; and a computer. The laser light travelled from the laser source up to the microscope via an optical fiber cable (LightGuideOptics, Germany).

Flow images were acquired using the microscope lens HI PLAN 10× (Leica Microsystems, Germany). For this lens, the depth of correlation (Olsen & Adrian 2000), which estimates the depth of field, is 35 μm. The velocity fields were calculated using the correlation and analysis algorithms available in the PIV acquisition software (DynamicStudio version 2.30, Dantec Dynamics, Denmark).

**Impermeable slit cell**

The impermeable slit cell consisted in a 200 mm length channel with two different rectangular cross-sections: 1.2 mm height × 30 mm width for the open channel and 1.5 mm height × 30 mm width for the ribbed channel (Almeida et al. 2010). The channel surfaces were made of smooth poly(methyl methacrylate) plates, but the bottom wall surface can be replaced by others with transverse circular ribs placed at distinct distances between each other, as sketched in Figure 4-8a. In this work the circular ribs (nylon filaments) had $d_f$ = 0.7 mm and the $l_f$ = 9.9 mm. The external case of the slit channel was made of machined aluminum, as shown in Figure 4-8b. The large top transparent wall and the two lateral windows of the slit cell made possible to acquire velocimetry data at several stations.

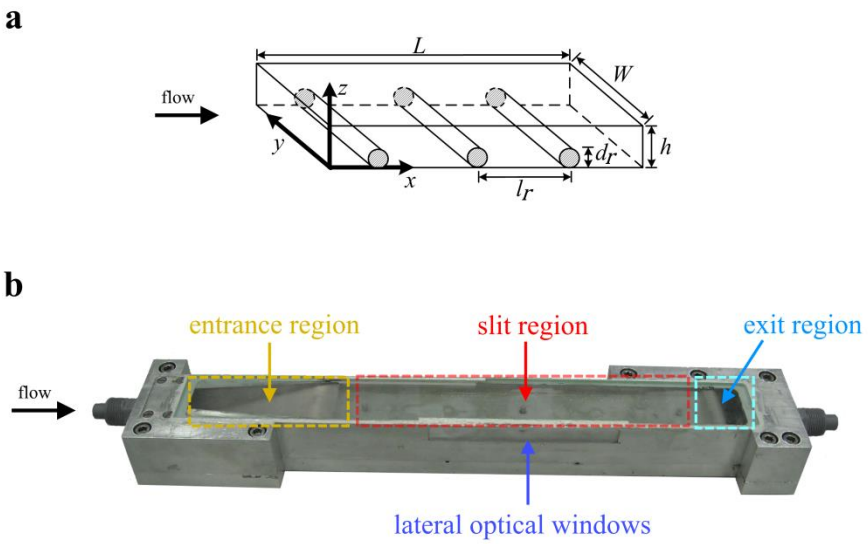


Figure 4-8 – Impermeable slit cell: a) sketch showing the geometry of the slit channel; b) actual slit cell.

### 4.3.2 Experimental setup for concentration measurement by holographic interferometry

The experimental setup consisted of a hydraulic system to deliver the solution from a sample reservoir to the nanofiltration cell, and a holographic interferometry system to generate light interferences and acquire the interferograms for CP visualization. The nanofiltration TFF cell was at the core of those two systems, interconnecting them. A sketch of the experimental setup is depicted in Figure 4-9a, while Figure 4-9b display a picture of the holographic interferometry system placed on an anti-vibration optical table.

**Hydraulic system**

The feed solution was placed in a 2-litre stainless steel reservoir and a positive-displacement pump (Hydra-Cell G-03-S, Wanner Engineering Inc., USA) promoted the flow through the hydraulic system. The flow rate through the nanofiltration TFF cell and the applied pressure were both controlled using a back-pressure valve (BP-3, Go Regulator, USA) and a needle valve (model 710.3312, SITEC-Sieber Engineering AG, Switzerland). The system pressure was monitored by a manometer (model 312.20, Wika, Germany) and it was assumed that the pressure drop due to friction in the tubing, from the pump up to the needle valve, was negligible when compared to the applied pressure. It was also assumed that the permeate side of the nanofiltration TFF cell was at atmospheric pressure and, thus, the transmembrane pressure was equal to the pressure shown by the manometer. The rotameter (model D10A1197D, Bailey Fisher & Porter, Netherlands) provided an estimate of the concentrate flow rate and was used for setting up the flow rate. To obtain the actual flow rate, and thus to calculate the average liquid velocity at the channel entrance, $U_0$, both the permeate and concentrate flow rates were determined by weighting the amount of liquid exiting these streams in a certain period of time.

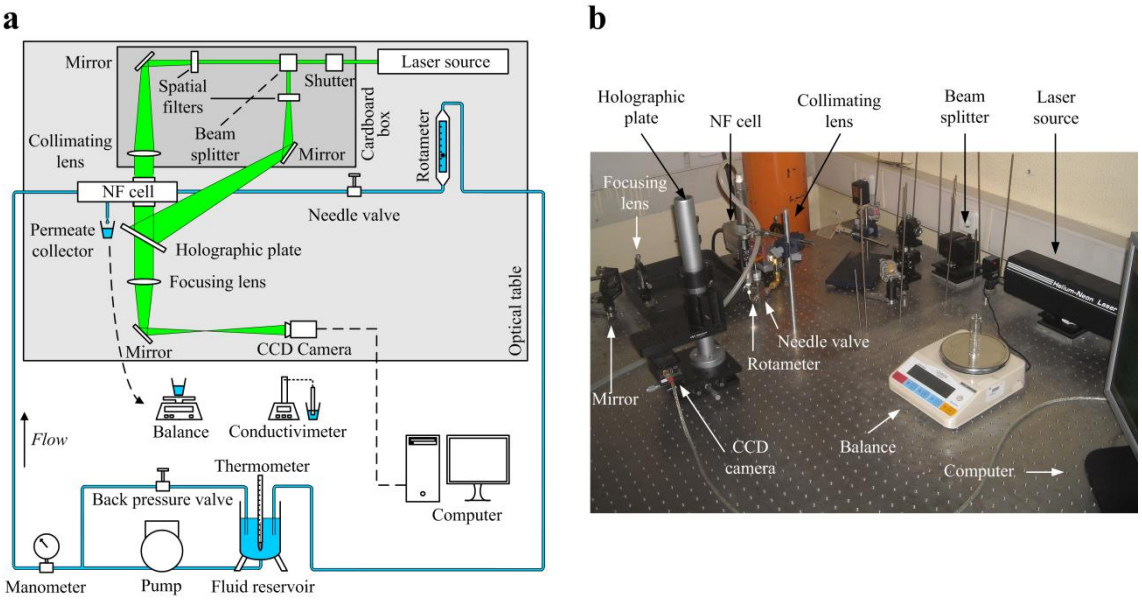


Figure 4-9 – Experimental setup used for the visualization of the CP layer using holographic interferometry: a) sketch of the holographic interferometry system and of the hydraulic system; b) main components of the holographic interferometry system. Adapted from (Completo et al. 2016).

**Holographic interferometry system**

An interferometry system permits to obtain interferograms which are the resulting images of the superposition, at the focal plane, of the object and reference light fields. Unlike classical interferometry systems, which require two individual cells (one being the object cell and the

other the reference cell), in the used holographic interferometry system the reference light field is reconstructed when the laser light passes through a holographic plate with the recorded reference state. Changes of the liquid properties in the object cell result in the bending and delay of the light beam crossing it, when compared with that occurred in the reference cell (or with that recorded in the holographic plate). Thus, when the object and reference light fields are superimposed the image formed at the focal plane presents interferences or fringes. These fringes can then be transposed to the concentration field.

The holographic interferometry system used in the experiments is sketched in Figure 4-9 and consisted of several optical parts and of the TFF cell. Briefly, a beam of coherent red laser light (633 nm wavelength) was emitted from a He–Ne laser source (model 31425, Research Electro Optics, USA), passed through a shutter and was split, at the beam splitter (model M-930-63, Newport Corporation, USA), into two independent beams. Light aberrations were eliminated by filtering both beams in spatial filters and by collimating the light beam in a lens (model PAC091, Newport Corporation, USA) before they crossed the TFF cell and the holographic plate. The light field that emerges from the TFF cell is referred as object beam, while the reference beam results from the interaction of the laser beam with the recorded hologram in the holographic plate (model Ultimate 08-00 Red 610–660, Ultimate Holography, France). The object and reference beams interfered with each other and, after passing a focusing lens (model PAC091, Newport Corporation, USA), the combined light field was registered in a CCD camera (model LightWise, Imaging Solutions Group, USA) and recorded in a computer using the Streampix software (version 3.24.1, Norpix, Canada).

The reference state was recorded in the holographic plate using deionized water as working fluid. The holographic recording process was made following the procedure described in (Rodrigues et al. 2013).

**TFF nanofiltration cell**

The TFF nanofiltration cell used in this part of the work was a straight slit channel with height, $h$, of 2 mm, width, $W$, of 15 mm and length, $L$, of 150 mm. The channel could be used in open geometry, with constant rectangular cross-section, or could have transverse square ribs on the top wall of the channel. The ribs were located in the corresponding region of the porous support placed on the bottom wall of the channel. The beginning of the porous support was at 60 mm downstream the inlet channel and ended 25 mm before the outlet channel. That way the flow fully developed at the entrance section. Similarly, the exit section had the purpose to dampen disturbances near the outlet tubing that could affect the flow structure near the membrane. These lengths were enough for flow development in the used operating conditions,

since they were larger than the necessary entrance length, $L_e$, which for laminar flow inside open channels with rectangular cross-section is estimated by (Geraldes et al. 1998)

$$L_e = 0.1254 Re_h h \tag{4-7}$$

In the ribbed-wall channel, 11 transverse ribs were placed on the top wall (top cavity configuration), being the rib height, $h_r$, 1 mm, the rib width, $W_r$, 15 mm and the rib length, $L_r$, 1 mm. The distance between two consecutive ribs, $l_r$, was 7.6 mm. Thus, the ratio $l_r/h$ is close to 4, which was found to be the optimal $l_f/h$ value for the ratio between the characteristic dimension of the spacer and the height of the channel for cylindrical filaments (Li, W. Meindersma, et al. 2002).

The TFF nanofiltration cell was comprised of three main parts made of stainless steel: a) a bottom part, which functioned as the bottom wall of the channel and included the porous support where the membrane was fixed and the permeate channel for permeate removal; b) a top part, which operated as the lateral wall of the channel, and included two windows for optical access (through which the laser beam has passed) but did not include the ribs and the channel top wall; c) plates, which defined the top wall of the channel. The constitution of the cell can be easily understood by looking at its sketch depicted in Figure 4-10a (which is not at scale). The assembly of the cell is shown in Figure 4-10b. To create the open channel, the plate defining the top wall was flat, whereas for the top cavity channel the plate was provided with transversal square ribs. These plates were assembled on the top part with screws.

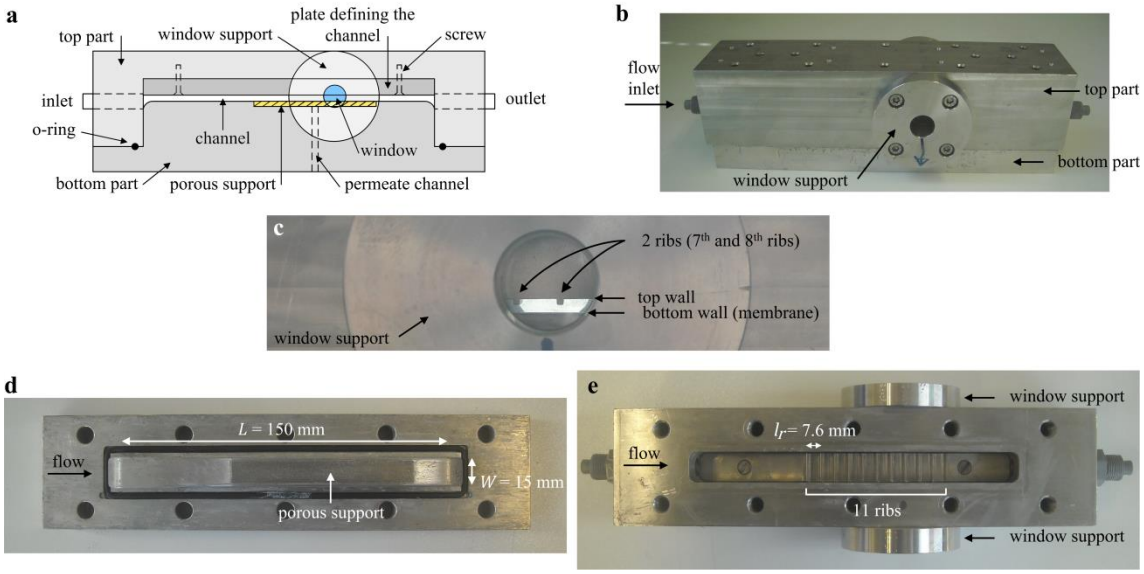


Figure 4-10 – Sketch and pictures of the TFF nanofiltration cell: a) longitudinal sketch of the cell; b) assembled cell; c) detail of the optical window; d) top view of the bottom part of the cell; e) bottom view of the top part of the cell. Adapted from (Completo et al. 2016).

The optical windows covered the channel region between 52 and 67 mm, downstream the beginning of the porous support, and were made of borosilicate glass discs (Maxos S-200, Schott, USA) assembled on windows supports, which were screwed to the lateral sides of the top part of the TFF cell. When using the top cavity channel, the optical windows covered the region between the 7$^{th}$ and 9$^{th}$ ribs (Figure 4-10c). To seal the cell, a nitrile O-ring was placed in between the top and bottom parts and the parts were tighten using 10 screws. Plastic inlet and outlet connectors (Serto, Switzerland) were used to connect the cell to the hydraulic system. Figure 4-10d and Figure 4-10e show the bottom and top parts of the cell.

### 4.3.3 Materials

For the visualization of the velocity field, using micro-PIV, a suspension of tracer particles (1 μm red nile FluoSpheres, Invitrogen, USA) was mixed with deionized water (6 mL of tracer particle suspension per liter of water). For the visualization of the CP phenomenon, using HI, aqueous solutions of potassium sulfate ($K_2SO_4$) were used. Feed solutions of the salt ($c_f$ = 2 g/L and $c_f$ = 4 g/L) were prepared dissolving reagent grade $K_2SO_4$ (Scharlau, Spain) within deionized water. The deionized water was produced by an ion exchange resin module and its conductivity was lower than 10 μS/cm.

The used membrane was the Desal TFM-50 membrane (GE Osmonics, USA). A suitable size piece of membrane was placed over the porous support of the bottom part of the NF cell and fixed using silicone glue (Gymcol, Spain).

### 4.3.4 Methods

**Determination of velocity fields using micro-PIV**

The velocity fields were obtained at a station 14 cm downstream the end of the entrance section, defined in Figure 4-7b, for $Re_h$ between 50 and 250. At that station, the flow is developed both in open channel and in channel filled with transverse ribs. For open channel only 2.3 cm of entrance length are necessary at the highest used $Re_h$. For the ribbed channels, the measurements were made in a station after more than 10 rib sections have been crossed by the flow; therefore, the flow hydrodynamics was stable, provided that $Re_h$ was lower than the critical value, as discussed in the section 4.2.3.

Micro-PIV measurements were performed in two orientations. According to Figure 4-8, vertical velocity maps ($xz$ plane) were obtained through the lateral optical window up to 4 mm

from the side wall, while horizontal velocity maps ($xy$ plane) were obtained through the top optical window.

The vertical velocity maps were performed with a minimum microscope stage displacement of 40 μm, corresponding to a displacement of the focal plane of 54 μm which is larger than the estimated depth of correlation (Completo et al. 2014). As a consequence, there was no overlap between consecutive measurement planes in these velocity maps. On the other hand, the measurements through the top access were done with a narrower objective displacement, 20 μm, in order to try to define an accurate velocity profile and, therefore, a small overlap exists since the displacement of the focal plane was only 27 μm.

Since the area of analysis covered by the lens during each acquisition is very small (0.8 mm × 1.2 mm), when compared to the channel width, the measurements through the top window were performed only close to the middle width of the channel where one can assume the occurrence of the velocity plateau. Similarly, for the measurements through the lateral window, the velocity maps only partially cover the height of the channel.

Only the steady characteristics of the flows are considered since the time interval between the two consecutive images of the flow varied between 30 μs and 500 μs, depending on the flow rate. In addition, each map results from the averaging of 100 pairs of images of the flow. Nevertheless, the obtained velocity maps are enough to visualize the most important structures of the flows.

The experimental velocity fields for water flows inside open channel slits can be compared with the analytical expression for the velocity of developed flows of Newtonian fluids inside rectangular channels (Completo et al. 2016), given by $u(y,z)$

$$u(y,z) = \frac{48Q}{\pi^5 W h}\left[\frac{\sum_{n,odd}^{\infty}\frac{1}{n^3}\left[1-\frac{cosh\left(n\pi\frac{y}{h}\right)}{cosh\left(n\pi\frac{W}{2h}\right)}\right]sin\left(n\pi\frac{z}{h}\right)}{1-\sum_{n,odd}^{\infty}\frac{192h}{n^5\pi^5 W}tanh\left(n\pi\frac{W}{2h}\right)}\right] \quad (4\text{-}8)$$

where $Q$ is the volumetric flow rate.

**Determination of concentration fields using holographic interferometry**

To study the time evolution of the CP phenomenon and the influence of several operating conditions, the nanofiltration experiments of $K_2SO_4$ aqueous solutions ($c_f$ = 2 g/L and 4 g/L) were performed at three different transmembrane pressures ($\Delta p_m$ = 3 bar, 5 bar and 8 bar) using flows at low Reynolds numbers (0 < $Re_h$ < 125) typical of microfluidic sytems. The $Re_h$ values

were determined based on the inlet velocity, and on the density and viscosity of the feed solution. The exception was the case when the needle valve, at the exit of the cell, was fully closed. In those scenarios, the $Re_h$ value was set equal to 0. The temperature of the liquid was monitored inside the sample reservoir, which varied between 30 °C ± 3 °C. Before and after each set of experiments the hydraulic permeability of the membrane was measured to ensure that there were no leakages and that the water flux has recovered after each cleaning process.

Five different parameters were studied to evaluate their influence on the CP phenomenon: time, flow rate (given by $Re_h$), feed solute concentration, transmembrane pressure and channel geometry (open or top cavity channel).

The first study was devoted to verify the temporal evolution of the CP layer, for representative flow conditions ($Re_h$ = 0 or $Re_h$= 5), checking the number of fringes of the interferograms obtained at distinct time instants. This is important to ensure that for the subsequent studies the interferograms would be obtained at steady-state conditions. Thus, the interferograms were acquired at the initial time, when the needle valve was opened (defined as $t$ = 0 s) and at the time instants of: 10 s, 20s, 1 min, 2 min, 5 min, 10 min, 15 min, 30 min (in some cases at 60 min also), after adjusting the need valve for the desired inlet flow rate. Due to operational limitations, the real acquisition times may vary ± 10 s, which is insignificant for $t$ > 1 min, but can result in some inconsistencies for $t \leq$ 1 min.

After defining the necessary time to reach steady state, the study was devoted to verify the effect of $Re_h$ on the CP layer. Based on the results from previous studies (section 3.5.3), it was defined that for $Re_h \geq 5$ the interferograms would be acquired at $t$ = 10 min, whereas for $Re_h < 5$ the interferograms would be acquired at $t$ = 30 min.

The subsequent step was to compare NF experimental data with the corresponding one obtained by numerical simulations. Thus, the interferograms were converted into concentration profiles, along the height of the channel, and those compared with the corresponding numerical ones. To do that, pairs of the solute mass fraction, $w$, versus the $z$-location were obtained from the interferograms, being $z$ at the membrane surface defined as 0. Counting the number of pixels from the top wall of the channel to the middle of a fringe, and knowing that $h$ = 2 mm, it is possible to determine the average $z$-location of each fringe. To determine the concentration at the fringe the following equation was used (Completo et al. 2016)

$$\Delta w = \frac{\lambda}{a \rho L_o} \tag{4-9}$$

which gives the variation of the solute mass fraction between consecutive fringes, $\Delta w$, as function of the liquid density, of the light wave length, $\lambda$, of the geometrical path length travelled by the light in the medium, $L_o$, and of the slope of the linear relationship between the

refractive index and the solute concentration, $a$ (Rodrigues et al. 2013). In this case, $L_o = W$ = 15 mm, $\lambda$ = 633 nm, $a$ = 1.05×10$^{-4}$ m$^3$/kg for $K_2SO_4$ solutions, and $\rho$ is that of the feed solution. The solute mass fraction at the first fringe is given by $w = w_f + \Delta w$, where $w_f$ is the solute mass fraction in the feed.

### 4.3.5 Chemical analysis

The liquid streams consisted only of aqueous $K_2SO_4$ solutions and, for that reason, their salt concentration was determined by conductometry analysis as described in section 3.4.4.

## 4.4 Numerical simulations

Two types of flows were simulated by CFD: flows with or without mass transfer processes. For the former only the hydrodynamics, i.e. the momentum transfer, is accounted and these simulations were performed for comparison purposes with micro-PIV measurements. For the latter, both hydrodynamics and mass transfer are modelled and their aim was threefold: a) compare CFD and HI data obtained for channels with ribs on the top wall (validation purpose); b) study of the effect of channel geometry; c) apply and validate of the hybrid method to predict nanofiltration data. In practice, the momentum model is the same in the two types of flows.

In terms of mass transfer, two types of processes were simulated: the nanofiltration of $K_2SO_4$ solutions; and the mass transport of $K_2SO_4$ in a non-suction process of impermeable-dissolving wall. Although the transport equations are the same for both cases, the boundary conditions are different: a semi-permeable wall, in the first case, and an impermeable wall with constant solute concentration at the surface, in the second case.

The hydrodynamics simulations of flows inside impermeable channels to be compared with micro-PIV made use of two channel geometries: open channel and channels with transverse circular ribs on the bottom wall.

For the mass transfer processes, two sets of geometries were used. In the first set, only the permeation processes were simulated and the domains resembled the geometry of the channels used in the experimental nanofiltration TFF cell ($L$ = 150 mm in open channel or with 11 transverse square ribs on the top wall, as defined in section 4.3.2). In the second set, the channels were longer ($L \approx$ 300 mm in open channel or with 30 ribs on the top wall) and both permeation and dissolving wall processes were simulated. Moreover, in the second set, not only the flows inside open and top cavity channel were simulated, but also the corresponding flows inside channels with bottom ribs and in the zigzag geometry.

### 4.4.1 Geometry of the simulation domain

The geometry of the channels used for the simulation of the hydrodynamics in slits was already presented in the Figure 4-8a. Given the used slit dimensions ($W$ = 30 mm and $h$ = 1.2 mm or $h$ = 1.5 mm) and the range of the applied Reynolds number ($Re_h \leq 250$), the flow was two-dimensional in most of the slit channel (as it will be seen later, there is variation of the velocity magnitude in the $y$-direction near the lateral wall, but only up to a small depth). Similarly, the flows inside the channels of the TFF nanofiltration cell were also two-dimensional in the studied Reynolds number range ($Re_h \leq 125$). For that reason, all the numerical simulations are performed in 2D domains.

The geometry of the channels of the TFF nanofiltration cell was similar to the one depicted in Figure 4-11. The simulation domain was the internal part of the channel with length $L$ (in the $x$-direction) and height $h$ = 2 mm (in the $z$-direction). If no ribs were present the channel was named as open channel. On the other hand, ribs could be present on the top wall (top cavity geometry), on the bottom wall (bottom cavity cavity) or alternately on top and bottom walls (zigzag geometry). Mimicking the actual cell, the length and height of each rib, $L_r$ and $h_r$, were both 1 mm. The distance between equivalent points of consecutive rib sections, $l_r$, was 7.6 mm. On the bottom wall, a portion of the surface, with a length $L_d$ was set as a semi-permeable membrane (for the nanofiltration processes simulations) or as an impermeable-dissolving wall (for the non-suction processes). Prior and after this portion of the channel, there were open sections to prevent entrance and exit effects. According to equation (4-7) the adopted entrance and exit open sections were long enough to achieve developed flow.

As mentioned above, the number of rib section used in the simulations to be used for comparison with the experimental results was 11 (as in the nanofiltration TFF cell), while for the other simulations the total number of rib sections was 30.

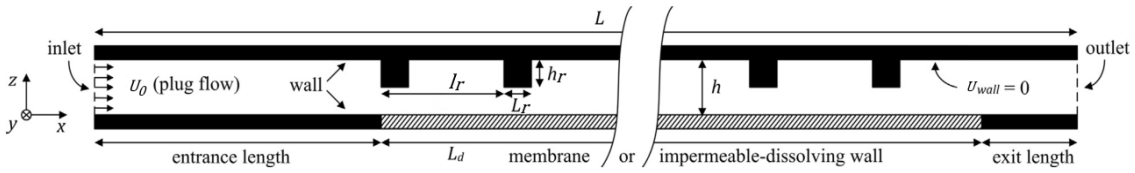


Figure 4-11 – Sketch of the generic two-dimensional domain used for the simulations.

### 4.4.2 Momentum and mass transport modelling

The transport phenomena (momentum and mass) occurring inside the slit are described by the global continuity equation, the Navier-Stokes equations, and the solute continuity equation. Assuming that the pressure gradient is the only driving force of the flow (neglecting

gravitational and any other forces), that the fluids are Newtonian and that the density is constant, then those equations are given, respectively, by

$$\nabla \cdot \boldsymbol{U} = 0 \tag{4-10}$$

$$\frac{\partial \boldsymbol{U}}{\partial t} + (\boldsymbol{U} \cdot \nabla)\boldsymbol{U} = \nu(\nabla^2 \boldsymbol{U}) - \frac{\nabla p}{\rho} \tag{4-11}$$

$$\frac{\partial w}{\partial t} + \nabla \cdot (\boldsymbol{U} w) = \nabla \cdot (D_{AB} \nabla w) \tag{4-12}$$

where $\boldsymbol{U}$ is the velocity vector, $\nu$ is the kinematic viscosity, $D_{AB}$ is the diffusion coefficient of the solute $A$ in the solvent $B$ (in this case $K_2SO_4$ in water), and $w$ is the mass fraction of the solute.

To solve the differential equations (4-10) to (4-12) it is necessary to define the adequate boundary conditions. The velocity at the entrance of the channel was defined as a plug-flow profile, i.e.:

$$U_x = U_0 \tag{4-13}$$

$$U_y = U_z = 0 \tag{4-14}$$

where $U_0$ is a constant. The no-slip condition was imposed at the impermeable walls, while for the nanofiltration process there is a $z$-component of the velocity at the membrane surface

$$-U_z|_{membrane} = J_v = \frac{1}{\mu R_m}\left[\Delta p_m - C\left(w_m - w_f(1 - R_a)\right)\right] \tag{4-15}$$

where $C$ is a constant of proportionality between the solute mass fraction and the osmotic pressure. In addition, also for the membrane process, a solute mass balance close the membrane surface imposes the following equation for the gradient of the solute mass fraction normal to the membrane surface

$$\left.\frac{\partial w}{\partial z}\right|_{membrane} = \frac{J_v\left[w_m - w_f(1 - R_a)\right]}{D_{AB}} \tag{4-16}$$

Details on the deduction of equations (4-15) and (4-16) are shown in the Appendix D. Conversely, for the impermeable-dissolving wall process, a constant solute mass fraction was

imposed to the surface. Since the mass coefficient is independent of the wall concentration (Saeed et al. 2015), then, it was arbitrarily set to $w_m$ = 0.01. The relative pressure at the exit of the channel was constant and equal to zero.

The CFD results for the impermeable-dissolving wall simulations were validated using the Graetz-Lévêque correlation (Pickett & Stanmore 1972) which considering $h$ as the characteristic length results in

$$Sh = 1.468\left(Re_h Sc \frac{h}{L_d}\right)^{1/3} \quad (4\text{-}17)$$

### 4.4.3 Discretization and solving the model equations

The numerical simulations of nanofiltration and impermeable-dissolving wall processes were computed using the OpenFOAM software (version 1.7). This software uses the finite volume method to discretize the governing partial differential equations of the model into their algebraic forms. The OpenFOAM software allows the user to customize the solvers and the parameters used for the discretization, as well as the solving schemes. In addition, OpenFOAM software includes packages to generate the mesh of the domain and to perform post-treatment and visualization of the generated data.

Time derivatives were discretized using a second order implicit scheme (backward). The gradient terms were discretized using a second order with linear interpolation scheme (Gauss linear). The divergence terms were discretized using a mixed linear/upwind scheme (Gauss limitedLinear 1.0). The Laplacian term of the solute continuity equation was discretized using a second-order scheme (Gauss linear corrected), while the Laplacian terms of the Navier-Stokes equations were discretized using a blended of first and second order schemes (Gauss linear limited). The gradient normal to the surface was set using explicit non-orthogonal correction, while interpolations were performed using a linear scheme. Detailed description of these discretization methods is available elsewhere (OpenCFD Limited, 2008a; OpenCFD Limited, 2008b).

The geometric-algebraic multi-grid (GAMG) solver was used to solve the discretized algebraic equations, which speeds up the simulation process by first solving the set of equations for a coarse grid and subsequently refining the mesh up to the one defined by the user. To couple the pressure and velocity fields PISO algorithm (Versteeg & Malalasekera 2007) with four correctors was used. The time step between consecutive time iterations was automatically adjusted by the algorithm to keep the Courant number below 0.8. Under-relaxation coefficients for pressure, velocity and mass fraction were set to 0.3, 0.7 and 0.8, respectively.

Setting the initial conditions to

$$\boldsymbol{U} = 0 \; \forall x, y, z \neq 0 \text{ at } t = 0 \tag{4-18}$$

and

$$w = w_f \; \forall x, y, z \text{ at } t = 0 \tag{4-19}$$

results in a transient flow process that, after a non-specified number of time steps (depending on the initial conditions), tends to a steady-state flow, as verified by monitoring the values of $\boldsymbol{U}$ and $w$ at fixed locations, namely at the entrance region and at the mid-position between consecutive ribs.

The grid independency was accessed by comparing, in a preliminary study, the simulation results of the NF processes obtained for domains equivalent to the experimental channels but using three grids with different number of cells: $136\times10^6$ cells, $545\times10^6$ cells and $2180\times10^6$ cells. Since the relative deviations, in terms of $\boldsymbol{U}$ and $w$, between the results obtained using the different grids for an illustrative scenario, were less than 0.3 % at the above-mentioned monitored locations only the coarser grid was used in the subsequent numerical studies. For the larger channels (30 ribs) the number of cells was increased accordingly but the cell size was kept the same.

In addition, the simulations were performed with constant density and viscosity since it was verified that they have small influence on the results: relative deviations of 0.4 % on the $J_v$ and 0.2 % on the $w_m$ at middle point between the 7$^{th}$ and 8$^{th}$ ribs when the simulations were performed with $\rho$ and $\mu$ as functions of the solute concentration.

The simulations to be compared with the experimental results were done with liquid properties similar to those of the feed (temperature, water permeability and apparent rejection), while for the simulations to evaluate the effect of the channel geometry, the operating conditions were set to $c_f$ = 4 g/L, $T$ = 30 °C, $R_a$ = 0.95, $P_w = 4.3\times10^{-15}$ m and $\Delta p_m$ = 8 bar. The density and viscosity data for the $K_2SO_4$ solutions used in the present section were obtained from the works of Laliberté *et al.* (Laliberté & Cooper 2004; Laliberté 2007). The constant $C$ was assumed independent of the temperature and was set equal to $3.214\times10^4$ Pa by fitting the osmotic pressure of $K_2SO_4$ solutions as function of solute mass fraction (Sourirajan 1970).

### 4.4.4 Evaluation of periodicity in the solute concentration

Given that there was a good agreement between the experimental results obtained by HI and those obtained by numerical simulations, CFD was used to assess the periodicity of the flow

in terms of the solute concentration. The verification of the periodicity of the flow makes use of the ratio between the solute mass fraction at specific points and the bulk solute mass fraction, $\frac{w}{w_b}$. This ratio is a generic expression. Two forms of this expression were used to evaluate the periodicity: in one of the forms the periodicity of the solute concentration is determined along the membrane surface, while in the other one the periodicity of the solute concentration is determined along the height of the channel. Since the determination of the bulk mass fraction, $w_b$, as function of the $x$-position was impractical, it was decided to determine an average bulk solute mass fraction in each of the rib sections using the logarithmic mean, $w_{bLN,sec}$. A rib section is the whole region, with length $l_r$, between two consecutive ribs, as is defined graphically in Figure 4-12. The $w_{bLN,sec}$ value for each section is calculated as

$$w_{bLN,sec} = \frac{w_b^{in} - w_b^{out}}{ln\left(w_b^{in}/w_b^{out}\right)} \tag{4-20}$$

similarly to the mean concentration defined by Kaufman et al. (Kaufman et al. 2012), where $w_b^{in}$ and $w_b^{out}$ are the average bulk solute mass fraction at the entrance and exit of each section. The $w_b^{in}$ value for each section was calculated according to the averaging equation

$$w_b^{in} = \frac{\sum A_{c,i} \cdot w_{c,i}}{\sum A_{c,i}} \tag{4-21}$$

where $A_{c,i}$ is the cross-sectional area of the cell $i$ (of the finite volume domain discretization) along the height of the channel at the section entrance location and $w_{c,i}$ is the solute mass fraction on the same cell. A similar expression was used to calculate $w_b^{out}$.

One of the used methods to evaluate mass transfer periodicity was to apply the $\frac{w}{w_b}$ ratio at the membrane surface, being $w$ given by the average solute mass fraction at the membrane surface at each section, $w_{m,sec}$, calculated by

$$w_{m,sec} = \frac{\sum A_{m,i} \cdot w_{m,i}}{\sum A_{m,i}} \tag{4-22}$$

where $A_{m,i}$ is the area of the cell $i$ (of the finite volume domain discretization) that makes part of the membrane and $w_{m,i}$ is the solute mass fraction at the membrane surface at that cell. Thus, in this first form, the periodicity of the solute concentration is evaluated using the ratio $\frac{w_{m,sec}}{w_{bLN,sec}}$.

The second form to evaluate the solute concentration periodicity consisted in verifying the evolution of the ratio $\frac{w(z)}{w_{bLN,sec}}$, where $w(z)$ is the solute mass fraction along the channel height ($z$-direction). The value of $\frac{w(z)}{w_{bLN,sec}}$ was determined at locations distancing 1.75 mm from the beginning of each section, as depicted in Figure 4-12.

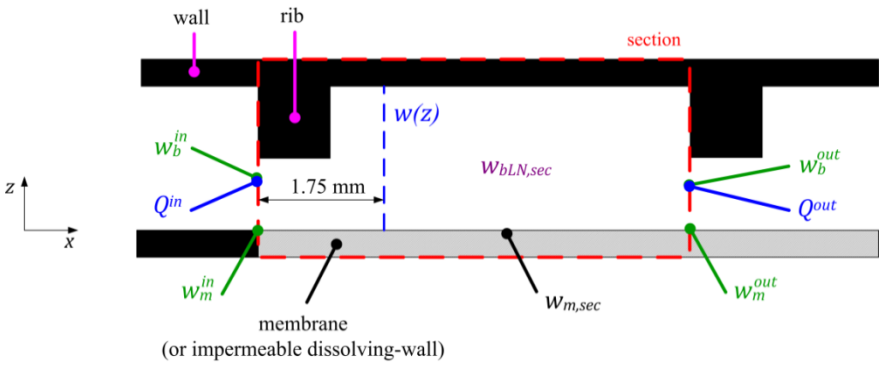


Figure 4-12 – Sketch of a section of channel and the definition of several solute concentrations and flow rates.

In Figure 4-12 other parameters that will be used later in section 4.4.5 are also referred, including the solute mass fraction at the membrane surface at the entrance and exit of the section, $w_m^{in}$ and $w_m^{out}$, and the flow rates at the entrance and exit of the section, $Q^{in}$ and $Q^{out}$.

### 4.4.5 Development of a hybrid method to predict NF data

The hybrid method that makes use of the Geraldes and Afonso's methodology (section 4.2.4) is applied to predict NF data, including the permeate flux and the solute mass fraction at the membrane surface and at bulk solution, respectively. To achieve this, the mass transfer coefficients obtained for the non-suction process, $k_{c,0}$, were determined by simulating the impermeable-dissolving wall process in channels with the same geometry as those used for the experimental nanofiltration.

The mass transfer coefficient is generically defined as the proportional constant between the diffusion mass flux of the solute, $j_A$, and a defined concentration difference, as expressed by equation (2-15). Accordingly, the mass transfer coefficient of the non-suction mass transfer process was calculated by the following definition

$$k_{c,0} = \frac{j_A}{\rho \Delta w_{LNwb}} \tag{4-23}$$

The $j_A$ value was determined integrating $D_{AB}\frac{\partial(\rho w)}{\partial z}$ along the membrane surface of each region, while $\Delta w_{LNwb}$ is the logarithmic mean difference (Bird et al. 2007) for the solute mass fraction between the membrane surface and the bulk solution at the inlet and outlet of each section, as defined by

$$\Delta w_{LNwb} = \frac{\left(w_m^{in} - w_b^{in}\right) - \left(w_m^{out} - w_b^{out}\right)}{ln\left(\frac{\left(w_m^{in} - w_b^{in}\right)}{\left(w_m^{out} - w_b^{out}\right)}\right)} \tag{4-24}$$

Once $k_{c,0}$ for each channel section (or for the whole channel) is determined, one can predict nanofiltration data using the algorithm shown in Figure 4-13. Briefly, the algorithm consists of setting for each channel geometry the membrane properties ($R_a$ and $P_w$), the solute properties ($w_b^{in} = w_f$ and $C$), the inlet flow rate ($Q_{in}$), and the proper $k_{c,0}$. Then, the solute concentration at the membrane and in bulk are determined by guessing an initial $J_v$ value and iterating over the series of equations, which quantifies the system, until the difference between the $\Gamma$ calculated by equations (4-2) and by (4-6) is smaller than a defined $\varepsilon$ value (Figure 4-13). The calculated parameters at the exit of the section are then used as inputs for the calculations of the subsequent section. In addition to the previous equations, two other equations are necessary to run the algorithm. From a mass balance to the given section one determines the value of the average solute bulk mass fraction at the exit of the section, $w_b^{out}$. Considering that $\rho$ is constant, then

$$w_b^{out} = \frac{J_v A_m w_p - Q^{in} w_b^{in}}{J_v A_m - Q^{in}} \tag{4-25}$$

where $A_m$ is the membrane area of section. In the algorithm, the solute bulk mass fraction is replaced by its logarithmic mean defined in the equation (4-20). Additionally and admitting that the solution density is constant, the definition of the apparent rejection, defined in equation (2-6) is replaced by

$$R_a = \frac{w_f - w_p}{w_f} \tag{4-26}$$

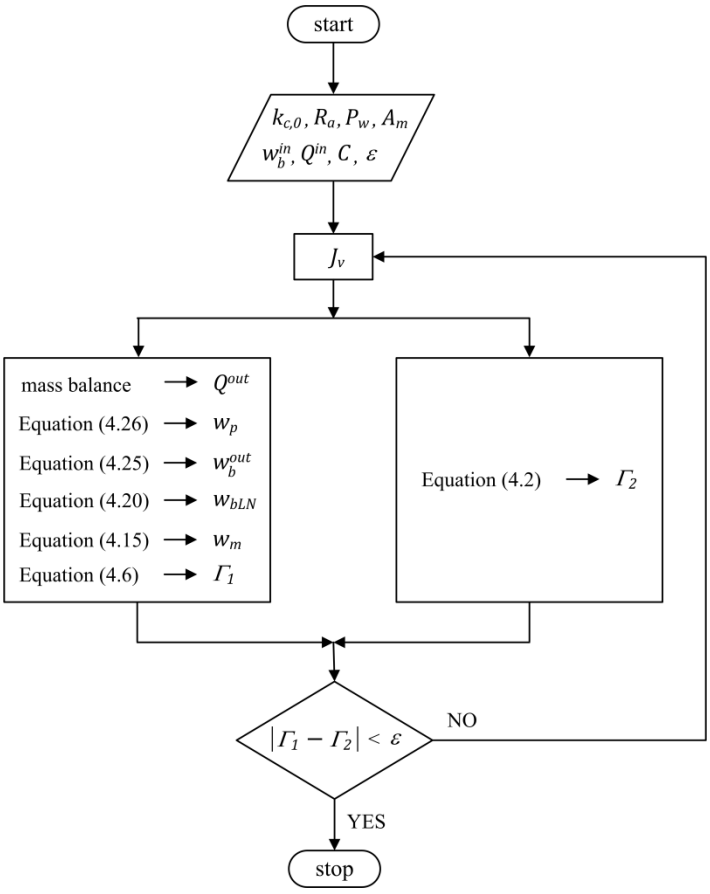


Figure 4-13 – Algorithm to calculate $J_v$, $w_m$ and $w_b$ given $k_{c,0}$, given the membrane and solution properties. Adapted from (Completo et al. 2016).

## 4.5 Results and discussion

The results and discussion presented in this section are grouped into five parts. First, the flows in slit channels are characterized using the micro-PIV technique (section 4.5.1) which is followed by the visualization of the CP phenomena using the HI technique (section 4.5.2). Then it will be discussed the validity of the CFD simulations based on the experimental data (section 4.5.3). Considering that the CFD simulations are valid, it will be discussed the effect of the channel geometry on the velocity and solute concentration field patterns with special focus on its periodicity (section 4.5.4). Finally, it will be demonstrated that the developed hybrid method is valid to predict nanofiltration data for scenarios where low Reynolds and ribbed-wall channels are used (section 4.5.5).

### 4.5.1 Characterization of the flows within TFF slits

Slits are channels in which the width-to-height ratio is large and, therefore, the flow can be considered mainly two-dimensional. Micro-PIV was used to assess the flow structures in

open and ribbed slit channels and to validate the part of the CFD model that deals solely with the hydrodynamics of the flows. For that CFD results were compared with the corresponding experimental flows inside impermeable slits, both in the open and ribbed channels configurations.

In open slit channels, the velocity profile in the $xz$-plane should be parabolic. This is what was verified both experimentally (Figure 4-14) and by CFD simulations (not shown here). In Figure 4-14a it is shown the reconstruction of a quasi-3D profile by superposing velocity profiles obtained in the $xz$-plane at distinct $y$ distances from the lateral window of the cell. The velocity $U_x(z)$ is the velocity magnitude in the $x$-direction as function of the $z$-location in the channel; since in open channels the flow is two-dimensional then $\boldsymbol{U_x} = \boldsymbol{U}$. It is clear that the effect the velocity magnitude stabilizes for distances larger than 1 mm from the lateral window, which means that the lateral wall effect is insignificant in slits. Since the velocimetry data was obtained at a station 14 cm downstream the entrance of the channel, one can assume that the flow is developed in the $x$-direction.

There is a good agreement between the experimental results and the CFD (or analytical) predictions as shown in Figure 4-14b. The data in this figure refers to the velocity of the fluid at mid-width of the channel and it was obtained through the top window of the slit, overlapping the average velocity at several $z$-planes.

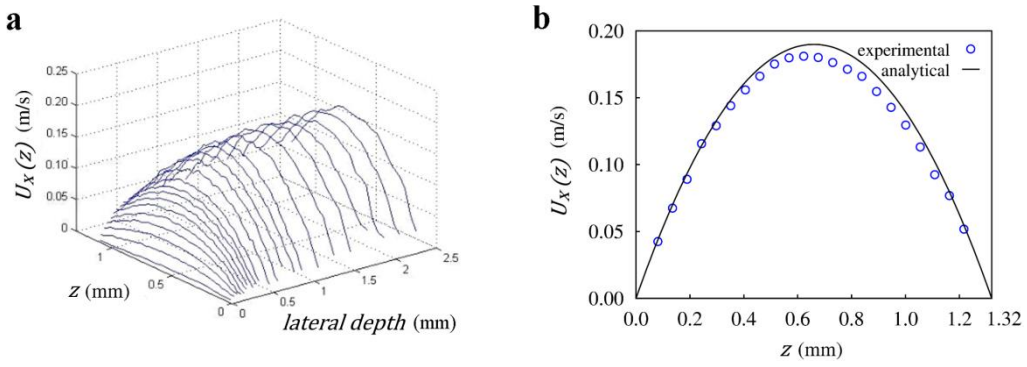


Figure 4-14 – Experimental micro-PIV velocity profiles of water flows inside an open channel at $Re_h$ = 160: a) quasi-3D reconstruction of the velocity field using velocity profiles acquired through the lateral window; b) 2D reconstruction of the profile at channel mid-width using profiles acquired through the top window.

The insertion of ribs inside the channel changes the flow structure, which has to stretch and compress due to the geometrical constraints. Unless the $Re_h$ is too low (creeping flow), recirculation zones appear. For instance, Figure 4-15 shows as the recirculation zone grows when the $Re_h$ is increased. The velocity maps refers to a location between 2.0 mm and 2.9 mm downstream a filament, as sketched in Figure 4-15a. Since standard micro-PIV produces only two-dimensional velocity maps, the vectors $\boldsymbol{U_{xz}}$ depicted in the figure are the $xz$-components of vector $\boldsymbol{U}$ and its magnitude is represented by the color scale. The solid lines are streamlines

placed in the map for clearer visualization of the flow structure. For low $Re_h$, as in Figure 4-15b, the recirculation zone does not reach the visualization area, since all the velocity vectors point in the bulk velocity direction. However, as the $Re_h$ is increased the recirculation zone expands and the reattachment point gets closer to the upstream filament, as can be seen in the maps of Figure 4-15c, Figure 4-15d and Figure 4-15e. It is clear that micro-PIV is a very visual technique capable to show flow structure both qualitatively and quantitatively.

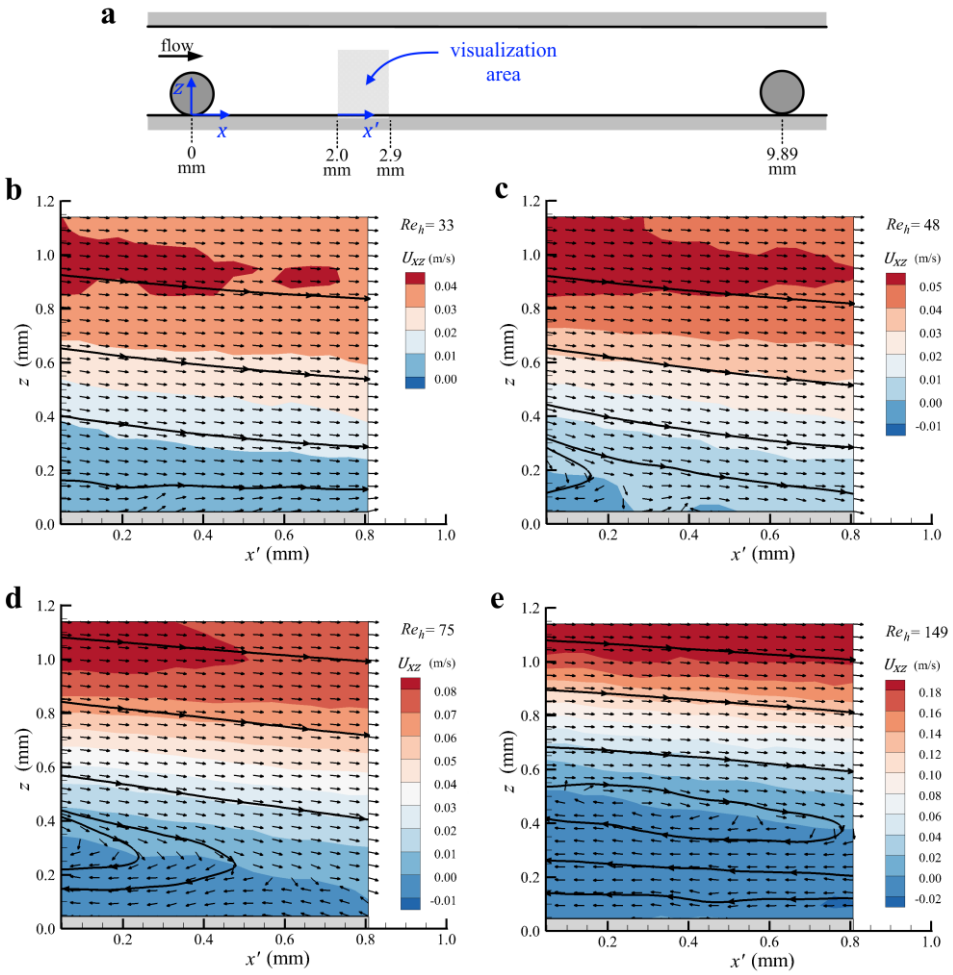


Figure 4-15 – Effect of $Re_h$ on the velocity field obtained for water flows at a specific station between 2.0 mm and 2.9 mm downstream a transverse circular rib: a) location of the acquired maps; b) velocity map for $Re_h$ = 33; c) velocity map for $Re_h$ = 48; d) velocity map for $Re_h$ = 75; e) velocity map for $Re_h$ = 149. The maps were acquired at the focal plane $y$ = 1.10 mm.

In order to validate the CFD model for the flows inside ribbed channels, representative numerical results were compared with the corresponding experimental ones obtained using micro-PIV, as shown in Figure 4-16. The experimental velocity profiles of this figure were reconstructed by superposition of the average velocity at different $x$-locations obtained from the velocity maps in the $xy$-plane acquired at the mid-width of the channel, through its top window, at distinct $z$-depths. Figure 4-16a shows the locations of each of the velocity profiles, which are indicated as the $x'$-position from that specific tranverse circular rib. The results show that there

is good agreement between CFD and micro-PIV results, both in terms of the shape and magnitude of the velocity profile. Therefore, the hydrodynamics numerical model, and its applications by the software, can be further complemented by mass transfers models to predict nanofiltration and dissolving-wall processes. The use of such mass transport models will be validated in section 4.5.3 by experimental solute concentration data, obtained by HI, which are shown in the following section.

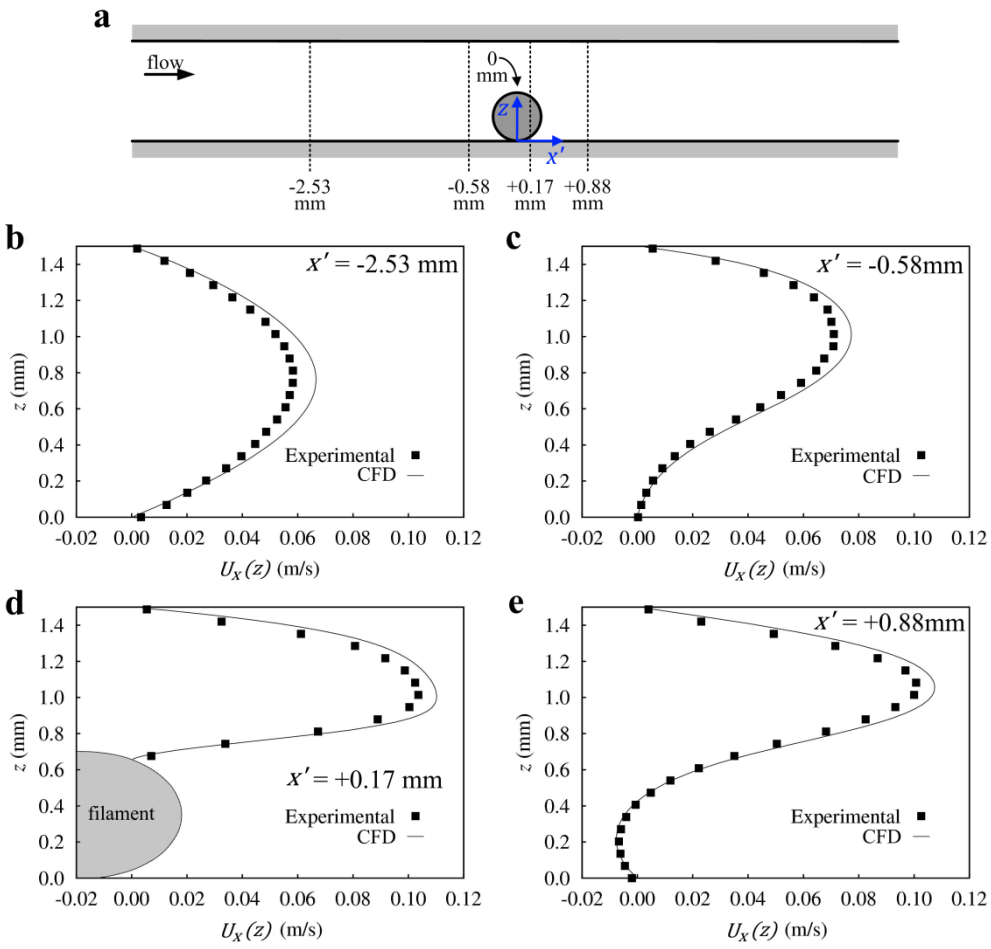


Figure 4-16 – Comparison between experimental and CFD velocity data for water flows ($Re_h$ = 75) obtained at several $x$-positions around a transverse circular rib at channel mid-width: a) location of each velocity profile; b) profiles at $x'$ = -2.53 mm; c) profiles at $x'$ = -0.58 mm; d) profiles at $x'$ = +0.17 mm; e) profiles at $x'$ = +0.88 mm.

### 4.5.2 Visualization of concentration polarization by holographic interferometry

In this section, experimental data obtained using the holographic interferometry technique are presented to show that in nanofiltration processes the CP phenomenon occurs. Moreover, the magnitude of the CP phenomenon evolves along the permeation time and depends on the flow conditions and channel geometry. The magnitude of the concentration polarization is given by the number of fringes in the interferogram, while the thickness of the concentration boundary layer can be estimated by the region of the channel occupied by the fringes.

**Temporal evolution of the concentration polarization**

The evolution of the CP layer with time in NF processes can be assessed acquiring interferograms at distinct time instants. The temporal evolution of the CP was monitored in two scenarios: for the case when the needle valve, downstream the nanofiltration TFF cell, was completely closed (resembling a dead-end process and defined as $Re_h$ = 0) and for the case when the Reynolds number at the inlet was set to $Re_h$ = 5 (corresponding to $U_0$ = 0.2 cm/s).

Figure 4-17 shows a series of interferograms, obtained between the initial time instant of the permeation ($t$ = 0 s) and $t$ = 60 min, for the nanofiltration of a 2 g/L $K_2SO_4$ aqueous solution, at $\Delta p_m$ = 8 bar and $Re_h$ = 5 inside the open channel. From this figure, several phenomena are evident: i) the number of fringes increases over time (in this case from zero at $t$ = 0 up to 6 at $t$ = 60 min); ii) the height of the CP layer also increases over time, even when the number of fringes remains unchanged over a large period of time (compare the sequence from Figure 4-17f to Figure 4-17j); iii) the CP phenomenon is triggered immediately after the beginning of the nanofiltration, as there are already two fringes at t = 10 s.

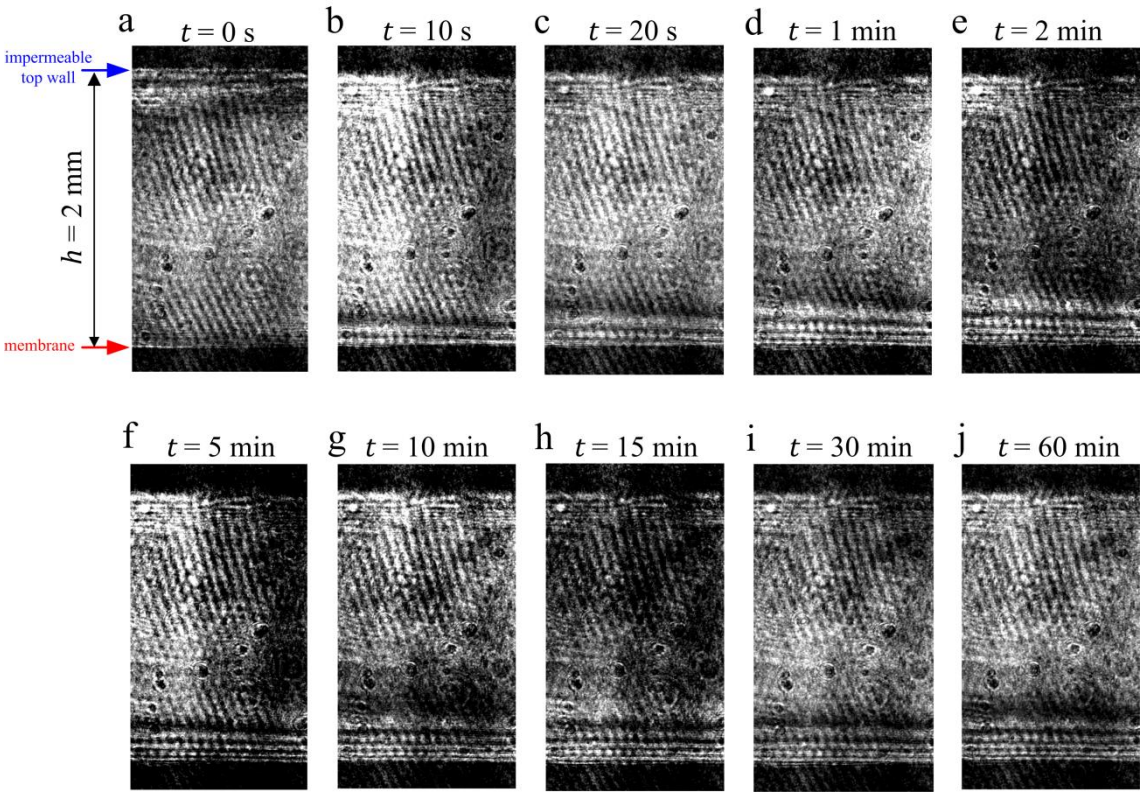


Figure 4-17 – Holographic interferograms showing the temporal evolution of the nanofiltration of a $K_2SO_4$ aqueous solution ($c_f$ = 2 g/L) at $\Delta p_m$ = 8 bar and $Re_h$ = 5 inside an open channel. The interferograms were captured at a region 56 mm and 57 mm downstream the beginning of the membrane and at distinct time instants from the start of the NF process: a) initial time; b) 10 s; c) 20 s; d) 1 min; e) 2 min; f) 5 min; g) 10 min; h) 15 min; i) 30 min; j) 60 min.

Despite not clearly visible, since each raw image of Figure 4-17 was cropped, there is another feature observed in the acquired interferograms that is characteristic of the permeation process in open channels (without buoyancy effects): in a small region, the fringes are parallel to the membrane. The same horizontal fringe pattern has already been observed for UF, NF and RO by other authors, both in TFF (Fernández-Sempere et al. 2010; Rodrigues et al. 2013; Salcedo-Díaz et al. 2014) and dead-end processes (Fernández-Sempere et al. 2006; Fernández-Sempere et al. 2007; Fernández-Sempere et al. 2009; Fernández-Sempere et al. 2012). The fact that the fringes are parallel to the membrane surface in the whole region of the optical window, i.e. between 52 and 67 mm from the beginning of the porous support, indicates that the changes in the solute concentration are small in this region. In fact, although the CP layer develops along the channel, as was experimentally observed by other authors (Salcedo-Díaz et al. 2014), the region covered by the optical access window is too narrow to capture enough distortion of the fringes.

In Figure 4-18 the interferograms obtained for practically the same conditions of those of the Figure 4-17 are shown, the only difference being the fact that the needle valve is now closed downstream the cell. Thus, the system works nearly as a dead-end process. In such conditions, there are two main differences in the interferogram series of the experiments at $Re_h$ = 0 (Figure 4-18) when compared to those obtained for $Re_h$ = 5 (Figure 4-17). First, for the same acquisition moment, there are more fringes in the interferograms at $Re_h$ = 0 than in the corresponding ones at $Re_h$ = 5, indicating higher concentration in the former. The rise of the concentration in the filtration chamber for $Re_h$ = 0 is expected since no concentrate stream leaves the cell and thus, the solute accumulates at a greater extent upstream the membrane. However, as one will see later, the obtained higher concentration in the concentrate is at an expense of a poorer quality of the permeate (lower solute rejection). The second difference, and probably the most important one, is that unlikely for TFF flow conditions (Figure 4-17), in the scenario of $Re_h$ = 0 the number of fringes did not stabilize during the 60 minutes of the experiment. At $Re_h$ = 0 the number of fringes detected at $t$ = 60 min was 24, while for the nanofiltration at $Re_h$ = 5 the number of fringes at the same moment was 6 (its maximum reached in less than 5 min).

The introduction of transverse ribs on the top wall of the channel (top cavity geometry) modifies the fringe pattern in the interferograms, as can be verified in Figure 4-19 that represents the nanofiltration process of a 2 g/L $K_2SO_4$ aqueous solution ($\Delta p_m$ = 8 bar, $Re_h$ = 5), monitored during 30 minutes. It is clear that the the fringes are no longer parallel to the membrane surface, but they bend and stretch in the region near the ribs. This indicates that the thickness of the CP layer is thinner in that region.

Despite not being totally visible in all the individual images, it also looks like that the number of fringes is smaller in the vicinity of the rib than in the middle of the zone between the

ribs. For instance, while the interferograms for $t$ > 10 min present 4 fringes in the middle region, they look to exhibit only 2 or 3 fringes (not clear in the images) below the rib. Thus, besides the CP layer being thinner below the rib, the solute concentration at the membrane surface might also be lower than in the middle region.

Another evident distinction, when compared with the interferogram obtained for the open channel, is the fact that, for the same elapsed time, the number of fringes is smaller: 4 fringes (at $t$ = 30 min) for the top cavity channel and 6 fringes for the open channel. Therefore, the concentration polarization has a smaller magnitude when using the top cavity channel than when using the open channel.

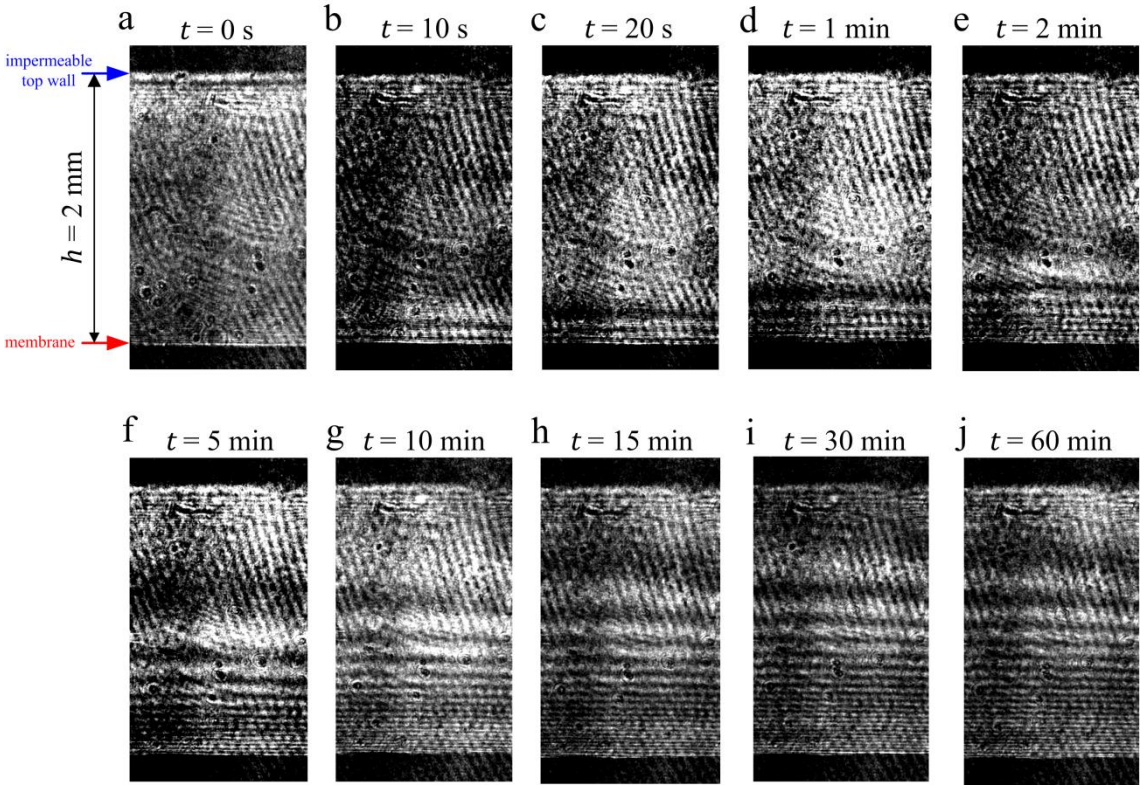


Figure 4-18 – Holographic interferograms showing the temporal evolution of the nanofiltration of a $K_2SO_4$ aqueous solution ($c_f$ = 2 g/L) at $\Delta p_m$ = 8 bar and $Re_h$ = 0 (closed needle valve) inside an open channel. The interferograms were captured at a region 56 mm and 57 mm downstream the beginning of the membrane and at distinct time instants from the start of the NF process: a) initial time; b) 10 s; c) 20 s; d) 1 min; e) 2 min; f) 5 min; g) 10 min; h) 15 min; i) 30 min; j) 60 min.

To the best knowledge of the author, this is the first time that the CP phenomenon was visualized in permeation processes using top cavity channels by holographic interferometry technique. All the previous HI works performed by other authors, dealing with permeation processes, were conducted using solely open channels. Interferometry has previously been used to monitor mass transfer processes inside top cavity channels but for electrochemical processes (Fischl et al. 1985), where, as in the present work, it was observed that the inclusion of ribs

inside the channel causes changes in the solute concentration pattern when compared with the open channel case.

The number of fringes in the interferogram and, thus, the magnitude of the concentration polarization depends on several factors including the Reynolds number, the transmembrane pressure, the feed solute concentration and the geometry of the channel where the permeation occurs. The effects of these factors can be seen in Figure 4-20 for some illustrative cases, where the number of fringes is plotted as function of time.

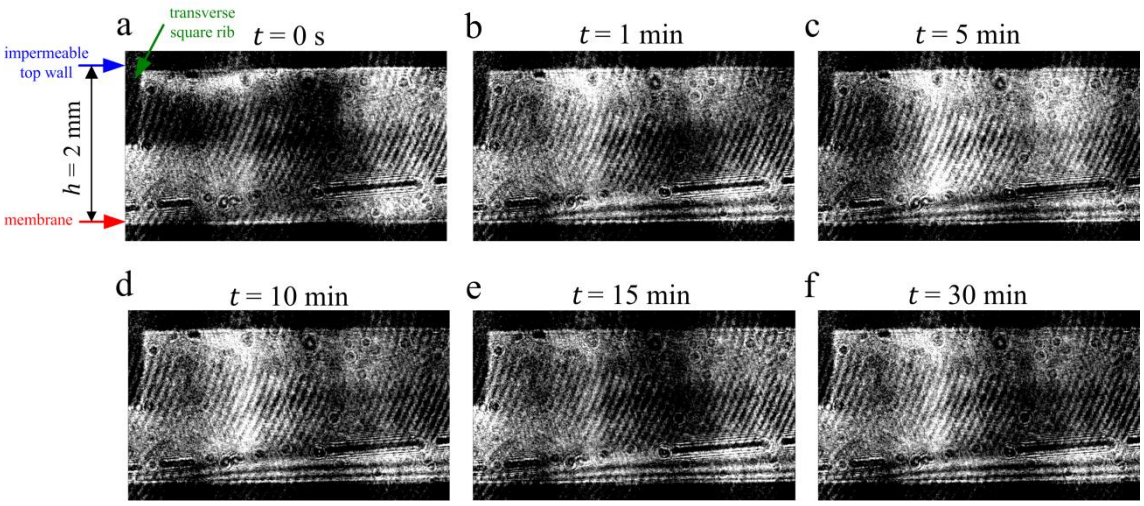


Figure 4-19 – Holographic interferograms showing the temporal evolution of the nanofiltration of a $K_2SO_4$ aqueous solution ($c_f$ = 2 g/L) at $\Delta p_m$ = 8 bar and $Re_h$ = 5 inside a top cavity channel. The interferograms were captured between the 7th and 8th rib (at a region between 53 mm and 61 mm downstream the beginning of the membrane) and at distinct time instants from the start of the nanofiltration: a) initial time; b) 1 min; c) 5 min; d) 10 min; e) 15 min; f) 30 min.

From Figure 4-20a, it is clear that the number of fringes for TFF processes reach rapidly a plateau, whereas for the "dead-end" process ($Re_h$ = 0) the number of fringes increases continuously. Figure 4-20b shows that, for the same conditions, the number of fringes increases as the transmembrane pressure increases. This is an expected result since higher pressures lead to higher permeate flux and, since back-diffusion is a slow process, the solute concentration in the vicinity of the membrane increases by the dominating convection mechanism.

Several aspects should be taken into consideration when analysing the effect of the feed concentration on the number of fringes, as depicted in Figure 4-20c. It should be reminded that each fringe represents an increment in the solute concentration and it is not a quantitative measure of the CP modulus. Thus, although the nanofiltration of the 4 g/L solution produces a larger number of fringes, the CP modulus of the nanofiltration of the 2 g/L solution is higher. This can be explained by the fact that the 4 g/L solution has a higher osmotic pressure and, therefore, the permeate flux is lower, resulting in a smaller relative increase of the solute concentration and, thus, of the CP phenomenon. This result suggests that although the concentration on the membrane increases as $c_f$ increases, the rise in the CP modulus is slower.

This same behaviour has already been verified by other authors using CFD simulations (de Pinho et al. 2002).

Finally, it is clear that the use of the top cavity channel diminishes the CP effects, resulting in lowering of the number of fringes detected in the interferogram, as can be seen in Figure 4-20d. This behaviour is related to the increase of the average velocity inside the channel and with the change of the flow structure, yielding an increase of the cleansing wall shear stresses.

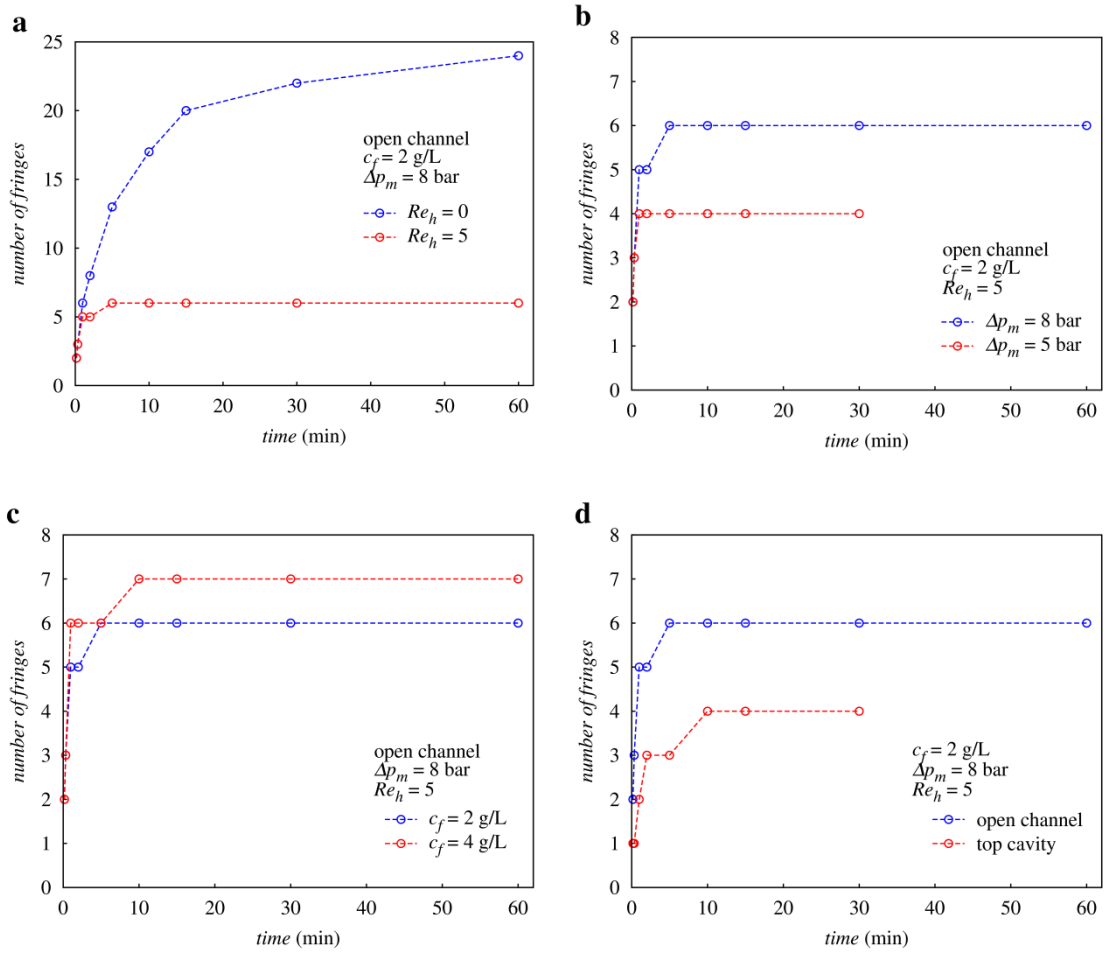


Figure 4-20 – Temporal evolution of the number of fringes, detected in the holographic interferograms, for the nanofiltration of a $K_2SO_4$ aqueous solution. Comparisons between: a) no flow ($Re_h$ = 0) versus flow at $Re_h$ = 5 ($U_0$ = 0.20 cm/s), inside the open channel, for $c_f$ = 2 g/L and $\Delta p_m$ = 8 bar; b) different transmembrane pressures ($\Delta p_m$ = 5 bar versus $\Delta p_m$ = 8 bar), for $c_f$ = 2 g/L and flow at $Re_h$ = 5 inside the open channel; c) different $K_2SO_4$ concentrations ($c_f$ = 2 g/L versus $c_f$ = 4 g/L), for $\Delta p_m$ = 8 bar and flow at $Re_h$ = 5 inside the open channel; d) different channel geometry (open channel versus top cavity channel), for $c_f$ = 2 g/L, $\Delta p_m$ = 8 bar and flow at $Re_h$ = 5.

Above a certain $Re_h$ threshold value, the number of fringes appears to stabilize after some time, as it can be seen in Figure 4-17 and in the Figure 4-20. However, the thickness of the CP layer increases with time, despite the number of fringes remains the same. This behaviour is clearly visible by plotting the distance from the first fringe (from the bulk) to the membrane surface, $z_{1f}$, as function of the nanofiltration time, as shown in Figure 4-21. After the initial

period, where both the number of fringes and $z_{1f}$ increase, the thickness of the CP layer continues to grow even that is not detected by any change on the number of fringes (Figure 4-20c). For the conditions of Figure 4-21 (nanofiltration of a 2 g/L $K_2SO_4$ aqueous solution at $\Delta p_m$ = 8 bar and $Re_h$ = 5), $z_{1f}$ increases from 0.315 mm, at 10 min, to 0.355 mm, at 60 min, while the number of fringes remained the same (6) in that period. These results agree well with the ones shown in section 3.5.3 for the assessment of CP phenomena by measuring the flux decline over time. In that part of the work it was verified that, for the nanofiltration of binary solutions in TFF processes, the major part of the permeate flux reduction occurs in the first 10 minutes and that the further decrease is very slow.

Despite the continuous increase of the CP over time, especially at low $Re_h$, the time considered necessary to reach steady-state for the experiments at $Re_h \geq 5$ was 10 minutes. Therefore, in the study to assess the effect of the flow rate on the CP phenomenon, the interferograms were acquired at $t$ = 10 min, for $Re_h \geq 5$, and at $t$ = 30 min, for $Re_h < 5$.

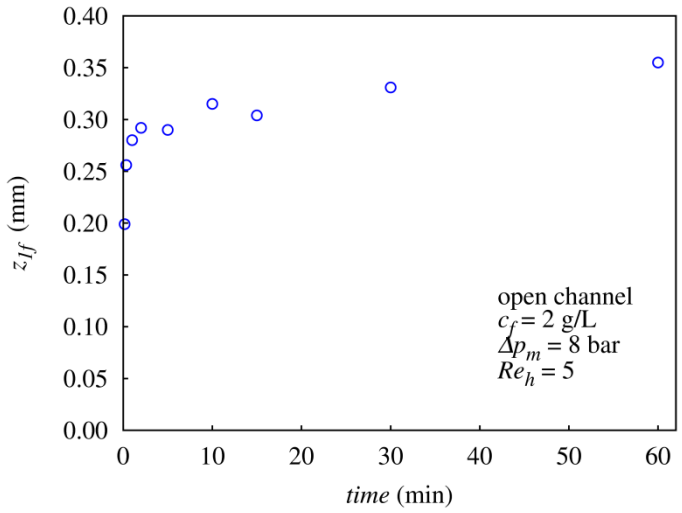


Figure 4-21 – Temporal evolution of the $z$-location of the first fringe, $z_{1f}$, detected in the interferograms for the nanofiltration of a $K_2SO_4$ aqueous solution ($c_f$ = 2 g/L) at $\Delta p_m$ = 8 bar and $Re_h$ = 5 inside an open channel.

**Effect of the Reynolds number on the concentration polarization**

The effect of the Reynolds number on the concentration polarization phenomenon is clearly visible in the interferogram series shown in Figure 4-22, for the open channel, and in Figure 4-23, for the top cavity channel. The number of fringes and the height of the concentration boundary layer decreases as the Reynolds number increases. Similar results have already been obtained by other authors both for NF (Rodrigues et al. 2013) and for RO (Salcedo-Díaz et al. 2014) processes.

The results have also shown that better NF performance is obtained using the top cavity channel, rather than the open channel. In fact, for the same conditions (equal $c_f$, equal $Re_h$ and

equal $\Delta p_m$) the number or fringes is smaller for top cavity channels (compare Figure 4-24a and Figure 4-24b). In addition, not only the permeate produced by the top cavity channel is of higher quality, i.e. of higher $R_a$ (Figure 4-24c), but it is also produced at a higher rate, especially at low $Re_h$ (Figure 4-24d). This is of particular importance if one intends to use NF in microfluidic membrane devices, since at that scale the $Re_h$ is usually low.

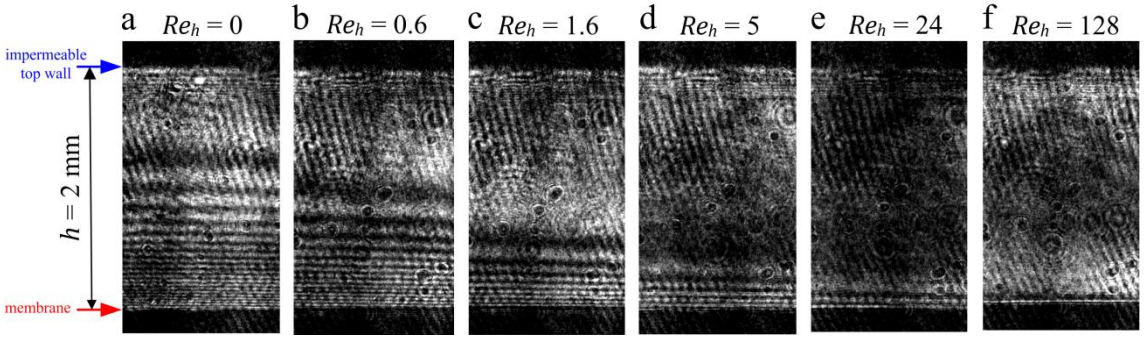


Figure 4-22 – Holographic interferograms showing the reduction of the CP phenomenon as the Reynolds number increases, for the nanofiltration of a $K_2SO_4$ aqueous solution ($c_f$ = 2 g/L) at $\Delta p_m$ = 8 bar inside the open channel. The interferograms were captured at a region between 56 mm and 57 mm downstream the beginning of the membrane and at distinct flow conditions: a) no flow ($Re_h$ = 0); b) $Re_h$ = 0.6; c) $Re_h$ = 1.6; d) $Re_h$ = 5; e) $Re_h$ = 24; f) $Re_h$ = 128.

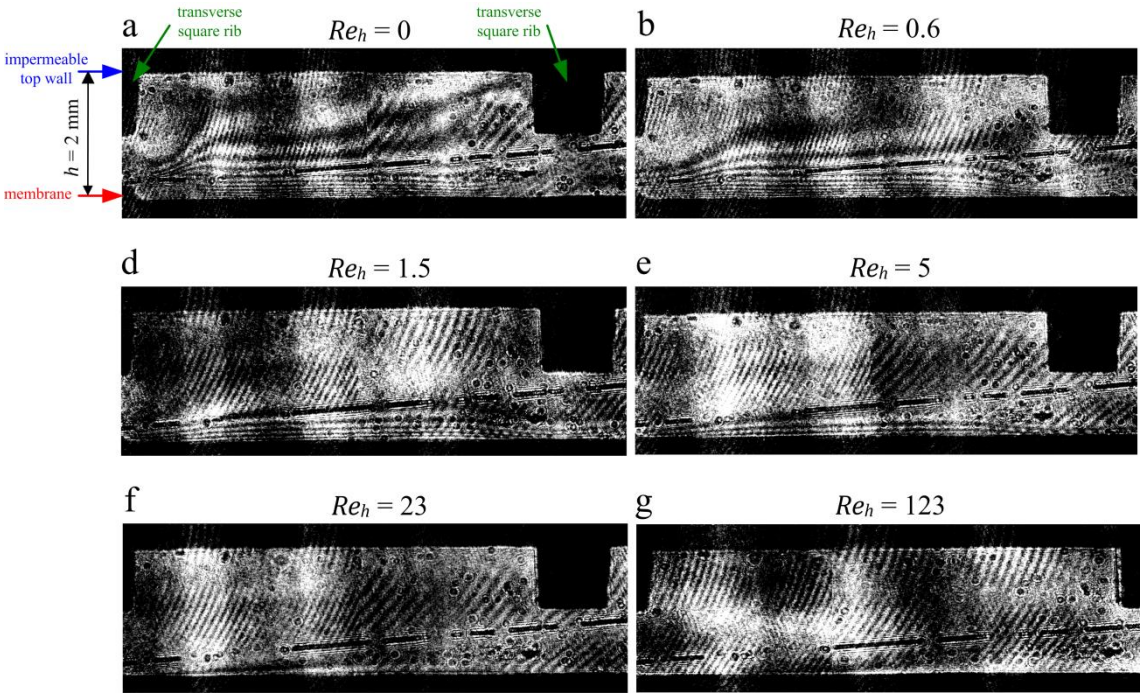


Figure 4-23 – Holographic interferograms showing the reduction of the CP phenomenon as the Reynolds number increases, for the nanofiltration of a $K_2SO_4$ aqueous solution ($c_f$ = 2 g/L) at $\Delta p_m$ = 8 bar inside the top cavity channel. The interferograms were captured at a region between the 7$^{th}$ and 8$^{th}$ ribs (placed between 53 mm and 61 mm downstream the beginning of the membrane) and at distinct flow conditions: a) no flow ($Re_h$ = 0); b) $Re_h$ = 0.6; c) $Re_h$ = 1.6; d) $Re_h$ = 5; e) $Re_h$ = 24; f) $Re_h$ = 128.

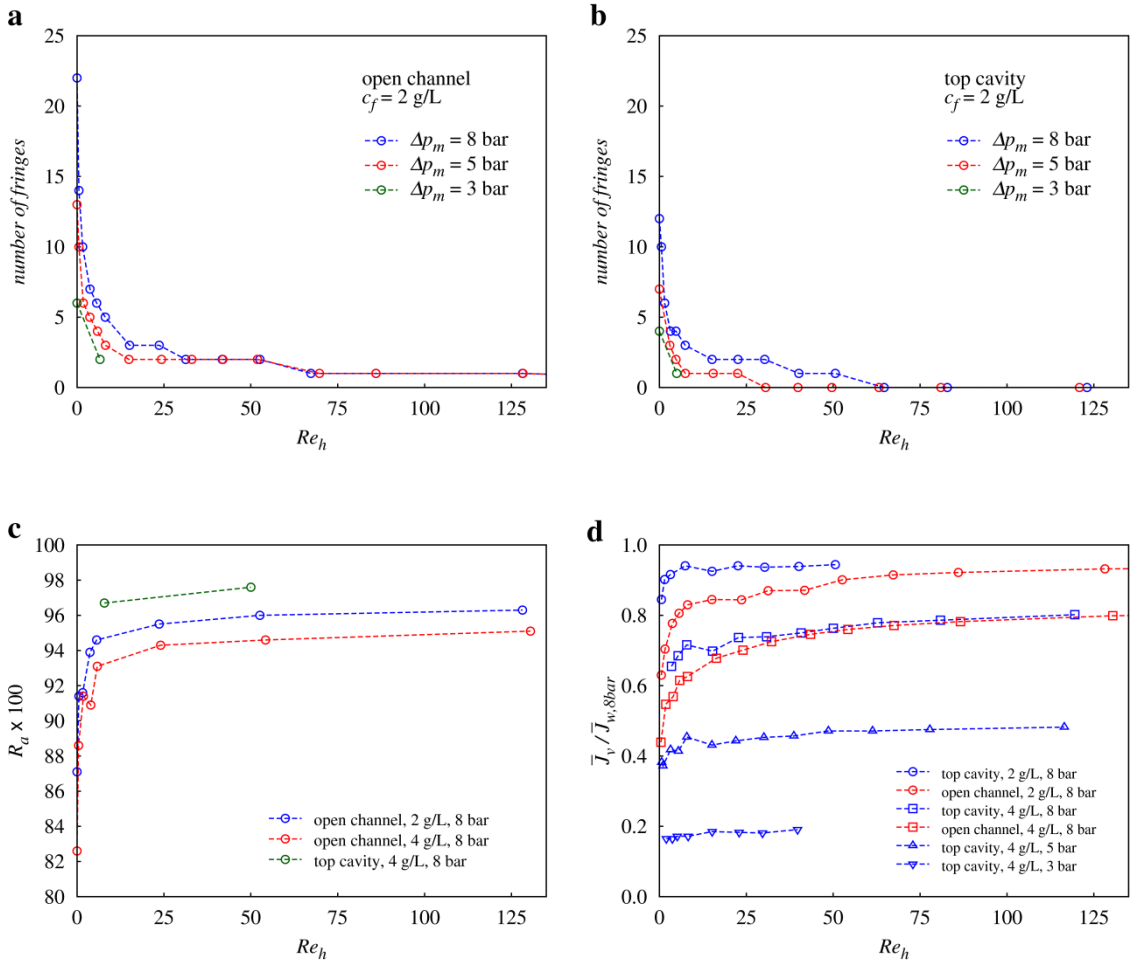


Figure 4-24 – Influence of the Reynolds number on the CP phenomenon in the nanofiltration of $K_2SO_4$ aqueous solutions, given in terms of: a) number of fringes detected in the nanofiltration in the open channel; b) number of fringes detected in the nanofiltration in the top cavity channel; c) apparent rejection; d) $\bar{J}_v/\bar{J}_w$ ratio.

It is also interesting to verify that, for low $Re_h$, despite the fact that there is a significant difference in the number of fringes obtained at distinct $\Delta p_m$ (see Figure 4-24a), the difference in terms of the distance from the first fringe to the membrane surface is not so significant, as can be seen in Figure 4-25. This suggests that, although occupying almost the same portion of the channel height, the concentration gradient gets sharper as the pressure increases. However, it must be emphasized that the plot of Figure 4-25 contains data only for two values of $\Delta p_m$ and even those are relatively near one another (5 bar and 8 bar).

In section 4.5.1 it was shown that momentum boundary layer develops from the wall up to the middle of the channel, since the viscosity effect (momentum diffusivity) actuates on both top and bottom walls, resulting in parabolic velocity profiles. For high $Sc$ numbers, as in liquids, the ratio between mass and momentum diffusivities is low and for that reason the concentration boundary layer develops slower. Thus, for medium-to-high $Re_h$, the concentration boundary layer occupies only a small portion of the channel height, although the hydrodynamics is already full developed. For $Re_h$ > 50 the concentration boundary layer spans over less than 15% of the channel height, as depicted in Figure 4-25. However, as $Re_h$ decreases the portion of the

channel height covered by the concentration boundary layer rises, which is in accordance with prediction model defined in equation (2-9), which states that the thickness of the concentration boundary layer increases as the velocity of the liquid decreases. There is a gap between the distance of the first fringe to the membrane surface, $z_{1f}$, and the thickness of the concentration boundary layer, $\delta_D$, given by equation (2-9). The reason is the fact that the former corresponds to the location where the solute concentration has risen by $\Delta w$ from the bulk concentration, as defined in equation (4-9), while the later corresponds to the classical definition of $\delta_D$, which is the location where the diference $(c_m - c)$ corresponds to 99 % of the difference $(c_m - c_b)$.

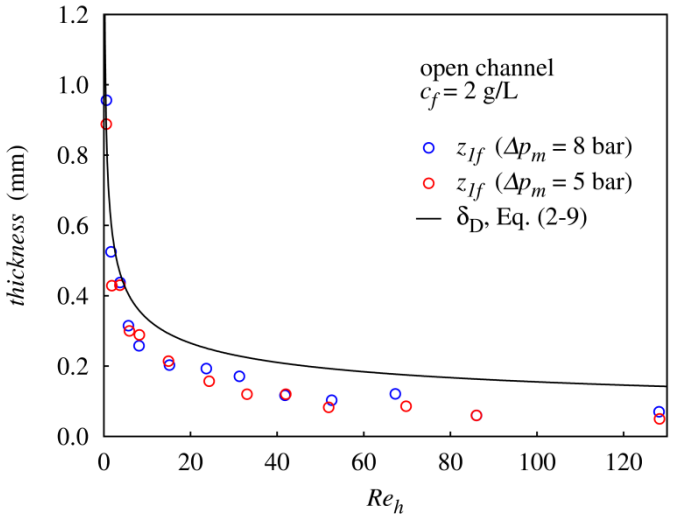


Figure 4-25 – Evolution of the $z$-location of the first fringe detected in the interferograms and of the thickness of the predicted concentration boundary layer, as function of the Reynolds number, in the nanofiltration of $K_2SO_4$ aqueous solutions.

### 4.5.3 Use of HI data to validate CFD simulations

In order to show that CFD simulations can predict nanofiltration performance in subsequent theoretical studies, it is advisable to validate the CFD model, described in section 4.4. The validation of the CFD model was done by comparing solute concentration profiles obtained from the experimental interferograms with the corresponding ones obtained from numerical simulations.

The simulated flow with highest inlet velocity had $Re_h \approx 125$, which corresponds to $Re_{dh} \approx 220$. In the literature there are no works on the effect of 2D square ribs on the transition from steady laminar to unsteady flows. The most similar study was performed by Santos *et al.* (Santos et al. 2007) where 3D domains with transverse and longitudinal square ribs were used. They have concluded that for spacers with $l_f/h \approx 4$ the critical $Re_h$ is above 150. Since longitudinal ribs have small influence in the flow, it is possible to admit that this value is valid for 2D flows. Moreover, the used Reynolds range is considerably below the critical Reynolds

for circular ribs which is above $Re_h \approx 300$ (Schwinge et al. 2003; Ahmad & Lau 2006; Fimbres-Weihs et al. 2006), both for cavity and zigzag configurations. Therefore, it is safe to assume that the flows under the studied conditions in this work are in steady laminar regime.

The experimental and numerical concentration profiles, obtained at a station located between the 7th and 8th ribs, are displayed in Figure 4-26 for three scenarios. Each scenario contains the three figures on each column, including, from top to bottom: the experimental interferograms; the velocity streamlines and isoconcentration lines obtained by CFD; and the comparison of concentration profiles in the $z$-direction at the middle of the section between the two consecutive ribs.

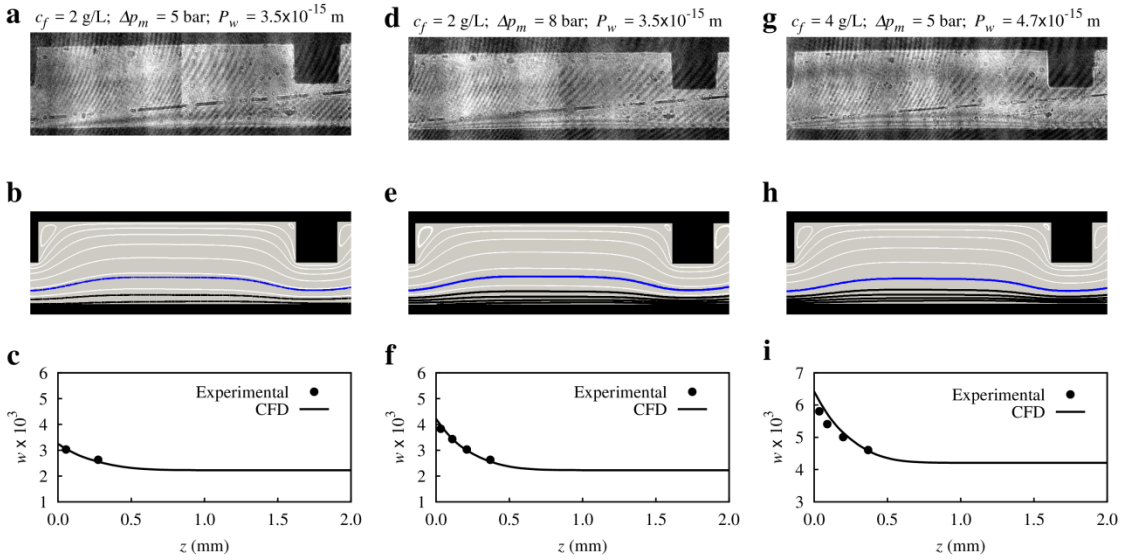


Figure 4-26 – Comparison of experimental and CFD solute concentration fields for the nanofiltration of $K_2SO_4$ aqueous solutions, at $Re_h$ = 5, in a region between the 7th and 8th ribs. From top to bottom are displayed: the interferogram; the velocity and concentration fields obtained numerically (white lines: velocity streamlines; blue lines: isoconcentration lines where $w = 1.01 \cdot w_f$; black lines: isoconcentration lines matching the solute concentration in the interferogram fringes); and the concentration profiles obtained in the $z$-direction at the mid-point between ribs.

The inlet liquid velocity of the scenarios of Figure 4-26 corresponds to $Re_h$ = 5, while the remaining operating conditions are referred at the top image. The difference of the water permeability (given by $P_w$) is due to the change of membrane piece between the second and third scenarios. In spite of that, it is notorious that the CFD model produced results similar to those of the experimental interferograms, both in terms of the shape and the magnitude of the solute concentration profiles. No correction was applied to the solute concentration calculated using equation (4-9) since the ratio $\Delta n_{mb}/\delta_D$ is smaller than 1 m$^{-1}$, as proposed by other authors (Rodrigues et al. 2013).

Overall, there is a good agreement between the experimental results and those yielded by the adopted CFD model to simulate the NF of binary aqueous solutions. This gives confidence to further use the CFD model described in section 4.4 on studies related with the influence of

the channel geometry on the permeation performance (section 4.5.4) and to verify that the hybrid method used to determine permeation data is valid for low Reynolds numbers and ribbed channels (section 4.5.5).

### 4.5.4 Effect of channel geometry on the velocity and concentration fields and assessment of periodic conditions

The presence of ribs inside a channel changes the flow field from the typical parabolic shape for open channels, in the laminar regime, to a flow structure where flow separation can exist, as in the experimental velocity maps obtained by micro-PIV (section 4.5.1). Flow separation occurs whenever there is an adverse pressure gradient, for instance due to the expansion created downwards the rib, generating recirculation zones. Although there are recirculation zones before and after the geometrical constriction imposed by the rib, the latter are usually larger. In addition, the velocity magnitude in the vicinity of the rib is much larger than in the region between two consecutive ribs. These patterns are confirmed by the CFD simulations performed in the present work. Figures 4-27, 4-28 and 4.29 shows the velocity fields for the flows ($Re_h$ from 0.8 to 124) inside channels where the nanofiltration of $K_2SO_4$ aqueous solutions is performed at the bottom wall, for the cavity top, bottom cavity and zigzag geometries, respectively[14]. It must be referred that the channel section shown in those figures lies between the 26$^{th}$ and the 28$^{th}$ ribs of a series of 30 ribs.

The obtained velocity maps shows that for low $Re_h$ the size of the recirculation zones is very small and the flow is approximately the same as the creeping flow. With the increase of $Re_h$ the recirculation zone immediately after the rib enlarges, and occupies the whole region between consecutive ribs in the scenario of $Re_h$ = 124 for the top cavity configuration (Figure 4-27e).

Due to the permeation process, there is a continuous loss of liquid to the permeate stream, resulting in the global decrease of the average velocity along the channel. The feed recovery decreases as $Re_h$ increases, and that is the reason why for the same location in the geometric constriction, near the ribs, the magnitude of the velocity approaches its maximum velocity in the channel as $Re_h$ increases. This can be seen by the fact that, in the previous figures, the red color becomes paler, near rib, as the $Re_h$ decreases.

In terms of hydrodynamics, the flow structures in top cavity and bottom cavity channels (Figure 4-27 and Figure 4-28, respectively) are similar, but symmetrical relatively to the longitudinal axis of the channel. For the studied geometries, the wall shear stress at the

[14] Only representative velocity vectors are shown; otherwise, showing all the vectors would turn the velocity maps illegible. The shown velocity fields refer only to the internal domain of the channel, the velocity at the membrane surface related to the permeate flux is being omitted.

membrane surface in the top cavity configuration is higher than in the bottom cavity configuration due to higher flow velocity at the constriction generated by the ribs opposite to the membrane. In the latter, the higher shear stress occurs on the top impermeable wall and not on the membrane[15].

The flow structure in the zigzag is to a certain extent a mix of the flow structures observed for the top and bottom cavity configuration. However, in the zigzag configuration, it is not possible to obtain recirculation regions covering the whole distance between consecutive ribs because the bulk flow must change its direction between consecutive ribs (Schwinge et al. 2002c).

Good agreement exists between the present CFD results and the ones obtained by other authors. Although many authors refer the use of squared ribs (Geraldes et al. 2002a; Song & Ma 2005; Ma & Song 2006; Ahmad et al. 2005; Ahmad & Lau 2006) only in the work of Geraldes and colleagues (Geraldes et al. 2002a) exhibits flow fields for a channel filled with squared ribs with a similar $l_f/h$ ratio (ca. 4).

The assumption that the flow structure in top cavity configuration is similar to the symmetrical of the flow structure in bottom cavity configuration allows comparing the results of the present work with the ones of Geraldes and colleagues (Geraldes et al. 2002a). In that work, it was verified that it is necessary a $Re_h$ between 100 and 200 for the recirculation downwards a rib to reach the next rib, preventing that way the flow reattachment. According to Figure 4-27e, for $Re_h$ = 124 the recirculation covers the entire region between two consecutive ribs. Thus, this results is in agreement with the findings of Geraldes and colleagues (Geraldes et al. 2002a).

On the other hand, one can compare the flow fields obtained in this work with the ones obtained by other authors using cylindrical ribs. Schwinge and colleagues (Schwinge et al. 2002c) showed that for steady laminar flow inside channels with cavity geometry with $l_f/h$ = 4 and $d_f/h$ = 0.5 the recirculation zone reaches the following rib for $Re_{dh}$ between 171 and 300. As said before, in the present work, at $Re_h$ = 124 (corresponding to $Re_{dh}$ = 220) the same behaviour is observed.

[15] It must be emphasized that these differences only happen since a single membrane surface was defined in the CFD model.

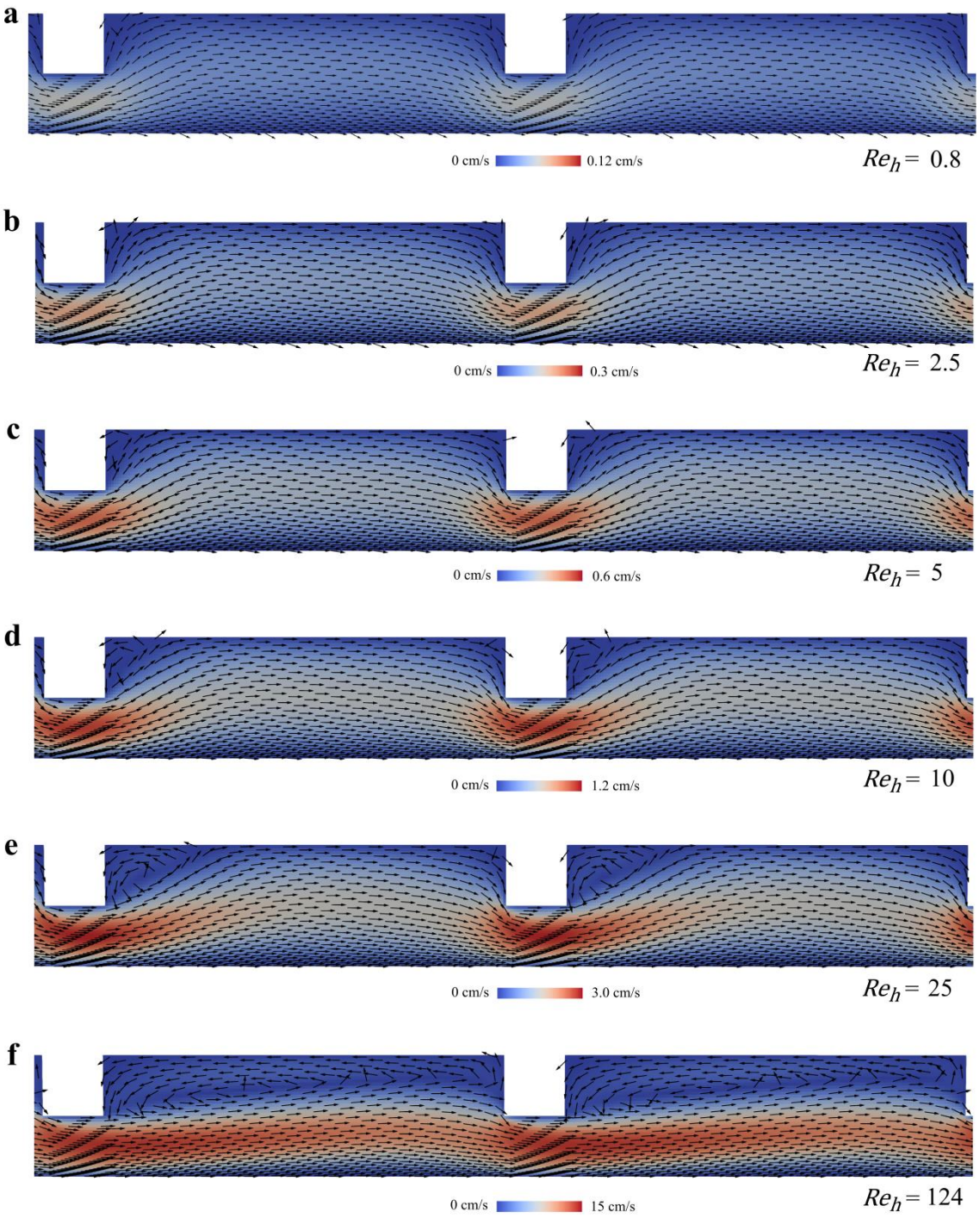


Figure 4-27 – Velocity field inside top cavity channels in the nanofiltration of a $K_2SO_4$ aqueous solution ($c_f$ = 4 g/L) at $\Delta p_m$ = 8 bar at distinct feed flow rate: a) $Re_h$ = 0.8; b) $Re_h$ = 2.5; c) $Re_h$ = 5; d) $Re_h$ = 10; e) $Re_h$ = 25; f) $Re_h$ = 124. The shown regions are located between the 26$^{th}$ and 28$^{th}$ ribs.

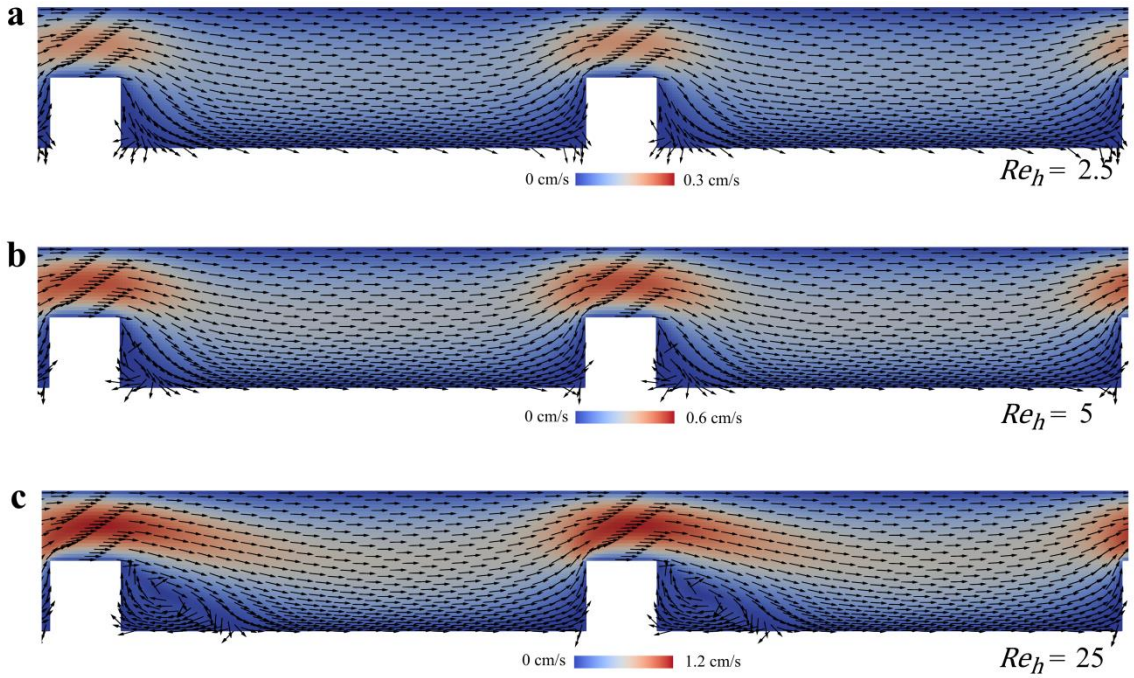


Figure 4-28 – Velocity field inside bottom cavity channels in the nanofiltration of a $K_2SO_4$ aqueous solution ($c_f$ = 4 g/L) at $\Delta p_m$ = 8 bar at distinct feed flow rate: a) $Re_h$ = 2.5; b) $Re_h$ = 5; c) $Re_h$ = 25. The shown regions are located between the 26$^{th}$ and 28$^{th}$ ribs.

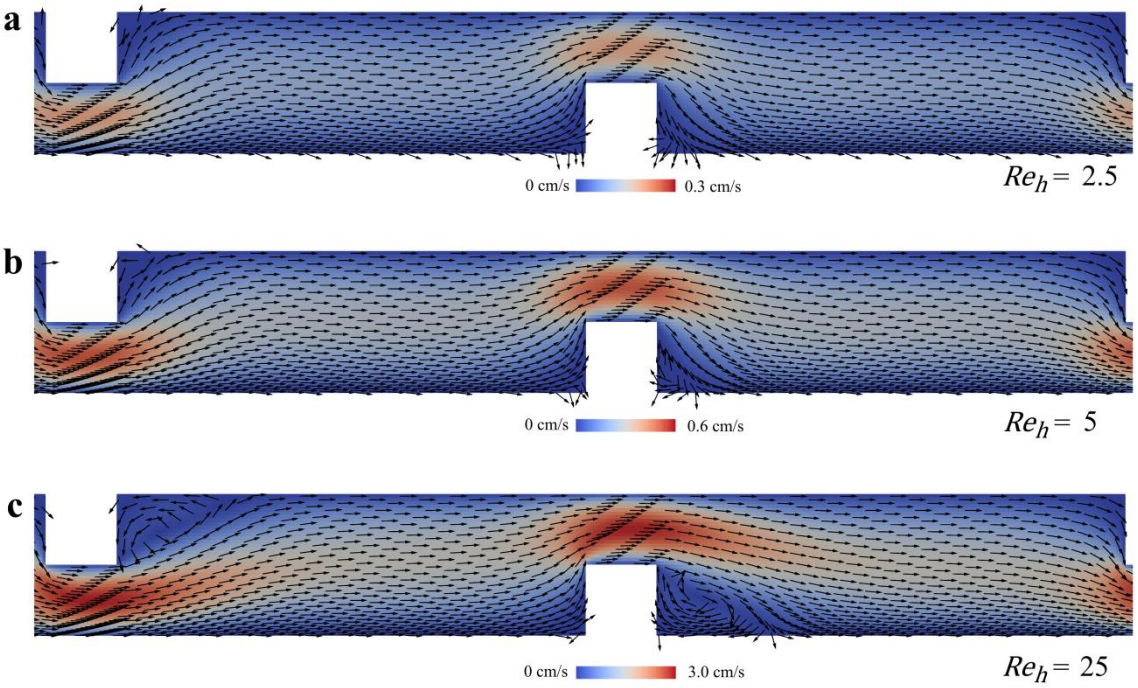


Figure 4-29 – Velocity field inside channels with ribs in a zigzag geometry in the nanofiltration of a $K_2SO_4$ aqueous solution ($c_f$ = 4 g/L) at $\Delta p_m$ = 8 bar at distinct feed flow rate: a) $Re_h$ = 2.5; b) $Re_h$ = 5; c) $Re_h$ = 25. The shown regions are located between the 26$^{th}$ and 28$^{th}$ ribs.

The differences, in terms of solute concentration, for the permeation processes inside channels of the four distinct geometries (open channel, cavity with ribs on the top or bottom walls, and in zigzag configurations) are shown in Figure 4-30, for illustrative scenarios of the nanofiltration of $K_2SO_4$ aqueous solutions ($c_f$ = 4 g/L , $\Delta p_m$ = 8 bar and $Re_h$ = 5).

Concentration polarization phenomenon occurs in all the channel geometries but with distinct magnitude and solute distributions, as can be seen in Figure 4-30a for a location between the 26$^{th}$ and the 28$^{th}$ ribs (in a series of a 30 rib channel). In the scenario of the open channel (the first image from the top, in Figure 4-30a), the mass fraction value in the vicinity of the membrane can go up to almost 3 times the value of the feed concentration. For the top cavity configuration (the second image counting from the top, in Figure 4-30a), the solute concentration distribution is similar to the open case but the CP layer is thinner and its magnitude is smaller. In addition, in the regions below the ribs, there is a decrease in the solute concentration, due to the local increase in the velocity. This same behaviour has been previously seen in the experimental interferograms. A distinct distribution of the solute concentration occurs for the bottom cavity and for the zigzag geometries, the third and fourth images from the top in Figure 4-30a. In these scenarios, the solute concentration increases sharply on both sides of the ribs placed on the membrane surface. The concentration peaks are caused by the permeation in a region where a recirculation zone exists (see Figure 4-28 and Figure 4-29). On the contrary, in the recirculation zones near the top ribs, the solute concentration remains equal to the feed concentration since no permeation occurs at those places.

The effect of the channel geometry can also be evaluated plotting the profile of the solute concentration at the membrane surface along the channel length, $w_m$, as shown in Figure 4-30b. It is clear that in the region where permeation occurs (the white area in Figure 4-30b) $w_m$ tends to increase along the channel. For the open channel, $w_m$ increases monotonically, while for the other geometries there are fluctuations inherent to the presence of ribs. Although the open channel is known for having poor capability for the mitigation of the CP phenomenon, the $w_m$ in the vicinity of ribs placed on the membrane surface (as in bottom cavity and zigzag geometries) is even higher than the corresponding values for the open channel. On the contrary, the $w_m$ value for the channel with ribs placed solely on the top wall is always smaller than the corresponding one for the open channel.

For a better insight into the solute concentration profile along the channel length, it is shown in Figure 4-30c a magnification of the $w_m$ profiles in the region from upstream the 26$^{th}$ rib to downstream the 28$^{th}$ rib. In this figure the grey areas correspond to the location of the ribs placed on the membrane surface. As can be seen, the $w_m$ increases slowly and steadily in the open channel, which exhibits the highest average $w_m$ value of the four studied geometries. In the channel with ribs on the top wall, the $w_m$ is always smaller than that for the open channel. However, the smallest $w_m$ values are achieved in the channel with ribs placed solely on the membrane suface, but only in the middle region between two consecutives ribs, since near the ribs there is a sharp concentration peak. The channel with the zigzag configuration presents a mixed behaviour between the channels with ribs on the top or bottom walls. The very high

concentration near the ribs on the membrane surface can be problematic, since it both decreases the permeate flux in that region and can trigger scaling and fouling phenomena.

All the above results are similar to the ones obtained by other authors, both in terms of the solute concentration field and of the $w_m$ profile along the channel length[16].

Due to permeation, the solute concentration increases along the channel (Figure 4-30b). Nevertheless, it would be of great importance to verify if any kind of periodicity exists. Periodic conditions are widely used in CFD to minimize computational effort (Fimbres-Weihs & Wiley 2010; Keir & Jegatheesan 2014). However, in the literature, the authors justify that assumption based on empirical knowledge or on the similar assumption used for heat transfer processes.

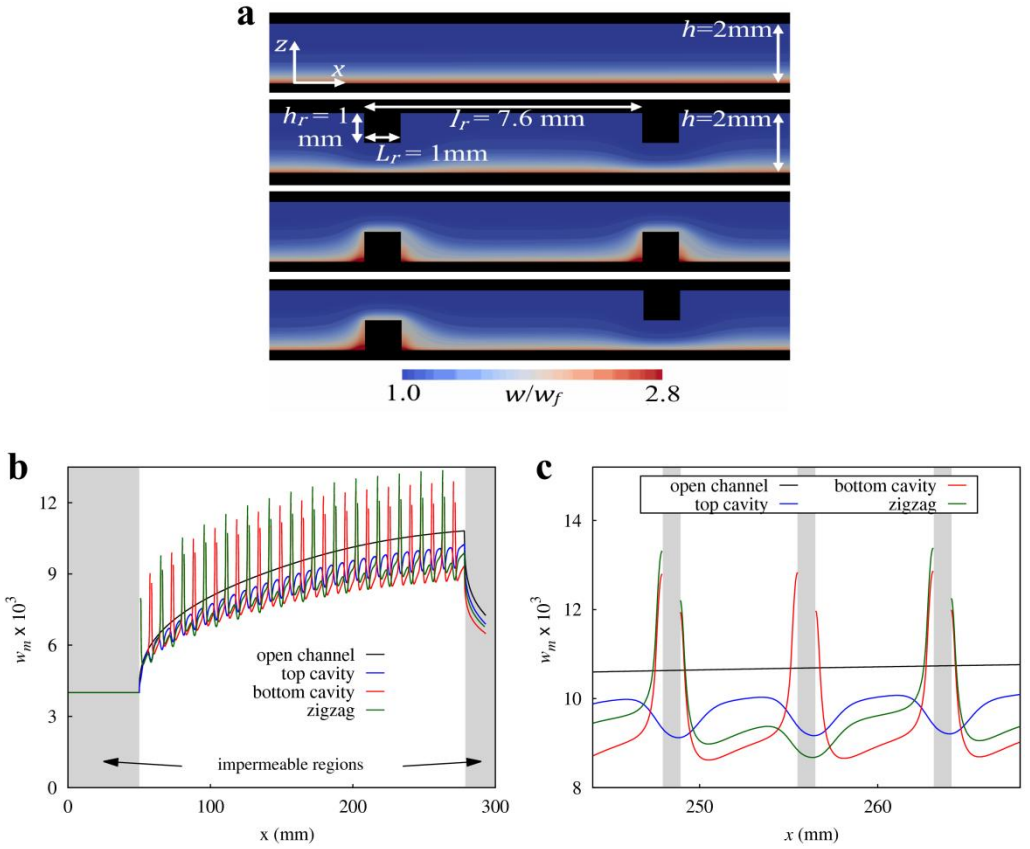


Figure 4-30 – Effect of the channel geometry on the concentration profiles, obtained using CFD, for the nanofiltration of a $K_2SO_4$ aqueous solution ($c_f$ = 4 g/L) at $\Delta p_m$ = 8 bar and $Re_h$ = 5: a) $w/w_f$ ratio for open channel and ribbed-wall channels; b) $w_m$ profile along the channel length, for the four geometries; c) zoom of the $w_m$ profile in the region corresponding to the vicinity from the 26th rib to the 28th rib. Grey regions correspond to impermeable areas.

In this work, the mass transfer periodicity is assessed by using the ratio between the solute mass fraction at a specific location and the average solute mass fraction in the bulk flow region. The periodicity along the membrane surface, given as the ratio $w_{m,sec}/w_{bLN,sec}$ (Figure

[16] Some minor differences exist between the results of this and other authors works, due to fact that in some works a dual membrane channel was simulated. However, the overshoots in the concentration field near ribs was verified by all the authors, independently of the shape of rib, providing that the rib is placed on the membrane surface.

4-31a), and the periodicity along the $z$-direction, given as the ratio $w(z)/w_{bLN,sec}$ (Figure 4-31b and Figure 4-31c), are assessed using the methodology described in section 4.4.4.

The ratio $w_{m,sec}/w_{bLN,sec}$ ratio tends to stabilize along the channel (with the exception for the zigzag configuration where the ratio tends to fluctuate around two values because of the alternate locations of the ribs). Some authors have shown that the momentum reaches periodic conditions after a couple of static mixer units (Alexiadis et al. 2007). However, it is possible to verify that for the operating conditions of the NF process represented in Figure 4-31a, the $w_{m,sec}/w_{bLN,sec}$ ratio only stabilizes after a significant number of rib sections (between 15 and 25). The main reason for this distinct behaviour is the fact that mass diffusivity is three orders of magnitude smaller than momentum diffusivity (kinematic viscosity), which results in slower mass transfer by molecular mechanism than the momentum transfer by the same mechanism. Therefore, the flow hydrodynamics stabilizes in a lower amount number of ribs than the $\frac{w}{w_b}$ ratio. Moreover, the studies that have dealt with the stabilization of the flow structure have used impermeable walls. In permeation processes, there is a continuous loss of mass to the permeate stream. Therefore, the flow structure is continuously changing, which is more significant for high recovery rates.

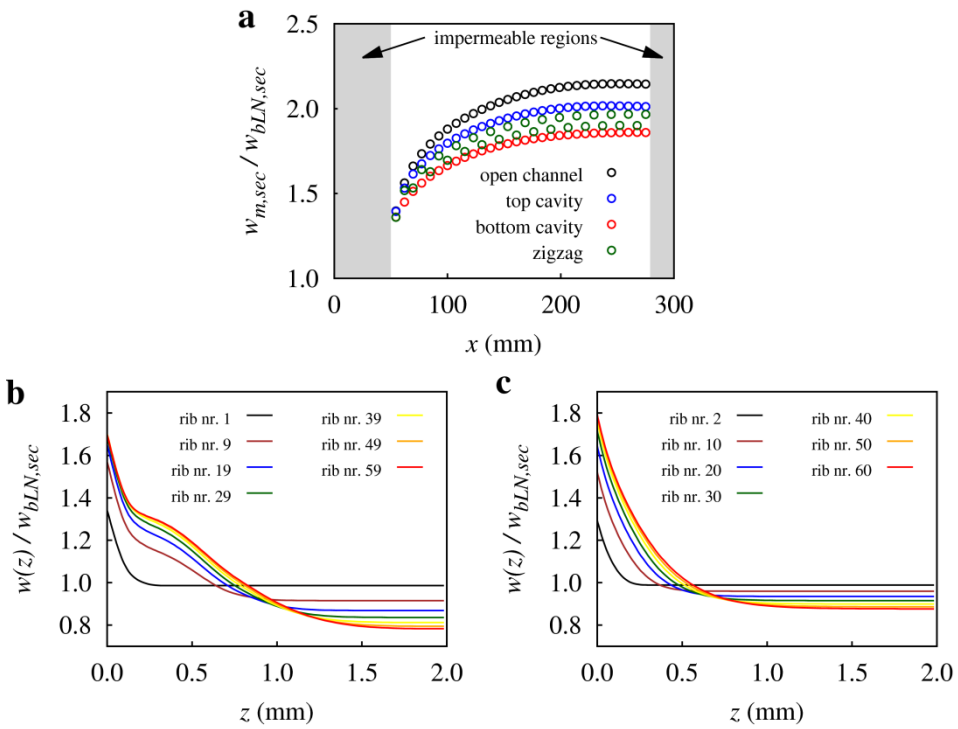


Figure 4-31 – Evaluation of the periodicity of the solute concentration along the channel, obtained using CFD, for the nanofiltration of a $K_2SO_4$ aqueous solution ($c_f$ = 4 g/L) at $\Delta p_m$ = 8 bar and $Re_h$ = 5: a) section averaged $w_{m,sec}/w_{bLN,sec}$ ratio along the channel (in a channel with 30 ribs); b) $w(z)/w_{bLN,sec}$ ratio along the $z$-direction for locations at 1.75 mm from the beginning of each odd rib (in a channel with 60 ribs); c) $w(z)/w_{bLN,sec}$ ratio along the $z$-direction for locations at 1.75 mm from the beginning of each even rib (in a channel with 60 ribs).

Figure 4-31b and Figure 4-31c show the evolution of $w(z)/w_{bLN,sec}$ ratio at locations 1.75 mm downstream the beginning of each section for consecutive odd and even sections, respectively. Although the $w(z)/w_{bLN,sec}$ profiles also exhibit a tendency to stabilize, a larger number of rib sections are necessary for that stabilization than in the case of the $w_{m,sec}/w_{bLN,sec}$ profiles. In fact, while the profiles of the Figure 4-31a result from the simulation of the NF process inside channels with 30 ribs and $l_r$ = 7.6 mm, the profiles of the Figure 4-31b/c were obtained from simulations with the same channel length but with twice the number of ribs, which results in rib sections with half size of the original ones ($l_r$ = 3.8 mm). It should be mentioned that equivalent profile evolutions were verified for other $x$-locations (but with different profile shapes and not shown here). These results suggest that for permeation processes at low $Re$ it is possible to reach periodic conditions, but a considerable number of repetitive static mixers units is necessary. This means that, in ribbed channels that lead to 2D flows, the mass transfer entrance effects dominates a large fraction of the feed channel, and must be taken into account for design purposes.

### 4.5.5 Prediction of nanofiltration data using the hybrid method

The hybrid computational / semi-empirical method requires the knowledge of the mass transfer coefficients for the non-suction system corresponding to the channel with semi-permeable membranes under study. For this reason, it was simulated the mass transfer in impermeable-dissolving wall channels with the same geometries investigated before.

The obtained $Sh_0$ values as function of $Re_h$ are plotted in Figure 4-32. The mass transfer of the impermeable-dissolving wall process in open channels is in agreement with the Graetz-Lévêque correlation, equation (4-17). Moreover, the flows in ribbed-wall geometries yield mass transfer coefficients higher than in open channel. The $Sh_0$ value seems to be larger for bottom and zigzag than for the top geometry[17].

Before using the hybrid method to obtain NF data, it is necessary to evaluate if the $\Gamma$ correlation given by equation (4-2) still stands for such processes at low $Re_h$ in open and ribbed-wall channels. From the data extracted from NF simulations, $\Gamma$ was calculated using equation (4-6), plotted as function of $\phi$ and compared with the $\Gamma$ correlation proposed by Geraldes and Afonso (Geraldes & Afonso 2006). This comparison is shown in Figure 4-33 and good agreement is obtained for all the scenarios (different channel geometries and $Re_h$ between and 0.8 and 2.5). This clearly shows that the $\Xi$ correlation that was originally derived for $Re_h$

[17] Similar observations have already been made by other authors who studied permeation in creeping flows inside open channels and channels with transversal circular ribs (Fimbres-Weihs & Wiley 2008) and they are related with the distinct effective membrane area in each channel geometry.

between 30 and 1000 (Geraldes & Afonso 2006) can be extended for lower Reynolds numbers and for 2D spacer geometries.

Since the global permeation results fit well the $\Gamma$ correlation, it is legitim to expect that the proposed hybrid method (Figure 4-13) is suitable to predict the permeate flux, the solute concentration at the membrane surface and the bulk solute concentration.

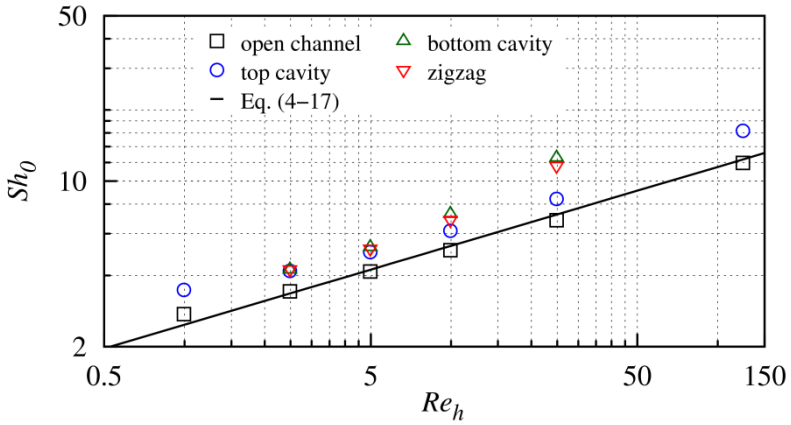


Figure 4-32 – Effect of the Reynolds number on the average mass transfer coefficient for impermeable-dissolving wall processes inside open and ribbed-wall channels with $L$ = 300 mm.

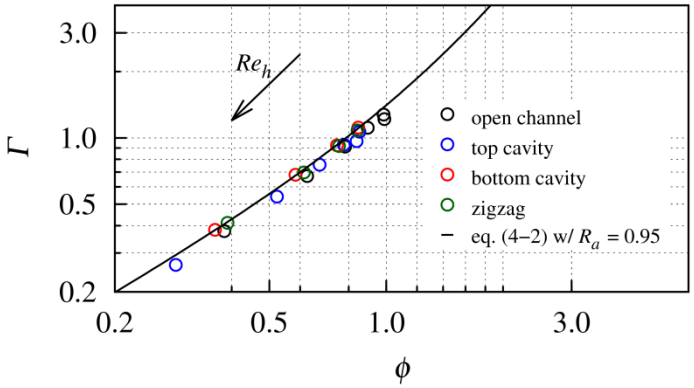


Figure 4-33 – Comparison between the averaged $\Gamma$ (along the channel) obtained by CFD (symbols) for different channel geometries and the calculated by the generalized mass transfer correction factor correlation (solid line).

The hybrid method was applied to several scenarios of the nanofiltration of $K_2SO_4$ aqueous solutions. Three of them are presented in Figure 4-34, resulting in deviations lower than 10 % between the data estimated by the hybrid method and by CFD simulations of the nanofiltration process. Therefore, the hybrid method shows to be a valid alternative to predict permeation data in very computational demanding systems, providing that the mass transfer coefficient for the non-suction mass transfer is available.

Examples of application for the hybrid algorithm are the development of more efficient permeation devices using intricate shape channels or static mixers of complex geometry. In these cases, $k_{c,0}$ can be determined in advance using any convenient method (for instance the

limit current technique or CFD simulations) and then the hybrid method is applied to estimate the permeate flux and the concentration polarization modulus.

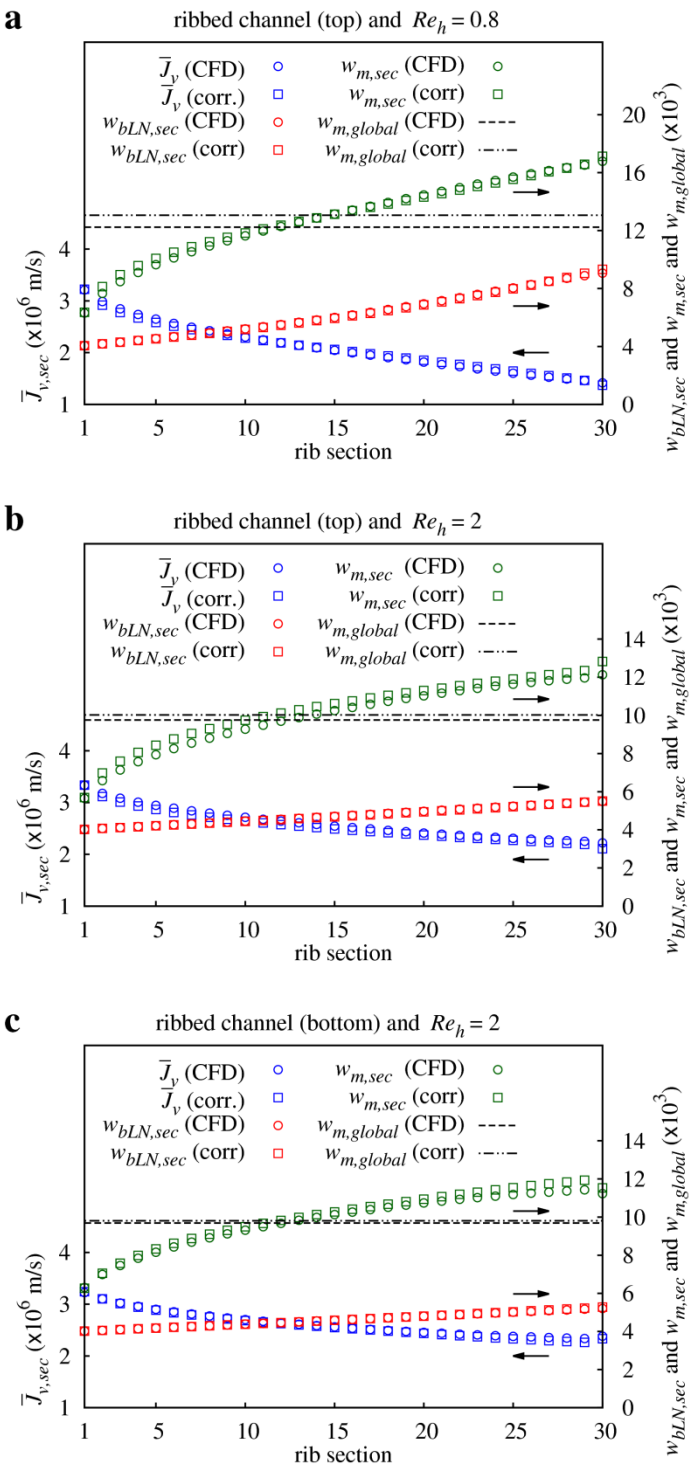


Figure 4-34 – Comparison between nanofiltration data obtained by CFD simulation versus that obtained using the hybrid method. The nanofiltration refers to the permeation of a $K_2SO_4$ aqueous solution ($c_f$ = 4 g/L) at $\Delta p_m$ = 8 bar in: a) top cavity channel and $Re_h$ = 0.8; b) top cavity channel and $Re_h$ = 2.5; c) bottom cavity channel and $Re_h$ = 2.5.

## 4.6 Conclusion

The focus of this chapter was twofold. First, it was intended to evaluate experimentally the concentration polarization phenomenon that occurs in nanofiltration processes and to validate the predictions obtained by CFD simulations for equivalent processes. The CFD validation was done comparing the numerical results with the outcomes from micro-PIV and HI experiments. Second, simulations using the validated CFD model were performed to assess both the periodicity of the mass transfer along the channel and to verify the validity of the developed hybrid method to predict nanofiltration data for processes at low Reynolds numbers. The outcomes of this study are relevant to those who intend to design and use tangential flow microfluidic devices with incorporated membranes.

Micro-PIV and holographic interferometry proved to be reliable real-time and non-invasive techniques to visualize the flow and concentration fields. The study on CP phenomena was performed using HI to monitor the nanofiltration of $K_2SO_4$ aqueous solutions. The influence of several operating parameters on the CP magnitude was studied, including: feed concentration ($c_f$ = 2 g/L and 4 g/L); applied pressure ($\Delta p_m$ = 3, 5 and 8 bar), inlet flow rate ($Re_h$ from 0 to 125); and channel geometry (open channel and top cavity channel with square ribs). To the autor's best knowledge, this is the first work were HI was used to visualize the CP phenomenon in nanofiltration channels with ribbed-walls.

In NF processes using ribbed-wall channels, the fringes bend in the vicinity of the rib, which is distinct from the typical almost-straight fringes, parallel to the membrane surface, obtained in open channels. By visual inspection of the interferograms, it is clear that the severity of the concentration polarization increases as the pressure is increased and as the flow rate is decreased. On the other hand, although the solute concentration near the membrane increases as the solute feed concentration increases, the CP modulus is inversely proportional to feed concentration. In addition, better permeation performance (lower CP, higher $J_v$ and higher $R_a$) is obtained when the ribbed-channel is used.

The ratios $w_m/w_b$ and $w/w_b$ tend to asymptotic values along the channel length but only after a considerable number of rib sections (more than 15). This result contrasts with the ones obtained by other authors, for the hydrodynamics periodicity, where they claim that periodic conditions are achieved in a small number of repetitive units (2 to 6). The reason for this distinct behaviour is the difference of magnitudes of the mass and momentum diffusivities. Therefore, permeation processes in channels with transversal ribs (2D flows) are affected by strong entrance effects and the use of cyclic conditions for CFD modeling low $Re_h$ flows inside small channels should be used cautiously.

Finally, it was verified that it is possible to apply the hybrid computational / semi-empirical method (based on a generalized mass transfer correction factor) to predict nanofiltration data, resulting in deviations smaller than 10 % from the simulations of the permeation process itself. Thus, this methodology can be very useful to study the effect of changing the operating conditions or the channel designs, providing that the mass-transfer correction factor for the non-suction process is known in advance.

As seen in Chapter 3, small-volume samples can be concentrated by nanofiltration using open channels in micro-TFF cells. Such channels may be inefficient depending on the feed concentration and applied pressure. Therefore, the hybrid method developed here can be used to evaluate innovative channel and static mixers designs, and thus is of particular interest for nanofiltration and concentration applications at microscale.

Another way to improve the concentration of small-volume samples containing low MW solutes is doing it by centrifugal filtration. Thus, in the next chapter, centrifugal nanofiltration (CNF) will be used to concentrate model solutions and to study the influence of the applied rotational speed, of the filtration chamber height, and of the angle between the centrifugal force and the membrane surface.

# 5 Centrifugal nanofiltration of small-volume samples of low molecular weight solutes

## 5.1 Introduction

This chapter describes the design and experimental work performed using the developed centrifugal nanofiltration (CNF) device for the concentration of low MW solutes in small-volume samples. Prior to the design and use of the CNF device, a comprehensive literature review was done on patented small-volume centrifugal filtration devices, on current and legacy commercial small-volume centrifugal filtration devices, and on other centrifugal filtration devices used in scientific research.

Centrifugal filtration was selected as a concentration technique based on its advantages when comparing it with other methods for the mitigation of concentration polarization and fouling, which were described in section 2.3.2. Since nanofiltration membranes will be used, the method applied herein is called centrifugal nanofiltration (CNF).

Centrifugal filtration can be performed in both continuous and non-continuous processes. Centrifugal filtration can be coupled to continuous processes, but these are usually associated with hydraulic circuits and to external pumping (which originate issues related to retention volumes and pump priming). Moreover, batch centrifugal filtration devices have successfully been used in the last decades for the concentration of large MW solutes and particulate matter, especially in the biological and environmental field.

Safety issues are minimized when using batch centrifugal filtration, because these devices are watertight and, since no pumping circuit is needed, there is no risk of contamination of the sample or of the environment. The major concern about the use of batch centrifugal filtration is mechanical failure of the centrifuge rotor or of the centrifugal devices. Nevertheless, if the instructions of manufacturers are followed, then, hazard risks are low.

The developed CNF device will be optimized based on the effect of two geometric parameters on the concentration performance: the height of the filtration chamber, $h$, and the angle between the centrifugal force and the membrane surface, $\beta$. The range of $h$ varied between 0.1 and 2.4 mm while $\beta$ varied between -10° and +10°.

The herein developed CNF technique is discontinuous in its nature resulting in an unsteady filtration. For this reason, temporal evolution of the concentration is evaluated during the filtration cycle. In addition, the effect of the solute and of its concentration is also assessed.

In the following sections of this chapter a brief literature review on centrifugal filtration devices is first presented, then the developed CNF device (Geraldes et al. 2018) and the

adaptors used to modify the $\beta$ angle are described, and finally the results obtained for the centrifugal nanofiltration using model solutions are shown (Completo et al. 2017).

## 5.2 Literature review

The sources of information about centrifugal filtration devices and techniques can be grouped in two groups, as sketched in Figure 5-1. On the one hand, there are the works where small-volume batch devices are used for the microfiltration and ultrafiltration of samples. These can be further divided into works showing the development and design of the centrifugal filtration devices (mainly disclosed in patent form) and the works where, using commercial devices, the centrifugal filtration is merely a separation process for sample treatment. In all the above-mentioned works only MF and UF membranes were applied. On the other hand, there are the works where RO membranes were applied but only using continuous processes.

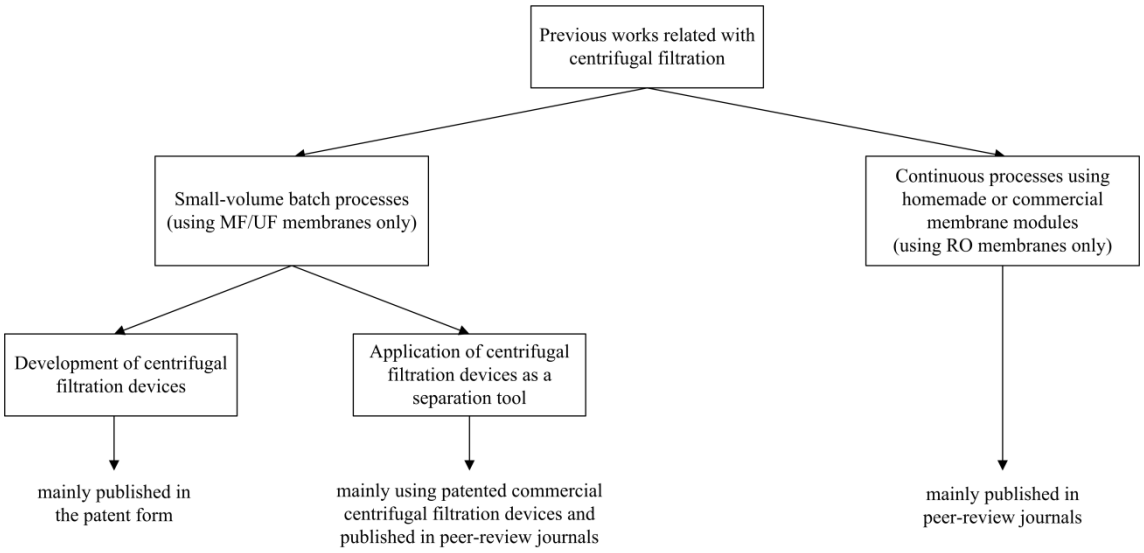


Figure 5-1 – Sources of information about centrifugal filtration devices and techniques.

Current centrifugal filtration batch devices to be operated in lab-scale centrifuges and that use micro- and ultrafiltration membranes are usually similar to the generic one sketched in Figure 5-2. Briefly, it consists of a large chamber (herein named as sample chamber) where the sample is placed before the filtration cycle, and a large chamber (herein named as permeate chamber) where the permeate, which passes through the membrane, is collected. Additionally, the device can have a small volume chamber (herein named as concentrate chamber) where the concentrated fluid retained by the membrane is accumulated. The concentrate chamber does not exist in all the current centrifugal devices, and, in some cases, it is just the region in the extremity of the sample chamber. By spinning the centrifugal filtration device around an axis of

rotation, at an angular velocity $\vec{\omega}$, pressure is generated by the centrifugal force (section 2.3.2). The pressure difference between any two arbitrary points, located at $r_1$ and $r_2$, can be determined using equation (2-48).

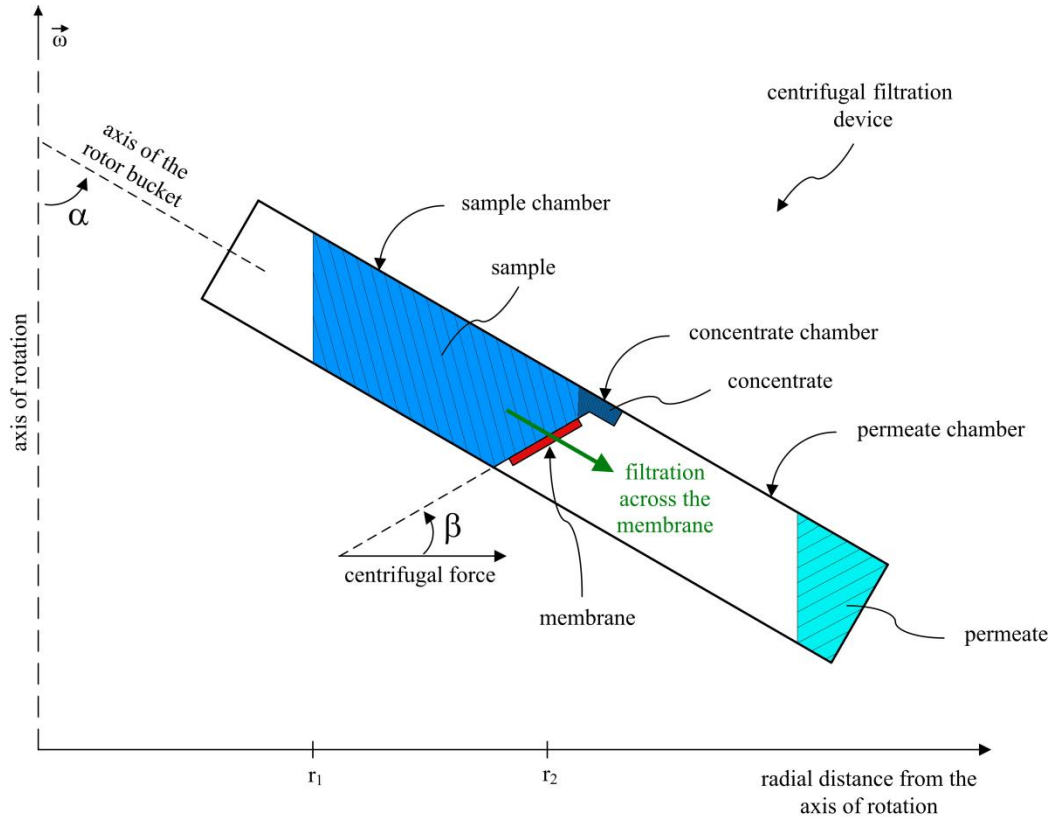


Figure 5-2 – Scheme of a generic centrifugal filtration batch device.

Before describing the patented centrifugal devices to concentrate small-volume samples, some definitions used in the centrifugation field of study, or used in this work, must be given.

To perform centrifugal filtration, any kind of apparatus that makes the centrifugal filtration devices to spin around an axis of rotation is necessary. Unless one develops his centrifugal apparatus, a commercial centrifuge must be used. Lab scale centrifuges are usually categorized, in one of four groups, according to their maximum rotational speed or maximum RCF: benchtop centrifuges, microcentrifuges, high-speed centrifuges and ultracentrifuges (Wilson & Poole 2009). Benchtop centrifuges operate at low speed (up to 4000 rpm) and are used to separate large particulate matter like yeast and blood cells. Microcentrifuges have small rotor radii (and thus low volume capacity) and usually operate up to 15,000 RCF. The rotors of high-speed centrifuges are larger and can go up to 100,000 RCF. Ultracentrifuges can operate up to 1,000,000 RCF.

A rotor is a part of a centrifuge wherein the centrifugal filtration device is placed and secured inside rotor buckets. It is the rotor that engages on the rotating shaft of the centrifuge

and makes the centrifugal filtration device to spin. In terms of rotors, there are two main types: the fixed-angle rotors and the swinging-bucket rotors (Livshits et al. 2015). The distinction between them is related to the angle between its axis of rotation and the axis of the bucket that contains the centrifugal filtration device. While in fixed-angle rotors such angle is fixed, since the rotors of this type are solid blocks with empty holes that serve as buckets, in swinging-bucket rotors their buckets are allowed to swing and the mentioned angle depends on the imposed centrifugal force. Sketches of fixed-angle and swinging-bucket rotors standing still (not rotating) or rotating, are displayed in Figure 5-3. In the present work, the angle between the axis of rotation and the axis of the rotor bucket is named $\alpha$ and the angle between the centrifugal force and the membrane surface is named $\beta$, as defined in Figure 5-2.

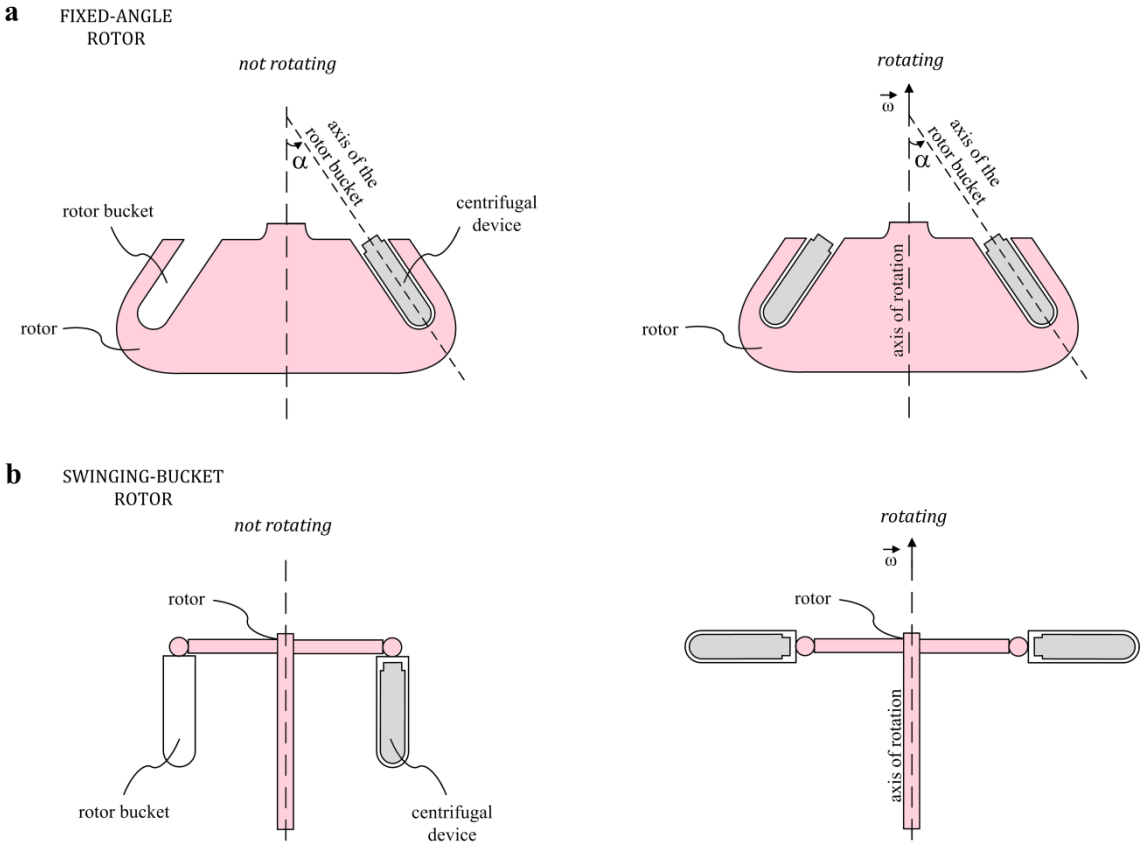


Figure 5-3 – Schemes of the two most common centrifuge rotors: a) fixed-angle rotor; b) swinging-bucket rotor.

### 5.2.1 Patented centrifugal filtration batch devices

For the last 60 years, several centrifugal filtration batch devices were disclosed via patents, aiming to overcome the problems of the devices already in use and, thus, turn into successful commercial products. Many of them were insufficient in achieving that goal, but they will be referred here for historical purposes. However, it is important to emphasize that all the centrifugal filtration batch devices were developed to be used for micro- and ultrafiltration

separations. To the best knowledge of the author, no device was disclosed to be used with nanofiltration or reverse osmosis membranes or to be used for the filtration of small-volume samples with high osmotic pressure, which is the subject of this thesis.

The main advances on centrifugal filtration batch devices are related to three major issues: prevention of filtration to dryness; optimization of the filtration performance; and the removal of the concentrate. Filtration to dryness occurs whenever the whole solvent passes through a membrane resulting in a dry sediment on the membrane surface, or even in its deposition in the internal structure of the membrane. Despite being possible to re-dissolve the sediments, filtration to dryness usually leads to low recovery of the substances that one pretends to concentrate. Optimization of the filtration performance is usually related to the selection of the best geometry for the device, including the orientation of the membrane relatively to the centrifugal force. Finally, special attention was placed on methodologies to remove the concentrate after the filtration cycle, in order to minimize solute losses.

The device invented by Rigopulos in the early 70's is probably the first centrifugal filtration batch device disclosed in a patent to be used for micro- and ultrafiltration of small samples (Rigopulos 1970). Rigopulos' patent device consists of conical or cylindrical structures that support a membrane and that are engaged on centrifuge tubes. An illustrative embodiment of the device is shown in Figure 5-4a, where a conical membrane was inserted inside the conical support. Even at that time, the author was concerned with the positioning of the membrane and suggested that the angle between the membrane surface and the centrifugal force should be preferably less than 15°. The proposed device was tested for the filtration of blood and urine proteins resulting in 100% rejection. The main problem with this device is that it does not avoid filtration to dryness if the filtration cycle is long enough. The same issue occurs in other devices (Lyman & Mathus 1987; Szabados 1988) with different geometries.

Filtration to dryness can be avoided by optimizing the geometry of the device. For instance, Bowers and Rigopulos (Bowers & Rigopulos 1986) disclosed a device for which the filtration stops when the liquid meniscus, in the sample chamber, reaches the radial position of the last permeate duct, below the membrane, and, thus, some amount of liquid remains inside the device regardless the amount of time of the filtration cycle, as can be seen in Figure 5-4b. Using this device, rejections higher than 95% were obtained for BSA and Vitamin B. Apparently, and given the good results obtained with this device, it turned into a successful product of Millipore: the Centricon®. In a more recent patent, a device was disclosed with an operation based on the same principle, but allowing for the user to select the final concentrate volume by unsealing the corresponding permeate ducts (Clark 2004). The main issue on this kind of devices is that losses by adsorption can occur due to the continuous contact between the concentrate and the membrane.

To minimize the physical contact between the membrane and the most concentrated fluid elements, the more recent devices were disclosed containing concentrate chambers (Miyagi et al. 1988; Vassarotti 1997; Bowers et al. 2002; Bonhomme et al. 2014). Since the concentrate chambers are placed in an outermost radial level than that of the membrane, the concentrate is directed towards that chamber due to the centrifugal force. As an illustrative example, the device disclosed by Vassaroti (Vassarotti 1997) is shown in Figure 5-4c. From these disclosures, the Bonhomme's patent (Bonhomme et al. 2014) is the only one showing experimental results and, depending on the MWCO of the used membrane, protein rejection can be higher than 95 %, while protein recovery (in the concentrate) is above 90%. Some of these devices became commercially successful. Many suppliers sell devices based on the Vassarotti's patent (Vassarotti 1997), whereas Bower's device (Bowers et al. 2002) is sold as Apollo® and Bonhomme's device (Bonhomme et al. 2014) is sold as Amicon® Ultra.

As referred in section 2.3.2, the orientation of the membrane, relatively to the centrifugal force, plays a major role in the filtration performance. In many of the first centrifugal filtration devices, membranes were placed over a support perpendicularly to the axis of the device (Wilson 1971; Bowers & Rigopulos 1986; Lyman & Mathus 1987; Sklar et al. 1997; Bowers & Yankopoulos 1998; Schwarzwald 2010; Szabados 1988; Cianci 1996; Klerks 2010). As an illustrative example, the device disclosed by Lyman and Mathus (Lyman & Mathus 1987) is shown in Figure 5-4d. This type of design is not the most efficient neither in fixed-angle rotors nor in swinging-bucket rotors, since the centrifugal force points towards the active surface of the membrane potentially leading to membrane clogging.

A better filtration performance can be achieved if the membrane is placed parallel to the axis of the centrifugal filtration devices or forming a certain angle with it (Shimizu & Ohtsubo 1986; Miyagi et al. 1988; Nakajima 1988; Zuk Jr. 1992; Vassarotti 1997; Zuk Jr. 2000; Vassarotti 2002; Bonhomme et al. 2014). An illustrative example of the latter design is shown in Figure 5-4e representing the device disclosed by Bonhomme and colleagues (Bonhomme et al. 2014).

Another typical design is to place the membrane in such orientation that the normal to the active surface of the membrane points in the positive radial direction, at least at some extent (Greenspan 1972; Hochstrasser 1976; Nussbaumer et al. 1985; Bowers & Tiffany 1989; Herczeg 1996; Chambers et al. 2001). This is usually done by supporting the membrane on the bottom surface of a piston that, due to the centrifugal force, is pushed against the liquid in the bottom of a tube and the permeate is collected in a reservoir inside the piston. The device disclosed by Bowers and Tifanny (Bowers & Tiffany 1989) is shown in Figure 5-4f as an illustrative example. The latter device, which apparently is still sold as Centriprep®, presented better performance, in terms of filtration time, for the concentration of BSA solution (1 mg/L) than the previously mentioned device Centricon®, which used a membrane perpendicular to its

axis (Bowers & Rigopulos 1986), as shown in Figure 5-4b. This result is another proof of the influence of the angle between the centrifugal force and the surface of the membrane. However, these devices, which use inverted membranes on the bottom of a piston, have the drawback of interrupting the filtration process when the liquid levels inside and outside the piston are the same (admitting the insignificant influence of liquid density).

Solute adsorption can increase when the area-to-volume increases, but the recent trend is to maximize the membrane area of the centrifugal filtration devices by covering the major portion of the internal surface of the sample chamber with the membrane (Bowers et al. 2002; Domanico et al. 2015). An illustrative example is shown in Figure 5-4g that constitutes the device disclosed by Bowers and colleagues (Bowers et al. 2002). Even when rectangular membrane pieces are used, instead of the conical/cylindrical pieces, the membrane area can be doubled by using two parallel membranes (Bonhomme et al. 2014).

Despite the fact that adsorption is an undesirable outcome in all the above-mentioned devices, there are cases where the centrifugal process is combined with an adsorption or targeting process (Nochumson & Goldberg 1996; Vlock et al. 1998; Kopaciewicz et al. 1998; Warner 2006). In these devices, a specific ligand is physically, or chemically, attached to the membrane surface, or to the bulk of the filtration medium. Then, during the filtration cycle, the specific target bounds to the ligand and is removed from the liquid that passes through the membrane. Depending on the objective of the filtration, the target may be recovered or discarded. As an illustrative example, Figure 5-4h shows the device disclosed by Nochumson and Goldberg (Nochumson & Goldberg 1996). In this device, the inventors conducted a separation of a mixture containing DNA of a bacteriophage, which was bound to the filter medium and then eluted, obtaining a recovery of 95 % of the DNA.

Another difference among the patented centrifugal filtration devices is the method to remove the concentrate at the end of the filtration device. While the permeate is easily recovered because it accumulates in the permeate chamber, which is detachable from the device, the withdraw of the concentrate is trickier since it has a much smaller volume of liquid that remains near the membrane. In the disclosed devices, there are three main methods to recover the concentrate: remove the concentrate by suction, using a tubing coupled to a syringe or a pipette; perform a reverse-spin at low speed (Bowers & Rigopulos 1986; Lee et al. 1996; Bonhomme et al. 2014); and perform an extra spin at low speed using a concentrate cup (Zuk Jr. 1992; Herczeg 1996). The use of tubing to remove the concentrate has two drawbacks. On the one hand, some solute and concentrate losses may occur due to adsorption or to the liquid get stuck in the tubing and syringe walls. On the other hand, the insertion of the tubing inside the devices can damage the membrane.

As discussed in this section, many improvements have been proposed and implemented, along the years on the batch centrifugal filtration devices disclosed in patents. However, none of

them are designed, or suited, to be used for the concentration of solutes with MW below 1000 g/mol, and, for that reason, innovative devices must be developed for such task.

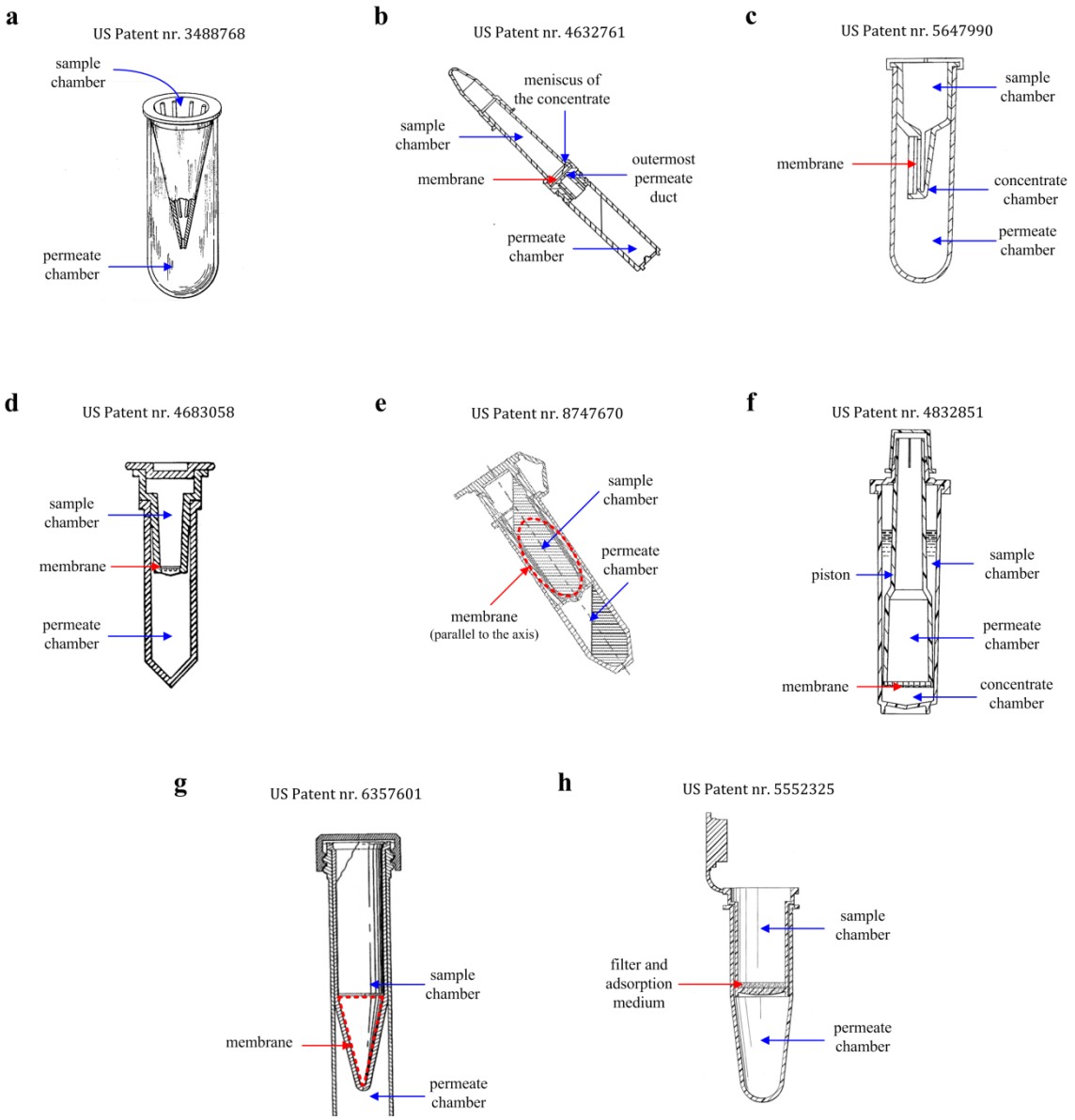


Figure 5-4 – Illustrative drawings of some of the patented centrifugal filtration batch devices.

### 5.2.2 Centrifugal filtration devices used on research

Centrifugal filtration is a widely used technology to filter small-volume samples from 0.5 to 100 mL. However, currently, it is used only for micro- and ultrafiltration. These devices are generically known as centrifugal ultrafiltration (CUF) devices and can be used to separate large particulate matter like bacteria (Wunderlich et al. 2016), viruses (Hata et al. 2014; Ahmed et al. 2015), nanoparticles (Liu & Hurt 2010; J. Liu et al. 2012), vesicles (Xu et al. 2014; Fraile et al. 2014), micelles (Liu et al. 2009; Taira et al. 2015), DNA fragments (Zhou et al. 2008; Borujeni

& Zydney 2012), colloids (Schlosser et al. 2013; El-Akl et al. 2015) or medium-to-large macromolecules like proteins (Zhloba & Subbotina 2014; Tang et al. 2015).

Although literature is quite vast on research works using CUF devices, only a few studies perform systematic comparisons between different devices (Mickowska et al. 2000; Sanchez et al. 2008; Greening & Simpson 2010; Kratzer et al. 2014). In these studies, it was found that different CUF devices have different filtration performances in spite of using the same membrane MWCO and the same operating conditions. This distinct behaviour was attributed to distinct designs of the devices, in particular the different orientation of the membrane (Greening & Simpson 2010). However, there is also the possibility that, despite having the same MWCO, the membranes have different properties since some are made of cellulose acetate derivatives and others of polyether sulfone. On the other hand, when compared with other protein separation techniques, the use of CUF devices was found to generally consume less time and present higher recovery rates than, for instance, precipitation (Cao et al. 2011), solid-phase extraction (Carlsson et al. 2001), liquid-liquid extraction (Rege et al. 2002), passive ultrafiltration (Blanco et al. 2004) and dialysis techniques (Su et al. 2006; Zimmerman et al. 2010; Cao et al. 2011).

The above-mentioned studies were performed with commercial CUF devices. A list of the CUF devices sold currently by the major manufacturers is presented in Table 5-1 and in Figure 5-5 some examples of such devices are shown.

Non-commercial CUF devices were also developed, handcrafted and used by other authors. Two examples are shown in Figure 5-6.

Hammond and colleagues (Hammond et al. 1980) have made a simple centrifugal filter using a small glass vial (6 mL), a tube (with a diameter smaller than the glass vial) and a dialysis membrane. The dialysis membrane was fixed in one of the sides of the tube by means of an elastic band, the tube was inserted inside the glass vial, which had a thick layer of filter paper on its bottom, and the liquid sample was placed inside the internal tube. The centrifugal force makes part of the sample to flow through the dialysis membrane and to be absorbed by the filter paper. A sketch of the Hammond's device is shown in Figure 5-6a. Hammond used his device, with a dialysis membrane, to separate free- from protein-bound steroids. Other authors have used devices similar to the one of Hammond but using ultrafiltration membranes (Bikle et al. 1984; van Hoof et al. 1998).

A different centrifugal filtration device was developed by Li and colleagues (J. Li et al. 2009), consisting of a cylindrical vial where a U-shaped hollow-fiber was inserted inside the vial and the liquid sample poured into the vial, as shown in Figure 5-6b. The centrifugal force makes part of the sample to permeate through the membrane into the inside of the hollow fiber. However, the purpose of this device is not to concentrate the sample but to collect a small portion of the filtrate. This device was mainly used to obtain portions of plasma that can be

considered representative of liquid in equilibrium with protein-bound substances, i.e. the plasma fraction containing non-protein-bound substances. The determination of free substances in the blood is important because, when administering drugs to patients, it is the free fraction that is considered active and not the total amount of drug in the blood (van Hoof et al. 1998). In addition, other studies revealed that the equilibrium depends on the concentration of the sample (Dong, Zhang, et al. 2013) and, for this reason, the use of common CUF devices is not suited to be used for the determination of the free-to-bound ratio in biological fluids. When using the hollow-fiber centrifugal filtration device, only a small volume of the sample is permeated and, hence, the sample concentration can be considered in equilibrium. Therefore, this type of device can be used instead of equilibrium dialysis method, which is very time-consuming. The hollow-fiber centrifugal filtration device was already used in the determination of the free-to-bound ratios of several substances in blood including vitamins (Xu et al. 2014), antibiotics (Li et al. 2010; Dong, Hou, et al. 2013), and other drugs (Dong, Zhang, et al. 2013; Zhang et al. 2013; Li et al. 2015).

Table 5-1 – Centrifugal ultrafiltration devices currently available in the market

| Supplier | Commercial name | Patent † | Max. initial volume (mL) ‡ | Min. final volume (mL) ‡ | Maximum RCF ‡ | Membrane area ($cm^2$) ‡ | MWCO or pore size ⸸ |
|---|---|---|---|---|---|---|---|
| EMD Millipore | Amicon® Ultra | US 8357296 | 0.5 – 15 † | 0.015 – 0.2 † | 5000 – 14000 † | 1 – 7.6 † | 3 – 100 kDa |
| | Microcon® | n.a. | 0.5 | 0.005 | 14000 | n.a. | 10 – 30 kDa |
| | Centrifree® | n.a. | 1 | 0.05 | n.a. | 0.92 | 30 kDa |
| | Centriprep® | US 4832851 | 2 – 15 | n.a. | n.a. | n.a. | 3 – 50 kDa |
| | Centricon® Plus | US 4632761 | 15 – 70 | 0.35 | n.a. | 16 | 3 – 100 kDa |
| | Ultrafree® | n.a. | 0.5 | n.a. | 12000 | 0.2 | 0.22 – 5 µm |
| Sartorius / Vivaproducts | Vivaspin® | US 5647990 | 0.5 – 20 | 0.005 – 0.05 | 3000 – 15000 | 0.5 – 7.2 | 2 – 1000 kDa |
| | Centrisart® | n.a. | 2.5 | 0.1 | 2000 | 0.79 | 5 – 300 kDa |
| | Vivafree® | n.a. | 0.5 – 2 | 0.005 – 0.55 | n.a. | 0.32 – 0.95 | 30 – 125 kDa |
| | Vivacon® | n.a. | 0.5 – 2 | 0.005 – 0.55 | n.a. | 0.32 – 0.95 | 2 – 125 kDa |
| | Vivacell® | US 6375855 | 70 – 100 | 0.15 – 0.35 | 1000 – 2000 | 20 – 23.5 | 5 – 1000 kDa |
| Corning | Spin-X® | US 5647990 | 0.5 – 20 | n.a. | n.a. | 0.5 – 6 | 5 – 100 kDa |
| Pierce | Pierce™ Protein Concentrator | US 5647990 | 0.5 – 100 | 0.015 – 0.02 | 2000 - 15000 | n.a. | 3 – 150 kDa |
| Pall | Nanosep®, Microsep®, Macrosep®, Jumbosep® | n.a. | 0.5 – 60 | 0.015 – 3.5 | 5000 – 14000 | n.a. | 3 – 1000 kDa |
| Orbital Biosciences | Apollo® | US 6357601 | 7 – 20 | 0.003 – 0.067 | 8500 | 5.2 – 12 | 9 – 150 kDa |

† most probable patent, some suppliers have not disclosed which patent is used in each device. ‡ depends on the size of the device. ⸸ range of the MWCO (kDa = kg/mol), or pore size, of the membrane, may not be available for all device sizes. n.a.: information not available.

Centrifugal filtration devices currently available are inefficient to concentrate low MW solutes even though MF/UF membranes are replaced by NF membranes. The main limitation of commercial CUF devices is the decrease of the pressure near the membrane as the volume of the unfiltered sample decreases, which leads to the interruption of the permeation for solutions with high osmotic pressure. The device designed by Hammond and colleagues have the same limitation, while the device developed by Li and colleagues is not suited to obtain high concentration factors ($CF$). Therefore, innovative centrifugal filtration devices are necessary to concentrate low MW solutes using NF membranes.

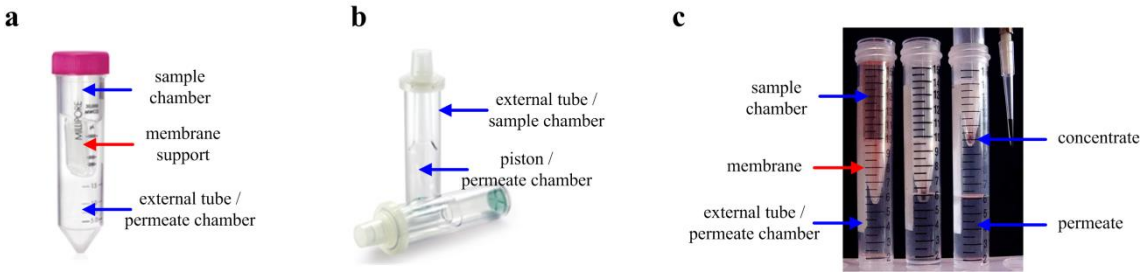


Figure 5-5 – Some of the commercial CUF devices currently available in the market: a) Amicon® Ultra centrifugal filter (15 mL); b) Centriprep® centrifugal filter; c) Apollo® concentrator. The figures a and b are propriety of EMD Millipore Corporation, their use was authorized for this work, and cannot be copied without their owner written permission. The figure c is propriety of Orbital Biosciences LLC, its use was authorized for this work, and cannot be copied without its owner written permission. Amicon is a trademark of Merck KgaA. Centriprep is a trademark of Merck KgaA. Apollo is a trademark of Orbital Biosciences LLC.

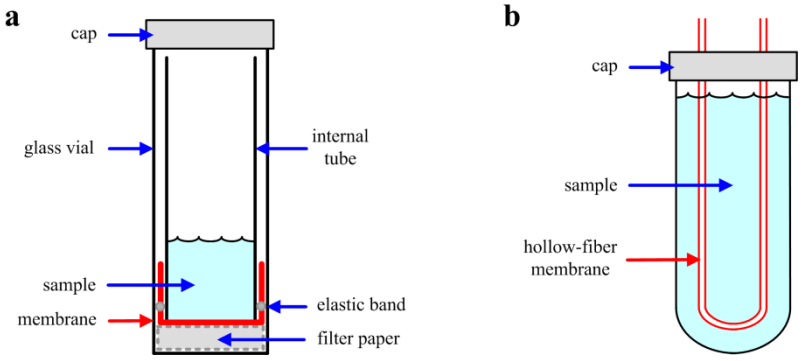


Figure 5-6 – Sketches of the handcraft centrifugal filtration devices developed by other authors: a) centrifugal ultrafiltration-dialysis; b) hollow-fiber centrifugal ultrafiltration.

## 5.3 Experimental part

### 5.3.1 New centrifugal nanofiltration device

An innovative centrifugal nanofiltration device was developed in this thesis to overcome the limitations of the common CUF devices. In common CUF devices (Figure 5-2), the sample occupies a large portion of the volume upstream the membrane and a high concentration factor

is only obtained when the meniscus of the liquid reaches a radial position close to concentrate chamber, after most of the liquid has been filtered. Since the pressure, given by the centrifugal force, decreases quadratically with the decrease of the liquid head, as defined by equation (2-49), a significant part of the liquid has to be filtered at a pressure much lower than the initial one. For centrifugal processes with MF and UF membranes, this issue only implies, usually, the increase of the filtration time (because the hydraulic permeability of these membranes is very high and the osmotic pressure of the liquids is very low). However, the separation of small molecules by NF membranes poses two other problems. First, the hydraulic permeability of the membranes is smaller than those of MF and UF membranes and, for that reason, a much higher pressure is needed. Thus, the decrease of the pressure as the liquid head decreases is a very important limitation that must be carefully addressed. Second, the filtration is even made more difficult by the increase of the osmotic pressure due to the increase of the solute concentration along the filtration cycle and due to the CP phenomenon.

Although the permeate flux can be increased, up to a certain threshold value, by increasing the rotational speed in the centrifuge, two issues may arise. On the one side, above particular angular velocities, the centrifuge may become unstable leading to mechanical rupture of the rotor or of the CNF device. In addition, increasing the pressure of the liquid may compact the membrane, resulting in a decrease of the permeate flux. On the other side, the available centrifuges may have inadequate rotational speed range to conduct the nanofiltration. Therefore, it is important to develop an efficient CNF device that takes all these constraints into to consideration.

## Design and material of the new centrifugal nanofiltration device

### *Design of the CNF device*

Ideally, the filtration of small solutes with significant osmotic pressure using centrifugal filtration would be performed in a device where the sample chamber is displaced, by a large distance, from the region where the filtration occurs (the filtration chamber), resulting in a large liquid head. An ideal centrifugal filtration device would be similar to that depicted in Figure 5-7a, where the sample chamber is connected to the filtration chamber by a long and thin neck channel (Geraldes et al. 2018). The neck channel would have to be long enough in order to maximize the distance between the positions $r_1$ and $r_2$, and thus increase the generated pressure for the same angular velocity $\omega$. At the same time, the neck channel should be as thin as possible to obtain high concentration factors when the liquid meniscus reached the position $r_1$. Additionally, the ideal centrifugal filtration device would have a concentrate chamber to avoid

filtration to dryness and to operate as a receptacle of most of the concentrated fluid elements, and a permeate chamber to collect the fluid that passed through the membrane.

The developed centrifugal nanofiltration device was first intended to be used with the commercial centrifuge rotor SS-34 (Sorvall, USA) and, for that reason, some physical limitations were imposed. The rotor buckets of that rotor have a diameter of 29 mm, a depth of 108 mm and semi-spherical bottom surface (Table E-1). Thus, to avoid tolerance issues in the manufacture of the CNF device, and to ease its removal from the rotor bucket, the designed CNF device has a diameter of 28.7 mm, a height of 103 mm and round shape on its bottom extremity. A sketch of the developed CNF device is depicted in Figure 5-7b and in Figure 5-7c. In both these figures the CNF device is shown placed at an angle $\alpha$ = 34°, which is the characteristic angle of the rotor SS-34, and, therefore, the membrane is aligned with the centrifugal force ($\beta$ = 0°).

In Figure 5-7b the internal chambers and channels of the CNF device are shown. Although in the ideal centrifugal filtration device (Figure 5-7a) the distance between $r_1$ and $r_2$ is arbitrarily large, in the actual CNF the physical dimensions of the rotor bucket and of the sample chamber limits that distance. In Figure 5-7b the radial positions $r_1'$ and $r_2'$ that will be used to calculate the average pressure at the membrane surface at the initial instant of the filtration cycle, $\bar{p}_0$, are also shown. Thus, $r_1$ is the radial position of the innermost extremity of the neck channel (outermost position of the sample chamber), $r_2$ is the radial position of the outermost extremity of the neck channel (innermost position of the filtration chamber), $r_1'$ is the radial position of the air-liquid meniscus in the sample chamber at the initial time instant of the filtration cycle (the innermost extremity of the sample chamber, if fully filled), and $r_2'$ is the radial position of the outmost extremity of the filtration chamber (innermost position of the concentrate chamber).

An extra channel exists in the developed CNF device, the auxiliary channel Figure 5-7b, which is used to inject the liquid sample into the device and to remove the concentrate.

In Figure 5-7c, the individual parts that assembled constitute the CNF device are identified. Thus, the developed CNF device was constituted by a membrane that is glued on the top surface of the membrane support part. The membrane support part was engaged on the top part and on the bottom part. Two O-rings kept these parts fixed and prevented liquid leakage. Over the membrane, and inside the top part, there was an internal block. It was this internal block that defined the sample chamber, the filtration chamber, the concentrate chamber, the neck channel and the auxiliary channel. Thus, the dimensions of these chambers and channels could be changed by replacing the internal block by a different one with a distinct geometry. On the top surface of the top part, there was a hole that was used for sample injection and for processed liquids removal (with the exception of the permeate which is removed by detaching

the bottom part). The hole in the top part was closed by a cap and was kept leakage free by an O-ring. To prevent pressure imbalance, vent holes were placed on the top and bottom parts. The

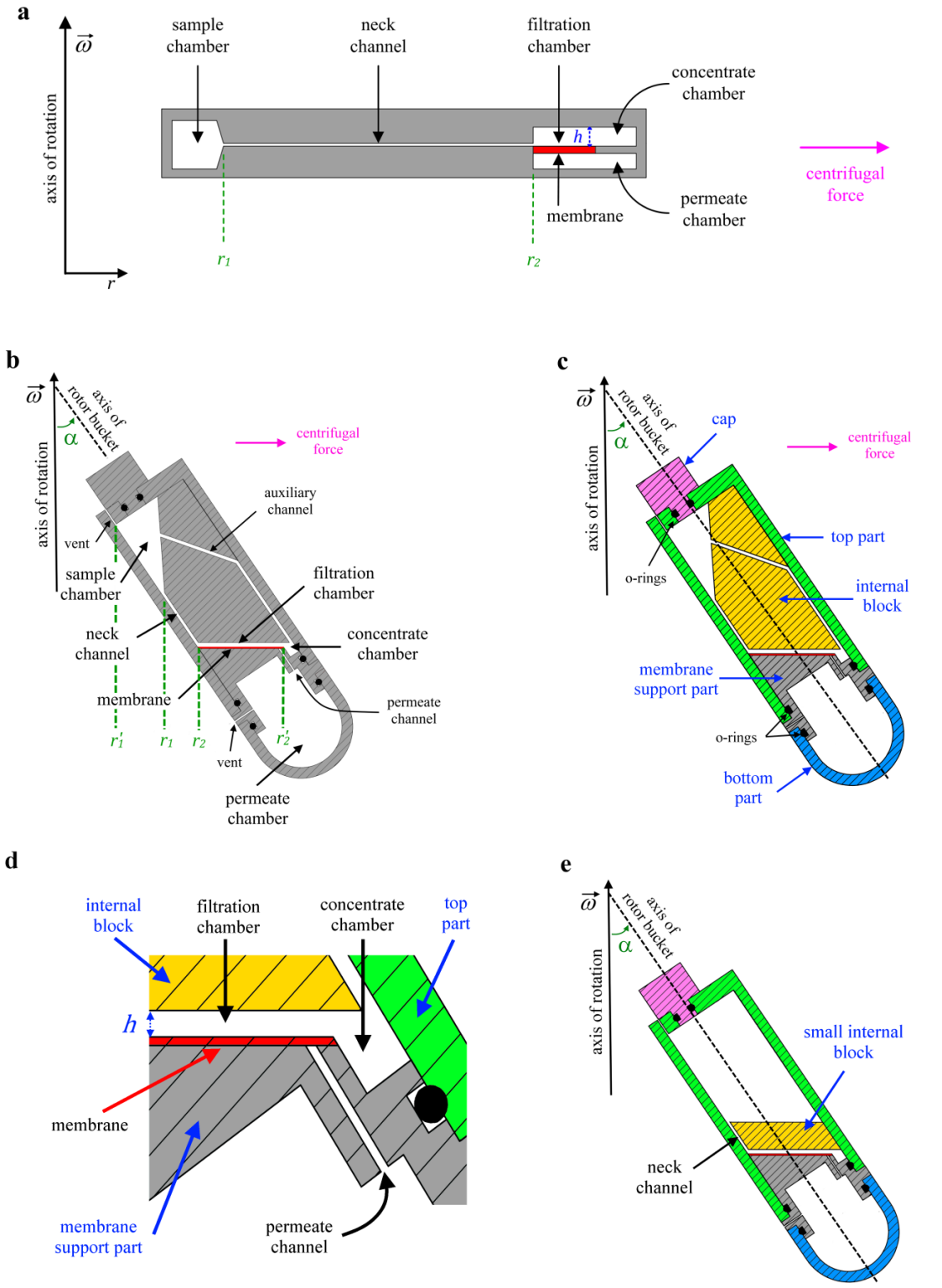


Figure 5-7 – Sketches of the centrifugal nanofiltration device developed in this work: a) generic idea for an efficient CNF device; b) internal chambers and channels of the CNF device; c) individual parts of the CNF device; d) zoom-in of the CNF device near the membrane region to show the definition of the height of the filtration chamber, $h$; e) small internal block used in the first experiments related to the study of the effect of $h$.

locations of these vents were designed such that, either during the filtration cycle or at rest, no liquid escapes from the sample chamber or from the permeate chamber to the exterior of the device, if it is kept upright or inside the rotor bucket in the proper orientation.

With no internal block inside the device, the volume of the chamber above the membrane is 20 mL. This internal chamber is defined by the walls of the membrane support part, top part and cap. Using any internal block the volume of the sample chamber is 2.9 mL. However, each of the internal blocks was machined to result in a different height of the filtration chamber, as defined in Figure 5-7d. Therefore, the total volume available for the sample varies from 3.1 mL (for $h$ = 0.1) to 4.0 mL (for $h$ = 2.4 mm).

The first experiments related to the study of the influence of $h$ on the CNF performance were performed using a smaller internal block, depicted in Figure 5-7e, but for the subsequent experiments (temporal evolution, $\beta$angle effect studies, and other studies on the effect of $h$) the device with the standard internal block, as sketched in Figure 5-7c, was used.

The expected volumetric concentration factor, defined as the ratio between the sample volume and the concentrate volume, depends on the height of the filtration chamber and at which radial position the liquid meniscus stops. Thus, if the filtration stops when the air-liquid interface is at the entrance of the filtration chamber (position $r_2$ in the Figure 5-7b) then the volumetric $CF$ should be 7, 11, 19 and 22 for the filtration channel heights of 1.3 mm, 0.6 mm, 0.2 mm and 0.1 mm, respectively. On the other hand, if the air-liquid interface stops at the end of the filtration chamber (position $r_2'$ in the Figure 5-7b) the volumetric $CF$ should be 44, 57, 70 and 74, for the same channel heights.

*Selection of the material for the CNF device*

The material to be used for the construction of the centrifugal filtration devices should fulfill two mandatory requirements: possess enough mechanical strength to withstand the centrifugal forces without suffering bending or mechanical damage, while, at the same time, to be light enough to not surpass the weight threshold per bucket specified by the centrifuge manufacturer. Since the objective of this work was to prove the feasibility of the centrifugal nanofiltration process, the focus was placed on the material physical properties rather than in the cost of the prototype.

The mechanical strength is the most important property for the selection of the material to be used. On the one hand, the CNF device must not break during spinning due to two reasons. First, if the device disintegrates during spinning it could damage the centrifuge and cause human injuries. Second, even minor damage or leakage of the liquids invalidates the running experiments. On the other hand, it is the purpose of the work to study the effect of the angle between the centrifugal force and the membrane surface. Excessive bending of the surface

where the membrane is supported would impair the validity of the experiments. Thus, the selected material should guarantee enough mechanical strength to not brake neither bend.

Stainless steel, aluminum and acrylic plastic were pre-selected as candidate materials. By design, the volume of material to be used in the construction of the centrifugal nanofiltration was ca. 29 $cm^3$ (excluding the internal block part). Since the threshold of weight per rotor bucket for the two smaller used rotors is 115 g (Kendro Laboratory Products 2003), the use of stainless steel was immediately discarded. The selection between acrylic and aluminum was based on the tensile strength and on the bending magnitude when under stress.

Ideally, a comprehensive mechanical study of the behaviour of the centrifugal filtration device under stress should have been performed. Since part of the external case of the CNF device is supported by rotor bucket, only a basic analysis of the bending of the top surface of the membrane support part was done. The top surface of the membrane support part is subject to the pressure of the liquid, thus, it is important to access how much it bends under stress.

Admitting that the top surface of the membrane support part functions as a circular plate, with its edges clamped, and that a uniform load is applied on the surface, the maximum deflection, $w_{max}$, occurs at the center of the plate (Chandrashekhara 2001) and it is given by

$$w_{max} = \frac{q r_p^4}{64D} \tag{5-1}$$

where $q$ is the load (i.e. the pressure), $r_p$ is the radius of the circular plate, and $D$ is the flexural rigidity. This latter parameter is defined as

$$D = \frac{E t^3}{12(1-\upsilon^2)} \tag{5-2}$$

where $t$ is the thickness of the plate, and $E$ and $\upsilon$ are, respectively, the Young's modulus and the Poisson's ratio of the material. Under the assumed conditions, the maximum bending stress, $M_{max}$, also occurs at the center of the plate and is given by

$$M_{max} = \frac{q r_p^2 (1+\upsilon)}{16} \tag{5-3}$$

If the top surface of the membrane support part was made of acrylic with a thickness of 3 mm, then a load of 50 bar would result in the bending magnitude of 0.24 mm. Since it is intended to perform centrifugal nanofiltration in devices with filtration chamber channel height as low as 0.1 mm, then the use of acrylic would lead to biased results. More significant is the fact that, for a load of 50 bar, the maximum bending stress is higher, or very close, than the

tensile strength of the acrylic (48 – 80 MPa), which would lead to mechanical rupture of the material. The use of aluminum, or aluminum alloys, results in lower bending magnitude, have higher tensile strengths, and, for that reason, an aluminum alloy was selected as the material to be used in the construction of the centrifugal nanofiltration device (with the exception of the internal block part). Bending magnitudes and bending stresses for loads of 25 and 50 bar are shown in Table 5-2. The Young modulus for acrylic and aluminum are 3 GPa and 70 GPa, respectively, while the Poisson ratios for both materials are 0.38 and 0.35 (Comte & von Stebut 2002; Shareef & Schmitt 2004; Matbase, 2017).

Table 5-2 – Bending magnitude and bending stress of acrylic and aluminum clamped circular plates with 3 mm thickness for a loads of 25 and 50 bar.

| Material | $q$ (bar) | $w_{max}$ (mm) | $M_{max}$ (MPa) |
|---|---|---|---|
| Acrylic | 50 | 0.238 | 61.1 |
| | 25 | 0.099 | 30.5 |
| Aluminum | 50 | 0.011 | 58.9 |
| | 25 | 0.004 | 29.4 |

Two remarks should be made about these basic mechanical calculations. First, during the filtration cycle, the load on the surface is not uniform, since the centrifugal pressure varies with radial distance. Second, despite the thickness of the top surface of the membrane support part is, by design, 3 mm, the fact is that, due to the manufacturing process, some sections below the surface are thicker. Nevertheless, these two deviations of the actual system in relation to the model used to design them do not discredit the reasoning adopted for the material selection

Due to the weight per rotor bucket threshold, the internal block part is made of Teflon™. Since this is a solid part with more than 10 mm thickness no significant bending is expected.

The O-rings were made of nitrile because the samples were non-corrosive and mild temperature was applied during centrifugation (20 °C).

**The prototype**

The final prototype of the developed CNF device is shown in Figure 5-8. Parts are engaged due to the stress of the O-rings pressing against their surfaces. After some initial tests to select both the best available glues and the method to fix a piece of dry membrane on the membrane support part of the CNF device, a well-defined procedure was adopted, which is described in the Procedure F-8 (Appendix F).

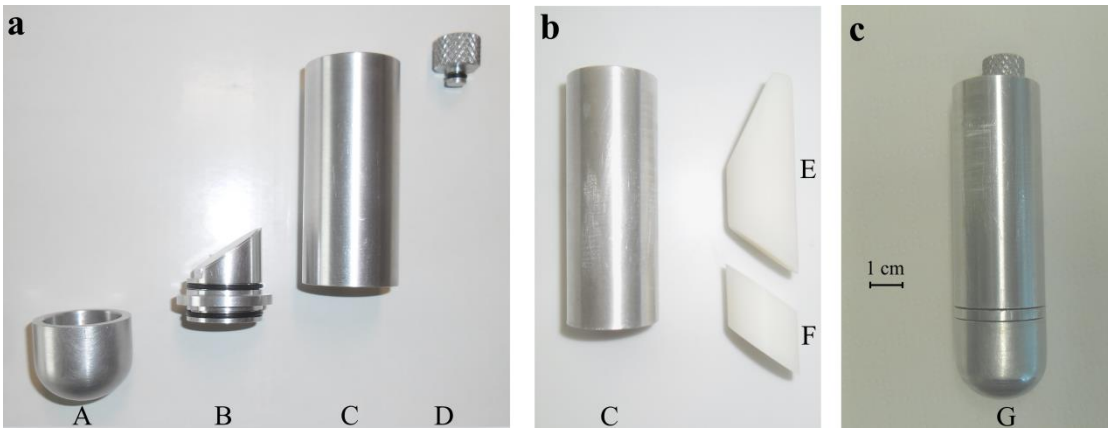


Figure 5-8 – Final prototype of the developed CNF device: a) the parts of the CNF include the bottom part A, the membrane support part B, the top part C, the cap D; b) the internal block part E or the small internal block F are used to create the sample chamber, the filtration chamber, the concentrate chamber, the neck and auxiliary channels; c). assembly of the device. Figure adapted from (Completo et al. 2017).

**Adaptors for changing the $\beta$ angle of the centrifugal nanofiltration device**

In order to manipulate the $\beta$ angle, four different adapters were manufactured, by 3D-printing. These adaptors are shown in Figure 5-9. Therefore, when the CNF device is inserted inside each one of the adaptors the membrane gets a distinct $\beta$ angle relative to the centrifugal force. These adapters were designed to be used with the F10-6x500y rotor. While the SS-34 and the SA-300 are rotors have an $\alpha$ angle of 34° and each bucket takes 50 mL vials, the F10-6x500y rotor has a characteristic $\alpha$ angle of 23° and each bucket withstands vials of 500 mL. In this way, it was possible to slightly change the positioning of the CNF device during the filtration cycle, creating adaptors for $\beta$ = -10°, 0°, +2° and +10°. These adaptors could be used only inside the F10-6x500y rotor. The $\beta$ angle in the SS-34 and in the SA-300 rotors was fixed to $\beta$ = 0°.

The adapters were manufactured in an Ultimaker 2+ 3D-printer (Ultimaker, The Netherlands) using filaments of polylactic acid plastic. The original Autocad® files were converted to “iges” format file, imported to Onshape cloud and then printed using Cura software with the following parameters: infill = 50%, outside shell = 1.2 mm, and height resolution = 0.1 mm.

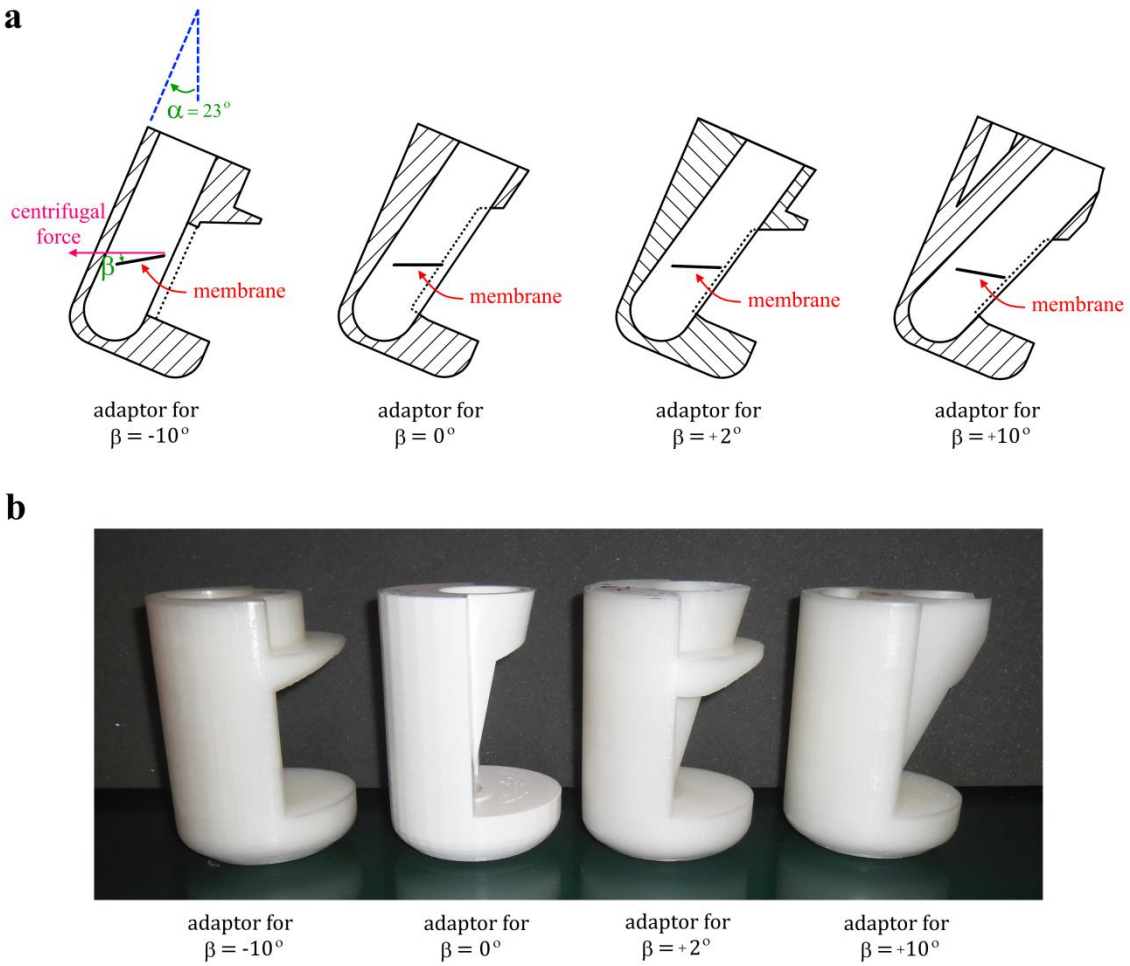


Figure 5-9 – Rotor adapters used to manipulate the angle $\beta$: a) cross-section sketches of the adapters and location of the membrane; b) 3D-printed adapters.

### 5.3.2 Experimental setup

The centrifugal nanofiltration experiments were performed using the CNF device and the rotor adaptors described in section 5.3.1. Three different fixed-angle centrifuge rotors were used. The SS-24 (Thermo Fisher Scientific Incorporated, 2010) and SA-300 (Thermo Fisher Scientific Incorporated, 2014c) rotors have a bucket volume of 50 mL and a characteristic $\alpha$ angle of 34°, the F10-6x500y (Thermo Fisher Scientific Incorporated, 2014b) rotor has a bucket volume of 500 mL and $\alpha$ angle of 23°. The total volume of the CNF device is around 50 mL and, therefore, it fits tightly inside the SS-24 and SA-300 rotors, while to be securely placed inside the F10-6x500y rotor the 3D-printed rotor adaptors are needed. The geometric characteristics of the three rotors, of the four rotor adaptors and of the CNF device when engaged on the centrifuge are expressed in Table 5-3.

The rotors were made to spin in a RC6 centrifuge (Sorvall, USA) (Figure 5-10) at 20 °C (set at the centrifuge control panel). The rotational speed of the centrifuge is limited by the rotors specifications. According to the manufacturers, and admitting that the maximum weight

per rotor bucket is not surpassed, the smaller SS-34 and SA-300 rotors can rotate up to 20,000 rpm, while the bulkier F10-6x500y rotor is limited to 10,000 rpm.

Table 5-3 – Specifications of the rotors, rotor adaptors and CNF device when engaged in the centrifuge.

| Rotor | $\alpha$ (º) | bucket volume (mL) | adaptor | $\beta$ (º) | $r_{max}$ † (mm) | $r_1$ (mm) | $r_2$ (mm) | $r_2'$ (mm) |
|---|---|---|---|---|---|---|---|---|
| SS-34 | 34 | 50 | no | 0 | 107 | 41.0 | 67.3 | 88.1 |
| SA-300 | 34 | 50 | no | 0 | 96.7 | 30.6 | 57.0 | 77.8 |
| F10-6x500y | 23 | 500 | yes | -10 | 158 | 95.3 | 115.3 | 135.8 |
| | | | yes | 0 | 158 | 84.9 | 111.3 | 132.2 |
| | | | yes | +2 | 158 | 82.9 | 110.5 | 131.4 |
| | | | yes | +10 | 158 | 75.8 | 107.8 | 128.3 |

† $r_{max}$ is the maximum radial position inside the rotor bucket.

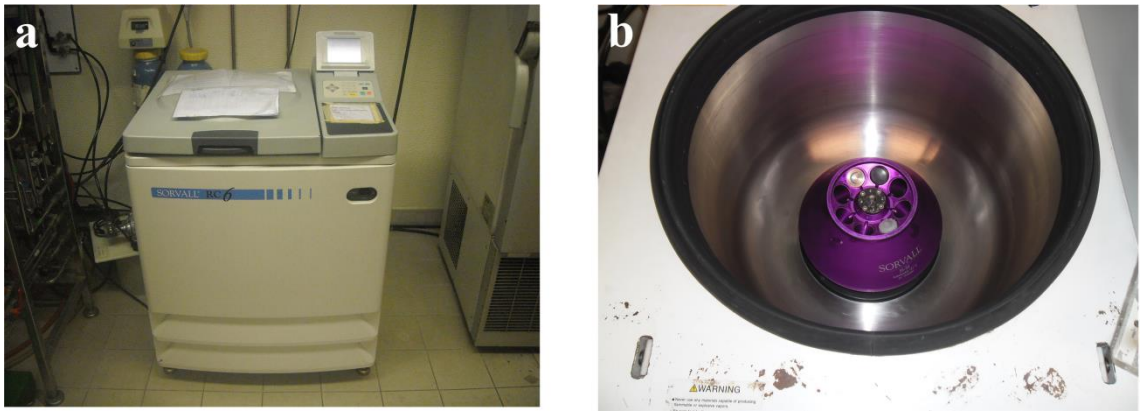


Figure 5-10 – Centrifugal equipment used in this work: a) RC6 centrifuge; b) SS-34 rotor engaged on the centrifuge.

### 5.3.3 Materials

The samples fed to the CNF device consisted of binary aqueous solutions using as model solutes: potassium sulfate ($K_2SO_4$) of reagent grade (Scharlau, Spain), D(+)-sucrose (hereafter designated as sucrose) of analysis grade (Panreac, Spain) and polyethylene glycol (hereafter designated as PEG-1000). The solutions were prepared by dissolving precise amounts of the solute in deionized water. The deionized water was produced in an ion exchange resin module, and its conductivity being lower than 10 µS/cm. In this part of the work, the solute concentrations were selected such that the osmotic pressure of the samples were: $\pi_f$ = 0.6 bar, $\pi_f$ = 2.6 bar and $\pi_f$ = 7.6 bar. Therefore, the solute concentrations are those defined in Table 5-4.

Three different membranes were tested, but only two of them were used in a consistent way. The relationship between the permeate flux and the rotational speed performed at low concentration factors was obtained using the Desal TFM-50 membrane (GE Osmonics, USA),

which is the same membrane used in the nanofiltration TFF experiments performed to study the CP phenomena by holographic interferometry (Chapter 4). The NFX membrane (Synder Filtration, USA) was used in all the experiments related with high concentration factor, with the influence of the filtration chamber height, with the influence of the angle $\beta$, or to assess the temporal evolution of the CNF process. NFX was one of the membranes used in the experimental work developed for the concentration of small-volume samples by micro-TFF (Chapter 3). Exploratory experiments were also performed with cupons cut from M-N2540A9 membrane module (Applied Membranes Inc., USA) but it was discarded since it presented surface dents and lower sucrose rejection than the NFX membrane.

Table 5-4 – Selected solute concentrations to be used in the CNF experiments.

| | Solute | | |
|---|---|---|---|
| | $K_2SO_4$ | Sucrose | PEG-1000 |
| $c$ (g/L) for $\pi$ = 0.6 bar | 2 | 7.7 | 23.1 |
| $c$ (g/L) for $\pi$ = 2.6 bar | 8 | 30.7 | 78.4 |
| $c$ (g/L) for $\pi$ = 7.6 bar | 24 | 88.9 | 160.9 |

### 5.3.4 Methods

In this sub-section, the methodologies used to run each type of CNF experiments and to calculate the effective area of the membrane glued on the CNF device are presented. The procedures to fix the membrane in the CNF device, to inject the sample or to withdraw liquids from the device are described in Appendix F.

As in any pressure-driven membrane process, the performance of the CNF process depends on the applied pressure on the liquid at the membrane surface. In the CNF process, the pressure is generated by centrifugal force, which in turn is function of the rotational speed, of the distance to the axis of rotation, of the liquid density and of the liquid head. For ease of comparison, the performances from different experiments are compared based on the centrifugal pressure at the initial instant of the filtration, $\bar{p}_0$, calculated by integration of equation (2-49) over the entire membrane area defined as in Figure 5-11, which is a sketch of the top view of the membrane. Thus the membrane is assumed as a partial ellipse centered at $c$, with semi-major and semi-minor radii $a$ and $b$, respectively.

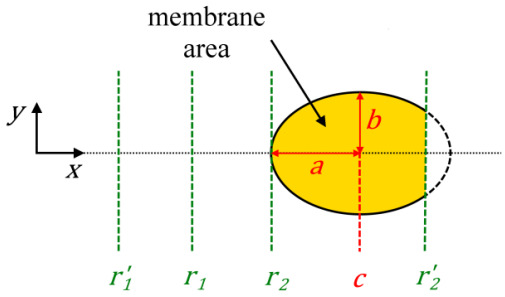


Figure 5-11 – Top view sketch of the membrane used in the developed CNF device.

Therefore, an estimate of $\bar{p}_0$ is given by

$$\bar{p}_0 = \frac{\iint_{A_m} \Delta p \cdot dA}{\iint_{A_m} dA} \approx \frac{\int_{r_2}^{r_2'} \int_{-\sqrt{b^2(1-(x-c)^2/a^2)}}^{\sqrt{b^2(1-(x-c)^2/a^2)}} \left( {}^1\!/_2 \, \rho\omega^2 \left( \left(\sqrt{x^2+y^2}\right)^2 - (r_1')^2 \right) \right) \cdot dydx}{\int_{r_2}^{r_2'} \int_{-\sqrt{b^2(1-(x-c)^2/a^2)}}^{\sqrt{b^2(1-(x-c)^2/a^2)}} dydx} \quad (5\text{-}4)$$

To calculate $\bar{p}_0$ it was assumed that at the beginning of the filtration cycle the sample chamber is fully filled with a liquid of constant density ($\rho$ = 1000 kg/m$^3$) and that different radial locations are those expressed in Table 5-3. For $\beta$ = 0°, the correspondence between the rotational speed and $\bar{p}_0$ is given in Table 5-5. For the sake of clarity the $\bar{p}_0$ values are rounded to the near unity.

Table 5-5 – Correspondence between rotational speed and $\bar{p}_0$ for the used rotors and and rotor adaptors at $\beta$ = 0°.

| rotational speed (rpm) | $\bar{p}_0$ (bar) | | |
|---|---|---|---|
| | rotor | | |
| | SS-34 | SA-300 | F10-6x500y (with the rotor adaptor for $\beta$ = 0°) |
| 6000 | 9 | – | 16 |
| 7000 | – | – | 21 |
| 7500 | 14 | – | – |
| 8000 | – | – | 28 |
| 9000 | 20 | – | 35 |
| 10000 | 25 | – | 43 |
| 11000 | 30 | – | – |
| 12000 | 36 | – | – |
| 13000 | 42 | – | – |
| 16000 | – | 52 | – |
| 19500 | – | 77 | – |

**Proving the concept of centrifugal nanofiltration**

To the best knowledge of the present thesis' author, no previous studies dealing with the nanofiltration of small-volume samples by centrifugal filtration have ever been disclosed in the open literature. Thus, the first step in this work, prior to sample concentration at high $CF$, was to evaluate whether nanofiltration by centrifugation is viable, i.e. if it is possible to obtain high-quality permeate (high $R_a$) at fair permeate fluxes ($J_v$). To do this, centrifugal nanofiltration of all the model solutions (Table 5-4) were performed at distinct rotational speeds, given in terms of $\bar{p}_0$, using the Desal TFM-50 membrane.

To obtain consistent and comparable results, the experiments were conducted such that the amount of collected permeate was ca. 1 mL. The exceptions were the scenarios of permeation at low $\bar{p}_0$ and high $\pi_f$, where the permeate flux is very low. In these cases, the minimum acceptable permeate volume was ca. 0.3 mL.

For these preliminary experiments the SS-34 rotor was used, so $\beta$ = 0°. Moreover, the experiments were performed in the so called open chamber mode, where no internal block part was placed inside the CNF device. Therefore, above the membrane there was a 20 mL sample chamber where the liquid could move freely. In addition, these preliminary experiments were performed using a single membrane piece, which remained functional during the whole period of these experiments.

Since the rotor was stored overnight in a refrigerated room (at 4 °C) the first step to be taken every day was to stabilize the temperature by performing once or twice 20-minute filtration cycle with deionized water. In that way, the temperature of both the centrifuge and the CNF devices reached 20 °C, while, at the same time, the assembly was checked for leakages.

The influence of the $\beta$ angle on the CNF performance at low concentration experiments, in the open chamber mode, was also assessed. These were performed using the four F10-6x500y rotor adaptors and their results will be later compared with the ones performed using the internal block part to obtain high $CF$ values. In these experiments and in all the following ones the NFX membrane was used.

**Temporal evolution of a concentration process by centrifugal nanofiltration**

After proving that the CNF device was capable of nanofilter small-volume samples, the next step was to verify if it was also appropriate to concentrate binary solutions of high osmotic pressure up to high concentration factors ($CF \approx 10$). To evaluate the performance of the CNF device for such task, the experiments were performed using the internal block part inside the device. Several internal block parts were manufactured with different specifications leading to

distinct heights of the filtration channel. However, prior to the study of the influence of $h$ and $\beta$ on the CNF performance, one must evaluate how the CNF process develops with time. This will provide an insight on the necessary time to concentrate a specific solution.

The temporal evolution of the solute concentration inside the CNF device depends on several parameters. Moreover, it is not always possible to obtain complete filtration. By complete filtration, it is meant the filtration up to the condition where the whole liquid injected into the sample chamber has receded into the filtration and/or concentration chambers, leaving the sample chamber empty at the end of the filtration cycle. Complete filtration occurs only when the generated pressure is higher than the osmotic pressure at the membrane surface during the whole filtration cycle and provided that the filtration cycle is long enough. Conversely, if at any moment the generated pressure is not enough to overcome the osmotic pressure, the permeation stops and some amount of liquid remains inside the sample chamber at the end of the filtration cycle. Therefore, it is important to know in advance the necessary time to obtain complete filtration or the moment when the filtration process is interrupted. Otherwise, one will not achieve the highest possible $CF$ value or one will waste time and principally cause unnecessary mechanical stress on the centrifuge and centrifuge rotor.

To have a glimpse of the temporal evolution of the filtration process, some experiments were performed with sucrose solutions ($\pi_f$ = 2.6 bar) where the resulting liquids (permeate, concentrate and liquid remaining inside the sample chamber) were collected, at distinct filtration moments, and further analysed. The temporal evolution was evaluated for different scenarios where both the rotational speed and height of the filtration chamber were changed. Three rotational speeds (those resulting in $\bar{p}_0$ = 16 bar, 21 bar and 35 bar) and two filtration chamber heighs ($h$ = 0.1 mm and 1.3 mm) were tested. For these experiments, it was used the F10-6x500y rotor coupled to the rotor adaptor with $\beta$ = 0°.

**Influence of $h$ and $\beta$ for solution concentration at high $CF$**

The CNF device was optimized regarding the height of the filtration chamber, $h$, and the angle between the centrifugal force vector and the tangent to the membrane surface, the $\beta$ angle. To verify the influence of $h$ several internal block parts were used. Each of these internal block parts have different rim heights on their bottom surface resulting in distinct $h$ values ($h$ = 0.1 mm, 0.2 mm. 0.6 mm, 1.3 mm and 2.4 mm). The effect of the $\beta$ angle was accessed using the four rotor adaptors (section 5.3.1) to be used with the F10-6x500y rotor. By design, each one of the four rotors define different $\beta$ angles ($\beta$ = -10°, 0°, +2° and +10°).

Since the positioning of the CNF device is different in each rotor adaptor, the membrane is located at slightly distinct radial positions, as was already defined in Table 5-3. Therefore, to

study the influence of the $\beta$ angle on the CNF performance, the rotational speed for each rotor adaptor was adjusted to give equivalent $\bar{p}_0$ values. For $\bar{p}_0$ = 16 bar and $\bar{p}_0$ = 35 bar the equivalent rotational speeds (in rpm) are expressed in Table 5-6.

Table 5-6 – Rotational speeds (in rpm) equivalent to $\bar{p}_0$ = 16 bar and $\bar{p}_0$ = 35 bar, when using the rotor adaptors for the F10-6x500y rotor.

| $\beta$ (º) | $\bar{p}_0$ (bar) | |
|---|---|---|
| | 16 | 35 |
| +10 | 5860 | 8800 |
| +2 | 5990 | 8980 |
| 0 | 6000 | 9000 |
| -10 | 6480 | 9720 |

**Measurement of the effective membrane area**

Different concentration scenarios (effect of $\bar{p}_0$, $h$, $\beta$, $c_f$) were compared using data from experiments where distinct membrane assemblies were used. For instance, the permeate flux is often used to compare the nanofiltration performance. However, the membrane permeability varies every time a new membrane piece is glued on the CNF device. This occurs both due to heterogeneities on the membrane surface and to change of the membrane area in every assembly covered by the glue. For this reason, the permeate flux is usually presented as the ratio $\bar{J}_v/\bar{J}_w$ in order to permit correct comparison.

For illustrative purposes, the effective membrane areas of some assemblies were determined to show their variation. In addition, due to the used method to glue the membrane to the membrane support part (Procedure F-8), the effective membrane area varies not only between different assemblies but also between the top side (feed side) and the bottom side (permeate side). The effective membrane areas were determined by digitally scanning images of both sides of the membrane and converting the number of pixels of the glue-free zones to surface area, using a scale.

### 5.3.5 Chemical analysis

Since the samples and liquids resulting from the CNF processes are binary aqueous solutions of the salts and neutral molecules listed in section 5.3.3, its quantitative analysis was performed by conductometry and differential refractometry in accordance to the methodology already described in section 3.4.4.

## 5.4 Results and discussion

### 5.4.1 Particularities of the handcrafted gluing process

The handmade process of gluing a membrane piece on the CNF prototype results in some degree of variance of the effective membrane area and of the membrane durability. Herein, membrane durability is referred as the time that the assembly withstands without leaking. Other characteristics, like the permeate rate and the hydraulic permeability, depend on the effective area of the membrane and on the membrane piece itself.

**Impact of the gluing process on the membrane area, hydraulic permeability and solute rejection**

Illustrative data for five membrane assemblies are shown in Table 5-7 in terms of the effective membrane area, the water permeate flux (obtained at $\bar{p}_0$ = 16 bar) and the solute rejection for the centrifugal nanofiltration (low $CF$) of a 30.7 g/L sucrose aqueous solution (also obtained at $\bar{p}_0$ = 16 bar).

To fix a membrane to the CNF device, the glue is spread over and under the membrane with two objectives: to seal the filtration and permeate chambers and to protect the active surface of the membrane from the stress caused by the weight of the internal block. However, the adopted gluing process turns the glue-free area over the membrane larger than the corresponding one under the membrane: 2.5 ± 0.1 $cm^2$ on the top side of the membrane (active side) versus 2.1 ± 0.1 $cm^2$ on the bottom surface (permeate side).

In terms of water permeate fluxes, which were determined based on the effective membrane areas, differences up to 40 % were verified for the membranes mentioned in Table 5-7. According to membrane manufacturers, deviations up to 20% are expected due to heterogeneities in small membrane pieces.

Two factors could have caused the verified larger discrepancy. First, $\bar{p}_0$ does not correspond to $\Delta p_m$, neither to an average pressure along the filtration cycle. Thus, different amounts of collected water in the permeate chamber result in distinct average pressures, despite the same value of $\bar{p}_0$. Another cause for the large $\bar{J}_w$ differences is the inadequate removal of the membrane protective layer: the two 30 min cycles of water permeation at $\bar{p}_0$ = 16 bar is probably insufficient for the complete cleaning of the membrane. However, since each membrane gluing has a limited durability, it was decided to proceed with the experiments with the membrane as is. In terms of the membrane rejection, for the first experiment after the measurement of $\bar{J}_w$, the $R_a$ values (for open chamber mode) were always above 99% for the

tested sucrose solution.

The issue of membrane area variation and of hydraulic permeability variation, from device to device, is twofold. First, different permeate rates on different devices result, for the same sample and filtration cycle, in different $CF$ values. Second, different permeate rates may cause mass imbalance, which makes the centrifuge stop spinning in the best scenario, but can cause damage to the CNF device, to the centrifuge or even for the operator in the worse scenario. For the used CNF device, which withstand small volumes from 3 to 4 mL, mass imbalances were rare and, therefore, that was not an issue in the present work. However, if larger devices are made to accommodate larger sample volumes, this issue must be taken into account. Even though, mass imbalance depends on the specifications of the equipment. Thus, further studies on the mechanical stability of the systems are required to ensure safe operation. Nevertheless, the risks can be minimized by optimizing the membrane assembly process, so that the active area is constant, and using membranes that guarantee homogeneous permeability.

Table 5-7 – Membrane area, permeate flux and sucrose rejection, for some illustrative membrane pieces.

| Membrane | Area ($cm^2$) | | $\bar{J}_w$ ($L \cdot m^{-2} h^{-1}$) † | $R_a$ ‡ |
|---|---|---|---|---|
| | (top surface) | (bottom surface) | (top surface) | |
| 2016-07-18 | 2.49 | 2.05 | 25.1 | 98.8 |
| 2016-07-21 | 2.70 | 2.15 | 17.5 | 99.8 |
| 2016-09-05 | 2.58 | 1.86 | 17.7 | 99.5 |
| 2016-09-15 | 2.30 | 2.10 | 29.7 | 99.5 |
| 2016-09-22 | 2.55 | 2.03 | 16.2 | 99.7 |

† at $\bar{p}_0$ = 16 bar; ‡ 30.7 g/L sucrose aqueous solution at $\bar{p}_0$ = 16

**Membrane durability**

The durability of the membrane, in terms of the absence of leakages, is related to the amount of glue used and with the applied mechanical stress it experiences. If the venting system works properly, centrifugal force does not damage the membrane up to 42 bar. Above this pressure threshold only two experiments were run (one at $\bar{p}_0$ = 52 bar and another at $\bar{p}_0$ = 77 bar) and both for a limited time period (1.2 hours each). Leaking has occurred only when the glue peeled off from the aluminum surface of the membrane support part.

A trade-off had to be made in terms of the amount of the used glue. Too few glue was not enough to give stress resistance. Conversely, if a large amount of glue was used it spread under the membrane support layer during the membrane gluing process resulting in low and variable membrane area. On the other hand, the internal block part could cause damage to the membrane if the membrane had not a protective glue coating: bulges on the glue coating were visible after some filtration cycles at high $\bar{p}_0$.

As illustrative examples, the durabilities of several membrane assemblies are shown in Table 5-8. The data suggest that the durability of the membrane decreases as the mechanical stress increases (given in terms of the $\bar{p}_0$). Nevertheless, when the gluing process was properly done, a minimum durability of circa six hours could be expected if the CNF device was not subjected to stress higher than $\bar{p}_0$ = 35 bar.

The membranes referred in Table 5-8 were used when the CNF device contained the internal block in its interior; however, in the initial experiments defined in section 5.3.4, the CNF device was used without the internal block. In such circumstances, the experiments were obtained using a single gluing assembly, since it withstood circa 130 hours on use, for more than 2 months. This indicates that part of the problem of the low membrane duration may be attributed to the friction between the internal block and the membrane surface.

Table 5-8 – Examples of the durability of the membrane assembly.

| Membrane | Hours in use without leakage | | | | | | | | |
|---|---|---|---|---|---|---|---|---|---|
| | F10-6x500y rotor | | | | | SA-300 rotor | | | Total |
| | $\bar{p}_0$ (bar) | | | | | $\bar{p}_0$ (bar) | | | |
| | 16 | 21 | 28 | 35 | 43 | 16 | 52 | 77 | |
| 2016-07-04 | 12.2 | 6.7 | 2.1 | – | – | – | – | – | 21.0 |
| 2016-07-12 | 1.0 | – | 3.3 | 6.7 | – | – | – | – | 11.0 |
| 2016-07-18 | 2.5 | – | – | 6.7 | – | – | – | – | 9.5 |
| 2016-07-21 | 1.5 | – | – | 6.0 | – | – | – | – | 7.5 |
| 2016-09-05 | 3.5 | – | – | 12.3 | – | – | – | – | 15.8 |
| 2016-09-15 | 2.9 | – | – | 1.2 | 1.2 | 1.1 | 1.2 | 1.2 | 8.8 |
| 2016-09-22 | 1.5 | – | – | 8.0 | – | – | – | – | 9.5 |
| 2016-09-28 | 6.8 | – | – | 8.0 | – | – | – | – | 14.8 |
| 2016-10-20 | 5.0 | – | – | 4.5 | – | – | – | – | 9.5 |

### 5.4.2 The proof of concept – centrifugal nanofiltration with open chamber configuration

The CNF device can work with and without the internal block part. This part confines the sample chamber and defines the neck channel. When the CNF is used without the internal block part the liquid that fills the space (20 mL) above the membrane flows freely. Thus, in this open chamber configuration, it is expected an efficient self-cleaning mechanism provided by centrifugation, because the flow adjacent to the membrane is not confined by a top wall. At the same time, since the collected permeate volume was low (ca. 1 mL) the concentration factor is small ($CF \approx 1.05$).

Two types of centrifugal nanofiltration experiments were performed in the open chamber configuration. First, it was evaluated the influence of the rotational speed (given in terms of $\bar{p}_0$)

in the nanofiltration of $K_2SO_4$, sucrose and PEG-100 solutions with distinct osmotic pressures. Then, it was assessed whether the $\beta$ angle affects the nanofiltration performance.

**Effects of the rotational speed for different solute solutions**

The effects of the rotational speed, given in terms of $\bar{p}_0$, for the centrifugal nanofiltration in open chamber configuration and $\beta$ = 0° are shown in Figure 5-12. In these experiments, the Desal TFM-50 membrane was used. The plots of Figure 5-12 are grouped by rows and by columns. Each row contains the nanofiltration data of the solutions with the same feed osmotic pressure. Thus, the first, second and third rows show data for the solutions of $\pi_f$ = 0.6 bar, $\pi_f$ = 2.6 bar and $\pi_f$ = 7.6 bar, respectivelly. As for the columns layout, in the first column it is shown the permeate flux, given by the ratio $\bar{J}_v/\bar{J}_{w,42bar}$, i.e. the ratio of the permeate flux at a given $\bar{p}_0$ and the pure water flux at $\bar{p}_0$ = 42 bar. In the second column it is shown the apparent rejection.

The experimental $\bar{J}_v/\bar{J}_{w,42bar}$ ratio (given by the symbols) shows a linear relationship with $\bar{p}_0$ which suggests that, in the studied range, the limiting flux was not reached. Therefore, the CP effect is small when using the CNF device in the open chamber configuration. However, it is clear that, even for solutions with the same initial $\pi_f$, the permeate flux depends on the solute. For the three disctinct $\pi_f$ values, a clear trend exists: the permeate flux decreases as the Schmidt number increases (the order of the Schmidt number of the solutions is $K_2SO_4$ < sucrose < PEG-1000). In addition, as the $\pi_f$ increases the behaviour of the PEG-1000 clearly departed from the corresponding ones of $K_2SO_4$ and sucrose. This fact can also be justified by the evolution of the Schmidt number for PEG-1000 solutions. While $K_2SO_4$ and sucrose solutions have small variation of their Schmidt number as $\pi_f$ increases (from $Sc$ = 670 to $Sc$ = 790 for $K_2SO_4$ and from $Sc$ = 1710 to $Sc$ = 1810 for sucrose, i.e. $Sc$ increased 18 % and 6 %, respectively), in the case of the PEG-1000 the Schmidt number increased 90% from $Sc$ = 3400 to $Sc$ = 6500, mainly due to changes in viscosity.

Another fact supporting the idea of small CP effect (in the open chamber configuration) and of the influence of the viscosity on the mass transport is that the $J_v$ estimates determined by the osmotic model, using the feed solution viscosity in equation (2-26), agree well with the experimental results (compare the symbol points and the solid lines in Figure 5-12).

The observed solute rejection coefficient confirms that the CP effect is not relevant when the CNF is performed in open chamber configuration. The experimental $R_a$ values are very high and stabilize as $\bar{p}_0$ increases, for all the solutes at feed concentrations of low-to-moderate $\pi_f$, i.e. the solutions with $\pi_f$ = 0.6 bar and $\pi_f$ = 2.6 bar. Moreover, the $R_a$ value approaches 100 % for sucrose and PEG-1000 solutions. The maximum $R_a$ value for the $K_2SO_4$ solutions (ca. 97.5 %)

is lower than those for the other two solutes, but it is in accordance with the obtained values for the TFF experiments (also with the Desal TFM-50 membrane) in open channels (Figure 4-24c).

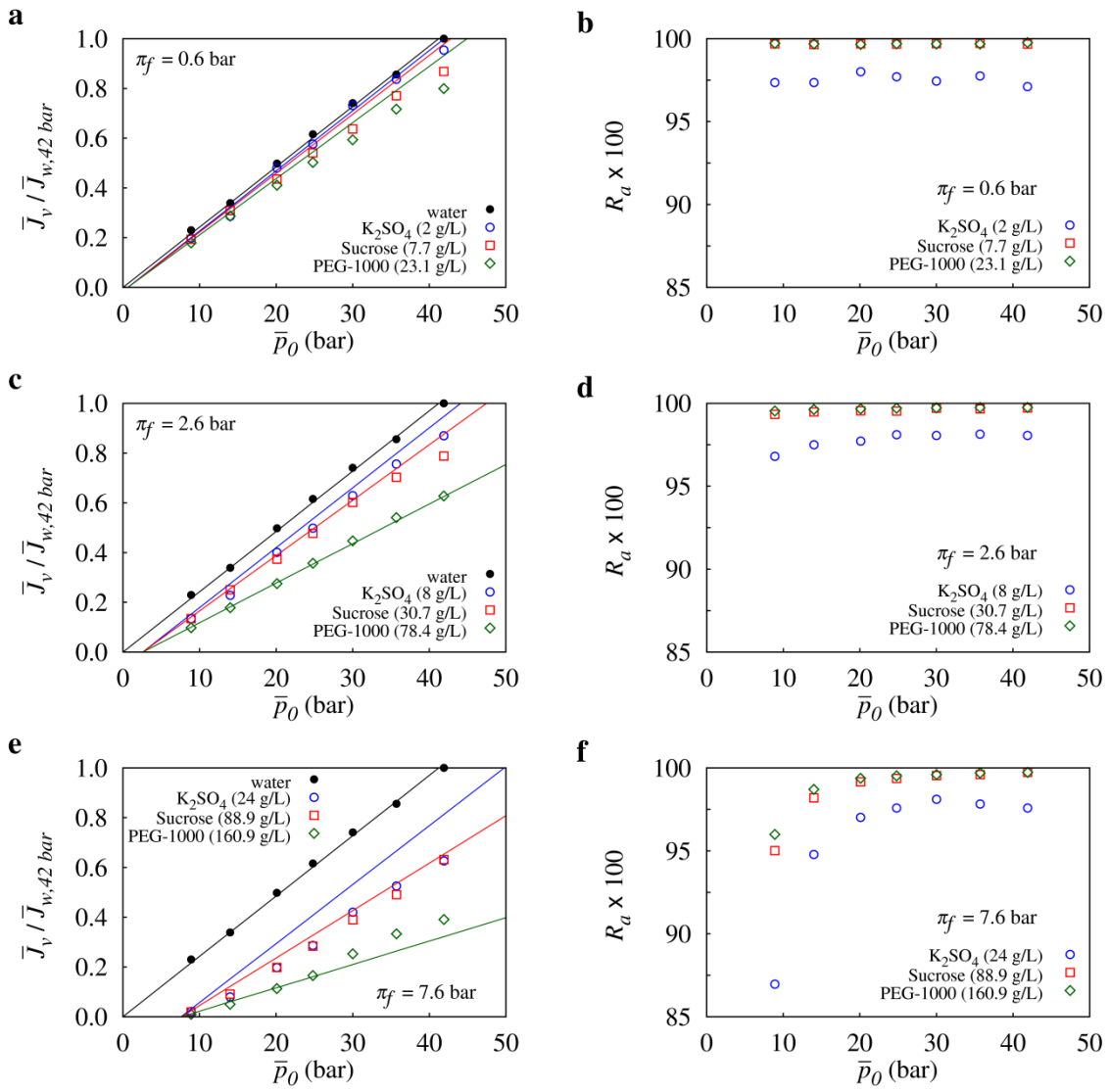


Figure 5-12 – Comparison of the relative permeate fluxes, $\bar{J}_v/\bar{J}_{w,42bar}$, and apparent rejections, $R_a$, as function of the rotational speed, expressed as $\bar{p}_0$, for the centrifugal nanofiltration of $K_2SO_4$, sucrose and PEG-1000 aqueous solutions using the CNF device without the internal block part (open chamber configuration), $\beta$ = 0° and the Desal TFM-50 membrane. In (a) and (b) are shown the data for the lower concentration solutions ($\pi_f$ = 0.6 bar). In (c) and (d) are shown the data for the intermediate concentration solutions ($\pi_f$ = 2.6 bar). In (e) and (f) are shown the data for the higher concentration solutions ($\pi_f$ = 7.6 bar). Symbols express experimental data and lines the fluxes predicted by the osmotic pressure model using $\pi_m = \pi_f$.

In addition, the behaviour of the $R_a$ data as function of $\bar{p}_0$ agrees well with the solution-diffusion transport model: for the same solute and solute concentration, $R_a$ increases with the increase of $\bar{p}_0$, i.e. with $J_v$. The solution-diffusion model assumes that the solute transport through the membrane is constant and independent of $\Delta p_m$. However, the solvent flux is proportional to $\Delta p_m$ so the permeate gets more diluted as $\bar{p}_0$ increases, which is clearly visible for the solutions of the highest concentration ($\pi_f$ = 7.6), as shown in Figure 5-12f. For the

smaller concentrations (Figure 5-12b and Figure 5-12d) the solvent flux is always high leading to $R_a$ > 97 %.

Looking at the data, the decrease of the $R_a$ value (as $\bar{p}_0$ decreases) starts when the permeate flux drops below 25 % of the water flux for the same $\bar{p}_0$ ($\bar{J}_v < \bar{J}_w/4$). For instance, for the 24 g/L $K_2SO_4$ solution the apparent rejection dropped from more than 97 % (at $\bar{p}_0$ > 20 bar) to 87 % (at $\bar{p}_0$ = 9 bar), as can be seen in Figure 5-12f. Similar results, but to a lesser extent, were observed for the sucrose and PEG-1000 solutions.

Although the encouraging results obtained in these initial experiments, the use of $\bar{p}_0$ as independent variable is arguable. In fact, $\bar{J}_v$ is function of not only $\bar{p}_0$ but also of the time period of the filtration cycle. Nevertheless, as described in section 5.3.4, the experiments (with some exceptions) were performed in such conditions that the amount of permeate volume was 1.0 mL ± 0.3 mL. Thus, despite the average pressure on the membrane surface dropped ca. 20 % due to the reduction of the liquid head (from the beginning to the end of the filtration cycle), the variation in the actual pressure between different experiments was small (less than 6 %). As an illustrative example, for the experiments performed at $\bar{p}_0$ = 42 bar (41.9 bar), the average pressure on the membrane surface at the end of the cycle was 36.1 bar if the collected volume of permeate was 0.7 mL and 34.2 bar if the corresponding collected volume was 1.3 mL. Similar differences in the pressure values were obtained for the other conditions (different $\bar{p}_0$).

**Effect of the angle $\beta$ in the nanofiltration at open chamber configuration**

In the open chamber configuration, the CNF performance is not significantly affected by the $\beta$ angle, as can be seen in Figure 5-13. Both the permeate fluxes and the rejection coefficients are practically constant in the studied $\beta$ range.

Two factors contribute to the above-mentioned behaviour. First, in the open chamber configuration, there is no physical constraint to the free movement of the liquid above the membrane. This improves the mixing over the entire sample chamber and reduces the CP effect. In addition, the studied $\beta$ angle range is relatively small (from -10° to +10°), which in conjunction with the open chamber configuration allows the easy dragging of the more concentrated fluid elements. A more evident influence of the $\beta$ on the CNF performance is expected to occur at larger $\beta$ angles or when the CNF device is used for concentration experiments, i.e. when the internal block part is used over the membrane.

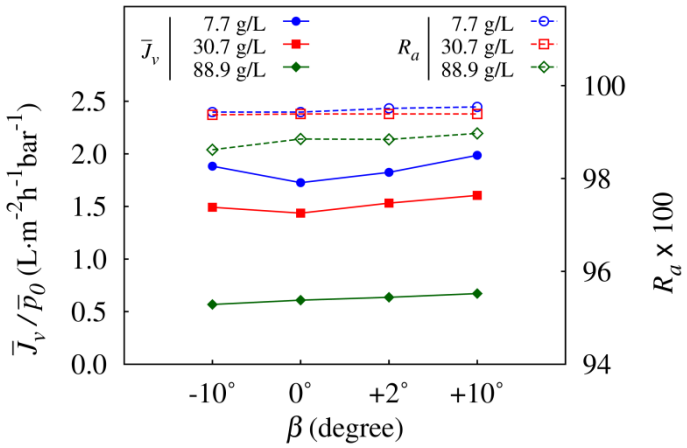


Figure 5-13 – Influence of the $\beta$ angle on the CNF performance in open chamber configuration. The data was obtained for the filtration of three sucrose aqueous solutions at $\bar{p}_0$ = 16 bar, using the NFX membrane.

### 5.4.3 The proof of feasibility – reaching high concentration factors

**Temporal evolution of centrifugal nanofiltration processes**

To evaluate the potential of the CNF device to reach high concentration factors it is necessary to know in advance or at least have an estimate of the necessary time to reach de desired concentration factor. Thus, the study of the temporal evolution of the CNF process shows that, for the same feed sample, the time necessary to obtain complete concentration depends on the applied rotational speed and on the height of the filtration chamber.

In Figure 5-14 several scenarios are presented for the concentration of a 30.7 g/L sucrose solution, showing the temporal evolution of $\bar{J}_v$, $R_a$, $CF$ and the amount of liquid remaining inside the sample chamber as function of filtration time and rotational speed (given in $\bar{p}_0$). It must be emphasized that each data point represents an individual experiment initiated with a fresh sample. In these experiments the F10-6x500y rotor and the rotor adaptor for $\beta$ = 0° were used.

Figure 5-14a and Figure 5-14b show the data obtained when the concentration was performed at three distinct rotational speeds (corresponding to $\bar{p}_0$ = 16 bar, 21 bar and 35 bar) having the filtration chamber a height of 1.3 mm. Under such conditions, complete concentration was obtained since no liquid has remained inside the sample chamber after the filtration cycle. At the initial instants, the permeate flux is directly proportional to $\bar{p}_0$. However, at high $\bar{p}_0$, the higher initial $\bar{J}_v$ leads to a faster decrease in the liquid head resulting in a sharper decline of $\bar{J}_v$. In fact, after some time the permeate flux is higher for lower $\bar{p}_0$ than for higher $\bar{p}_0$, as shown in Figure 5-14a. Nevertheless, the sample filtration gets globally faster as $\bar{p}_0$ increases. In the shown example, complete filtration was obtained in less than 60 min for $\bar{p}_0$ = 35 bar, it took nearly 90 min for $\bar{p}_0$ = 21 bar, while for the lowest applied $\bar{p}_0$ (16 bar) at least 180 min are

necessary. In fact, for the latter conditions the filtration is near the limit between complete and incomplete. Still, the filtration behaviour is distinct from the one for thinner feed chamber as discussed below (Figure 5-14c and Figure 5-14d).

In terms of the concentration factor, although the experiments performed with $h$ = 1.3 mm resulted in complete filtration, the determined $CF$ increased with $\bar{p}_0$, as shown in Figure 5-14b. This fact suggests that different amounts of liquid remained inside the filtration and concentrate chambers, and that the filtration has not stopped at the entrance of the filtration chamber; otherwise the $CF$ value should have to be the same for the three $\bar{p}_0$ conditions. In fact, the amount of liquid recovered from the filtration and concentrate chamber was 0.61 mL, 0.56 mL and 0.46 mL for the three increasing $\bar{p}_0$ (16 bar, 21 bar and 35 bar).

Figure 5-14c and Figure 5-14d show similar $\bar{J}_v$, $R_a$, $CF$ and liquid volume data but for the CNF process with $h$ = 0.1 mm and just for two $\bar{p}_0$ (16 bar and 35 bar). As before, at the initial instants, larger $\bar{J}_v$ are obtained for the highest $\bar{p}_0$, but for both $\bar{p}_0$ values $\bar{J}_v$ decreases fast to zero and the filtration halts before the whole liquid inside the sample chamber is depleted (incomplete filtration). The amount of liquid remaining inside the sample chamber is proportional to $\bar{p}_0$. In the shown examples, such remaining liquid varied between 1.5 mL for $\bar{p}_0$ = 16 bar and 0.3 mL for $\bar{p}_0$ = 35 bar. In addition, while the $R_a$ for complete concentration experiments was always above 99 %, in the cases of incomplete filtration, the rejection coefficient has dropped to 94 %, for $\bar{p}_0$ = 16 bar, and to 97 %, for $\bar{p}_0$ = 35 bar, as can be seen in Figure 5-14c.

The $CF$ values presented in Figure 5-14d are those of the liquids withdrawn from the filtration and concentrate chambers (after removing the liquid remaining in the sample chamber). It is interesting to note that the magnitude of the $CF$ is similar to those obtained at full filtration. However, the volume of the filtration chamber corresponding to $h$ = 0.1 mm is smaller than that of $h$ = 1.3 mm. Thus, the amount of recovered solute is smaller. The results obtained for $h$ = 0.1 mm suggest that the solute concentration in the chamber increases sharply, leading to the interruption of the filtration.

The time required to completely filter the 30.7 g/L sucrose solution was then used as the minimum running time for filtration cycles performed in the following sections of the work (provided $\bar{p}_0$ and sample concentration were the same). However, to count on issues related with the decrease of $h$, and variation on the effective membrane area, the time of the filtration cycles were slightly incremented. The 30.7 g/L sucrose solution corresponds to $\pi_f$ = 2.6 bar, which was the highest osmotic pressure in the following work. For the concentration of solutions with lower osmotic pressure the time period of the filtration cycles can be reduced.

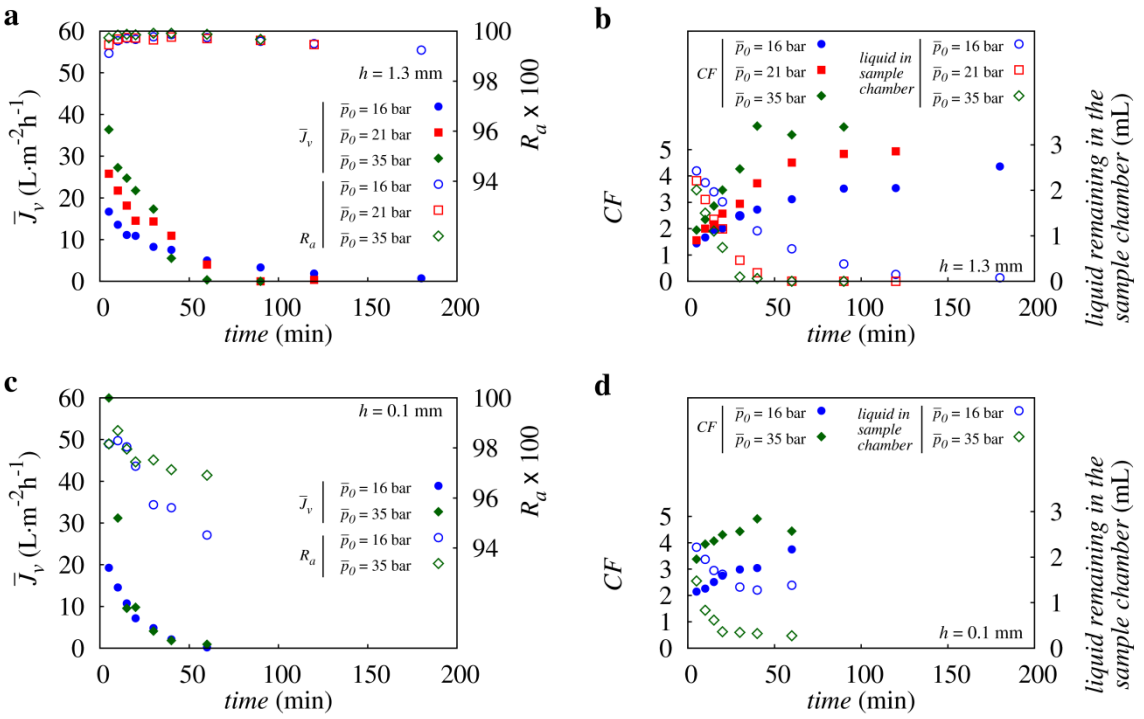


Figure 5-14 – Temporal evolution of the CNF process. In these examples, the sucrose aqueous solution ($c_f$ = 30.7 g/L) was filtered using the NFX membrane at three rotational speeds (at $\beta$ = 0°), corresponding to $\bar{p}_0$ = 16 bar, 21 bar and 35 bar, for $h$ = 0.1 mm and $h$ = 1.3 mm. In (a) are shown the data of permeate flux, $\bar{J}_v$, and apparent rejection, $R_a$, for $h$ = 1.3 mm. In (b) are shown the data of the concentration factor, $CF$, and of the volume of liquid remaining in the sample chamber after the filtration cycle, for $h$ = 1.3 mm. In (c) and (d) are shown the corresponding (a) and (b) plots for $h$ = 0.1 mm.

The results of this sub-section suggest that, whenever possible, a temporal evolution study for the CNF of particular samples of interest should be conducted. In addition, it is also important that, to ensure reliable operation, effective membrane area and membrane permeability do not vary significantly; otherwise the necessary time to perform complete filtration is not the same at distinct runs.

**Effect of the height of the filtration chamber**

The influence of $h$ on the CNF performance was assessed for the filtration of sucrose solutions in two conditions: concentration at low $CF$ and concentration at high $CF$ (the latter to reach complete filtration).

For the concentration experiments at low $CF$, the small internal block part (Figure 5-7e) was used and a small amount of permeate was collected (ca. 1 mL). Thus, this set of experiments refers only to the initial part of the filtration cycle, where the concentration effects can be almost neglected. The obtained permeation data, as a function of $h$, are plotted in Figure 5-15 in terms of $\bar{J}_v/\bar{J}_w$, $CF$ and $R_a$. For the concentration experiments at high $CF$ the larger internal block part (Figure 5-7c) was used, and filtration times considered sufficient to deplete

the whole liquid of the sample chamber were adopted. The $CF$ and $R_a$ values for the complete filtration experiments are shown later Figure 5-16.

The concentration experiments at low $CF$ show that the height of the filtration chamber influences the filtration performance at the initial instants of the filtration cycle, as can be seen in Figure 5-15. The permeate flux decreases as $h$ decreases, for any sample concentration, as can be seen in Figure 5-15a, where the filled symbols represents experimental data. However, the influence of $h$ is smaller than the effect of the solute concentration itself. More interesting in this figure is the observation that experimental permeate fluxes are higher than the ones determined using the osmotic pressure model, given by the open symbols. For the osmotic pressure model, the osmotic pressure was calculated based on the logarithmic mean between the solute concentration in the concentrate and in the feed, defined as $(c_c - c_f)/ln(c_c - c_f)$, where the former was determined by mass balance.

Also for the concentration experiments at low $CF$, the concentration factor of the liquid withdrawn from filtration and concentrate chamber increases as $h$ decreases (up to $h$ = 0.2 mm), as shown in Figure 5-15b. This demonstrates the faster rise of the concentration inside the filtration chamber and justifies the decrease of $\bar{J}_v/\bar{J}_w$ shown in Figure 5-15a. Despite the fact that $R_a$ shows a tendency to decrease as $h$ decreases, the variation of $R_a$ is not significative, especially for low sample concentrations. These results suggest that, for the initial instants of the filtration cycle, the centrifugal force minimizes the CP effects in such a way that the concentrated fluid elements are dragged away from the membrane to the concentrate chamber.

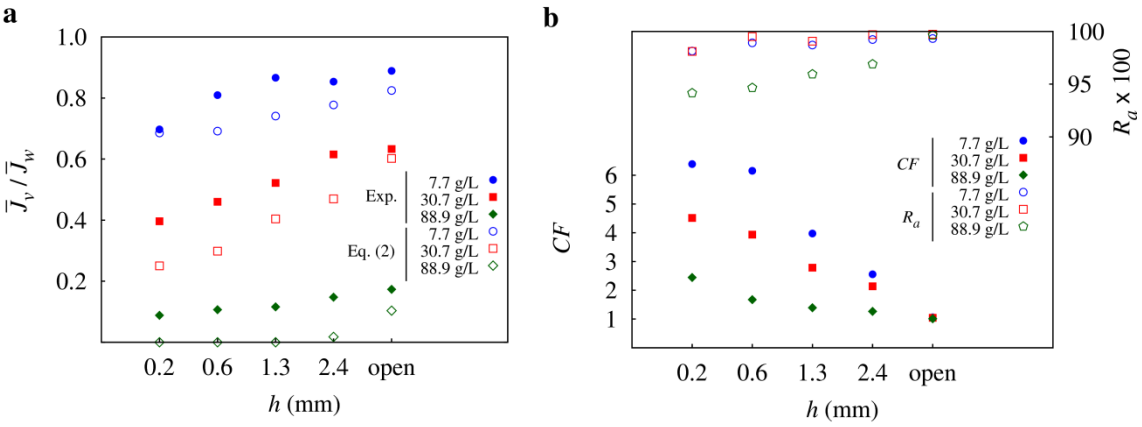


Figure 5-15 – Effect of the filtration chamber height, $h$, on the CNF performance at the initial part of the filtration cycle. The runs were performed with sucrose solutions at $\bar{p}_0$ = 9 bar, $\beta$ = 0° and using the NFX membrane. In (a) are shown the data of the relative permeate fluxes, $\bar{J}_v/\bar{J}_w$, for the experimental data (filled symbols), and predictions by the osmotic pressure model (open symbols). In (b) are shown the data of the concentration factor, $CF$, and of the apparent rejection, $R_a$.

The influence of the $h$ on the filtration process to reach high $CF$ was also evaluated using sucrose solutions. Only two concentrations were used: $c_f$ = 7.7 g/L and $c_f$ = 30.7 g/L. The

higher sucrose concentration solution ($c_f$ = 88.9 g/L) was not tested since it would result in very low $CF$ or incomplete filtration, for the tested pressures.

The results obtained for the CNF concentration using four different $h$ values are shown in Figure 5-16. The data demonstrate that it is possible to concentrate samples using $h$ = 0.1 mm, but only if the sample is diluted; otherwise the filtration is interrupted (marked with the crossed symbols). In addition, even when complete filtration is achieved, no practical benefit results by using $h$ = 0.1 mm, because the obtained $CF$ is smaller than the one for $h$ = 0.2 mm. However, since the volume in the filtration chamber is directly proportional to $h$, the $CF$ value also drops for $h$ larger than 0.2 mm. Therefore, the optimal height of the filtration chamber, among the values tested, seems to be $h$ = 0.2 mm.

For the sucrose solution, there is a weak tendency on $R_a$ to decrease as $h$ decreases. For instance, although for $h$ = 0.2 mm a relatively high concentration factor was obtained ($CF$ = 16), the rejection has remained high ($R_a$ = 96.9 %). This shows that either the concentrated fluid elements are displaced from the membrane vicinity, or the contact of highly concentrated fluid elemnts with the membrane does not deteriorate significantly the permeate quality.

The above results (including the ones obtained for the study of the temporal evolution) demonstrate that the height of the filtration chamber plays an important role in the CNF performance. However, they also show that other parameters contribute to the CNF efficiency, including the sample initial concentration and the rotational speed. In the next section, the effect of the $\beta$ angle on the CNF performance when the filtration chamber height is confined by the internal block part will be assessed.

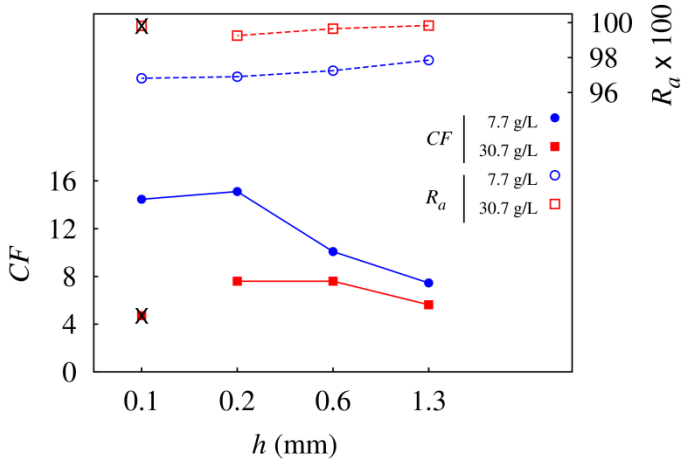


Figure 5-16 – Influence of the height of the filtration chamber, $h$, on the CNF performance of two sucrose aqueous solutions, for $\beta$ = 0° and with complete filtration (unless stated). The 7.7 g/L solution was filtered at $\bar{p}_0$ = 16 bar during 45 min, while the 30.7 g/L solution was filtered at $\bar{p}_0$ = 35 bar during 60 min. All the solutions were filtered with the NFX membrane. Crossed symbols indicate that the filtration was incomplete (sample remaining inside the sample chamber after the filtration cycle).

**Effect of the $\beta$ angle on the centrifugal nanofiltration performance with confined filtration chamber**

As shown in Figure 5-13, the influence of the $\beta$ angle is not relevant in the open chamber configuration. However, to obtain high $CF$ values the centrifugal nanofiltration must be conducted using the internal block part inside the CNF device, i.e. the filtration chamber is confined between the membrane surface and the bottom surface of the internal block part.

The influence of $\beta$ when performing, or trying to perform, complete filtration is here assessed through the major results shown in Figure 5-17 and Figure 5-18. The impact of the $\beta$ angle on the CNF is more easily observed when the filtration is incomplete. In these cases, the CNF concentration at different $\beta$ angles results in distinct amounts of liquid remaining inside the filtration chamber after the filtration cycle has finished. Thus, the $\beta$ angles leading to a smaller amount of that liquid are considered as more efficient.

In Figure 5-17 the performance of CNF concentration is evaluated based on the liquid remaining inside the sample chamber after the filtration cycle and on the corresponding $CF$ value. Three distinct scenarios are considered.

The first scenario consists of the concentration of a 7.7 g/L ($\pi_f$ = 0.6 bar) sucrose solution using $\bar{p}_0$ = 16 bar and $h$ = 0.1 mm during 80 min. In this scenario, complete concentration was obtained for all the studied $\beta$ angles (-10°, 0° and +10°); so, for dilute solutions complete filtration occurs even for $h$ = 0.1 mm, as already seen in Figure 5-14.

The second scenario consists of the concentration of a 30.7 g/L ($\pi_f$ = 2.6 bar) sucrose solution during 80 min using also $h$ = 0.1 mm but for $\bar{p}_0$ = 35 bar. In this case, the filtration is complete only for $\beta$ = -10° and the amount of liquid remaining inside the sample chamber increases with the $\beta$ angle. These last results are in accordance with the ones obtained for the temporal evolution of the CNF process. As seen in Figure 5-14c, at the end of the filtration cycle and for $\beta$ = 0°, ca. 0.3 mL remained inside the filtration chamber, while in the current experiment that amount was near 0.5 mL, but still comparable. However, almost 0.9 mL were found on the sample chamber for $\beta$ = +10°. Thus, it is clear that the $\beta$ angle plays a major role on the CNF performance, the filtration being more efficient for negative angles, i.e. when the normal to the membrane surface points radially outwards.

This same conclusion is reinforced by the results of the third scenario, where a 78.4 g/L ($\pi_f$ = 2.6 bar) PEG-1000 solution was concentrated at $\bar{p}_0$ = 35 bar and $h$ = 0.6 mm during 70 min. In this case the filtration runs were always incomplete but the same previous trend was observed for the relationship between the amount of liquid remaining inside the sample chamber and the $\beta$ angle .

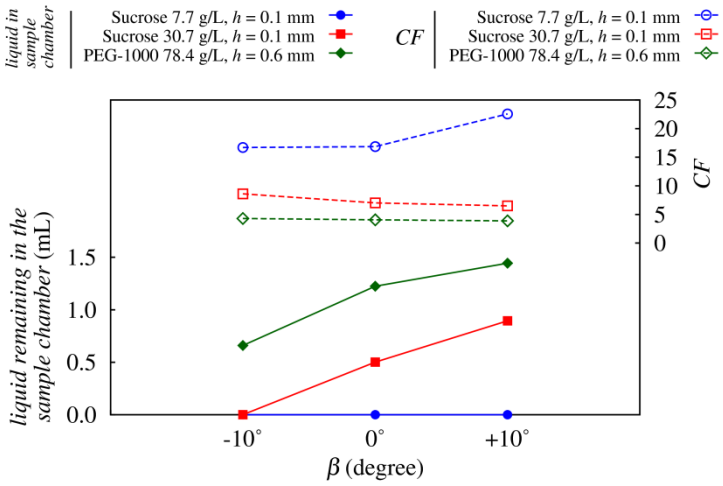


Figure 5-17 – Influence of the angle $\beta$ on the centrifugal nanofiltration performance using the CNF device with the internal block part. The data was obtained for the filtration of sucrose and PEG-1000 solutions using the NFX membrane. The 7.7 g/L sucrose solution was filtered at $\bar{p}_0$ = 16 bar while the other two solutions were filtered at $\bar{p}_0$ = 35 bar. The filtration time for sucrose and PEG-1000 solutions were 80 and 70 min, respectively.

An interesting comparison can be made between the CNF performance obtained when changing the rotational speed or the $\beta$ angle for the concentration of a 78.6 g/L PEG-1000 solutions, as seen in Figure 5-18. In none of the runs complete filtration was obtained. Thus, the comparison is made based on the amount of liquid remaining inside the sample chamber after the filtration cycle. The effect of increasing the applied pressure or rotation speed (for $\beta$ = 0°) is shown in the Figure 5-18a. Increasing $\bar{p}_0$ from 35 bar to 77 bar the amount of liquid remaing inside the sample chamber decreased from 1.22 mL to 0.76 mL. On the other hand, the effect of the $\beta$ angle on the CNF performance (for $\bar{p}_0$ = 35 bar) is shown in the Figure 5-18b. The figure shows that the amount of liquid remaining inside the sample chamber diminished from 1.44 mL, for $\beta$ = +10°, to 0.66 mL for $\beta$ = -10°. Therefore, with the simple change of the membrane orientation, an extra volume of 0.5 mL was filtered (at $\bar{p}_0$ = 35 bar). This effect was more pronounced than the increase of pressure from $\bar{p}_0$ = 35 bar to $\bar{p}_0$ = 77 bar.

By manipulating the $\beta$ angle, it is possible to mitigate the concentration polarization and thus to operate the CNF device at lower transmembrane pressures (lower rotational speeds).. Operating at lower pressure reduces substantially the risk of unbalance of a pair of devices and also the adverse effects of irreversible compaction of the membranes. Indeed, if the pressure is above a certain threshold the membrane structure can compact irreversibly, leading to a decrease of the permeate flux (McGovern et al. 2015). For instance, despite the runs of highest rotational speed resulted in $\bar{p}_0$ = 77 bar, the pressure in the membrane section close to the concentrate chamber can reach 100 bar.

The above results show that the $\beta$ angle plays a significant role in the CNF performance. For that reason the CNF device should be designed in such a way that the concentrated fluid elements are pulled away from the membrane surface. A similar conclusion was obtained by

other authors who developed continuous devices for water desalination by reverse osmosis (Bergen et al. 2000). However, in their work the aim was water desalination and not the concentration of small-volume samples. Thus, device optimization should be focused on the adequacy of the membrane orientation and not on the simple use of brute force provided by the increase of rotational speed. In fact, this work shows a remarkable increase in the CNF performance just by tilting the membrane by 10°. A substantial increase is expected if larger $\beta$ angles are used.

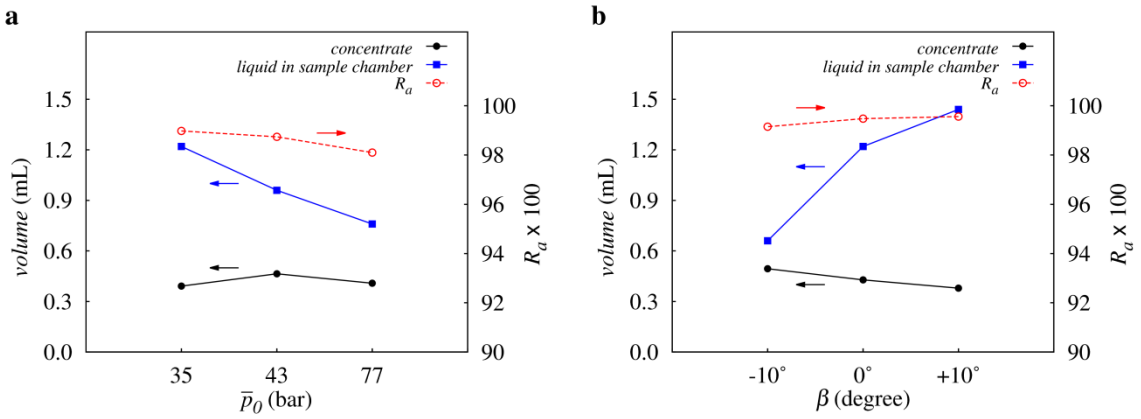


Figure 5-18 – Influence of $\bar{p}_0$ and $\beta$ on the CNF performance for the concentration of PEG-1000 solution with $c_f$ = 78.4 g/L ($\pi_f$ = 2.6 bar) and using the NFX membrane. The effect of $\bar{p}_0$ and $\beta$ is assessed in terms of the amount of liquid remaining in the sample chamber after the filtration cycle, as the amount of liquid withdrawn as concentrate and as the apparent rejection. In a) $\bar{p}_0$ changes for constant $\beta$ = 0°, while in b) $\beta$ changes for constant $\bar{p}_0$ = 35 bar. In all the experiments the filtration is incomplete, so the concentrate refers to the portion of liquid withdrawn after the removal of liquid remaining inside the sample chamber.

**Other remarks on the developed centrifugal nanofiltration device**

In this section, some final remarks on the developed CNF device are discussed. These include issues like the replicability of the results, the comparison between experimental and expected $CF$ values, the concentration stratification inside the filtration chamber, the undesired liquid mixing between chambers during the filtration cycle, and the discussion on alternatives to CNF devices with larger sample volume.

*Replicability of the centrifugal nanofiltration experiments*

A good replicability of results for distinct experiments performed under the same operating conditions was achieved. Some representative results are shown in Table 5-9. In this table, $V$ stands for the amount of liquid not filtered, i.e. the sum of liquid volume remaining inside the concentrate, the filtration and the sample chambers. For the sets A and B the filtration is complete and, therefore, $V$ is small (less than 0.2 mL). Conversely, for the set C the filtration

is incomplete resulting in a larger $V$. Coherent $CF$ values were obtained for the runs of each set which were done with the same membrane assembly.

Table 5-9 – Representative data showing the replicability of CNF filtration between runs.

| set | $h$ (mm) | $c_f$ (g/L) | $\beta$ (degree) | rotation speed (rpm) | filtration time (min) | run # | $CF$ | $V$ (mL) |
|---|---|---|---|---|---|---|---|---|
| A | 0.1 | 7.7 | -10 | 6000 | 45 | 1 | 11.6 | 0.171 |
| | | | | | | 2 | 11.7 | 0.163 |
| B | 0.1 | 7.7 | 0 | 6000 | 80 | 1 | 18.1 | 0.119 |
| | | | | | | 2 | 16.9 | 0.115 |
| C | 0.1 | 30.7 | +10 | 9000 | 80 | 1 | 7.8 | 1.284 |
| | | | | | | 2 | 7.7 | 1.259 |

*Comparison between the experimental $CF$ and nominal $CF$*

As referred in section 5.3.1, the nominal volumetric $CF$ is function of the filtration chamber height and of the location of the air-liquid meniscus when the filtration halts. For instance for $h$ = 0.1 mm, if the air-liquid meniscus stops at the entrance of the filtration chamber the volumetric $CF$ is 22, while the $CF$ value is 74 if the air-liquid meniscus reaches the end of the filtration chamber.

The maximum observable $CF$, as defined by equation (2-46), was 22 for $\beta$ = +10° and around 16 for the other $\beta$ angles. Thefore, for complete filtration processes, the magnitude of the observable $CF$ is in accordance with the expected one for $\beta$ = +10° but for the other $\beta$ angles its values are slightly smaller. Since for complete filtration no liquid remains inside the filtration chamber after the filtration cycle, then, these results show that the global volume of the filtration and concentrate chambers are larger than the designed one. Two factors may contribute to this fact: larger filtration chamber heights than the designed one, due to the glue spread on the top of the membrane surface; and retention volume pockets between the internal block and the top parts (the internal block part was manufactured with some tolerance to be possible to insert and remove it from the CNF device). Therefore, future designs of CNF devices and of membrane assembly technique should be improved to avoid these issues.

*Stratification of the solute concentration inside the CNF device*

The self-cleaning mechanism of centrifugal filtration drags the most concentrated fluid elements towards the concentrate chamber. Thus, concentration stratification exists inside the filtration and concentrate chambers. This fact can be exploited to obtain concentrate fractions richer than the whole concentrate liquid but at the expense of low solute recovery in each

portion (smaller volumes). By withdrawing separate fractions from the concentrate chamber at the end of the filtration chamber, through the auxiliary channel, the first portion of liquid is generally more concentrated than the following ones. Illustrative examples are shown in Figure 5-19 where the average value of the concentrate is compared with the corresponding one of the first 60 μL portion of the concentrate.

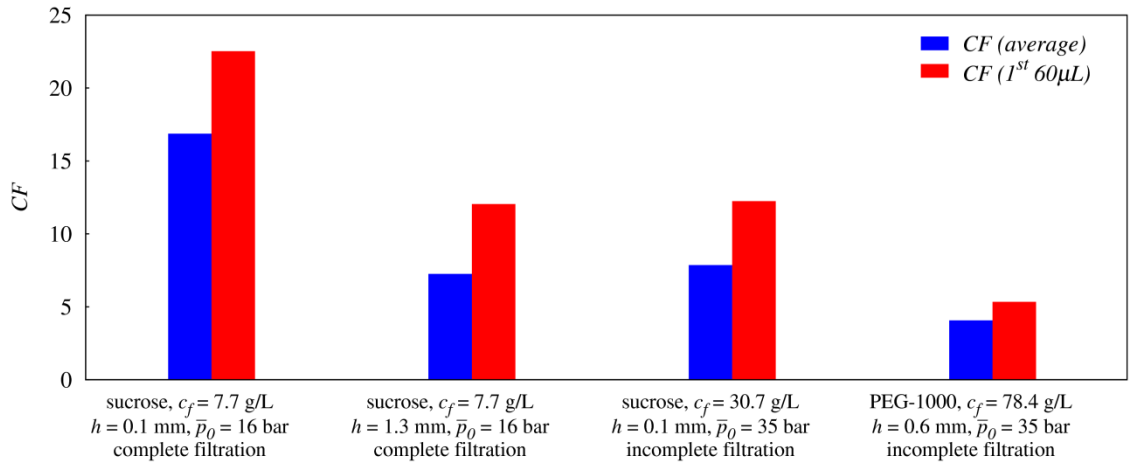


Figure 5-19 – Stratification of solute concentration inside the filtration and concentrate chambers. In all experiments, the NFX membrane was used.

*Liquid mixing between chambers*

The developed CNF device is made of parts that engage on each other, which could lead to unwanted retention volumes and interconnections between the different chambers. Nevertheless, whenever a CNF run was performed there was no significant variation of the solute concentration inside the sample chamber, at least during the most part of the filtration cycle. However, as the filtration approaches its final stages, it is possible that small amounts of concentrated liquid infiltrate into the sample chamber increasing its concentration. As a representative case, the temporal evolution of the solute concentration inside the sample chamber and of the liquid withdrawn as concentrate is shown in Figure 5-20. These data were obtained from the same experiments performed to assess the temporal evolution of the CNF, i.e. the results that have been shown before in Figure 5-14a and Figure 5-14b. The solute concentration inside the sample chamber increases only in the final stage of the filtration cycle when a small amount of liquid remains there. The cause might be the flow reversal (coming back) from the concentrate chamber to the sample chamber through the auxiliary channel. This issue should be taken into account in future designs of the CNF device.

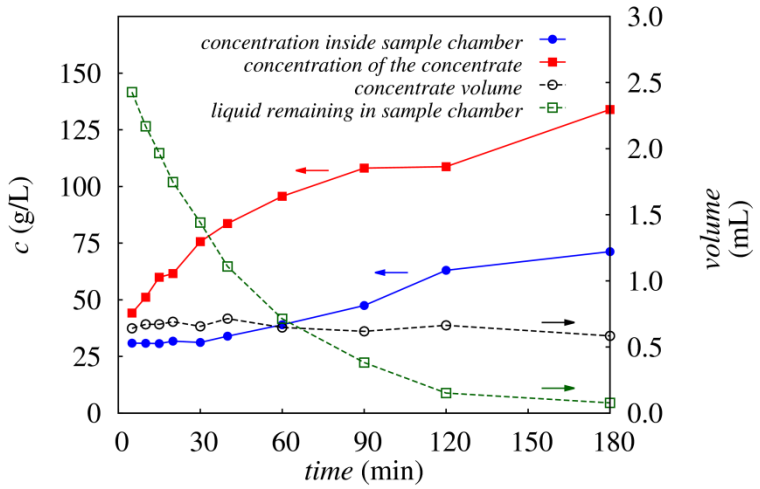


Figure 5-20 – Comparison between the solute concentrations of the liquid inside the sample chamber and of the liquid withdrawn as concentrate, for the concentration of a sucrose solution ($c_f$ = 30.7 g/L) at $\bar{p}_0$ = 16 bar, $h$ = 1.3 mm, $\beta$ = 0° and using the NFX membrane.

*Concentration of larger volume samples*

The designed and tested CNF device has the capability to withstand sample volumes of ca. 3 mL. Recall that, as referred in Chapter 1, the objective of the present thesis was to develop methods to concentrate small-volume samples in the niche up to 100 mL. To accomplish this objective with similar devices to the one designed in the present chapter the maximum sample volume is 25 mL and larger rotors must be used.

The CNF device presented in this work (section 5.3.1) can be used in commercial fixed-angle centrifuge rotors having standard 50 mL rotor buckets and round bottom or with large volume fixed-angle rotors when using adequate adapters. For instance, the CNF device was used in a centrifuge rotor with bucket volume of 500 mL.

To be possible to insert 25 mL of sample in a device, centrifuge rotors with volume of 1000 mL per bucket are needed. Smaller buckets are inadequate for twofold issues: insufficient space to separate the sample chamber from the filtration chamber by a neck channel and/or insufficient volume in the permeate chamber to avoid wetting of the membrane support part by the permeate during the filtration cycle. Figure 5-21 shows a possible design for a CNF device with a 25 mL sample chamber with $\beta$ = -4°. It must be mentioned that the characteristic $\alpha$ angle of typical commercial 1000 mL fixed-angle centrifugal rotors is 20°, instead of $\alpha$ = 23° and $\alpha$ = 34° for the 500 mL and 50 mL fixed-angle centrifuge rotors, respectively.

The advantage of a CNF device like the one in Figure 5-21 is that it has a long neck channel that maintains the pressure on the liquid in the filtration chamber at high levels when spinning in an appropriate centrifuge rotor, as expressed in Table 5-10. The average pressure on the membrane was calculated using equation (5-4) for the radial positions obtained for the centrifuge rotor F10-4x1000 (Thermo Fisher Scientific Incorporated 2014a). The main

drawback of the device of Figure 5-21 is its small $\beta$ angle (-4°). To achieve negative $\beta$ angles with larger magnitude the design of the device must be altered and/or the volume must decrease.

To process larger sample volumes (more than 25 mL), an alternative is to use CNF devices for swinging-bucket centrifuge rotors since they stay horizontal when spinning; so, by design, they can accommodate larger sample chambers. However, two main issues arise from the use of swinging-bucket rotors. First, they operate at lower rotational speed than fixed-angle rotors. This drawback may be compensated with proper design of the device since in swinging-bucket rotors the radial distance between the sample and filtration chamber may be larger. Second, due to the larger radial span of the swinging-bucket rotors when spinning, the inertial mass center is displaced in a larger extent than for fixed-angle rotors. This last factor increases as the sample volume increases and may lead to centrifuge imbalance if the permeability of the membranes used in opposite buckets differs. Differences in the hydraulic permeability can occur even for the same membrane type, as seen previously in Table 3-6 and Table 3-7. Therefore, fixed-angle rotors are safer for centrifugal filtration and fair sample volumes (15 to 25 mL) can be processed at once if proper devices and rotors are used.

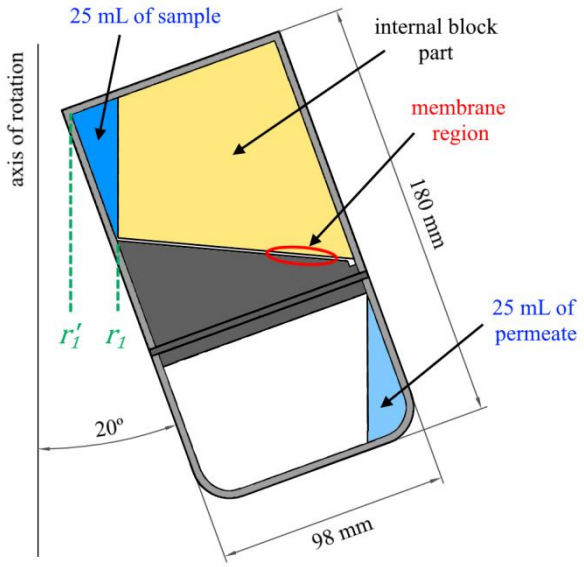


Figure 5-21 – CNF device with a 25 mL sample chamber designed to fit in standard 1000 mL centrifuge rotors.

Table 5-10 – Correspondence between rotational speed and average pressure on the membrane for the proposed CNF device of Figure 5-21 when spinning in the F10-4x1000 rotor.

| rpm | $\bar{p} = \bar{p}_0$ (air-liquid meniscus at $r_1'$) | $\bar{p}$ (air-liquid meniscus at $r_1$) |
|---|---|---|
| 6000 | 28 | 26 |
| 7000 | 38 | 35 |
| 8000 | 50 | 46 |
| 9000 | 63 | 58 |
| 9500 | 71 | 64 |

## 5.5 Conclusion

Centrifugal filtration was identified as one of the techniques capable of minimizing concentration polarization and, in this part of the work, its potential to concentrate small-volume samples (ca. 3 mL) of binary solutions of low MW solutes was evaluated. Given the MW range of the solutes and the fact that NF membranes were used, the technique developed herein was named as centrifugal nanofiltration (CNF). Currently, there are several commercial centrifugal devices available to concentrate small samples but they are adequate only to separate particulate matter or medium-to-large solutes (MW > 1000 g/mol). However, they would be inefficient to concentrate small molecules (MW < 1000 g/mol) even if the MF/UF membranes would be replaced by a NF membrane, being their main limitation the significant pressure drop as the filtration cycle proceeds.

To overcome the strong reduction of the driving force with time, an innovative centrifugal nanofiltration was designed, manufactured and tested with model binary solutions of $K_2SO_4$, sucrose and PEG-1000. The main innovation of the developed CNF device is that the sample chamber is separated from the filtration chamber by a thin neck channel. This neck channel concept, which was never used by other authors or in commercial devices, permits to place the majority of the sample away from the filtration chamber and, in that way, to maintain the transmembrane pressure at high levels during most part of the filtration cycle. The performance of the CNF process depends on three main factors: rotational speed, height of the filtration chamber and the angle between the centrifugal force and the membrane surface.

When the applied rotational speed leads to pressures that are, at any instant, higher than the osmotic pressure, complete concentration is obtained and no liquid remains in the sample chamber at the end of the filtration cycle. Conversely, if the generated pressure is not enough to overcome the osmotic pressure at the membrane surface, the permeation is interrupted and some amount of liquid remains inside the sample chamber.

In terms of the height of the filtration chamber, it was verified that $CF$ increases as $h$ decreases but only down to a certain threshold. Due to a balance between the osmotic pressure and the liquid mixing inside the filtration chamber, there is no benefit in decreasing $h$ below 0.2 mm. For filtration chamber heights smaller than this threshold, the osmotic pressure increases sharply, at the initial instants of the filtration cycle, and inefficient mixing of the liquid occurs. Therefore, the experimental results suggest that, among the values investigated, there is an optimal value of $h$ of 0.2 mm.

The $\beta$ angle (the angle between the centrifugal force and the membrane surface) also plays a significant role on the performance of the centrifugal filtration, especially when the CNF aims at reaching high $CF$ values. Higher CNF performance is obtained when the membrane is

oriented such that the centrifugal force pulls the fluid elements of the concentration boundary layer away from the membrane surface (negative $\beta$). On the contrary, if the centrifugal force squeezes the concentration boundary layer against the membrane (positive $\beta$) the filtration becomes less efficient. In the performed experiments, the influence of $\beta$ was particularly visible when the filtration is incomplete. Under these conditions of interruption of the filtration cycle, the amount of liquid remaining inside the filtration chamber decreases as $\beta$ gets more negative (in the +10° to -10° angle range). Thus, the obtained results confirm other authors' conclusions about the effect of the $\beta$ angle on the disruption of the CP layer.

Also interesting is the evidence that the centrifugal filtration process results in a stratification of the solute concentration inside the filtration and concentrate chambers. In fact, it was verified that the first portion (60 μL) withdrawn from the concentrate chamber is more concentrated than the next portions and, thus, its solute concentration is higher than the average concentrate concentration.

Although studies on the concentration of multicomponent solutions or of solutions containing foulants should be addressed, the CNF device designed, manufactured and used in the present work was able to fulfill the main objective of the thesis: to show that it is feasible to concentrate small-volume samples of high osmotic pressure, i.e. solutions containing low MW solutes, using membrane processes in a simple and replicable way.

# 6 Comparison between centrifugal and tangential flow nanofiltration

## 6.1 Introduction

The main objective of the present thesis was to develop techniques and devices capable of efficiently concentrate small-volume samples of binary solutions with high osmotic pressure, using pressure-driven membrane processes. After the literature review on the subject, two techniques emerged as potential candidates to successfully accomplish such task: micro-TFF and CNF. Therefore, it is important to assess the benefits and limitations of each technique, viewing the selection of the most adequate one for specific scenarios.

Both micro-TFF and CNF techniques have proved to be capable of producing fair concentration factor values ($CF$ > 10) when the samples have medium-to-low osmotic pressure, of the order of $\pi_f$ = 0.6 bar. For samples with medium-to-high osmotic pressure, of the order of $\pi_f$ = 2.6 bar, smaller $CF$ values are obtained and complete filtration may not even be achieved. Therefore, in this chapter the advantages and disadvantages of each technique are reviewed and some illustrative results are presented to evidence the differences between both techniques.

Although the results discussed in this chapter prove that CNF presents a higher performance than that of TFF for sample concentration, they refer to controlled experiments dealing with model binary solutions. For future work, it may be interesting to know the CNF and micro-TFF performances when multicomponent solutions, or solutions containing foulants, are used.

## 6.2 Direct comparison between micro-TFF and CNF

Both micro-TFF and CNF give comparable results when the osmotic pressure of the sample solution is low. In fact, for a similar filtration channel heights ($h$ = 0.25 mm for the micro-TFF and $h$ = 0.2 mm for the CNF device) the concentration of a dilute sucrose solution ($c_f$ = 7.7 g/L, $\pi_f$ = 0.6 bar) resulted in $CF$ = 16 and $CF$ = 15 for the micro-TFF and CNF processes, respectively. However, while these CF values were obtained at a relatively low rotational speed when using the CNF technique ($\bar{p}_0$ = 16 bar), for the micro-TFF case the use of equivalent low pressure, generated by a 17 bar BPV, was not enough: it was necessary to use a 34 bar BPV to avoid small feed recovery values. In addition, as discussed in section 5.4.3, a

better efficiency could have been obtained by CNF if $\beta$ was made negative; however, for comparison purposes only the experiments performed at $\beta$ = 0° are used in this chapter.

When the sample concentration increases it becomes more difficult to obtain complete filtration since the osmotic pressure near the membrane also increases. These are precisely the experimental conditions that make relevant the self-cleaning mechanism of the centrifugal filtration, leading to better efficiency of the CNF filtration and, thus, to higher $CF$ values.

For intermediate sample osmotic pressure ($\pi_f$ = 2.6 bar), the comparison between the micro-TFF and CNF efficiencies is shown in Figure 6-1, for three model solutions (fructose, $K_2SO_4$ and sucrose). In this range of osmotic pressure, CNF yields higher $CF$ values (Figure 6-1a). The reason for this behaviour is the drag by the centrifugal force of the most concentrated fluid elements towards the concentrate chamber, being this fluid replaced by one with lower concentration. This mechanism lowers the osmotic pressure near the membrane and its values become smaller than those for the micro-TFF process, which has a insignificant tangential velocity near the membrane (remember that to obtain high $CF$ values by micro-TFF the $Re_h$ at the entrance of the channel had to be as small as 0.2, and it drops to almost zero at the end of the channel).

It must be mentioned that the CNF concentration of the fructose solution was performed in a device with $h$ = 0.6 mm, instead of $h$ = 0.2 mm used for the other solutions. According to the reasoning presented in section 5.4.3, CNF is more efficient when $h$ = 0.2 mm. Thus, if $h$ = 0.2 mm was used for the fructose experiments, the differences shown in Figure 6-1a between the micro-TFF and CNF results would be at least of the same magnitude. Therefore, it can be concluded that as the concentration of the sample increases, CNF gets more efficient than micro-TFF and, for that reason, CNF is preferred.

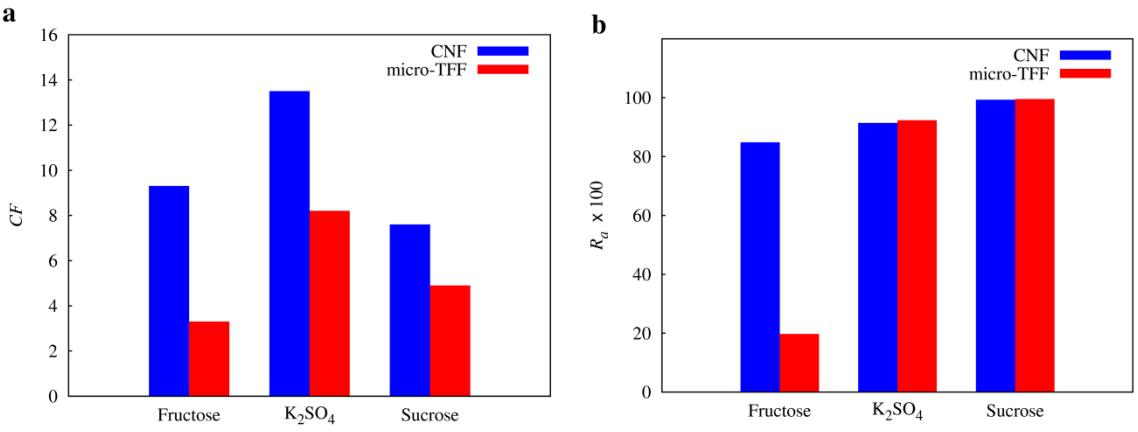


Figure 6-1 – Comparison between micro-TFF and CNF performance, in terms of $CF$ and $R_a$, for the nanofiltration of fructose, $K_2SO_4$ and sucrose aqueous solution ($c_f$ = 19 g/L, $c_f$ = 8 g/L and $c_f$ = 30.7 g/L, respectively). The CNF was performed at $\bar{p}_0$ = 35 bar, $h$ = 0.2 mm ($h$ = 0.6 mm for the fructose experiment) and $T$ = 20 °C, while the micro-TFF was performed with the 34 bar back-pressure valve using the 10 mm width channel ($h$ = 0.25 mm) at $Q_p$ = 0.1 mL/min, $Re_h \approx 0.2$ and $T$ = 20 ± 3 °C). In all the experiments the NFX membrane was used.

The better CNF efficiency is also suggested by the solute rejection data obtained for the three model solutes (Figure 6-1b). For the concentration of $K_2SO_4$ and sucrose solutions, there is no significant distinction between the $R_a$ values obtained for the micro-TFF (34 bar) and CNF (35 bar) processes. In the experiments of both these two techniques a NFX membrane was used; this is a polyamide membrane, which presents negative electrical charge on the membrane active surface at pH ≈ 7 (D'Costa 2018). Moreover, the NFX membrane exhibits a MWCO between 150 and 300 g/mol. Therefore, very high intrinsic rejections are expected for $K_2SO_4$, due to electrical charge effects, and for sucrose, due to steric hindrance.

Conversely, fructose is a neutral molecule with a MW of 180 g/mol that is very close to the lower limit of the MWCO of the membrane. Therefore, the membrane intrinsic rejection for fructose is low. In fact, the $R_a$ obtained by micro-TFF is only of 20 %, when using the same operating conditions used for the other solutions ($Re_h \approx 0.2$ and the 34 bar BPV) as seen in section 3.5.4. Higher fructose rejections are obtained for other conditions but they result at lower recovery rates (for instance, $R_a$ = 73 % when $Re_h \approx 8$ using the 17 bar BPV, as seen in section 3.5.2). On the other hand, when using the CNF device the fructose rejection was even higher (86 %) than that obtained with the TFF process at low recovery rates. Therefore, CNF retained more effectively the fructose in the concentrate, resulting in a more than twofold increase in the $CF$ when compared to the micro-TFF ($CF$ = 8.1 versus $CF$ = 3.3, respectively). The reason for this behaviour is again the self-cleaning mechanism provided by the CNF process. Since the more concentrated fluid elements are continuously swept from the membrane surface, the permeate that crosses the membrane is poorer in fructose. This fact proves that CNF is much more efficient than TFF when one intends to concentrate neutral molecules of MW close to the lower limit of the MWCO of the membrane, which constitutes a valid reason to select CNF for such task.

The presented results show that CNF technique is more efficient than micro-TFF for the concentration of small samples. However, CNF devices and equipment may be unavailable and, in this scenario, micro-TFF is the only option. In addition, even though CNF performs better it also presents some drawbacks. Therefore, in the next sub-section, the main benefits and limitations of CNF and micro-TFF are discussed qualitatively.

## 6.3 Advantages and disadvantages of micro-TFF and CNF

Both micro-TFF and CNF have their benefits and limitations. For the concentration of solutions with low osmotic pressure, both techniques perform well and the obtained concentration factors are similar, provided the intrinsic rejection is high. However, as the samples become more concentrated, differences in the obtained results emerge.

Overall, the CNF technique has proved to be more efficient than micro-TFF. The reason for its superior performance is the self-cleaning mechanism provided by the centrifugal force, which drags the concentrated fluid elements from the filtration chamber to the concentrate chamber. Therefore, CNF technique mitigates the CP phenomenon, resulting in a concentration process more efficient than micro-TFF. However, the use of micro-TFF must not be completely discarded. In fact, not all the labs have access to centrifugal equipment suited for the task and, as discussed before, super speed centrifuges capable to accommodate large centrifuge rotors are necessary to perform CNF. Thus, micro-TFF can be used to concentrate samples with fair $CF$ provided that the used membranes efficiently block the solute permeation. If the membrane used in the micro-TFF device is unable to retain those molecules, poor $CF$ values are obtained. Moreover, micro-TFF presents other advantges over CNF, which includes better sample volume management and the possibility to monitor and control the pressure inside the device.

Micro-TFF can process any amount of a certain sample provided that it is clean and diluted: the only difference when concentrating 3 mL or 6 mL of the same sample is the duration of the filtration cycle. However, the same task performed with a CNF device brings about some issues. The lab would have to acquire CNF devices with distinct nominal sample chamber volumes. In addition, if the amount of sample was larger than the volume of the sample chamber, more than one device was needed (increasing the cost of labware) or multiple filtration cycles had to be done (increasing the mechanical stress on the centrifuge and rotor).

On the other hand, micro-TFF technique presents several drawbacks. The main disadvantage of the micro-TFF technique is its prone character to CP and fouling phenomena. Since there is no self-cleaning mechanism in micro-TFF equivalent to the one in CNF, high solute concentration near the membrane and/or foulants deposition occur. For this reason, the permeate fluxes in micro-TFF are lower, resulting in longer filtration cycles. The need for pressurized systems is another drawback. In the case of using external pumping as a pressurizing device, solute losses or dilution issues arise when withdrawing the concentrate from the filtration chamber. This latter disadvantage can be reduced by improving the cell design, such that tubing connections can be easily attached and detached from the cell, minimizing the mixture between concentrate and unfiltered liquids. Although mass production of such cartridges could reduce their unit cost, it would prevent the easy interchange of membranes, which is a plus in experimental devices.

Despite resulting in similar concentration factors when the sample is diluted, CNF is more efficient than micro-TFF when using concentrated solutions. This is the main advantage of CNF. Other advantages include the shorter filtration cycles to achieve equivalent concentration, and the fact that several samples can be filtered at the same time (provided that the same filtration cycle is adequate). Therefore, different samples can be processed simultaneously

saving time and money. Since pressure is generated by the centrifugal force, CNF does not require external pumping, minimizing equipment and cleaning costs.

Despite the above-mentioned advantages of CNF over the micro-TFF, that technique also presents some limitations. The main one is the requirement of adequate centrifuges, centrifuge rotors and filtration devices. In addition, the volumetric capacity of the CNF device must be compatible with the sample size, otherwise, loss of efficiency may occur.

One of the purposes of this thesis was to prove that CNF is an adequate option to concentrate small-volume samples. For that, a CNF device with a sample chamber volume of ca. 3 mL was used. This device was designed to fit in standard 50 mL rotor buckets. According to the reasoning presented in Chapter 1 techniques to concentrate samples smaller than 100 mL are urged. The scale-up of the developed device to such sample volume levels must be studied carefully since larger rotor buckets would have to be used. The fitting in the device of both the 100 mL sample chamber and the neck channel may become a difficult task. Related to this issue is the fact that several rotor adaptors or devices may be needed to cover all the sample volumes range (from 0.5 mL to 100 mL) for a large set of rotors. Nevertheless, since one of the CNF advantages is the possibility of filtering several devices at the same time, the 100 mL of the sample could be divided into several portions, to be filtered simultaneously. At the end of the day, all comes down to commercial viability.

In terms of the used CNF prototype, there were some limitations on its use. First, the method to fix a membrane to the CNF device is tedious and can take more than 48 hours as there are several gluing steps. Although the curing time is irrelevant in automated and large-scale production, the use of a single prototype as done in the present thesis is very restrictive in terms of experimental work production. In addition, the effective membrane area (free of glue) can vary each time a new assembly is produced. The other problem is that this method does not allow for the reuse of membranes.

Balancing all the previously-discussed advantages and disadvantages of micro-TFF and CNF techniques (that are summarized in Table 6-1) it is clear that CNF equipment is preferable over micro-TFF when the former is available. It must be reminded that the CNF concentration data used to compare with the corresponding data for micro-TFF was obtained at $\beta = 0°$. As confirmed in Chapter 5 the $\beta$ angle plays an important role on the CNF performance. Therefore, an even more superior performance of CNF over micro-TFF would be noticed if the $\beta$ angle was negative.

Table 6-1 – Advantages and disadvantages of the used micro-TFF and CNF techniques and devices.

| | Advantages | Disadvantages |
|---|---|---|
| Micro-TFF | • Centrifugal equipment is not needed.<br>• For low concentration and clean samples, micro-TFF is as much efficient as CNF.<br>• Easy to apply a constant pressure and to monitor it.<br>• Any volume of sample can be handled.<br>• *Membrane replacement is possible without damaging it.* | • More prone to CP and fouling phenomena.<br>• External pressurization system is needed (pumps or pressurized gas).<br>• Filtration cycles longer than those for the CNF are needed.<br>• If pumps are used, some amount of liquid will remain unfiltered inside the tubing.<br>• If several samples are to be treated, its simultaneous processing needs one micro-TFF system for each.<br>• *Unfiltered sample inside tubing may mask the obtained concentration factor.* |
| CNF | • Better efficiency, comparatively to micro-TFF, as the feed concentration increases.<br>• Self-cleaning mechanism by centrifugal and Coriolis forces.<br>• Several devices can be used simultaneously, which is relevant when processing different samples.<br>• Filtration cycles smaller than those when using micro-TFF.<br>• External pumping is not needed.<br>• Easy to perform if disposable devices are available | • A centrifuge with large diameter rotor is needed.<br>• Several devices with different volume capacities may be needed.<br>• The sample chamber must be fully filled for better efficiency.<br>• *The active membrane area may vary in every new assembly.*<br>• *Tedious work to replace a membrane.*<br>• *Membranes cannot be reused.* |

Note: items written with italic style refer to properties of the used device.

## 6.4 Conclusion

In this thesis, micro-TFF and CNF techniques were evaluated in terms of their potential to concentrate small-volume samples of binary solutions of low MW solutes, with osmotic pressures varying between 0.6 and 2.6 bar. Direct comparison between micro-TFF and CNF shows that, for diluted samples, similar concentration factors can be obtained. Nevertheless, for these scenarios, micro-TFF requires the application of pressures higher than those for CNF. Special care should be taken when one intends to concentrate substances that already present small rejections ($R_a$ < 90-95 %) at mild conditions in TFF (low recovery experiments). In these cases, the rejection of such substances will be very low if the concentration is performed by micro-TFF.

Both micro-TFF and CNF techniques present their benefits and limitations. CNF requires adequate centrifuges, rotors and CNF devices. In turn, it produces higher $CF$ due to its inherent

self-cleaning mechanism of membrane surface. On the other and, micro-TFF technique has no special equipment requirements, but it needs external pumping, or pressurizing systems, and results in lower $CF$.

It must be emphasized that the direct comparison between both techniques was based on the nanofiltration results obtained with the membrane surface placed horizontally, both in micro-TFF and CNF ($\beta$ = 0°). As seen before in Chapter 5, the $\beta$ angle influences the CNF performance. Therefore, larger differences between micro-TFF and CNF are expected if the latter is performed with negative $\beta$, which should even result in a higher performance of the CNF technique. On the other hand, the micro-TFF technique can become more efficient if channels with higher performance are to be used, instead of the simple open straight channel operated in this work. These optimized channels should enhance flow hydrodynamics and disrupt the concentration polarization layer. Therefore, the hybrid computational / semi-empirical method, developed in Chapter 4 to determine the performance of nanofiltration systems, is a valuable tool to speed up the selection of the most efficient channels and spacers.

Overall, the CNF technique has proved to be more efficient than micro-TFF. The experiments performed with the CNF device developed in this work have shown that CNF technique is viable to concentrate low MW solutes in small-volume samples. In addition, the perspectives for performance improvement are good by modifying the CNF device, especially in terms of the membrane orientation.

# 7 Conclusions and future work

## 7.1 Conclusions

The present work was devoted to develop pressure-driven membrane techniques capable of concentrating low molecular weight solutes in small-volume samples. The aim was to obtain concentration factors above 10. Although similar techniques already exist, they are only available for medium-to-large sample volumes (above 100 mL) or for medium-to-large MW (above 1000 g/mol). Hence, efficient techniques to concentrate sample ranges not covered by the existent methods are urged. Such techniques may be useful not only to concentrate low MW solutes but also to fractionate them. An important example that can benefit from the availability of such concentrating and fractionating devices is the study of human peptidome. Peptides are usually separated from larger proteins using centrifugal ultrafiltration, but no subsequent treatment to the resulting permeate is performed. Further concentration or fractionation of that permeate would allow better interpretation of peptidome analysis. Therefore, techniques to concentrate (or fractionate) small-volume samples containing small solute would be of great interest for biological and environmental fields or for chemical synthesis and analysis.

The performance of pressure-driven membrane processes is affected by concentration polarization (CP) and fouling phenomena, leading to permeate flux decline and to loss of permeate quality (Sablani et al. 2001). After performing a comprehensive literature review of the state-of-art on methods used to mitigate those phenomena (W. Zhang et al. 2015), centrifugal filtration has emerged as a strong candidate for the intended task (Andeen 1981; Bergen et al. 2000). Since the objective is to concentrate small molecules, nanofiltration membranes are used and, for that reason, the developed centrifugal technique is named herein as centrifugal nanofiltration (CNF). However, and in spite of being prone to generate concentration polarization and fouling at the membrane surface, tangential flow filtration (TFF) is still a potential candidate to concentrate low molecular weight solutes in small-volume samples and, therefore, was not discarded; hence its capability to perform concentration of low molecular weight solutes was also assessed. To process small-volume samples, it turned out that the design of the tangential flow should be performed in channels with a thickness of 250 μm. For this reason, tangential flow filtration is herein called micro-TFF.

In practical applications, the samples to be concentrated are usually multicomponent. However, a fundamental study of new devices is more adequate when performed with model solutions with a unique solute that permits a better insight into the governing mechanisms. Hence, as a first approach to evaluate the performance of micro-TFF and CNF techniques, only the concentration of binary water-solute solutions was evaluated. Representative solutes with

molecular weights below 1000 g/mol were selected to assess the performance of the micro-TFF and CNF techniques. In particular, potassium sulfate, fructose, sucrose and polyethylene glycol (with average MW of 1000 g/mol) were used as model solutes. To characterize the used membranes additional solutes were used (sodium chloride, magnesium chloride, magnesium sulfate and sodium sulfate).

The used solute feed concentration depended on the type of experiments. Solute solutions with an osmotic pressure of 1.6 bar were used for the characterization of membranes in terms of their solute rejection, while for the concentration experiments solutions of different osmotic pressures were tested: 0.6 bar and 2.6 bar. Three different nanofiltration membranes were utilized: the NFX membrane (Synder Filtration), the NF90 membrane (Dow Chemical Company) and Desal TFM-50 (GE Osmonics). All these membranes have high intrinsic rejection (above 98%) to divalent salts. The NFX membrane was selected because its MWCO cover an intermediary range of the MW of the used model solutes. There are few data, in the literature, on the nanofiltration performance of the NFX membrane and, for that reason, the NF90 membrane was used as benchmark for micro-TFF. The Desal TFM-50 membrane was used in preliminary CNF experiments and in holographic interferometry studies.

Micro-TFF evaluation was performed using a small open slit channel of rectangular cross-section. This channel had constant height of $h$ = 0.25 mm and with of $W$ = 10 mm in almost all its 69 mm length (there are small entrance and exit sections, of 5 mm each, for flow stabilization). Although the performance of the micro-TFF was expected to deteriorate, due to exacerbated concentration polarization, it was possible to reach high $CF$ values, between 10 and 20, for diluted solutions with $\pi_f$ = 0.6 bar. For such diluted solutions, the $CF$ values obtained by micro-TFF are similar to the ones obtained by CNF. However, for more concentrated solutions, with $\pi_f$ = 2.6 bar, the permeate flux and solute rejection for the micro-TFF are much worse than for CNF. In addition, fair $CF$ values are only obtained by micro-TFF for very low Reynolds numbers, which practically turns the filtration in a dead-end process, with the consequent increase of the CP phenomenon.

To mitigate the negative effect of the CP phenomenon on tangential flow filtration, more efficient filtration devices should be used, which usually rely on CP disruption by flow instabilities. Thus, the filtration performance may be increased by improving liquid mixing using channels with grooved walls (Stroock et al. 2002; Islami & Khezerloo 2017). An alternative is to insert static mixers like meshes inside the channel (Gao et al. 2013). However, to quantify the enhancement of the filtration performance, one must have adequate means to predict permeation data in such systems. Although such data are obtainable with the use of CFD simulations, with suitable models for momentum and mass transport, three-dimensional simulations are very demanding in computational terms, especially if one intends to study the

permeation process in the whole channel domain. This issue gets even more severe if the channel or the static mixers have an intricate shape, leading to the need of very refined meshes and to an increase of the required time and computational power. Therefore, a hybrid computational / semi-empirical method, which combines detailed CFD computations for the mass transfer of non-suction processes in periodic domains with filtration performance data of the membrane, was developed herein. This hybrid method allows the study of nanofiltration processes, and thus of their performance in such channels with complex geometry, using only a small fraction of the computational time that was spent in the initial CFD computations. Therefore, this new hybrid approach paves the way for finding efficient channels and spacers that can mitigate concentration polarization in TFF devices.

The developed hybrid method to estimate nanofiltration data (permeate flux, bulk and membrane solute concentrations) makes use of a generalized mass transfer correction factor correlation (Geraldes & Afonso 2006). Determining the Sherwood number for the non-suction mass transfer process, $Sh_0$, and using the referred correlation, the nanofiltration data is predicted by an iterative algorithm using some input parameters (like the membrane properties). The algorithm can be applied globally to the whole filtration channel or locally, to sequential channel sections, in a march forward way (Completo et al. 2016).

The application of the above-mentioned hybrid method to predict nanofiltration data resulted in deviations lower than 10 % from the corresponding data obtained with detailed CFD simulations of the permeation process itself, in a filtration channel with transverse ribs. The local and global values of $Sh_0$ were determined by CFD, by simulating the mass transfer process inside impermeable-dissolving wall channels. Nevertheless, $Sh_0$ can be obtained by any other convenient techique, like the limiting current technique.

The CFD models used in this thesis for the simulation of permeation processes, of non-suction mass transfer processes and of flows without mass transfer, were validated using micro-particle image velocimetry (micro-PIV) and holographic interferometry (HI) techniques. Flow velocity fields were obtained using the former technique, while concentration fields were obtained using the latter. These non-invasive techniques were very useful to validate the momentum and mass transfer numerical models. The simulations were restricted to 2D computational domains, because the rectangular cross-section channels used in the experimental nanofiltration cell had a large width-to-height ratio, and the flow was admitted laminar.

The comparison between experimental and numerical results was done in two stages. First, water flow hydrodynamics inside impermeable open and ribbed channels were compared. Notice should be given to the fact that in NF and RO processes with low feed recovery the velocity profiles in the main flow direction are not particularly affected by permeation. Thereafter, the concentration patterns obtained for NF processes of $K_2SO_4$ solutions were compared, also for open and ribbed channels, but for a system where one of the walls (the

bottom one) was semi-permeable. For the hydrodynamics study, the ribbed channel had ribs adjacent to the bottom surface, while for the nanofiltration setup the ribs were placed on the top wall, opposed to the membrane.

In terms of the hydrodynamics in open channels, the velocity profiles are parabolic at any $xz$-plane (vertical planes in the main flow direction) and the lateral walls affect the velocity magnitude up to a $y$-distance of ca. 1 mm from each side. Above that value the velocity profile is nearly constant in the whole width of the channel. When transverse ribs are placed on the wall, the flow structure changes, due to the geometrical constrains, and recirculation zones appear in both sides of each rib. The largest recirculation zone occurs downstream the rib and its size increases with $Re_h$.

In terms of the solute concentration field in NF processes, concentration gradients appear in the vicinity of the semi-permeable wall, i.e. a concentration boundary layer develops near the membrane. The solute concentration is higher at the membrane surface and decreases to the bulk concentration value at the limit of the concentration boundary layer. The shape of such concentration gradients depends on the channel geometry, as was verified with the use of HI. While for open channels the interferometric fringes remain nearly parallel to the membrane, for ribbed channels the fringes bend towards the membrane in the vicinity of the rib, evidencing the existence of a thinner concentration boundary layer in that zone. In this part of the work, the effect of several operating parameters on the concentration polarization was also studied, by analysis of the acquired interferograms. It was verified that CP modulus increases with time and with the applied pressure, but decreases with $Re_h$ and with the feed concentration. The dependence with time is only significant for very small $Re_h$ (less than 5) where the permeation practically occurs as a dead-end process, otherwise the concentration field stabilizes in ca. 10 min. An important evidence verified by both nanofiltration experiments and by CFD predictions is the fact that in ribbed channels the concentration polarization decreased (when compared to the process in open channels) leading, thus, to higher permeate fluxes and permeate quality.

Very good agreement was obtained between experimental and numerical results of the concentration profiles for the different solution tested, even without applying the algorithm proposed by Rodrigues and colleagues (Rodrigues et al. 2013) to correct experimental interferometry data, since the ratio $\Delta n_{mb}/\delta_D$ is smaller than 1 $m^{-1}$. Therefore, the CFD model was applied to further study the effect of the channel geometry on the nanofiltration processes and whether periodicity on mass transport was achieved or not. Four channel geometries were considered to study the effect of the location of the transversal ribs: open channel (without ribs); top cavity (ribs placed on the top wall, opposed to the membrane); bottom cavity (ribs placed on the bottom wall, adjacent to the membrane); and zigzag (ribs placed sequentially on the top and bottom walls).

Simulations of NF processes in the above-mentioned geometries show appreciable differences in the solute concentration fields. For open channels, and as expected, the concentration boundary layer grows monotonically along the channel length. A similar pattern occurs for the top cavity geometry, but the ribs placed on the opposite wall reduce the concentration boundary layer thickness in their vicinity, due to local higher shear stress that exerts a cleansing effect on the membrane surface. In bottom cavity channels, high concentration zones occur on both sides of the ribs, due to the accumulation of solute inside the recirculation ones, which are regions of very low shear stress. For that reason, the solute concentration in these regions is even higher than those in any section of the corresponding open channel. Nevertheless, outside the recirculation zones, the concentration is lower than that in open and top cavity channels. Finally, the zigzag geometry produces concentration fields that can be seen as a mix between those observed for the top and bottom cavity geometries. In zigzag geometry, the solute concentration field pattern near the ribs is similar to the corresponding one of top geometry in the regions where the rib is placed on the top surface, whereas it is similar to the corresponding bottom cavity geometry one in the regions where the rib is placed on the bottom surface. Thus, while for top and bottom geometries the pattern of the solute concentration profile repeats at consecutive rib sections, for the zigzag configuration the pattern repeats at every two consecutive spacers.

The periodicity of mass transfer along the channel was assessed using the $w/w_b$ ratio extracted from the CFD simulation data, which is the ratio between a given solute mass fraction and the bulk solute mass fraction in a defined section of the channel (the repetitive section between consecutive ribs). The value of $w_b$ was calculate as the logarithmic mean of the solute mass fraction at the entrance and exit of each section, as defined by equation (4-20) through the variable $w_{bLN,sec}$. Two types of $w/w_b$ ratios were used. In the first one, $w$ refers to the average of the solute mass fraction at the membrane surface, as defined by equation (4-22) through the variable $w_{m,sec}$. In the second one, $w$ is the solute mass fraction along the channel height (in the $z$-direction) determined at locations distancing 1.75 mm from the beginning of the section. The ratio $w_{m,sec}/w_{bLN,sec}$ stabilizes after 15 to 25 channel sections, depending on the channel geometry. The ratio $w(z)/w_{bLN,sec}$ needs, at least, the same amount of repetive unit cells. These results contrast with those obtained by other authors for flow hydrodynamics in impermeable channels, where it is accepted that flows in impermeable ribbed channels reach periodic conditions in just a few number (between 2 and 6) of repetitive unit cells (Alexiadis et al. 2007; Shakaib et al. 2009). The explanation for this difference lies in the much lower mass diffusivity values (when compared to those of momentum diffusivity), which makes of mass transport a much slower process than momentum transport. Therefore, the use of periodic conditions for

mass transfer modeling should be carefully evaluated, especially in the scenarios of small channels with high feed recoveries.

As discussed above, micro-TFF proved to be capable of concentrating small-volume samples of binary water-solute solutions of low MW solutes. However, micro-TFF has its limitations, especially related to potentially severe CP effects. Conversely, CNF that was also identified as a candidate to perform the concentration of such solutions present a self-cleaning mechanism that mitigates CP and fouling problems. Since CNF has never been used before for such task, it was necessary to design a new and innovative device suitable for the purpose.

Centrifugal filtration devices are common for micro- and ultrafiltration of small-volume samples and are designated in the literature as CUF devices. The simple replacement of the MF/UF membranes of CUF devices by NF membranes would not be enough to perform the concentration conveniently. In CUF devices the sample chamber occupies most of the volume above the membrane which means that high CF values are obtainable only when the liquid head reduces almost to zero. Consequently, the pressure generated by the centrifugal force drops significantly during the filtration cycle. Although this fact may not be very important in MF and UF processes since low pressure is needed (usually up to 2 bar), it would be inadequate to nanofiltration. First, NF needs much higher transmembrane pressures (10 to 40 bar). Second, the meniscus position is unknown in real-time so high rotational speed kicks can irreversibly compact the NF membrane leading to further flux decline. Therefore, to perform NF by centrifugation a device capable of maintaining the applied pressure during the major part of the filtration cycle is needed.

The main innovation of the developed CNF is the physical separation of the sample chamber from the filtration chamber. The connection between these chambers is made through a thin neck channel, which permits the liquid to flow from the sample chamber to filtration chamber. Since the sample chamber is placed at a smaller radial location the liquid in the filtration chamber is pressurized by the liquid head of the sample.

The CNF potential was assessed at three main levels: a) evaluation that adequate nanofiltration of model solutions occurs by centrifugation; b) study of the effect of the filtration chamber height, $h$, on the CNF performance; c) study of the influence of the angle between the centrifugal force and the membrane surface, the $\beta$ angle, on the CNF performance.

First, it was assessed that the developed CNF device was adequate to perform nanofiltration of aqueous solutions. To do that, permeate fluxes and the corresponding apparent rejections were measured as function of the average pressure at the membrane surface at the initial instant of the filtration cycle, $\bar{p}_0$. In this first part, the CNF device was used in open chamber mode (i.e. without using the internal block part that delimitates the filtration chamber), the $\beta$ angle was set to 0°, and the filtration cycles were short to collect small permeate samples (ca. 1 mL), since it was intended to obtain clean permeates to prove the concept of the CNF

technique. In this study, and in the following ones dealing with CNF, the initial average transmembrane pressure, the $\bar{p}_0$ parameter, was used, since there is no simple way to know the instantaneous pressure in real-time. Nevertheless, knowing the dimensions of the rotors and of the CNF device, the use of $\bar{p}_0$ allows comparing the results obtained for distinct centrifuge rotors.

The results show that clear permeates ($R_a$ > 98 %) can be obtained by CNF when the applied rotational speed (given by $\bar{p}_0$) is such that $\bar{J}_v$ > ¼ $\bar{J}_w$; otherwise, the solvent flux is so low that the rejection drops as $\bar{p}_0$ decreases. For low concentration experiments in open chamber configuration, the relationship between $\bar{J}_v$ and $\bar{p}_0$ was linear for the studied $\bar{p}_0$ range, indicating that the limiting flux plateau was never reached. In addition, the experimental permeate fluxes are well predicted by the osmotic pressure model (using the feed concentration to calculate the osmotic pressure on the feed side). These results show that under these scenarios the CP phenomenon is not significant. Therefore, CNF can be used to nanofilter small samples of high osmotic pressure. The next natural step was to show that it can also concentrate samples up to fairly high CF values (i.e. $CF$ above 10).

Sample concentration by CNF was performed using the internal block part inside the CNF device. Several different internal block parts were used, each one with distinct height edges on their bottom surface, which allowed studying the effect of $h$ on the CNF performance by using filtration chamber heights ranging from $h$ = 0.1 mmm up to $h$ = 2.4 mm. To assess the influence of the $\beta$ angle, the CNF device was placed in different rotor adaptors resulting in $\beta$ = -10°, 0°, +2° and +10°. However, prior to concentration experiments, the temporal evolution of the CNF process was assessed for several scenarios (all at $\beta$ = 0°) to estimate the necessary time to achieve complete filtration. Complete filtration was defined as the state where no liquid remained inside the filtration chamber after the filtration cycle. It was verified that in some scenarios (high sample concentration, low $\bar{p}_0$ and $h$ = 0.1 mm) the filtration was not complete.

In terms of the influence of $h$ on the CNF performance, $h$ = 0.2 mm resulted in higher $CF$ values. As an illustrative example for $\beta$ = 0°, the maximum $CF$ for the concentration of a 7.7 g/L sucrose solution was obtained for $h$ = 0.2 mm: $CF$ = 15. With the increase of $h$ for 0.6 mm and for 1.3 mm the CF value decreased 35 % and 50%, respectively. The reason to this behaviour is the fact that, for the used CNF device, as $h$ increases so do the volumes of the filtration and concentrate chambers and, consequently, for the same $\bar{p}_0$ a larger amount of concentrate remains inside those chambers but at a lower concentration. On the other hand, in some cases for $h$ = 0.1 mm the filtration is incomplete because the solute concentration grows sharply in the filtration chamber leading to high osmotic pressure and inefficient permeation.

The CNF performance is strongly influenced by the $\beta$ angle. However, the effect of $\beta$ is easier to observe when the filtration is not complete. In these cases, distinct $\beta$ angles result in

different amounts of liquid remaining inside the sample chamber at the end of the filtration cycle. It was verified that the amount of the unfiltered liquid drops as $\beta$ decreases, the best configurations being those where the $\beta$ angle is negative. As an example, for the CNF of a 30.7 g/L sucrose solution in a filtration chamber with $h$ = 0.1 mm, the filtration of the sample (3 mL) was complete for $\beta$ = -10°, while for $\beta$ = 0° and $\beta$ = +10° ca. 17 % and 30 % of the sample remained unfiltered, respectively. The explanation of such behaviour lies in the self-cleaning mechanism of the membrane that occurs in centrifugal filtration provided the membrane is placed in an adequate orientation. When $\beta$ is negative, the centrifugal force disrupts the CP layer by pulling the heavier fluid elements (and usually the most concentrated ones) from the membrane surface. These fluid elements are replaced by less concentrated ones resulting in lower osmotic pressure at the membrane surface and, therefore, the permeate flux increases and is maintained for a longer time. For $\beta$ = 0° the heavier fluid elements are dragged along the membrane surface resulting in a lower CNF performance. When $\beta$ becomes positive the heavier fluid elements are squeezed against the membrane, the CP layer is stabilized and the CNF performance drops. Therefore, whenever possible negative $\beta$ angles should be used.

It was also confirmed that CNF stratifies the solute concentration inside the device. This was verified by withdrawing individual 60 μL portions from the concentrate chamber. The first portion (the one corresponding to the liquid placed at the most outwards radial location in the concentrate chamber) was that with higher solute concentration. For the subsequent portions (corresponding to decreasing radial positions) the solute concentration decreased. Therefore, it was possible to reach local $CF$ values 15% to 30 % higher than the average ones for the whole concentrate, but at an expense of obtaining only a small volume of such high $CF$ liquid.

In this work, a single CNF device is used in each experimental run, its counterweight being a centrifugal tube filled with sand to match the weight of the CNF device at the end of the filtration cycle. The simultaneous use of paired devices or of larger devices may be problematic. Larger devices result in larger displacements of the centre of inertia of the device, which if not correctly followed by the device in the opposite rotor bucked may lead to rotor imbalance and, thus, at the best in the interruption of the centrifugation. A similar issue arises if the permeate flux at opposite devices is different, which can be caused by the use of membranes with distinct permeability or by the use of different samples with equivalent membranes. Therefore, to avoid hazards these issues must be addressed in future studies.

Comparing the application of micro-TFF and CNF techniques using the same aqueous solutions, it was shown that CNF is more effective than micro-TFF to concentrate low MW solutes in small-volume samples. Nevertheless, fair $CF$ values (above 10) can still be obtained by micro-TFF in specific conditions (sample solutions with low osmotic pressure and high applied pressure). Moreover, the management of different sample volumes is easier when using

micro-TFF. The clear advantages of the CNF technique are its yielding of higher CF, the non-requirement of external pump or tubing and the possibility to process simultaneously several samples, even of different compositions. However, to work conveniently, CNF needs a high speed centrifuge and suitable rotors, rotor adaptors and filtration devices. Nevertheless, CNF is preferable to concentrate small-volume samples containing low MW solutes, since the results obtained in this work shows that it is more efficient than micro-TFF. Although the good performance of the developed CNF device, there is still room for its improvement in regard to safety and performance.

Ultimately, the work performed in this thesis has successfully proved that low MW solutes in small-volume samples can be concentrated both by micro-TFF and CNF techniques. Although affected by the concentration polarization phenomena, tangential flow filtration provides a simple way to obtain fair concentration factors. Centrifugal nanofiltration, which was used for the first time in this work, resulted in even better concentration performance, due to its self-cleaning mechanism that pulls the concentrated fluid elements away from the membrane surface. Despite the fact that the used filtration devices can be further improved, it is clear that both the micro-TFF and CNF techniques can be useful for sample concentration in several scientific research and commercial applications.

## 7.2 Future work

The results obtained in the present work suggest that both micro-TFF and CNF are adequate to concentrate small-volume of liquid samples of high osmotic pressure. However, the design of both devices can be improved to provide better concentration performance, viewing mainly the development devices for commercialization. Thus, prospective work is proposed in four areas: a) further improvement of the CNF device; b) further improvement of the micro-TFF device; c) concentration of multicomponent liquid samples; d) numerical modeling of the CNF process.

*Further development of the CNF device*

The CNF device designed and applied in this work can be further developed in several ways to overcome some issues, or lacks, observed during its use, including: a) study the effect of more negative $\beta$ angles; b) redesign the CNF device to ensure a leakage free operation; c) redesign the CNF device to easily withdraw the concentrate liquid; d) redesign the CNF device to include a second membrane; e) develop a better process to fix the membrane to the device; f) apply membranes that guarantee homogeneity in their permeate fluxes.

For $\beta$ = 0°, relatively high $CF$ values ($CF \approx 20$) were obtained only for solutions with low osmotic pressure. For solutions with high osmotic pressure some amount of feed can remain inside the feed chamber, but results have shown that a negative $\beta$ angle of -10° enhances the concentration performance. Thus, it is important to test negative angles of higher magnitude than those used in the present work. Modification of the $\beta$ angle may also influence the durability of the assembly, in terms of the membrane gluing strength. Positive $\beta$ angles force the membrane towards its support, whereas negative $\beta$ angles results in forces pulling the membrane, and the glue, away from the membrane support. Consequently, devices with negative $\beta$ angles are more prone to faster peeling off of the membrane. In addition, the modification of the $\beta$ angle may require the redesign of the device.

Although spills through the vent holes did not occur when using the actual CNF device, the fact is that it is not complete leakage free and it permits air flowing from its interior to the external atmosphere. This can be a limitation for its use with toxic, biological samples and with those samples that form vapors. Therefore, to fulfill with leakage-free requirements, the CNF device must be redesigned so that it is completely closed to the exterior and the air flow is made exclusively in its interior, like in current commercial CUF devices.

To withdraw the concentrate from the actual CNF device, a piece of tubing is inserted through the auxiliary channel and the liquid is removed by making suction with a syringe. Therefore, a possible enhancement for the CNF device that must be considered is to redesign it such that the concentrate can be collected by inverse spinning, as is done in some of the current commercial CUF devices. Providing an optimal device design guarantees that the whole concentrate liquid is removed and it does not get stuck in air pockets.

A redesign of the CNF device to allow using simultaneously two opposing membranes (one in each side of the filtration channel) would lead to a decrease of the filtration time (since the membrane area would be larger) or to an increase of the pressure during the filtration (if each individual smaller membrane pieces are placed farther away from the axis of rotation). Therefore dual membrane devices should be considered. Possible starting points for dual membrane designs are those already devised in the patent application of the CNF device (Geraldes et al. 2018).

The used process to fix a membrane to the CNF prototype is tedious, time-consuming and prone to errors (including variations on the channel height and glue-free membrane area, due to the amount of glue spread over it). Thus, it is very important to develop easier and replicable methods to fix or replace the membrane.

As mentioned before (section 5.4.3), devices with sample chambers larger than the herein developed prototype were discussed. One of the issues related with the scale-up of CNF devices is that if the applied membranes have distinct hydraulic permeability, then, the permeate rate on each device can be significantly different, which can lead to centrifuge imbalance. In fact, as

shown in Table 3-6 and Table 3-7, the currently available commercial membranes present a large variability of their hydraulic permeability. To avoid imbalance during the centrifugation cycle, only membranes with precise and equal hydraulic permeability should be used at opposite rotor buckets. Therefore, the urge of membranes and membrane manufacture processes that minimize the above-mentioned problem should be instilled.

*Further improvement of the micro-TFF device*

Having proved that micro-TFF technique can be used to obtain high concentration factors, a subsequent objective should be to create micro-TFF devices with better concentration performance. Two routes can be devised to obtain higher $CF$ values: improve the design of the filtration channel and devise efficient and user friendly mechanisms to withdraw the concentrate liquid from the filtration chamber. In addition, micro-TFF systems that do not depend on the use of HPLC pumps can also be conceived.

To enhance concentration performance, different channel designs, or the inclusion of spacers, should be tested. These innovative channel designs enhance liquid mixing and, therefore, minimize the CP phenomena. The current method to change the channel geometry of the used micro-TFF device is not straightforward since it implies the replacement of flat plastic sheets with the desired channel design. A more convenient alternative is to use 3D-printing technology to manufacture plastic parts that already contain the desired channel design. As the spatial resolution of 3D-printers is increasing, it may be also possible, in a near future, to incorporate spacers with the adequate fine spatial resolution on the design of the channel at very low cost.

The best design candidates, for channels and spacers, can be selected based on the preliminary results obtained by using the hybrid computational / semi-empirical method developed in this work. This hybrid method has shown to be a valid tool to predict nanofiltration performance at low Reynolds numbers, since deviations lower than 10 % were obtained, in comparison with the CFD simulations of the nanofiltration process. Therefore, it can be considered as a means to investigate the impact of innovative feed spacers on the performance of the micro-TTF.

Another optimization that should be pursuing is to devise an adequate method to remove the concentrated liquid from the filtration chamber. The experiments performed with the micro-TFF device have shown that the concentrated liquid inside the filtration chamber presented higher $CF$ values than that of the concentrate stream. A cause for this behaviour is the mixing of the concentrated liquid with unfiltered sample present in the tubing downstream the micro-TFF. Therefore, more compact micro-TFF devices should be designed to take this issue into account, resulting in a correct flushing of the concentrate liquid.

Although in this work the system was pressurized using a back-pressure valve and an HPLC pump, it would be interesting to test systems where pressurized gas is used. Pressurization by compressed gas would not only decrease the investment in equipment but also turn most of the cleaning procedures unnecessary, and, therefore, make possible to simultaneously filter several samples at a fraction of the cost. The advantage of coupling pumps and valves to pressurize the liquid is that the flow rate is manageable. On the other hand, pressurization by gas would turn the filtration process almost into a dead-end one. As seen in this work, dead-end filtration works fine if the sample has low osmotic pressure (and no fouling agents), but for samples with high osmotic pressure some sort of mechanism/technique must be devised to mitigate flux decline.

Although concentration by micro-TFF poses some operational difficulties, it is clear that there is a wide scope for improvement.

*Concentration of multicomponent samples*

Despite the good results obtained for the concentration of binary solutions, multicomponent liquid samples should be tested to assess the capability of the devices to obtain similar results using more realistic mixtures.

Samples are seldom binary water-solute mixtures. In many cases, the liquids to be analysed come from environmental, biological, or synthesis media and, therefore, have complex compositions. Although sample pre-treatment can be applied to remove undesirable components that can cause the fouling phenomena, the CNF and micro-TFF devices should be assessed in their capability to handle multicomponent mixtures, especially those that can pose problems related with flux decline.

In addition, using multicomponent mixtures one can evaluate the capability of the micro-TFF and CNF devices to perform sample fractionation. Such study would include several model solutes and NF membranes with distinct MWCO. This study should also include both permeation studies and membrane autopsies to evaluate the impact of fouling.

*Modeling of the CNF process*

Predictions of the CNF concentration process can be performed using CFD. That way, time and money costs spent on the development of the CNF device can be minimized. The results of the numerical simulations would enlighten the influence of the $h$ and $\beta$ on the CNF performance. However, one must be aware that only with a fully expensive unsteady-state 3D simulation is it possible to simulate the complex flow structure that prevails inside the filtration chamber channel during the whole filtration cycle, which is driven by the centrifugal and

Coriolis forces. Buoyant-induced turbulence can eventually exist inside the CNF device, which adds an extra layer of complexity to the simulation. Therefore, to obtain numerically reliable and precise data on the CNF concentration process, the use of computer clusters of high performance is necessary.

# References


Abel, K., 1997. Influence of oscillatory flows on protein ultrafiltration. *Journal of Membrane Science*, 133, pp.39–55.

Adrian, R., 1991. Particle-imaging techniques for experimental fluid-mechanics. *Annual Review of Fluid Mechanics*, 23, pp.261–304.

Adrian, R., 2005. Twenty years of particle image velocimetry. *Experiments in Fluids*, 39, pp.159–169.

Agana, B., Reeve, D. & Orbell, J., 2012. The influence of an applied electric field during ceramic ultrafiltration of post-electrodeposition rinse wastewater. *Water Research*, 46, pp.3574–3584.

Ahmad, A., Lau, K. & Abu Bakar, M., 2005. Impact of different spacer filament geometries on concentration polarization control in narrow membrane channel. *Journal of Membrane Science*, 262, pp.138–152.

Ahmad, A. & Lau, K., 2006. Impact of different spacer filaments geometries on 2D unsteady hydrodynamics and concentration polarization in spiral wound membrane channel. *Journal of Membrane Science*, 286, pp.77–92.

Ahmad, A. et al., 2012. Membrane antifouling methods and alternatives: ultrasound approach. *Separation & Purification Reviews*, 41, pp.318–346.

Ahmed, W. et al., 2015. Comparison of concentration methods for quantitative detection of sewage-associated viral markers in environmental waters. *Applied and Environmental Microbiology*, 81, pp.2042–2049.

Akhondi, E. et al., 2014. Evapoporometry determination of pore-size distribution and pore fouling of hollow fiber membranes. *Journal of Membrane Science*, 470, pp.334–345.

Alexiadis, A. et al., 2007. Laminar flow transitions in a 2D channel with circular spacers. *Industrial & Engineering Chemistry Research*, 56, pp.5387–5396.

Almeida, A., Geraldes, V. & Semiao, V., 2010. Microflow hydrodynamics in slits: effects of the walls relative roughness and spacer inter-filaments distance. *Chemical Engineering Science*, 65, pp.3660–3670.

Altaee, A., Sharif, A. & Hamdan, M., 2016. Nanofiltration separation of highly concentrated multivalent electrolyte draw solution; a pilot plant study. *Desalination and Water Treatment*, 57, pp.20237–20247.

Ambrosi, A., Cardozo, N. & Tessaro, I., 2014. Membrane separation processes for the beer industry: a review and state of the art. *Food and Bioprocess Technology*, 7, pp.921–936.

Amokrane, M. et al., 2015. A study of flow field and concentration polarization evolution in

membrane channels with two-dimensional spacers during water desalination. *Journal of Membrane Science*, 477, pp.139–150.

Andanson, J. & Baiker, A., 2010. Exploring catalytic solid/liquid interfaces by in situ attenuated total reflection infrared spectroscopy. *Chemical Society reviews*, 39, pp.4571–4584.

Andeen, G., 1981. Effects of acceleration on reverse osmosis desalination. *Desalination*, 36, pp.265–275.

Andersson, H. & van den Berg, A., 2003. Microfluidic devices for cellomics: a review. *Sensors and Actuators B: Chemical*, 92, pp.315–325.

Artuğ, G. et al., 2007. A comprehensive characterization of commercial nanofiltration membranes. *Separation Science and Technology*, 42, pp.2947–2986.

Baker, R., 2004. *Membrane technology and applications* 2nd ed., John Wiley & Sons.

Bashir, R., 2004. BioMEMS: state-of-the-art in detection, opportunities and prospects. *Advanced drug delivery reviews*, 56, pp.1565–86.

Bateson, H. et al., 2011. Use of matrix-assisted laser desorption/ionisation mass spectrometry in cancer research. *Journal of Pharmacological and Toxicological Methods*, 64, pp.197–206.

Beebe, D., Mensing, G. & Walker, G., 2002. Physics and applications of microfluidics in biology. *Annual review of biomedical engineering*, 4, pp.261–86.

Benito-López, F. et al., 2008. High pressure in organic chemistry on the way to miniaturization. *Tetrahedron*, 64, pp.10023–10040.

van den Berg, G., Racz, I. & Smolders, C., 1989. Mass transfer coefficients in cross-flow ultrafiltration. *Journal of Membrane Science*, 47, pp.25–51.

Bergen, A. et al., 1997. Centrifugal membrane and density separation: a new spin on membrane fouling. *Membrane Technology*, 90, pp.8–10.

Bergen, A. et al., 2000. Flux enhancement in reverse osmosis using centrifugal membrane separation. *Journal of Membrane Science*, 176, pp.257–266.

Bergen, A. et al., 2003. An experimental assessment of centrifugal membrane separation using spiral wound RO membrane elements. *Desalination*, 154, pp.225–232.

Berger, S., Stawikowska, J. & Swaay, D., 2014. Continuous suspension of lipids in oil by the selective removal of chloroform via nicrofluidic nembrane separation. *Industrial & Engineering Chemistry Research*, 53, pp.9256–9261.

Berthier, E., Young, E. & Beebe, D., 2012. Engineers are from PDMS-land, biologists are from Polystyrenia. *Lab on a chip*, 12, pp.1224–37.

Bhagat, A. et al., 2010. Microfluidics for cell separation. *Medical & biological engineering & computing*, 48, pp.999–1014.

Bhattacharjee, S., Chen, J. & Elimelech, M., 2001. Coupled model of concentration polarization and pore transport in crossflow nanofiltration. *AIChE Journal*, 47, pp.2733–2745.

Bikle, D. et al., 1984. Free 1, 25-dihydroxyvitamin D levels in serum from normal subjects,

pregnant subjects, and subjects with liver disease. *The Journal of Clinical Investigation*, 74, pp.1966–1971.

Bird, R.B., Stewart, W.E. & Lightfoot, E.N., 2007. *Transport Phenomena* 2nd., John Wiley & Sons.

Blanco, S. et al., 2004. Centrifugal ultrafiltration method for rapid concentration of Legionella pneumophila urinary antigen. *Journal of Clinical Microbiology*, 42, p.4410.

Blanpain-Avet, P. et al., 1999. The effect of oscillatory flow on cross flow microfiltration of beer in a tubular mineral membrane system - membrane fouling resistance decrease and energetic considerations. *Journal of Membrane Science*, 152, pp.151–174.

Bode, K. et al., 2007. Pulsed flow cleaning of whey protein fouling layers. *Heat Transfer Engineering*, 28, pp.202–209.

Boer, R. et al., 1980. Fluidized beds as turbulence promoters in the concentration of food liquids by reverse osmosis. *Journal of Food Science*, 45, pp.1522–1528.

Bogner, A. et al., 2007. A history of scanning electron microscopy developments: Towards "wet-STEM" imaging. *Micron*, 38, pp.390–401.

Bollenbeck, P. & Ramirez, W., 1974. Use of a Rayleigh interferometer for membrane transport studies. *Industrial & Engineering Chemistry Fundamentals*, 13, pp.385–393.

Bonhomme, L. et al., 2014. Centrifugal filter. *US Patent* 8747670.

Borujeni, E. & Zydney, A., 2012. Separation of plasmid DNA isoforms using centrifugal ultrafiltration. *BioTechniques*, 53, pp.49–56.

Bouchoux, A., Balmann, H. & Lutin, F., 2005. Nanofiltration of glucose and sodium lactate solutions. Variations of retention between single- and mixed-solute solutions. *Journal of Membrane Science*, 258, pp.123–132.

Bowers, W. & Rigopulos, N., 1986. Centrifugal microconcentrator and methods for its use. *US Patent* 4632761.

Bowers, W. & Tiffany, D., 1989. Centrifugal force-enhanced filtration of fluids. *US Patent* 4832851.

Bowers, W. & Yankopoulos, B., 1998. Microconcentrator device. *US Patent* 5733449.

Bowers, W., Yankopoulos, B. & Towle, T., 2002. Ultrafiltration device and method of forming same. *US Patent* 6269957.

Broussous, L. et al., 2000. Hydrodynamic aspects of filtration antifouling by helically corrugated membranes. *Chemical Engineering Science*, 55, pp.5049–5057.

Bucs, S. et al., 2015. Experimental and numerical characterization of the water flow in spacer-filled channels of spiral-wound membranes. *Water Research*, 87, pp.299–310.

Buonomenna, M., 2013. Nano-enhanced reverse osmosis membranes. *Desalination*, 314, pp.73–88.

Cadotte, J. et al., 1980. A new thin-film composite seawater reverse osmotic membrane.

*Desalination*, 32, pp.25–31.

Cahill, D., Freger, V. & Kwak, S., 2008. Microscopy and microanalysis of reverse-osmosis and nanofiltration membranes. *MRS Bulletin*, 33, pp.27–32.

Cai, M., Zhao, S. & Liang, H., 2010. Mechanisms for the enhancement of ultrafiltration and membrane cleaning by different ultrasonic frequencies. *Desalination*, 263, pp.133–138.

Calvo, J. et al., 2011. Liquid-liquid displacement porometry to estimate the molecular weight cut-off of ultrafiltration membranes. *Desalination*, 268, pp.174–181.

Cao, Z., Wiley, D.E. & Fane, A.G., 2001. CFD simulations of net-type turbulence promoters in a narrow channel. *Journal of Membrane Science*, 185, pp.157–176.

Cao, J. et al., 2011. Comparison of alternative extraction methods for secretome profiling in human hepatocellular carcinoma cells. *Science China Life Sciences*, 54, pp.34–38.

Capretto, L. et al., 2011. Micromixing within microfluidic devices. *Topics in Current Chemistry*, 304, pp.27–68.

Carlsson, N. et al., 2001. Rapid Analysis of Inositol Phosphates. *Journal of Agricultural and Food Chemistry*, 49, pp.1695–1701.

Causserand, C. & Aimar, P., 2010. Characterization of filtration membranes. In E. Drioli & L. Giorno, eds. *Comprehensive membrane science and engineering*. Elsevier B.V., pp. 311–335.

Chambers, B. et al., 2001. Reverse-flow centrifugal filtration method. *US Patent* 6302919.

Chamier, J. et al., 2015. Aluminium (Al) fractionation and speciation; getting closer to describing the factors influencing Al3+ in water impacted by acid mine drainage. *Chemosphere*, 130, pp.17–23.

Chandrashekhara, K., 2001. *Theory of plates*, Universities Press.

Charrett, T., James, S. & Tatam, R., 2012. Optical fibre laser velocimetry: a review. *Measurement Science and Technology*, 23, p.32001.

Chau, T., 2009. A review of techniques for measurement of contact angles and their applicability on mineral surfaces. *Minerals Engineering*, 22, pp.213–219.

Chayer, B. et al., 2012. Velocity measurement accuracy in optical microhemodynamics: experiment and simulation. *Physiological measurement*, 33, pp.1585–602.

Chellam, S. & Cogan, N., 2011. Colloidal and bacterial fouling during constant flux microfiltration: comparison of classical blocking laws with a unified model combining pore blocking and EPS secretion. *Journal of Membrane Science*, 382, pp.148–157.

Chen, J., Li, Q. & Elimelech, M., 2004. In situ monitoring techniques for concentration polarization and fouling phenomena in membrane filtration. *Advances in Colloid and Interface Science*, 107, pp.83–108.

Chen, V., Li, H. & Fane, A., 2004. Non-invasive observation of synthetic membrane processes - a review of methods. *Journal of Membrane Science*, 241, pp.23–44.

Chen, X. & Shen, J., 2017. Review of membranes in microfluidics. *Journal of Chemical Technology and Biotechnology*, 92, pp.271–282.

Cheryan, M., 1998. *Ultrafiltration and microfiltration handbook*, CRC Press.

Childress, A. & Elimelech, M., 2000. Relating nanofiltration membrane performance to membrane charge (electrokinetic) characteristics. *Environmental Science and Technology Letters*, 34, pp.3710–3716.

Chinnov, E., Ron'shin, F. & Kabov, O., 2016. Two-phase flow patterns in short horizontal rectangular microchannels. *International Journal of Multiphase Flow*, 80, pp.57–68.

Cianci, G., 1996. Fluid filtration device. *European Patent* 0709132.

Clark, P., 2004. Fluid-filtration receptacle with user-variable semi-permeable drain assembly. *US Patent* 6719896.

Clifton, M. & Sanchez, V., 1979. Holographic interferometry applied to the measurement of boundary layers in electrodialysis and ultrafiltration. *Proc. SPIE Optics and Photonics Applied to Medicine*, 211, pp.111–115.

Cobry, K., Bright, V. & Greenberg, A., 2011. Integrated electrolytic sensors for monitoring of concentration polarization during nanofiltration. *Sensors and Actuators B: Chemical*, 160, pp.730–739.

Cochrane, T. & Cochrane, T., 2005. Osmotic potential properties of solutes common in the soil-plant solution continuum. *Soil Science*, 170, pp.433–444.

Cohen, J. & Highsmith, S., 1997. An improved fit to website osmotic presure data. *Biophysical Journal*, 73, pp.1689–1694.

Completo, C., Geraldes, V. & Semiao, V., 2014. Rheological and dynamical characterization of blood analogue flows in a slit. *International Journal of Heat and Fluid Flow*, 46, pp.17–28.

Completo, C., Semiao, V. & Geraldes, V., 2016. Efficient CFD-based method for designing cross-flow nanofiltration small devices. *Journal of Membrane Science*, 500, pp.190–202.

Completo, C. et al., 2017. Centrifugal nanofiltration for small-volume samples. *Journal of Membrane Science*, 540, pp.411-421.

Comte-Bellot, G., 1976. Hot-wire anemometry. *Annual Review of Fluid Mechanics*, 8, pp.209–232.

Comte, C. & von Stebut, J., 2002. Microprobe-type measurement of Young's modulus and Poisson coefficient by means of depth sensing indentation and acoustic microscopy. *Surface and Coatings Technology*, 154, pp.42–48.

Cooper, R., 1958. Schlieren studies of concentration gradients at a Cu|HCI anode. *Journal of the Electrchemical Society*, 105, pp.506–512.

Corning Incorporated, 2010. Corning® Spin-X® UF Concentrator. Selection and Use Guide (CLS-AN-119 REV1). Corning Incorporated.

Da Costa, A. et al., 1991. Optimal channel spacer design for ultrafiltration. *Journal of*

*Membrane Science*, 62, pp.275–291.

Da Costa, A. & Fane, A., 1994. Net-type spacers: effect of configuration on fluid flow path and ultrafiltration flux. *Industrial & Engineering Chemistry Research*, 33, pp.1845–1851.

Da Costa, A., Fane, A. & Wiley, D., 1994. Spacer characterization and pressure drop modelling in spacer-filled channels for ultrafiltration. *Journal of Membrane Science*, 87, pp.79–98.

Cui, Z., Chang, S. & Fane, A., 2003. The use of gas bubbling to enhance membrane processes. *Journal of Membrane Science*, 221, pp.1–35.

Daer, S. et al., 2015. Recent applications of nanomaterials in water desalination: a critical review and future opportunities. *Desalination*, 367, pp.37–48.

Darros-Barbosa, R., Balaban, M. & Teixeira, A., 2003. Temperature and concentration dependence of heat capacity of model aqueous solutions. *International Journal of Food Properties*, 6, pp.195–214.

Das, T. & Chakraborty, S., 2009. Biomicrofluidics: recent trends and future challenges. *Sadhana*, 34, pp.573–590.

Das, B., Chakrabarty, B. & Barkakati, P., 2016. Preparation and characterization of novel ceramic membranes for micro-filtration applications. *Ceramics International*, 42, pp.14326–14333.

Dash, D., Mallika, C. & Mudali, U., Temperature and concentration dependence of viscosity of binary mixtures of PEG-1000 + water. *Chemical Product and Process Modeling*, in press.

Deen, W., 1987. Hindered transport of large molecules in liquid-filled pores. *AIChE Journal*, 33, pp.1409–1425.

Dendukuri, D., Karode, S. & Kumar, A., 2005. Flow visualization through spacer filled channels by computational fluid dynamics-II: Improved feed spacer designs. *Journal of Membrane Science*, 249, pp.41–49.

Di, H., Martin, G. & Dunstan, D., 2017. A microfluidic system for studying particle deposition during ultrafiltration. *Journal of Membrane Science*, 532, pp.68–75.

Dickhout, J. et al., 2016. Produced water treatment by membranes: a review from a colloidal perspective. *Journal of Colloid And Interface Science*, 487, pp.523–534.

Ding, L. & Jaffrin, M., 2014. Benefits of high shear rate dynamic nanofiltration and reverse osmosis: a review. *Separation Science and Technology*, 49, pp.1953–1967.

Doku, G. et al., 2005. On-microchip multiphase chemistry—a review of microreactor design principles and reagent contacting modes. *Tetrahedron*, 61, pp.2733–2742.

Domanico, M. et al., 2015. Spin filter. *US Patent* 8980107.

Dong, Hou, et al. 2013. A simple sample preparation method for measuring amoxicillin in human plasma by hollow fiber centrifugal ultrafiltration. *Journal of Chromatographic Science*, 51, pp.181–186.

Dong, Zhang, et al. 2013. Effect of volume ratio of ultrafiltrate to sample solution on the

analysis of free drug and measurement of free carbamazepine in clinical drug monitoring. *European Journal of Pharmaceutical Sciences*, 48, pp.332–338.

Dow Chemical Company, n.d. a. Dow Filmtec NF90 nanofiltration elements for commercial systems (Form No. 609-00378-0811). Dow Chemical Company.

Dow Chemical Company, n.d. b. FILMTEC$^{TM}$ membranes addendum: osmotic pressure of sodium chloride (Form No. 609-02132-0107). Dow Chemical Company.

Drazevic, E., Kosutic, K. & Dananic, V., 2014. Mass transfer of differently sized organic solutes at spacer covered and permeable nanofiltration wall. *Chemical Engineering Journal*, 244, pp.152–159.

Du, X. et al., 2017. Shear stress in a pressure-driven membrane system and its impact on membrane fouling from a hydrodynamic condition perspective: a review. *Journal of Chemical Technology and Biotechnology*, 92, pp.463–478.

Dubsky, S. et al., 2012. Computed tomographic X-ray velocimetry for simultaneous 3D measurement of velocity and geometry in opaque vessels. *Experiments in Fluids*, 52, pp.543–554.

Dudchenko, A. et al., 2014. Organic fouling inhibition on electrically conducting carbon nanotube-polyvinyl alcohol composite ultrafiltration membranes. *Journal of Membrane Science*, 468, pp.1–10.

Dworecki, K. & Wasik, S., 1997. The investigation of time-dependent solute transport through horizontally situated membrane: the effect of configuration membrane system. *Journal of Biological Physics*, 23, pp.181–194.

Eid, J. & Andeen, G., 1983. Effects of acceleration on particulate fouling in reverse osmosis. *Desalination*, 47, pp.191–199.

El-Akl, P., Smith, S. & Wilkinson, K., 2015. Linking the chemical speciation of cerium to its bioavailability in water for a freshwater alga. *Environmental Toxicology and Chemistry*, 34, pp.1711–1719.

Elbarbary, A. & El-Sawy, N., 2016. Radiation synthesis and characterization of polyvinyl alcohol/chitosan/silver nanocomposite membranes: antimicrobial and blood compatibility studies. *Polymer Bulletin*, 74, pp.1–18.

Elimelech, M., Chen, W. & Waypa, J., 1994. Measuring the zeta (electrokinetic) potential of reverse osmosis membranes by a streaming potential analyzer. *Desalination*, 95, pp.269–286.

Elimelech, M. & Bhattacharjee, S., 1998. A novel approach for modeling concentration polarization in crossflow membrane filtration based on the equivalence of osmotic pressure model and filltration theory. *Journal of Membrane Science*, 145, pp.223–241.

Elkins, C.J. & Alley, M.T., 2007. Magnetic resonance velocimetry: applications of magnetic resonance imaging in the measurement of fluid motion. *Experiments in Fluids*, 43,

pp.823–858.

EMD Millipore Corporation, 2015. Protein purification and preparation. High purity and recovery for better discovery (Lit No. PB2778ENEU Rev. F). EMD Millipore Corporation.

Erickson, D. & Li, D., 2004. Integrated microfluidic devices. *Analytica Chimica Acta*, 507, pp.11–26.

Fan, B. et al., 2016. Fabrication and evaluation of an attapulgite membrane as the filter for recycling blowdown water from industrial boilers. *Journal of Water Reuse and Desalination*, 6, pp.399–412.

Feng, D., van Deventer, J. & Aldrich, C., 2006. Ultrasonic defouling of reverse osmosis membranes used to treat wastewater effluents. *Separation and Purification Technology*, 50, pp.318–323.

Fernández-Sempere, J., Ruiz-Beviá, F. & Salcedo-Díaz, R., 2004. Measurements by holographic interferometry of concentration profiles in dead-end ultrafiltration of polyethylene glycol solutions. *Journal of Membrane Science*, 229, pp.187–197.

Fernández-Sempere, J. et al., 2006. Measurement of concentration profiles by holographic interferometry and modelling in unstirred batch reverse osmosis. *Industrial & Engineering Chemistry Research*, 45, pp.7219–7231.

Fernández-Sempere, J. et al., 2007. Buoyancy effects in dead-end reverse osmosis: visualization by holographic interferometry. *Industrial and Engineering Chemistry Research*, 46, pp.1794–1802.

Fernández-Sempere, J. et al., 2008. Diffusion studies in polarized reverse osmosis processes by holographic interferometry. *Optics and Lasers in Engineering*, 46, pp.877–887.

Fernández-Sempere, J. et al., 2009. Visualization and modelling of the polarization layer and a reversible adsorption process in PEG-10000 dead-end ultrafiltration. *Journal of Membrane Science*, 342, pp.279–290.

Fernández-Sempere, J. et al., 2010. Experimental study of concentration polarization in a crossflow reverse osmosis system using digital holographic interferometry. *Desalination*, 257, pp.36–45.

Fernández-Sempere, J. et al., 2012. Buoyancy effect on the ultrafiltration of PEG 10,000. Visualization by digital holographic interferometry. *AIChe Journal*, 58, pp.3810–3817.

Fernández-Torres, M. et al., 1998. Visualization of the UF polarized layer by holographic interferometry. *AIChE Journal*, 44, pp.1765–1776.

Fernandez, A. & Phillies, G., 1983. Temperature dependence of the diffusion coefficient of polystyrene latex spheres. *Biopolymers*, 22, pp.593–595.

Fernández, J. et al., 2011. Thinking in terms of structure-activity-relationships (T-SAR): A tool to better understand nanofiltration membranes. *Membranes*, 1, pp.162–183.

Feron, P. & Solt, G., 1991. Mass transfer in narrow cells: flow visualisation. *Desalination*, 84,

pp.137–152.

Figueredo-Cardero, A. et al., 2012. Particle image velocimetry (PIV) study of rotating cylindrical filters for animal cell perfusion processes. *Biotechnology Progress*, 28, pp.1491–1498.

Fimbres-Weihs, G., Wiley, D. & Fletcher, D., 2006. Unsteady flows with mass transfer in narrow zigzag spacer-filled channels: a numerical study. Industrial & Engineering Chemistry Research, 45, pp.6594–6603.

Fimbres-Weihs, G. & Wiley, D., 2007. Numerical study of mass transfer in three-dimensional spacer-filled narrow channels with steady flow. Journal of Membrane Science, 306, pp.228–243.

Fimbres-Weihs, G. & Wiley, D., 2008. Numerical study of two-dimensional multi-layer spacer designs for minimum drag and maximum mass transfer. Journal of Membrane Science, 325, pp.809–822.

Fimbres-Weihs, G. & Wiley, D., 2010. Review of 3D CFD modeling of flow and mass transfer in narrow spacer-fille channels in membrane modules. Chemical Engineering and Processing, 49, pp.759–781.

Fiorini, G.S. & Chiu, D.T., 2005. Disposable microfluidic devices: fabrication, function, and application. *BioTechniques*, 38, pp.429–46.

Fischl, D. et al., 1985. Mass transfer enhancement by small flow obstacles in electrochemical cells. *Chemical Engineering Communications*, 38, pp.191–207.

Forgacs, C. et al., 1975. Interferometric study of concentration profiles in solutions near membrane surfaces. *Electrochimica Acta*, 20, pp.555–563.

Fraile, R. et al., 2014. Formulation of Span 80 niosomes modified with SDS for lactic acid entrapment. *Desalination and Water Treatment*, 56, pp.3463–3475.

Freymuth, P., 1993. Flow visualization in fluid mechanics. *Review of Scientific Instruments*, 64, pp.1–18.

Fuerstman, M. et al., 2007. The pressure drop along rectangular microchannels containing bubbles. *Lab on a Chip*, 7, p.1479.

Fujioka, T. et al., 2015. Probing the internal structure of reverse osmosis membranes by positron annihilation spectroscopy: gaining more insight into the transport of water and small solutes. *Journal of Membrane Science*, 486, pp.106–118.

Fyles, T. & Lycon, D., 2000. Fouling reduction using centrifugal membrane separation. *Journal of Membrane Science*, 176(October 1999), pp.267–276.

Gao, Y. et al., 2013. Characterization of fluid dynamics in spacer-filled channels for membrane filtration using Doppler optical coherence tomography. *Journal of Membrane Science*, 448, pp.198–208.

Ge, S. et al., 2017. Rejection rate and mechanisms of drugs in drinking water by nanofiltration

technology. *Environmental Engineering Research*, 22, pp.329–338.

Gekas, V. & Hallström, B., 1987. Mass-transfer in the membrane concentration polarization layer under turbulent cross flow I. Critical literature-review and adaptation of existing Sherwood correlations to membrane operations. *Journal of Membrane Science*, 30, pp.153–170.

Geraldes, V., Semião, V. & Pinho, M., 1998. Nanofiltration mass transfer at the entrance region of a slit laminar flow. *Industrial & Engineering Chemistry Research*, 37, pp.4792–4800.

Geraldes, V., 2000. *Estudo numérico e experimental de escoamentos e transferência de massa em módulos enrolados em espiral para nanofiltração e osmose inversa (PhD thesis)*. Universidade Técnica de Lisboa.

Geraldes, V., Semião, V. & de Pinho, M., 2002a. Flow management in nanofiltration spiral wound modules with ladder-type spacers. *Journal of Membrane Science*, 203, pp.87–102.

Geraldes, V., Semião, V. & de Pinho, M., 2002b. The effect of the ladder-type spacers configuration in NF spiral-wound modules on the concentration boundary layers disruption. *Desalination*, 146, pp.187–194.

Geraldes, V., Semião, V. & de Pinho, M., 2004. Concentration polarisation and flow structure within nanofiltration spiral-wound modules with ladder-type spacers. *Computers and Structures*, 82, pp.1561–1568.

Geraldes, V. & Afonso, M., 2006. Generalized mass-transfer correction factor for nanofiltration and reverse osmosis. *AIChE Journal*, 52, pp.3353–3362.

Geraldes, V., Semião, V., Rodrigues, M., Completo, C. 2018. Dispositivo de filtração centrífuga e método para concentração de misturas líquidas. Boletim da Propriedade Industrial, 163/2018, Pedido de Patente de Invenção Nacional nº 109932.

Gervais, L., de Rooij, N. & Delamarche, E., 2011. Microfluidic chips for point-of-care immunodiagnostics. *Advanced materials*, 23, pp.H151-76.

Ghosh, R. & Cui, Z., 1999. Mass transfer in gas-sparged ultrafiltration: upward slug flow in tubular membranes. *Journal of Membrane Science*, 162, pp.91–102.

Gimmelshtein, M. & Semiat, R., 2005. Investigation of flow next to membrane walls. *Journal of Membrane Science*, 264, pp.137–150.

Giwa, A. et al., 2016. A critical review on recent polymeric and nano-enhanced membranes for reverse osmosis. *RSC Advances*, 6, pp.8134–8163.

Gladden, J. & Dole, M., 1953. Diffusion in supersaturated solutions. II. Glucose solutions. *Journal of the American Chemical Society*, 75, pp.3900–3904.

Goh, P. et al., 2015. Inorganic nanomaterials in polymeric ultrafiltration membranes for water treatment. *Separation & Purification Reviews*, 44, pp.216–249.

Gomaa, H. & Rao, S., 2011. Analysis of flux enhancement at oscillating flat surface membranes. *Journal of Membrane Science*, 374, pp.59–66.

Gorzalski, A., Donley, C. & Coronell, O., 2017. Elemental composition of membrane foulant layers using EDS, XPS, and RBS. *Journal of Membrane Science*, 522, pp.31–44.

Gowman, L. & Ethier, C., 1997a. Concentration and concentration gradient measurements in an ultrafiltration concentration polarization layer. Part I: a laser-based refractometric experimental technique. *Journal of Membrane Science*, 131, pp.95–105.

Gowman, L. & Ethier, C., 1997b. Concentration and concentration gradient measurements in an ultrafiltration concentration polarization layer. Part II: application to hyaluronan. *Journal of Membrane Science*, 131, pp.107–123.

Graf von der Schulenburg, D. et al., 2008. Nuclear magnetic resonance microscopy studies of membrane biofouling. *Journal of Membrane Science*, 323, pp.37–44.

Graham, M. et al., 2011. Mechanisms controlling lateral and vertical porewater migration of depleted uranium (DU) at two UK weapons testing sites. *Science of the Total Environment*, 409, pp.1854–1866.

Greening, D. & Simpson, R., 2010. A centrifugal ultrafiltration strategy for isolating the low-molecular weight (< 25 K) component of human plasma proteome. *Journal of Proteomics*, 73, pp.637–648.

Greening, D. et al., 2013. Colon tumour secretopeptidome: Insights into endogenous proteolytic cleavage events in the colon tumour microenvironment. *Biochimica et Biophysica Acta - Proteins and Proteomics*, 1834, pp.2396–2407.

Greenspan, D., 1972. Serum separator type container. *US Patent* 3661265.

Grein, T. et al., 2013. Membrane supported virus separation from biological solutions. *Chemie Ingenieur Technik*, 85, pp.1183–1192.

Gryta, M., Bastrzyk, J. & Lech, D., 2012. Evaluation of fouling potential of nanofiltration membranes based on the dynamic contact angle measurements. *Polish Journal of Chemical Technology*, 14, pp.97–104.

Gu, B., Adjiman, C. & Xu, X., 2017. The effect of feed spacer geometry on membrane performance and concentration polarisation based on 3D CFD simulations. *Journal of Membrane Science*, 527, pp.78–91.

Gubala, V. et al., 2012. Point of care diagnostics: status and future. *Analytical chemistry*, 84, pp.487–515.

Guggenheim, E., 1954. The diffusion coefficient of sodium chloride. *Transactions of the Faraday Society*, 50, pp.1048–1051.

Guillen, G. et al., 2011. Preparation and characterization of membranes formed by nonsolvent induced phase separation: a review. *Industrial & Engineering Chemistry Research*, 50, pp.3798–3817.

Guo, W., Ngo, H.-H. & Li, J., 2012. A mini-review on membrane fouling. *Bioresource technology*, 122, pp.27–34.

Haaksman, V. et al., 2017. Characterization of feed channel spacer performance using geometries obtained by X-ray computed tomography. *Journal of Membrane Science*, 522, pp.124–139.

Haas, R. et al., 2015. Glycosphingolipids enhance bacterial attachment and fouling of nanofiltration membranes. *Environmental Science and Technology Letters*, 2, pp.43–47.

Haidari, A., Heijman, S. & van der Meer, W., 2016. Visualization of hydraulic conditions inside the feed channel of reverse osmosis: a practical comparison of velocity between empty and spacer-filled channel. *Water Research*, 106, pp.232–241.

Hammond, G. et al., 1980. Estimation of the percentage of free steroid in undiluted serum by centrifugal ultrafiltration-dialysis. *Journal of Biological Chemistry*, 255, pp.5023–5026.

Han, W. & Wang, H., 2012. Measurements of water flow rates for T-shaped microchannels based on the quasi-three-dimensional velocities. *Measurement Science and Technology*, 23, p.055301.

Hang, H. et al., 2015. Enzyme membrane reactor coupled with nanofiltration membrane process for difructose anhydride III from inulin conversion. *Chemical Engineering Journal*, 276, pp.75–82.

Hata, A. et al., 2014. Concentration of enteric viruses in large volumes of water using a cartridge-type mixed cellulose ester membrane. *Food and Environmental Virology*, 7, pp.7–13.

Hecht, E., 1998. *Óptica* 3ª ed., Lisboa: Fundação Calouste Gulbenkian.

Hendricks, T., Macquin, J. & Williams, F., 1972. Observations on buoyant convection in reverse osmosis. *Industrial & Engineering Chemistry Fundamentals*, 11, pp.276–279.

Herczeg, A., 1996. Filtration apparatus with membrane filter unit. *US Patent* 5490927.

Hessel, V., Löwe, H. & Schönfeld, F., 2005. Micromixers—a review on passive and active mixing principles. *Chemical Engineering Science*, 60, pp.2479–2501.

Hilal, N. et al., 2005. Methods employed for control of fouling in MF and UF membranes: a comprehensive review. *Separation Science and Technology*, 40, pp.1957–2005.

Hilal, N. et al., 2015. A combined ion exchange-nanofiltration process for water desalination: II. Membrane selection. *Desalination*, 363, pp.51–57.

Hochstrasser, H., 1976. Apparatus and method for isolating soluble blood components. *US Patent* 3960727.

Hoffmann, M., Schlüter, M. & Räbiger, N., 2006. Experimental investigation of liquid–liquid mixing in T-shaped micro-mixers using μ-LIF and μ-PIV. *Chemical Engineering Science*, 61, pp.2968–2976.

van Hoof, H. et al., 1998. Determination of non-protein-bound plasma 1,25-dihydroxyvitamin D by symmetric (rate) dialysis. *Analytical biochemistry*, 258, pp.176–183.

Hu, N. et al., 2011. Characterization of porous materials using combined small-angle X-ray and

neutron scattering techniques. *Journal of Membrane Science*, 379, pp.138–145.

Huang, H. & Schwab, K., 2009. Pretreatment for low pressure membranes in water treatment: a review. *Environmental Pollution*, 43, pp.3011–3019.

Ibl, N. & Muller, R., 1955. Optische untersuchungen der diffusionsschicht und der hydrodynamischen grenzschicht an belasteten elektroden. *Zeitschrift für Elektrochemie*, 59, pp.671–676.

Ikram, M. & Hussain, G., 1999. Michelson interferometer for precision angle measurement. *Applied Optics*, 38, pp.113–120.

Iritani, I., 2013. A review on modeling of pore-blocking behaviours of membranes during pressurized membrane filtration. *Drying Technology*, 31, pp.146–162.

Islami, S. & Khezerloo, M., 2017. Enhancement of mixing performance of non-newtonian fluids using curving and grooving of microchannels. *Journal of Applied Fluid Mechanics*, 10, pp.127–141.

Iza, M. et al., 2000. Determination of pore size distribution for mesoporous materials and polymeric gels by means of DSC measurements: thermoporometry. *Polymer*, 41, pp.5885–5893.

Jaffrin, M., 2008. Dynamic shear-enhanced membrane filtration: a review of rotating disks, rotating membranes and vibrating systems. *Journal of Membrane Science*, 324, pp.7–25.

Jaffrin, M., 2012. Hydrodynamic techniques to enhance membrane filtration. *Annual Review of Fluid Mechanics*, 44, pp.77–96.

Jang, A. et al., 2011. State-of-the-art lab chip sensors for environmental water monitoring. *Measurement Science and Technology*, 22, p.32001.

Johnson, A., 1974. Experimental investigation of polarization effects in reverse osmosis. *AIChE Journal*, 20, pp.966–974.

Johnson, D. & Hilal, N., 2015. Characterisation and quantification of membrane surface properties using atomic force microscopy: a comprehensive review. *Desalination*, 356, pp.149–164.

de Jong, J., Lammertink, R. & Wessling, M., 2006. Membranes and microfluidics: a review. *Lab on a chip*, 6, pp.1125–39.

Jonsson, G. & Macedonio, F., 2010. Fundamentals in reverse osmosis. In E. Drioli & L. Giourno, eds. *Comprehensive membrane science and engineering - volume 2*. Elsevier B.V., pp. 1–22.

Judy, J., 2001. Microelectromechanical systems (MEMS): fabrication, design and applications. *Smart materials and structures*, 10, pp.1115–1134.

Kallioinen, M. & Mänttäri, M., 2011. Influence of ultrasonic treatment on various membrane materials: a review. *Separation Science and Technology*, 46, pp.1388–1395.

Kang, I. & Chang, H., 1982. The effect of turbulence promoters on mass transfer: numerical

analysis and flow visualization. *International Journal of Heat and Mass Transfer*, 25, pp.1167–1181.

Kang, G. & Cao, Y., 2012. Development of antifouling reverse osmosis membranes for water treatment: a review. *Water research*, 46, pp.584–600.

Kapadnis, K. & Hiray, A., 2013. Density and viscosity studies of fructose solutions in water and in aqueous NaCl, NaBr, KCl and KBr solutions. *Chemical Science Review and Letters*, 1, pp.236–238.

Karabelas, A., Kostoglou, M. & Koutsou, C., 2015. Modeling of spiral wound membrane desalination modules and plants - review and research priorities. *Desalination*, 356, pp.165–186.

Karode, S. & Kumar, A., 2001. Flow visualization through spacer filled channels by computational fluid dynamics I . Pressure drop and shear rate calculations for flat sheet geometry. *Journal of Membrane Science*, 193, pp.69–84.

Kaufman, Y. et al., 2012. Microfluidic NF/RO separation: cell design, performance and application. *Journal of Membrane Science*, 396, pp.67–73.

Kaufman, Y. et al., 2014. Towards supported bolaamphiphile membranes for water filtration: roles of lipid and substrate. *Journal of Membrane Science*, 457, pp.50–61.

Kavianipour, O., Ingram, G.D. & Vuthaluru, H.B., 2017. Investigation into the effectiveness of feed spacer configurations for reverse osmosis membrane modules using Computational Fluid Dynamics. *Journal of Membrane Science*, 526, pp.156–171.

Keir, G. & Jegatheesan, V., 2014. A review of computational fluid dynamics applications in pressure-driven membrane filtration. *Reviews in Environmental Science and Biotechnology*, 13, pp.183–201.

Kendro Laboratory Products, 2003. Sorvall® superpeed fixed-angle. Operating instructions (PN 28505-13). Kendro Laboratory Products.

Kendro Laboratory Products, 2005. Introducing the Sorvall RC-6 superspeed centrifuge! (S00415). Kendro Laboratory Products.

Kennedy, T., Merson, R. & McCoy, B., 1974. Improving permeation flux by pulsed reverse osmosis. *Chemical Engineering Science*, 29, pp.1927–1931.

Khodaparast, S. et al., 2017. Bubble-driven detachment of bacteria from confined microgeometries. *Environmental Science and Technology*, 51, pp.1340–1347.

Khulbe, K. et al., 2000. X-ray diffraction analysis of dense PPO membranes. *Journal of Membrane Science*, 170, pp.81–89.

Khulbe, K. & Matsuura, T., 2000. Characterization of synthetic membranes by Raman spectroscopy, electron spin resonance, and atomic force microscopy; a review. *Polymer*, 41, pp.1917–1935.

Kim, R., Lee, S. & Kim, J., 2005. Application of a metal membrane for rainwater utilization:

filtration characteristics and membrane fouling. *Desalination*, 177, pp.121–132.

Kim, J. & Bruggen, B., 2010. The use of nanoparticles in polymeric and ceramic membrane structures: review of manufacturing procedures and performance improvement for water treatment. *Environmental Pollution*, 158, pp.2335–2349.

King, C., Walsh, E. & Grimes, R., 2007. PIV measurements of flow within plugs in a microchannel. *Microfluidics and Nanofluidics*, 3, pp.463–472.

Klerks, M., 2010. Microfilter centrifuge tube. *European Patent* 2260943.

Kolfschoten, R., Janssen, A. & Boom, R., 2011. Mass diffusion-based separation of sugars in a microfluidic contactor with nanofiltration membranes. *Journal of Separation Science*, 34, pp.1338–1346.

Kopaciewicz, W., Cann, I. & Sheer, D., 1998. Centrifugal adsorptive sample preparations device and method. *US Patent* 5833860.

Kostoglou, M. & Karabelas, A., 2013. Comprehensive simulation of flat-sheet membrane element performance in steady state desalination. *Desalination*, 316, pp.91–102.

Koutsou, C., Yiantsios, S. & Karabelas, A., 2004. Numerical simulation of the flow in a plane-channel containing a periodic array of cylindrical turbulence promoters. *Journal of Membrane Science*, 231, pp.81–90.

Koutsou, C., Yiantsios, S. & Karabelas, A., 2007. Direct numerical simulation of flow in spacer-filled channels: effect of spacer geometrical characteristics. *Journal of Membrane Science*, 291, pp.53–69.

Koutsou, C., Yiantsios, S. & Karabelas, A., 2009. A numerical and experimental study of mass transfer in spacer-filled channels: effects of spacer geometrical characteristics and Schmidt number. *Journal of Membrane Science*, 326, pp.234–251.

Kratzer, A. et al., 2014. Determination of free vancomycin, ceftriaxone, cefazolin and ertapenem in plasma by ultrafiltration: impact of experimental conditions. *Journal of Chromatography B*, 961, pp.97–102.

Krieg, H. et al., 2004. Salt rejection in nanofiltration for single and binary salt mixtures in view of sulphate removal. *Desalination*, 171, pp.205–215.

Kumar, V., Paraschivoiu, M. & Nigam, K., 2011. Single-phase fluid flow and mixing in microchannels. *Chemical Engineering Science*, 66, pp.1329–1373.

Kyllönen, H., Pirkonen, P. & Nyström, M., 2005. Membrane filtration enhanced by ultrasound: a review. *Desalination*, 181, pp.319–335.

La, M. et al., 2013. A centrifugal force-based serpentine micromixer (CSM) on a plastic lab-on-a-disk for biochemical assays. *Microfluidics and Nanofluidics*, 15, pp.87–98.

Lai, Z., Petrera, A. & Schilling, O., 2015. The emerging role of the peptidome in biomarker discovery and degradome profiling. *Biological Chemistry*, 396, pp.185–192.

Lalia, B. et al., 2013. A review on membrane fabrication: structure , properties and performance

relationship. *Desalination*, 326, pp.77–95.

Laliberté, M. & Cooper, W., 2004. Model for calculating the density of aqueous electrolyte solutions. *Journal of Chemical & Engineering Data*, 49, pp.1141–1151.

Laliberté, M., 2007. Model for calculating the viscosity of aqueous solutions. *Journal of Chemical & Engineering Data*, 52, pp.321–335.

Lamminen, M., 2004. Mechanisms and factors influencing the ultrasonic cleaning of particle-fouled ceramic membranes. *Journal of Membrane Science*, 237, pp.213–223.

Laser, D. & Santiago, J., 2004. A review of micropumps. *Journal of Micromechanics and Microengineering*, 14, pp.R35–R64.

Lau, K. et al., 2009. Feed spacer mesh angle: 3D modeling, simulation and optimization based on unsteady hydrodynamic in spiral wound membrane channel. *Journal of Membrane Science*, 343, pp.16–33.

Leaist, D. & Hao, L., 1992. Binary mutual diffusion coefficients of aqueous ammonium and potassium sulfates at 25$^{o}$C. *Journal of Solution Chemistry*, 21, pp.345–350.

Lee, Y. et al., 1996. Connection-type treatment system for micro solution and method of treatment. *US Patent* 5501841.

Lee, S. & Kim, S., 2009. Advanced particle-based velocimetry techniques for microscale flows. *Microfluidics and Nanofluidics*, 6, pp.577–588.

Lee, K., Arnot, T. & Mattia, D., 2011. A review of reverse osmosis membrane materials for desalination — development to date and future potential. *Journal of Membrane Science*, 370, pp.1–22.

Lee, A., Elam, J. & Darling, S., 2016. Membrane materials for water purification: design, development, and application. *Environ. Sci.: Water Res. Technol.*, 2, pp.17–42.

Lee, J. et al., 2016. The potential to enhance membrane module design with 3D printing technology. *Journal of Membrane Science*, 499, pp.480–490.

Lee, S. et al., 2017. Synchrotron X-ray nanotomography and three-dimensional nanoscale imaging analysis of pore structure-function in nanoporous polymeric membranes. *Journal of Membrane Science*, 535, pp.28–34.

Leung, W. & Ren, Y., 2013. Crossflow and mixing in obstructed and width-constricted rotating radial microchannel. *International Journal of Heat and Mass Transfer*, 64, pp.457–467.

Leung, W. & Ren, Y., 2014. Scale-up on mixing in rotating microchannel under subcritical and supercritical operating modes. *International Journal of Heat and Mass Transfer*, 77, pp.157–172.

Li, F., Meindersma, G., et al., 2002. Optimization of non-woven spacers by CFD and validation by experiments. *Desalination*, 146, pp.209–212.

Li, F., Meindersma, W., et al., 2002. Optimization of commercial net spacers in spiral wound membrane modules. *Journal of Membrane Science*, 208, pp.289–302.

Li, F. et al., 2004. Experimental validation of CFD mass transfer simulations in flat channels with non-woven net spacers. *Journal of Membrane Science*, 232, pp.19–30.

Li, F. et al., 2005. Novel spacers for mass transfer enhancement in membrane separations. *Journal of Membrane Science*, 253, pp.1–12.

Li, J. et al., 2007. Quantitative study of the effect of electromagnetic field on scale deposition on nanofiltration membranes via UTDR. *Water Research*, 41, pp.4595–4610.

Li, Y. & Tung, K., 2008a. CFD simulation of fluid flow through spacer-filled membrane module: selecting suitable cell types for periodic boundary conditions. *Desalination*, 233, pp.351–358.

Li, Y. & Tung, K., 2008b. The effect of curvature of a spacer-filled channel on fluid flow in spiral-wound membrane modules. *Journal of Membrane Science*, 319, pp.286–297.

Li, J. et al., 2009. Hollow-fiber ultrafiltration then centrifugation for LC analysis of water-soluble sucrose in a water-soluble high-molecular-mass gel matrix. *Chromatographia*, 70, pp.1023–1030.

Li, Y. et al., 2009. Mitigating the curvature effect of the spacer-filled channel in a spiral-wound membrane module. *Journal of Membrane Science*, 329, pp.106–118.

Li, J. et al., 2010. Pretreatment of plasma samples by a novel hollow fiber centrifugal ultrafiltrate device for the determination of cefaclor concentrations in human plasma. *Journal of Chromatography A*, 1217, pp.6824–6828.

Li, X. et al., 2011. High-flux and anti-fouling cellulose nanofiltration membranes prepared via phase inversion with ionic liquid as solvent. *Separation and Purification Technology*, 83, pp.66–73.

Li, J. et al., 2015. Pretreatment of plasma samples by a novel hollow fiber centrifugal ultrafiltration technique for the determination of plasma protein binding of three coumarins using acetone as protein binding releasing agent. *Journal of Chromatography B*, 1001, pp.114–123.

Li, J. et al., 2016. Anti-bacterial properties of ultrafiltration membrane modified by graphene oxide with nano-silver particles. *Journal of Colloid and Interface Science*, 484, pp.107–115.

Li, M., Bui, T. & Chao, S., 2016. Three-dimensional CFD analysis of hydrodynamics and concentration polarization in an industrial RO feed channel. *Desalination*, 397, pp.194–204.

Li, X. et al., 2017. In-situ monitoring techniques for membrane fouling and local filtration characteristics in hollow fiber membrane processes: a critical review. *Journal of Membrane Science*, 528, pp.187–200.

Liang, Y., W, F. & Wiley, D., 2014. CFD modelling of electro-osmotic permeate flux enhancement on the feed side of a membrane module. *Journal of Membrane Science*, 470,

pp.378–388.

Lim, Y., Kouzani, Z. & Duan, W., 2010. Lab-on-a-chip: a component view. *Microsystem Technologies*, 16, pp.1995–2015.

Lindken, R. et al., 2009. Micro-Particle Image Velocimetry (microPIV): recent developments, applications, and guidelines. *Lab on a chip*, 9, pp.2551–67.

Liu, M. & Williams, F., 1970. Concentration polarization in an unstirred batch cell: measurements and comparison with theory. *International Journal of Heat and Mass Transfer*, 13, pp.1441–1457.

Liu, J. et al., 2009. Determination of Benzalkonium Chloride partition in micelle solutions using ultrafiltration method. *Pharmaceutical Science and Technology*, 10, pp.1216–1223.

Liu, J. & Hurt, R., 2010. Ion release kinetics and particle persistance in aqueous nano-silver colloids. *Environmental Science and Technology*, 44, pp.2169–2175.

Liu, K. et al., 2010. Microfluidic systems for biosensing. *Sensors*, 10, pp.6623–6661.

Liu, J. et al., 2012. Degradation products from Consumer nanocomposites: a case study on quantum dot lighting. *Environmental Science and Technology*, 46, pp.3220–3227.

Liu, Z. et al., 2012. Nanofiltration process of glyphosate simulated wastewater. *Water Science and Technology*, 65, pp.816–822.

Liu, P. et al., 2014. Removal of trace antibiotics from wastewater: a systematic study of nanofiltration combined with ozone-based advanced oxidation processes. *Chemical Engineering Journal*, 240, pp.211–220.

Liu, P. et al., 2015. Influence of spacer on rejection of trace antibiotics in wastewater during forward osmosis process. *Desalination*, 371, pp.134–143.

Livshits, M. et al., 2015. Isolation of exosomes by differential centrifugation: theoretical analysis of a commonly used protocol. *Scientific Reports*, 5, p.17319.

Loeb, S. & Sourirajan, S., 1963. Sea water demineralization by means of an osmotic membrane. *Advances in Chemistry*, 38, pp.117–132.

Loeb, S., 1981. The Loeb-Sourirajan membrane: how it came about. In A. Turbak, ed. *Synthetic membranes*. American Chemical Society, pp. 1–9.

Long, Q. & Wang, Y., 2015. Sodium tetraethylenepentamine heptaacetate as novel draw solute for forward osmosis - Synthesis, application and recovery. *Energies*, 8, pp.12917–12928.

Luo, J. et al., 2009. Moving-part-free microfluidic systems for lab-on-a-chip. *Journal of Micromechanics and Microengineering*, 19, p.54001.

Luo, J. et al., 2011. A two-stage ultrafiltration and nanofiltration process for recycling dairy wastewater. *Bioresource Technology*, 102, pp.7437–7442.

Luther, S. & Braeuer, A., 2012. High-pressure microfluidics for the investigation into multi-phase systems using the supercritical fluid extraction of emulsions (SFEE). *Journal of Supercritical Fluids*, 65, pp.78–86.

Lyman, G. & Mathus, G., 1987. Filter for centrifuge tube. *US Patent* 4683058.

Ma, S. & Song, L., 2006. Numerical study on permeate flux enhancement by spacers in a crossflow reverse osmosis channel. *Journal of Membrane Science*, 284, pp.102–109.

Madou, M. et al., 2006. Lab on a CD. *Annual review of biomedical engineering*, 8, pp.601–28.

Mahlab, D., Yosef, N. & Beifort, G., 1978. Concentration polarization profile for dissolved species in unstirred batch hyperfiltration (reverse osmosis) - II transient case. *Desalination*, 24, pp.297–303.

Mahlab, D., Yosef, N. & Belfort, G., 1980. Interferometric measurement of concentration polarization profile for dissolved species in unstirred batch hyperfiltration (reverse osmosis). *Chemical Engineering Communications*, 6, pp.225–243.

Malsch, D. et al., 2008. μPIV-analysis of Taylor flow in micro channels. *Chemical Engineering Journal*, 135, pp.S166–S172.

Matbase, 2017. Matbase: the free and independent online materials properties resource [Online]. Available at: https://www.matbase.com (Accessed: 22 November 2017).

McDonald, J. & Whitesides, G., 2002. Poly(dimethylsiloxane) as a material for fabricating microfluidic devices. *Accounts of Chemical Research*, 35, pp.491–499.

McDonogh, R. et al., 1990. Concentration polarisation and adsorption effects in cross-flow ultrafiltration of proteins. *Desalination*, 79, pp.217–231.

McDonogh, R. et al., 1995. Experimental in situ measurement of concentration polarisation during ultra- and micro-filtration of bovine serum albumin and Dextran Blue solutions. *Journal of Membrane*, 104, pp.51–63.

McGovern, R., McConnon, D. & Lienhard V, J., 2015. The effect of very high hydraulic pressure on the permeability and salt rejection of reverse osmosis membranes. In *The International Desalination Association World Congress on Desalination and Water Reuse*. San Diego, p. IDAWC15-McGovern.

Mehdizadeh, H. & Dickson, J.M., 1989. Theoretical modification of the surface force-pore flow model for reverse osmosis transport. *Journal of Membrane Science*, 42, pp.119–145.

Mehdizadeh, H., 1990. *Modeling of transport phenomena in reverse osmosis membranes (PhD thesis)*. McMaster University.

Mickowska, B., Dulinski, R. & Kozik, A., 2000. Fast, isotope-free methods for the assay of thiamine-binding proteins and for the determination of their affinities to thiamine-related compounds. *Journal of Biochemical and Biophysical Methods*, 44, pp.95–107.

Mikulasek, P. & Filandrova, L., 1995. Use of fluidized bed for intensification of microfiltration on ceramic membranes. *Asia-Pacific Journal of Chemical Engineering*, 3, pp.139–149.

Min, S. & Notter, R., 1976. An interferometric technique for the study of steady state membrane transport. *AIChE Journal*, 22, pp.175–182.

Minhalma, M. et al., 2007. Optimization of “Serpa” cheese whey nanofiltration for effluent

minimization and by-products recovery. *Journal of Environmental Management*, 82, pp.200–206.

Miyagi, T., Matsui, S. & Hirajima, Y., 1988. Filter for centrifugal separator. *US Patent* 4722792.

Mojab, S. et al., 2014. Unsteady laminar to turbulent flow in a spacer-filled channel. *Flow, Turbulence and Combustion*, 92, pp.563–577.

Money, N., 1989. Osmotic pressure of aqueous polyethylene glycols. Relationship between molecular weight and vapor pressure deficit. *Plant Physiology*, 91, pp.766–769.

Morão, A., Alves, A. & Geraldes, V., 2008. Concentration polarization in a reverse osmosis/nanofiltration plate-and-frame membrane module. *Journal of Membrane Science*, 325, pp.580–591.

Mulder, M., 1996. *Basic principles of membrane technology* 2nd ed., Kluwer Academic Publishers.

Murthy, Z. & Gupta, S., 1997. Estimation of mass transfer coefficient using a combined nonlinear membrane transport and film theory model. *Desalination*, 109, pp.39–49.

Murthy, Z. & Gupta, S., 1999. Sodium cyanide separation and parameter estimation for reverse osmosis thin film composite polyamide membrane. *Journal of Membrane Science*, 154, pp.89–103.

Muthukumaran, S. et al., 2006. Application of ultrasound in membrane separation processes: a review. *Reviews in Chemical Engineering*, 22, pp.155–194.

Nabavi, M., 2009. Steady and unsteady flow analysis in microdiffusers and micropumps: a critical review. *Microfluidics and Nanofluidics*, 7, pp.599–619.

Nagai, S., 1966. Chemical Handbook II.

Nakajima, M., 1988. Centrifugal ultrafilter unit for ultrafiltration of biochemical solutions. *US Patent* 4769145.

Nakao, S. & Kimura, S., 1980. Analysis of solutes rejection in ultrafiltration. *Journal of Chemical Engineering of Japan*, 14, pp.32–37.

Naylor, D., 2003. Recent developments in the measurement of convective heat transfer rates by laser interferometry. *International Journal of Heat and Fluid Flow*, 24, pp.345–355.

Newbury, D. & Ritchie, N., 2013. Elemental mapping of microstructures by scanning electron microscopy-energy dispersive X-ray spectrometry (SEM-EDS): extraordinary advances with the silicon drift detector (SDD). *J. Anal. At. Spectrom.*, 28, pp.973–988.

Nguyen, N., 1997. Micromachined flow sensors—a review. *Flow Measurement and Instrumentation*, 8, pp.7–16.

Nguyen, N. & Wu, Z., 2005. Micromixers—a review. *Journal of Micromechanics and Microengineering*, 15, pp.R1–R16.

Nicolini, J., Borges, C. & Ferraz, H., 2016. Selective rejection of ions and correlation with surface properties of nanofiltration membranes. *Separation and Purification Technology*,

171, pp.238–247.

Nochumson, S. & Goldberg, B., 1996. Method for separations and recovery of biological materials. *US Patent* 5552325.

Noordman, T. et al., 2002. Application of fluidised particles as turbulence promoters in ultrafiltration improvement of flux and rejection. *Journal of Membrane Science*, 208, pp.157–169.

Noordman, T. et al., 2003. Concentration of aqueous extracts of defatted soy flour by ultrafiltration. Effect of suspended particles on the filtration flux. *Journal of Food Engineering*, 58, pp.135–141.

Nussbaumer, D., Perl, H. & Vihn, K., 1985. Apparatus for static membrane filtration. *US Patent* 4522713.

O'Brien, R., 1966. Concentration gradients at horizontal electrodes. *Journal of the Electrchemical Society*, 113, pp.389–392.

Oh, K. & Ahn, C., 2006. A review of microvalves. *Journal of Micromechanics and Microengineering*, 16, pp.R13–R39.

Ohno, K., Tachikawa, K. & Manz, A., 2008. Microfluidics: Applications for analytical purposes in chemistry and biochemistry. *Electrophoresis*, 29, pp.4443–4453.

Olayiwola, B. & Walzel, P., 2009. Effects of in-phase oscillation of retentate and filtrate in crossflow filtration at low Reynolds number. *Journal of Membrane Science*, 345, pp.36–46.

Olsen, M. & Adrian, R., 2000. Out-of-focus effects on particle image visibility and correlation in microscopic particle image velocimetry. *Experiments in Fluids*, 29, pp.S166–S174.

OpenCFD Limited, 2008a. Open∇FOAM The Open Source CFD Toolbox User Guide (version 1.5). OpenCFD Limited.

OpenCFD Limited, 2008b. Open∇FOAM The Open Source CFD Toolbox Programmer's Guide (version 1.5). OpenCFD Limited.

Orbital Biosciences, 2017. Apollo® Concentrators [Online]. Available at: http://orbitalbiosciences.com/ORBITAL_BIOSCIENCES-PRODUCTS/orbital_biosciences-products.html (Accessed: 22 November 1017).

Orvisky, E. et al., 2006. Enrichment of low molecular weight fraction of serum for MS analysis of peptides associated with hepatocellular carcinoma. *Proteomics*, 6, pp.2895–2902.

Pall Corporation, 2010. Centrifugal devices (PN33578). Pall Corporation.

Panico, A. et al., 2016. Antibacterial silver treatments on polymeric membranes for fouling control and disinfection in water filtration. *Journal of Applied Polymer Science*, 133, p.43848.

Patel, T. & Nath, K., 2013. Alleviation of flux decline in cross flow nanofiltration of two-component dye and salt mixture by low frequency ultrasonic irradiation. *Desalination*, 317, pp.132–141.

Paul, M. & Jons, S., 2016. Chemistry and fabrication of polymeric nanofiltration membranes: a review. *Polymer*, 103, pp.417–456.

Petersen, R., 1993. Composite reverse osmosis and nanofiltration membranes. *Journal of Membrane Science*, 83, pp.81–150.

Pharoah, J., Djilali, N. & Vickers, G., 2000. Fluid mechanics and mass transport in centrifugal membrane separation. *Journal of Membrane Science*, 176, pp.277–289.

Pickett, D. & Stanmore, B., 1972. Ionic mass transfer in parallel plate electrochemical cells. *Journal of Applied Electrochemistry*, 2, pp.151–156.

de Pinho, M. & Prazeres, D., 2008. *Fundamentos de transferência de massa*, IST Press.

de Pinho, M., Semião, V. & Geraldes, V., 2002. Integrated modeling of transport processes in fluid/nanofiltration membrane systems. *Journal of Membrane Science*, 206, pp.189–200.

Pitts, K. & Fenech, M., 2013. High speed versus pulsed images for micro-particle image velocimetry: a direct comparison of red blood cells versus fluorescing tracers as tracking particles. *Physiological measurement*, 34, pp.1363–74.

Poelma, C. et al., 2012. Accurate blood flow measurements: are artificial tracers necessary? *PloS one*, 7, p.e45247.

Qin, J. et al., 2010. Development of novel backwash cleaning technique for reverse osmosis in reclamation of secondary effluent. *Journal of Membrane Science*, 346, pp.8–14.

Qiu, T. & Davies, P., 2015. Concentration polarization model of spiral-wound membrane modules with application to batch-mode RO desalination of brackish water. *Desalination*, 368, pp.36–47.

Raffel, M. et al., 2007. *Particle image velocimetry*, Springer.

Ramon, G., Nguyen, T. & Hoek, E., 2013. Osmosis-assisted cleaning of organic-fouled seawater RO membranes. *Chemical Engineering Journal*, 218, pp.173–182.

Ranade, V. & Kumar, A., 2006a. Comparison of flow structures in spacer-filled flat and annular channels. *Desalination*, 191, pp.236–244.

Ranade, V. & Kumar, A., 2006b. Fluid dynamics of spacer filled rectangular and curvilinear channels. *Journal of Membrane Science*, 271, pp.1–15.

Rand, P., 2017. Osmotic stress [Online]. Available at: https://brocku.ca/researchers/peter_rand/osmotic/osfile.html (Accessed: 10 May 2017).

Rege, B., March, C. & Sarkar, M., 2002. Development of a rapid and sensitive high-performance liquid chromatographic method to determine CYP2D6 phenotype in human liver microsomes. *Biomedical Chromatography*, 16, pp.31–40.

Reichelt, G., 1991. Bubble point measurements on large areas of microporous membranes. *Journal of Membrane Science*, 60, pp.253–259.

Ren, Y. & Leung, W., 2013a. Flow and mixing in rotating zigzag microchannel. *Chemical Engineering Journal*, 215–216, pp.561–578.

Ren, Y. & Leung, W., 2013b. Vortical flow and mixing in rotating milli- and micro-chambers. *Computers and Fluids*, 79, pp.150–166.

Reyes, D. et al., 2002. Micro total analysis systems. 1. Introduction, theory, and technology. *Analytical chemistry*, 74, pp.2623–36.

Ribeiro, A. et al., 2006. Binary mutual diffusion coefficients of aqueous solutions of sucrose, lactose, glucose, and fructose in the temperature range from (298.15 to 328.15 ) K. *Journal of Chemical and Engineering Data*, 51, pp.1836–1840.

Rigopulos, P., 1970. Self-cleaning ultrafilter. *US Patent* 3488768.

Rios, G., Rakotoarisoa, H. & Fuente, B., 1987. Basic transport mechanisms of ultrafiltration in the presence of fluidized particles. *Journal of Membrane Science*, 34, pp.331–343.

Rios, G., Rakotoarisoa, H. & Fuente, B., 1988. Basic transport mechanisms of ultrafiltration in the presence of an electric field. *Journal of Membrane Science*, 38, pp.147–159.

Rodrigues, C. et al., 2010. On the prediction of permeate flux for nanofiltration of concentrated aqueous solutions with thin-film composite polyamide membranes. *Journal of Membrane Science*, 346, pp.1–7.

Rodrigues, C. et al., 2012. Mass-transfer entrance effects in narrow rectangular channels with ribbed walls or mesh-type spacers. *Chemical Engineering Science*, 78, pp.38–45.

Rodrigues, C. et al., 2013. Concentration boundary layer visualization in nanofiltration by holographic interferometry with light deflection correction. *Journal of Membrane Science*, 447, pp.306–314.

Rodrigues, C. et al., 2015. Enhancement of mass transfer in spacer-filled channels under laminar regime by pulsatile flow. *Chemical Engineering Science*, 123, pp.536–541.

Rohatgi, A. WebPlotDigitizer [Online]. Available at: http://arohatgi.info/WebPlotDigitizer/app/? (Accessed 10 May 2017).

Rosa, M., 1995. *Separação selectiva de compostos orgânicos de correntes aquosas por ultrafiltração e nanofiltração (PhD thesis)*. Universidade Técnica de Lisboa.

Rouina, M. et al., 2016. Effect of electromagnetic field on membrane fouling in reverse osmosis process. *Desalination*, 395, pp.41–45.

Rudie, B., Torgrimson, T. & Spatz, D., 1985. Reverse-osmosis and ultrafiltration membrane compaction and fouling studies using ultrafiltration pretreatment. *Acs Symposium Series*, 281, pp.403–414.

Ruiz-Bevia, F. et al., 1985. Liquid diffusion measurement by holographic interferometry. *The Canadian Journal of Chemical Engineering*, 63, pp.765–771.

Rundel, J., Paul, B. & Remcho, V., 2007. Organic solvent nanofiltration for microfluidic purification of poly(amidoamine) dendrimers. *Journal of chromatography A*, 1162, pp.167–74.

Sablani, S. et al., 2001. Concentration polarization in ultrafiltration and reverse osmosis: a

critical review. *Desalination*, 141, pp.269–289.

Saeed, A. et al., 2012. Effect of feed spacer arrangement on flow dynamics through spacer filled membranes. *Desalination*, 285, pp.163–169.

Saeed, A., Vuthaluru, R. & Vuthaluru, H.B., 2015. Investigations into the effects of mass transport and flow dynamics of spacer filled membrane modules using CFD. *Chemical Engineering Research and Design*, 93, pp.79–99.

Salcedo-Díaz, R. et al., 2014. Visualization and modeling of the polarization layer in crossflow reverse osmosis in a slit-type channel. *Journal of Membrane Science*, 456, pp.21–30.

Sanchez, A. et al., 2008. Effect of centrifugal ultrafiltration on the composition of aqueous extracts of Saffron spice (Crocus sativus, L.). *Journal of Agricultural and Food Chemistry*, 56, pp.7293–7301.

Santiago, J. et al., 1998. A particle image velocimetry system for microfluidics. *Experiments in Fluids*, 25, pp.316–319.

Santos, J. et al., 2007. Investigation of flow patterns and mass transfer in membrane module channels filled with flow-aligned spacers using computational fluid dynamics (CFD). *Journal of Membrane Science*, 305, pp.103–117.

Sarrazin, F. et al., 2006. Experimental and numerical study of droplets hydrodynamics in microchannels. *AIChE Journal*, 52, pp.4061–4070.

Sartorius GmbH, 2017. Laboratory filtration products (Publication No.: SLU0006-e170513). Sartorius Lab Instruments GmbH & Co. KG.

Schlosser, C., Streu, P. & Croot, P., 2013. Vivaspin ultrafiltration: a new approach for high resolution measurements of colloidal and soluble iron species. *Limnology and Oceanography: Methods*, 11, pp.187–201.

Schock, G. & Miquel, A., 1987. Mass-transfer and pressure loss in spiral wound modules. *Desalination*, 64, pp.339–352.

Schwarzwald, D., 2010. Membrane apparatus for receiving samples. *US Patent* 7658982.

Schwinge, J., Wiley, D. & Fletcher, D., 2002a. A CFD study of unsteady flow in narrow spacer-filled channels for spiral-wound membrane modules. *Desalination*, 146, pp.195–201.

Schwinge, J., Wiley, D. & Fletcher, D., 2002b. Simulation of the flow around spacer filaments between channel walls. 2. mass-transfer enhancement. *Industrial & Engineering Chemistry Research*, 41, pp.4879–4888.

Schwinge, J., Wiley, D. & Fletcher, D., 2002c. Simulation of the flow around spacer filaments between narrow channel walls. 1. Hydrodynamics. *Industrial & Engineering Chemistry Research*, 41, pp.2977–2987.

Schwinge, J., Wiley, D. & Fletcher, D., 2003. Simulation of unsteady flow and vortex shedding for narrow spacer-filled channels. *Industrial & Engineering Chemistry Research*, 42, pp.4962–4977.

Schwinge, J., Wiley, D. & Fane, A., 2004. Novel spacer design improves observed flux. *Journal of Membrane Science*, 229, pp.53–61.

Scott, K. & Lobato, J., 2004. Influence of dispersed particulates on mass transport in cross-corrugated structures. *Journal of Applied Electrochemistry*, 34(6), pp.631–636.

Settles, G. & Hargather, M., 2017. A review of recent developments in schlieren and shadowgraph techniques. *Measurement Science and Technology*, 28, p.42001.

Shah, T. et al., 2006. Rotating reverse osmosis and spiral wound reverse osmosis filtration: a comparison. *Journal of Membrane Science*, 285(1–2), pp.353–361.

Shah, A., Huang, C. & Kim, J., 2012. Mechanisms of antibiotic removal by nanofiltration membranes: model development and application. *Journal of Membrane Science*, 389, pp.234–244.

Shakaib, M., Hasani, S. & Mahmood, M., 2007. Study on the effects of spacer geometry in membrane feed channels using three-dimensional computational flow modeling. *Journal of Membrane Science*, 297, pp.74–89.

Shakaib, M., Hasani, S. & Mahmood, M., 2009. CFD modeling for flow and mass transfer in spacer-obstructed membrane feed channels. *Journal of Membrane Science*, 326, pp.270–284.

Shareef, S. & Schmitt, D.R., 2004. Point load determination of static elastic moduli using laser speckle interferometry. *Optics and Lasers in Engineering*, 42, pp.511–527.

Sheen, H. et al., 2007. Unsteady flow behaviours in an obstacle-type valveless micropump by micro-PIV. *Microfluidics and Nanofluidics*, 4, pp.331–342.

Sherwood, T. et al., 1965. Salt concentration at phase boundaries in desalination by reverse osmosis. *Industrial and Engineering Chemistry Fundamentals*, 4, pp.113–118.

Sherwood, T., Brian, P. & Fisher, R., 1967. Desalination by reverse osmosis. *Industrial and Engineering Chemistry Fundamentals*, 6, pp.2–12.

Shimizu, A. & Ohtsubo, S., 1986. Filter device for liquids. *US Patent* 4600507.

Shinohara, K. et al., 2004. High-speed micro-PIV measurements of transient flow in microfluidic devices. *Measurement Science and Technology*, 15, pp.1965–1970.

Shirazi, S., Lin, C. & Chen, D., 2010. Inorganic fouling of pressure-driven membrane processes - A critical review. *Desalination*, 250, pp.236–248.

Sile-Yuksel, M. et al., 2014. Effect of silver nanoparticle (AgNP) location in nanocomposite membrane matrix fabricated with different polymer type on antibacterial mechanism. *Desalination*, 347, pp.120–130.

Silva, G., Leal, N. & Semiao, V., 2008. Micro-PIV and CFD characterization of flows in a microchannel: velocity profiles, surface roughness and Poiseuille numbers. *International Journal of Heat and Fluid Flow*, 29, pp.1211–1220.

Sinton, D., 2004. Microscale flow visualization. *Microfluidics and Nanofluidics*, 1(1), pp.2–21.

Sklar, E., Graham, P. & Larson, J., 1997. Selective separation filter device. *US Patent* 5601711.

Slezak, A., Dworecki, K. & Anderson, J., 1985. Gravitational effects on transmembrane flux: the Rayleigh-Taylor convective instability. *Journal of Membrane Science*, 23, pp.71–81.

Soltanieh, M. & Gill, W., 1981. Review of reverse osmosis membranes and transport models. *Chemical Engineering Communications*, 12, pp.279–363.

Song, L. & Ma, S., 2005. Numerical Studies of the Impact of Spacer Geometry on Concentration Polarization in Spiral Wound Membrane Modules. *Industrial & Engineering Chemistry Research*, 44, pp.7638–7645.

Sorin, A. et al., 2004. $Cs^+/Na^+$ Separation by nanofiltration–complexation with resorcinarene. *Separation Science and Technology*, 39, pp.2577–2595.

Sourirajan, S., 1970. *Reverse Osmosis*, Logos Press Limited.

Sousa, P. et al., 2014. A CFD study of the hydrodynamics in a desalination membrane filled with spacers. *Desalination*, 349, pp.22–30.

Steijn, V., Kreutzer, M. & Kleijn, C., 2007. μ-PIV study of the formation of segmented flow in microfluidic T-junctions. *Chemical Engineering Science*, 62, pp.7505–7514.

Stratasys Limited, 2017. PolyJet material data sheet (MSS_PJ_PJMaterialsDataSheet_0517a). Stratasys, Ltd.

Stroock, A. et al., 2002. Chaotic mixer for microchannels. *Science*, 295, pp.647–651.

Su, X. et al., 2006. Biological fingerprinting analysis by liquid chromatography/mass spectrometry for evaluation of DNA structural selectivity of multiple compounds in natural products. *Journal of Combinatorial Chemistry*, 8, pp.544–550.

Subramani, A., Kim, S. & Hoek, E., 2006. Pressure, flow, and concentration profiles in open and spacer-filled membrane channels. *Journal of Membrane Science*, 277, pp.7–17.

Sun, C., Chen, S. & Hsiao, P., 2015. Mapping the salinity gradient in a microfluidic device with schlieren imaging. *Sensors*, 15, pp.11587–11600.

Sun, C., Lee, H. & Kao, R., 2011. Diagnosis of oscillating pressure-driven flow in a microdiffuser using micro-PIV. *Experiments in Fluids*, 52, pp.23–35.

Sutzkover, I., Hasson, D. & Semiat, R., 2000. Simple technique for measuring the concentration polarization level in a reverse osmosis system. *Desalination*, 131, pp.117–127.

Synder Filtration Incorporated, n.d. Sanitary Nanofiltration Spiral-Wound Element: NFX (150-300Da). Synder Fintration, Inc.

Szabados, A., 1988. Filtrationseinheit, insbesondere für medizinische proben. *European Patent* 0298513.

Taira, T. et al., 2015. Selective encapsulation of cesium ions using the cyclic peptide moiety of surfactin: highly efficient removal based on an aqueous giant micellar system. *Colloids and Surfaces B: Biointerfaces*, 134, pp.59–64.

Tanaka, Y., 1991. Concentration electrodialysis polarization in ion exchange membrane.

*Journal of Membrane Science*, 57, pp.217–235.

Tang, C., Kwon, Y.-N., Leckie, J., 2007. Fouling of reverse osmosis and nanofiltration membranes by humic acid – Effects of solution composition and hydrodynamic conditions. *Journal of Membrane Science*, 290, pp86–94.

Tang, C., Kwon, Y. & Leckie, J., 2009. Effect of membrane chemistry and coating layer on physiochemical properties of thin film composite polyamide RO and NF membranes I . FTIR and XPS characterization of polyamide and coating layer chemistry. *Desalination*, 242, pp.149–167.

Tang, P., Si, S. & Liu, L., 2015. Analysis of bovine serum albumin ligands from Puerariae flos using ultrafiltration combined with HPLC-MS. *Journal of Cheimstry*, 2015, p.648361.

Tao, Y. & Sun, D., 2015. Enhancement of food processes by ultrasound: a review. *Critical reviews in food science and nutrition*, 55, pp.570–594.

Teixeira, A., Santos, J. & Crespo, J., 2009. Sustainable membrane-based process for valorisation of cork boiling wastewaters. *Separation and Purification Technology*, 66, pp.35–44.

Temido, J., 2015. *Desenvolvimento de um processo de nanofiltração para remoção da acidez volátil em vinhos (Master thesis)*. Universidade de Lisboa.

Thermo Fisher Scientific Incorporated, 2007. European rotor guide Sorvall centrifuge rotors (PN 74165-10). Thermo Fisher Scientific Inc.

Thermo Fisher Scientific Incorporated, 2010. Superspeed Rotors Thermo Scientific SS-34 Rotor. Thermo Fisher Scientific Inc.

Thermo Fisher Scientific Incorporated, 2014a. Thermo Scientific Fiberlite F10-4x1000 LEX Rotor. Thermo Fisher Scientific Inc.

Thermo Fisher Scientific Incorporated, 2014b. Superspeed Rotors Thermo Scientific Fiberlite F10-6x500 Rotor. Thermo Fisher Scientific Inc.

Thermo Fisher Scientific Incorporated, 2014c. Superspeed Rotors Thermo Scientific SA-300 Rotor. Thermo Fisher Scientific Inc.

Thermo Fisher Scientific Incorporated, 2017. Protein concentrators [Online]. Available at: https://www.thermofisher.com/pt/en/home/life-science/protein-biology/protein-purification-isolation/protein-dialysis-desalting-concentration/protein-concentrators.html (Accessed: 22 November 1017).

Terry, S., Jerman, J. & Angell, J., 1979. A gas chromatographic air analyzer fabricated on a silicon wafer. *IEEE transactions on electron devices*, 26, pp.1880–1886.

Torres, J. et al., 2012. Development of phase-shifting interferometry for measurement of isothermal diffusion coefficients in binary solutions. *Optics and Lasers in Engineering*, 50, pp.1287–1296.

Vassarotti, V., 1997. Centrifugal method for concentrating macromolecules from a solution and

device for carrying out said method. *US Patent* 5647990.

Vassarotti, V., 2002. Method, device and apparatus for concentrating and/or purifying macromolecules in a solution. *US Patent* 6375855.

Verboom, W., 2009. Selected examples of high-pressure reactions in glass microreactors. *Chemical Engineering and Technology*, 32, pp.1695–1701.

Versteeg, H. & Malalasekera, W., 2007. *An introduction to computational fluid dynamics - the finite volume method* 2nd ed., Prentice-Hall.

Vilker, V., Colton, C. & Smith, K., 1981. Concentration polarization in protein ultrafiltration. Part I: an optical shadowgraph technique for measuring concentration profiles near a solution-membrane interface. *AIChE Journal*, 27, pp.632–637.

Vitagliano, V. & Lyons, P., 1956. Diffusion coefficients for aqueous solutions of sodium chloride and barium chloride. *Journal of the American Chemical Society*, 78, pp.1549–1552.

Vlock, D., Malakian, A. & Cann, I., 1998. Method and apparatus for isolation and purification of immune complexes. *US Patent* 5783087.

van der Waal, M. et al., 1977. Use of fluidised beds as turbulence promotors in tubular membrane systems. *Desalination*, 22, pp.465–483.

Wakeman, R. & Williams, C., 2002. Additional techniques to improve microfiltration. *Separation and Purification Technology*, 26(1), pp.3–18.

Wang, H. & Wang, Y., 2009. Measurement of water flow rate in microchannels based on the microfluidic particle image velocimetry. *Measurement*, 42, pp.119–126.

Wang, K. et al., 2013. Integrated membrane process for the purification of lactic acid from a fermentation broth neutralized with sodium hydroxide. *Industrial and Engineering Chemistry Research*, 52, pp.2412–2417.

Wang, T. et al., 2013. A novel highly permeable positively charged nanofiltration membrane based on a nanoporous hyper-crosslinked polyamide barrier layer. *Journal of Membrane Science*, 448, pp.180–189.

Wang, J., Dlamini, D., et al., 2014. A critical review of transport through osmotic membranes. *Journal of Membrane Science*, 454, pp.516–537.

Wang, J., Wei, Y. & Cheng, Y., 2014. Advanced treatment of antibiotic wastewater by nanofiltration: membrane selection and operation optimization. *Desalination and Water Treatment*, 52, pp.7575–7585.

Wang, Z. et al., 2014. Membrane cleaning in membrane bioreactors: a review. *Journal of Membrane Science*, 468, pp.276–307.

Wardeh, S. & Morvan, H., 2008. CFD simulations of flow and concentration polarization in spacer-filled channels for application to water desalination. *Chemical Engineering Research and Design*, 86, pp.1107–1116.

Wardeh, S. & Morvan, H., 2009. Detailed numerical simulations of flow mechanics and membrane performance in spacer-filled channels, flat and curved. *Desalination and Water Treatment*, 1, pp.277–288.

Wardrip, N. & Arnusch, C., 2016. Three-dimensionally printed microfluidic cross-flow system for ultrafiltration/nanofiltration membrane performance testing. *Journal of visualized experiments : JoVE*, (108), p.53556.

Warner, T., 2006. Molecule separation device and method combining mutiple filtration media. *US Patent* 7045064.

Weast (editor), R. ed., 1981. *Handbook of chemistry and physics* 62nd ed., CRC Press.

Wei, K. et al., 2015. Effects of operational parameters on electro-microfiltration process of NOM tailwater containing scaling metal ions. *Desalination*, 369, pp.115–124.

Wesełucha-Birczyńska, A. et al., 2015. Raman spectroscopy and the material study of nanocomposite membranes from poly(epsilon-caprolactone) with biocompatibility testing in osteoblast-like cells. *Analyst*, 140, pp.2311–2320.

Whitesides, G., 2006. The origins and the future of microfluidics. *Nature*, 442, pp.368–73.

Wibisono, Y. et al., 2014. Two-phase flow in membrane processes: a technology with a future. *Journal of Membrane Science*, 453(2014), pp.566–602.

Wijmans, J. & Baker, R., 1995. The solution-diffusion model: a review. , 107, pp.1–21.

Willems, P. et al., 2010. Use of particle imaging velocimetry to measure liquid velocity profiles in liquid and liquid/gas flows through spacer filled channels. *Journal of Membrane Science*, 362, pp.143–153.

Wilson, I. & Poole, C., 2009. *Handbook of Methods and Instrumentation in Separation Science, Volume 1*, Academic Press.

Wilson, O., 1971. Apparatus for the concentration of macromecules and subcellular partiicles from dilute solutions. *US Patent* 3583627.

Winzeler, H. & Belfort, G., 1993. Enhanced performance for pressure-driven membrane processes: the argument for fluid instabilities. *Journal of Membrane Science*, 80, pp.35–47.

Wunderlich, A. et al., 2016. Rapid quantification method for Legionella pneumophila in surface water. *Analytical and Bioanalytical Chemistry*, 408, pp.2203–2213.

Wyart, Y. et al., 2008. Membrane characterization by optical methods: ellipsometry of the scattered field. *Journal of Membrane Science*, 318, pp.145–153.

Wyart, Y. et al., 2014. Morphological analysis of flat and hollow fiber membranes by optical and microscopic methods as a function of the fouling. *Journal of Membrane Science*, 472, pp.241–250.

Xia, Y. & Whitesides, G., 1998. Soft lithography. *Angewandte Chemie (International ed. in English)*, 37, pp.550–575.

Xiang, T. et al., 2013. Surface hydrophilic modification of polyethersulfone membranes by

surface-initiated ATRP with enhanced blood compatibility. *Colloids and Surfaces B: Biointerfaces*, 110, pp.15–21.

Xie, M. & Gray, S., 2016. Transport and accumulation of organic matter in forward osmosis-reverse osmosis hybrid system: mechanism and implications. *Separation and Purification Technology*, 167, pp.6–16.

Xie, Y. et al., 2015. Filtration performance comparison of a metal membrane and an organic membrane in bioreactor. *Desalination and Water Treatment*, 54, pp.3566–3574.

Xu, M. et al., 2014. Effect of different pretreatment methods on the measurement of the entrapment efficiency of liposomes and countermeasures in free drug analysis. *Chromatographia*, 77, pp.223–232.

Xu, J. et al., 2015. Constructing antimicrobial membrane surfaces with polycation-copper(II) complex assembly for efficient seawater softening treatment. *Journal of Membrane Science*, 491, pp.28–36.

Xu, L. et al., 2017. A wide range and high resolution one-filtration molecular weight cut-off method for aqueous based nanofiltration and ultrafiltration membranes. *Journal of Membrane Science*, 525, pp.304–311.

Yang, L., Chu, L. & Chen, W., 2006. Study on the flow field inside the microfiltration separator with rotary tubular membrane. *Separation Science and Technology*, 41, pp.1513–1525.

Yang, R. et al., 2017. A comprehensive review of micro-distillation methods. *Chemical Engineering Journal*, 313, pp.1509–1520.

Yang, X. et al., 2015. Development of a mitochondria-based centrifugal ultrafiltration/liquid chromatography/mass spectrometry method for screening mitochondria-targeted bioactive constituents from complex matrixes: Herbal medicines as a case study. *Journal of Chromatography A*, 1413, pp.33–46.

Yeo, A., Law, A. & Fane, A., 2006. Factors affecting the performance of a submerged hollow fiber bundle. *Journal of Membrane Science*, 280, pp.969–982.

Yu, M., Zhang, H. & Yang, F., 2017. A study of a ferric-lactate complex as draw solute in forward osmosis. *Chemical Engineering Journal*, 314, pp.132–138.

Zaera, F., 2012. Probing liquid/solid interfaces at the molecular level. *Chemical Reviews*, 112, pp.2920–2986.

Zaki, M., Nirdosh, I. & Sedahmed, G., 2011. Mass transfer behaviour of annular ducts under conditions with superimposed pulsating flow. *Chemical Engineering & Technology*, 34(3), pp.475–481.

Zeidler, S. et al., 2014. Preparation and characterization of new low MWCO ceramic nanofiltration membranes for organic solvents. *Journal of Membrane Science*, 470, pp.421–430.

Zerai, B. et al., 2005. Flow characterization through a network cell using particle image

velocimetry. *Transport in Porous Media*, 60, pp.159–181.

Zhang, Q., Pan, W. & Cross, L., 1988. Laser interferometer for the study of piezoelectric and electrostrictive strains. *Journal of Applied Physics*, 63, pp.2492–2496.

Zhang, Q., Jang, S. & Cross, L., 1989. High-frequency strain response in ferroelectrics and its measurement using a modified Mach-Zehnder interferometer. *Journal of Applied Physics*, 65, pp.2807–2813.

Zhang, W. & Ethier, C., 2001. Direct pressure measurements in a hyaluronan ultrafiltration concentration polarization layer. *Colloids and Surfaces A: Physicochemical and Engineering Aspects*, 180, pp.63–73.

Zhang, C., Xing, D. & Li, Y., 2007. Micropumps, microvalves, and micromixers within PCR microfluidic chips: advances and trends. *Biotechnology advances*, 25, pp.483–514.

Zhang, F. et al., 2012. Compilation of 222 drugs' plasma protein binding data and guidance for study designs. *Drug Discovery Today*, 17, pp.475–485.

Zhang, L. et al., 2013. Accuracy assessment on the analysis of unbound drug in plasma by comparing traditional centrifugal ultrafiltration with hollow fiber centrifugal ultrafiltration and application in pharmacokinetic study. *Journal of Chromatography A*, 1318, pp.265–269.

Zhang, H. et al., 2015. A new folded plate membrane module for hydrodynamic characteristics improvement and flux enhancement. *Separation and Purification Technology*, 154, pp.36–43.

Zhang, W. et al., 2015. A review on flux decline control strategies in pressure-driven membrane processes. *Industrial and Engineering Chemistry Research*, 54, pp.2843–2861.

Zhang, Y., Benes, N. & Lammertink, R., 2016. Performance study of pervaporation in a microfluidic system for the removal of acetone from water. *Chemical Engineering Journal*, 284, pp.1342–1347.

Zhang, C., Bills, B. & Manicke, N., 2017. Rapid prototyping using 3D printing in bioanalytical research. *Bioanalysis*, 9, pp.329–331.

Zhao, D. & Yu, S., 2015. A review of recent advance in fouling mitigation of NF/RO membranes in water treatment: pretreatment, membrane modification, and chemical cleaning. *Desalination and Water Treatment*, 55, pp.1–22.

Zheng, Z. et al., 2016. Fabrication, characterization, and hemocompatibility investigation of polysulfone grafted with polyethylene glycol and heparin used in membrane oxygenators. *Artificial Organs*, 40, pp.E219–E229.

Zhloba, A. & Subbotina, T., 2014. Homocysteinylation score of high-molecular weight plasma proteins. *Amino Acids*, 46, pp.893–899.

Zhou, J. et al., 2008. Screening and mechanism study of components targeting DNA from the Chinese herb Lonicera japonica by liquid chromatography / mass spectrometry and

fluorescence spectroscopy. *Biomedical Chromatography*, 22, pp.1164–1172.

Ziemecka, I., Haut, B. & Scheid, B., 2017. Continuous separation, with microfluidics, of the components of a ternary mixture: from vacuum to purge gas pervaporation. *Microfluidics and Nanofluidics*, 21, pp.1–13.

Zimmerman, J., Barker, R. & Jack, R., 2010. Initial observations regarding free cortisol quantification logistics among critically ill children. *Intensive Care Medicine*, 36, pp.1914–1922.

Zin, G. et al., 2016. Fouling control in ultrafiltration of bovine serum albumin and milk by the use of permanent magnetic field. *Journal of Food Engineering*, 168, pp.154–159.

Zuk Jr., P., 1992. Filtration apparatus. *US Patent* 5112484.

Zuk Jr., P., 2000. Centrifugal filtration apparatus. *US Patent* 6156199.

# Appendix A Properties of the solutions

In this section are shown the expressions used to estimate the physical properties of the solutions, as function of the solute concentration, for the binary solute-water solutions used in this work. The selected physical properties shown here are: density, viscosity, osmotic pressure and diffusion coefficient. The solutes are grouped as salts and neutral compounds and ordered by their molecular weight.

Whenever possible, data from several literature sources are shown in order to access their reliability. The two main sources for the density, viscosity and osmotic pressure data are the *Handbook of chemistry and physics* (Weast (editor) 1981) and the Sourirajan's book *Reverse osmosis* (Sourirajan 1970). In the former book data refers to solutions at 20 °C, while in the latter data refers to solutions at 25 °C. Other literature sources were also used as an independent mean to compare data. Some of the obtained data was extracted from printed charts using the WebPlotDigizer software (Rohatgi 2017). Most of the data for the diffusion coefficient was found for 25 °C. The diffusion coefficient at 20 °C was calculated using the Walden's rule (Fernandez & Phillies 1983):

$$\frac{D_1 \mu_1}{T_1} = \frac{D_2 \mu_2}{T_2} \tag{A-1}$$

where $D_i$ and $\mu_i$are the diffusion coefficient and the dynamic viscosity at the temperature $T_i$.

# A.1 Salts

## A.1.1 NaCl

NaCl has a molecular weight of 58.44 g/mol. The relationships between some of the properties of the binary NaCl-water solutions (density, viscosity, osmotic pressure and diffusion coefficient) as function of NaCl concentration are shown in Figure A-1. The expressions for the data fittings of Figure A-1 are shown in Table A-1.

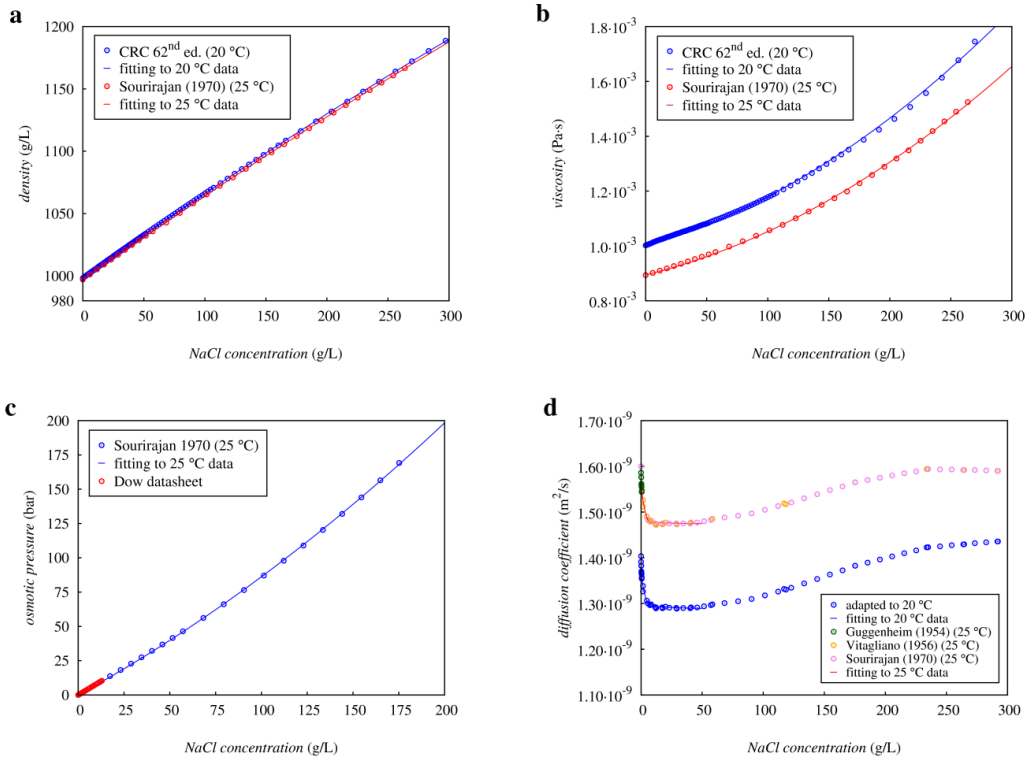


Figure A-1 – Properties of NaCl aqueous solutions as function of NaCl concentration: a) density; b) viscosity; c) osmotic pressure; d) diffusion coefficient.

Table A-1 – Expressions for the fittings of the density, viscosity, osmotic pressure and diffusion coefficient data of NaCl aqueous solutions as function of NaCl concentration.

| Property | Temperature | Expression | Condition |
|---|---|---|---|
| density | 20 °C | $\rho$ (g/L) = -2.009×10$^{-4}$ ·$c^2$ + 6.991×10$^{-1}$ · $c$ + 998.2 | $c$ < 300 g/L |
| | 25 °C | $\rho$ (g/L) = -1.745×10$^{-4}$ · $c^2$ + 6.874×10$^{-1}$ · $c$ + 997.1 | $c$ < 300 g/L |
| viscosity | 20 °C | $\mu$ (Pa·s) = 5.393×10$^{-9}$ · $c^2$ + 1.242×10$^{-6}$ · $c$ + 1.002×10$^{-3}$ | $c$ < 300 g/L |
| | 25 °C | $\mu$ (Pa·s) = 4.761×10$^{-9}$ · $c^2$ + 1.108×10$^{-6}$ · $c$ + 0.894×10$^{-3}$ | $c$ < 300 g/L |
| osmotic pressure | 25 °C | $\pi$ (bar) = 1.303×10$^{-3}$ · $c^2$ + 7.313×10$^{-1}$ · $c$ | $c$ < 170 g/L |
| diffusion coefficient | 20 °C | $D$ (m$^2$/s) = 1.404×10$^{-9}$ · (1 - 0.040 · $c^{0.368}$) | $c \leq$ 6 g/L |
| | | $D$ (m$^2$/s) = 1.404×10$^{-9}$ · (1 - 0.073 · $c^{0.030}$) | 6 < $c$ < 50 g/L |
| | 25 °C | $D$ (m$^2$/s) = 1.600×10$^{-9}$ · (1 - 0.040 · $c^{0.366}$) | $c \leq$ 6 g/L |
| | | $D$ (m$^2$/s) = 1.600×10$^{-9}$ · (1 - 0.074 · $c^{0.014}$) | 6 < $c$ < 50 g/L |

Table A-2 – Literature references cited in the charts of Figure A-1.

### A.1.2 $MgCl_2$

$MgCl_2$ has a molecular weight of 95.23 g/mol in its anhydrous form, and of 203.30 g/mol in its hexahydrate form. The relationships between some of the properties of the binary $MgCl_2$-water solutions (density, viscosity, osmotic pressure and diffusion coefficient) as function of $MgCl_2$ concentration are shown in Figure A-2. The expressions for the data fittings of Figure A-2 are shown in Table A-3.

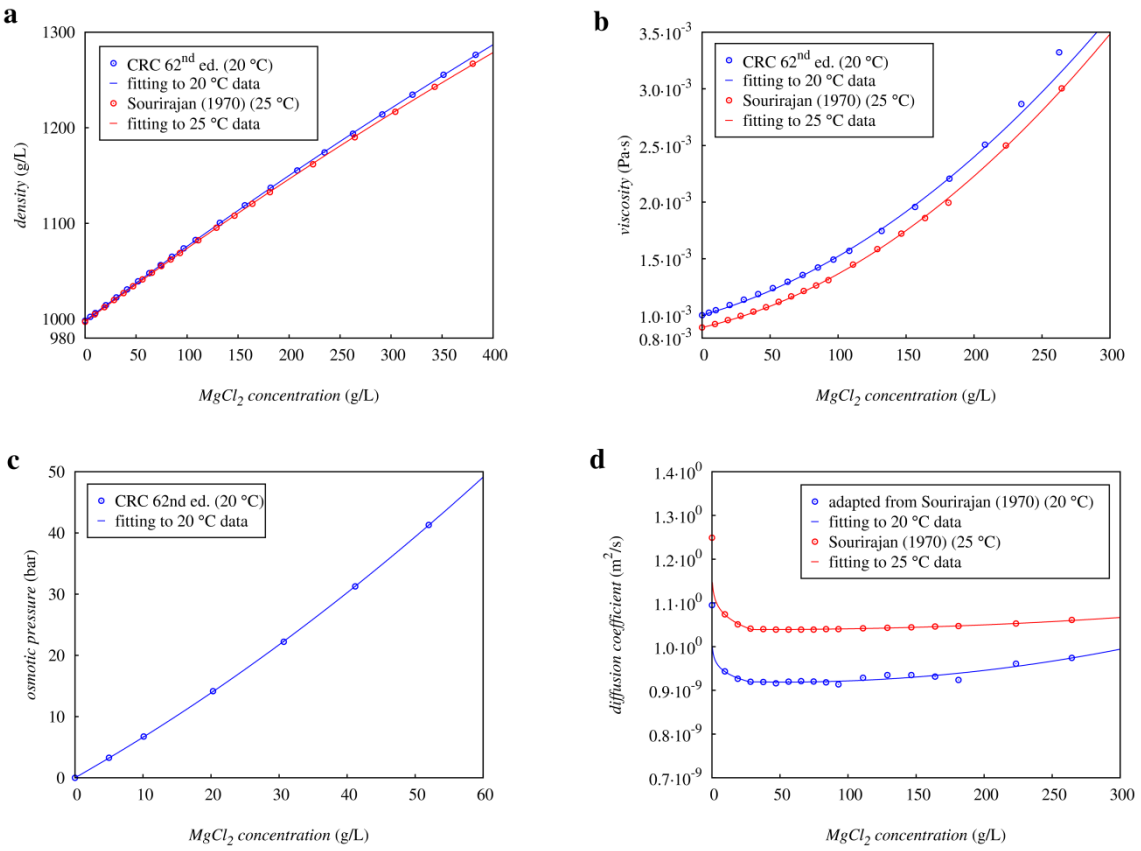


Figure A-2 – Properties of $MgCl_2$ aqueous solutions as function of $MgCl_2$ concentration: a) density; b) viscosity; c) osmotic pressure; d) diffusion coefficient.

Table A-3 – Expressions for the fittings of the density, viscosity, osmotic pressure and diffusion coefficient data of $MgCl_2$ aqueous solutions as function of $MgCl_2$ concentration.

| Property | Temperature | Expression | Condition |
|---|---|---|---|
| density | 20 °C | $\rho$ (g/L) = $-1.891\times10^{-4} \cdot c^2 + 7.973\times10^{-1} \cdot c + 998.2$ | $c$ < 400 g/L |
| | 25 °C | $\rho$ (g/L) = $-2.129\times10^{-4} \cdot c^2 + 7.889\times10^{-1} \cdot c + 997.1$ | $c$ < 400 g/L |
| viscosity | 20 °C | $\mu$ (Pa·s) = $1.791\times10^{-8} \cdot c^2 + 3.402\times10^{-6} \cdot c + 1.002\times10^{-3}$ | $c$ < 200 g/L |
| | 25 °C | $\mu$ (Pa·s) = $1.955\times10^{-8} \cdot c^2 + 2.766\times10^{-6} \cdot c + 0.894\times10^{-3}$ | $c$ < 200 g/L |
| osmotic pressure | 20 °C | $\pi$ (bar) = $3.141\times10^{-3} \cdot c^2 + 6.302\times10^{-1} \cdot c$ | $c$ < 60 g/L |
| diffusion coefficient | 20 °C | $D$ ($m^2$/s) = $1.095\times10^{-9} \cdot (1 - 0.103 \cdot c^{0.133})$ | $c \leq$ 30 g/L |
| | | $D$ ($m^2$/s) = $1.230\times10^{-6} \cdot c^2 - 1.298\times10^{-4} \cdot c + 0.922$ | 30 < $c$ < 300 g/L |
| | 25 °C | $D$ ($m^2$/s) = $1.249\times10^{-9} \cdot (1 - 0.098 \cdot c^{0.159})$ | $c \leq$ 30 g/L |
| | | $D$ ($m^2$/s) = $3.943\times10^{-7} \cdot c^2 - 2.780\times10^{-5} \cdot c + 1.040$ | 30 < $c$ < 300 g/L |

### A.1.3 $MgSO_4$

$MgSO_4$ has a molecular weight of 120.42 g/mol in its anhydrous form, and of 246.48 g/mol in its heptahydrate form. The relationships between some of the properties of the binary $MgSO_4$-water solutions (density, viscosity, osmotic pressure and diffusion coefficient) as function of $MgSO_4$ concentration are shown in Figure A-3. The expressions for the data fittings of Figure A-3 are shown in Table A-4.

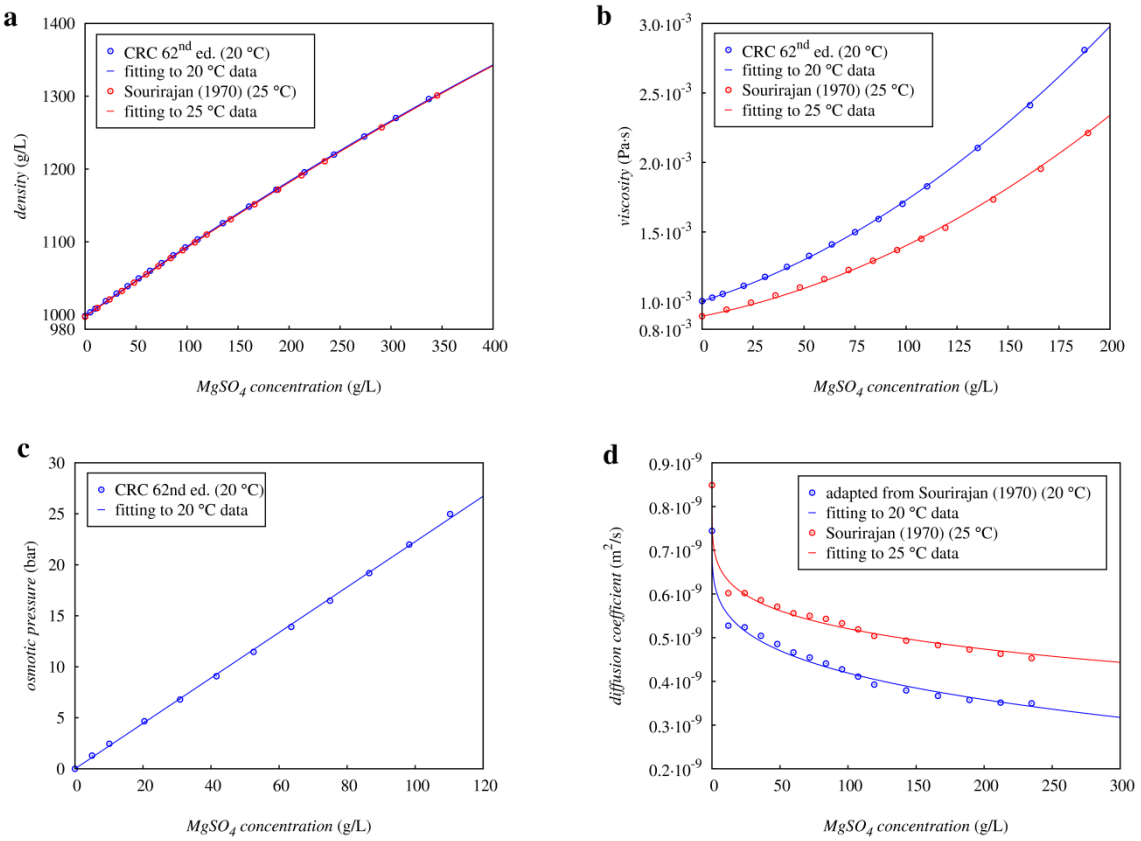


Figure A-3 – Properties of $MgSO_4$ aqueous solutions as function of $MgSO_4$ concentration: a) density; b) viscosity; c) osmotic pressure; d) diffusion coefficient.

Table A-4 – Expressions for the fittings of the density, viscosity, osmotic pressure and diffusion coefficient data of $MgSO_4$ aqueous solutions as function of $MgSO_4$ concentration.

| Property | Temperature | Expression | Condition |
|---|---|---|---|
| density | 20 °C | $\rho$ (g/L) = $-3.103\times10^{-4} \cdot c^2 + 9.863\times10^{-1} \cdot c + 998.2$ | $c$ < 350 g/L |
| | 25 °C | $\rho$ (g/L) = $-2.962\times10^{-4} \cdot c^2 + 9.809\times10^{-1} \cdot c + 997.1$ | $c$ < 350 g/L |
| viscosity | 20 °C | $\mu$ (Pa·s) = $2.629\times10^{-8} \cdot c^2 + 4.626\times10^{-6} \cdot c + 1.002\times10^{-3}$ | $c$ < 200 g/L |
| | 25 °C | $\mu$ (Pa·s) = $2.150\times10^{-8} \cdot c^2 + 2.927\times10^{-6} \cdot c + 0.894\times10^{-3}$ | $c$ < 200 g/L |
| osmotic pressure | 20 °C | $\pi$ (bar) = $2.227\times10^{-1} \cdot c$ | $c$ < 100 g/L |
| diffusion coefficient | 20 °C | $D$ ($m^2$/s) = $0.744\times10^{-9} \cdot (1 - 0.140 \cdot c^{0.247})$ | $c \leq$ 200 g/L |
| | 25 °C | $D$ ($m^2$/s) = $0.849\times10^{-9} \cdot (1 - 0.160 \cdot c^{0.192})$ | $c \leq$ 200 g/L |

### A.1.4 $Na_2SO_4$

$Na_2SO_4$ has a molecular weight of 142.04 g/mol. The relationships between some of the properties of the binary $Na_2SO_4$-water solutions (density, viscosity, osmotic pressure and diffusion coefficient) as function of $Na_2SO_4$ concentration are shown in Figure A-4. The expressions for the data fittings of Figure A-4 are shown in Table A-5.

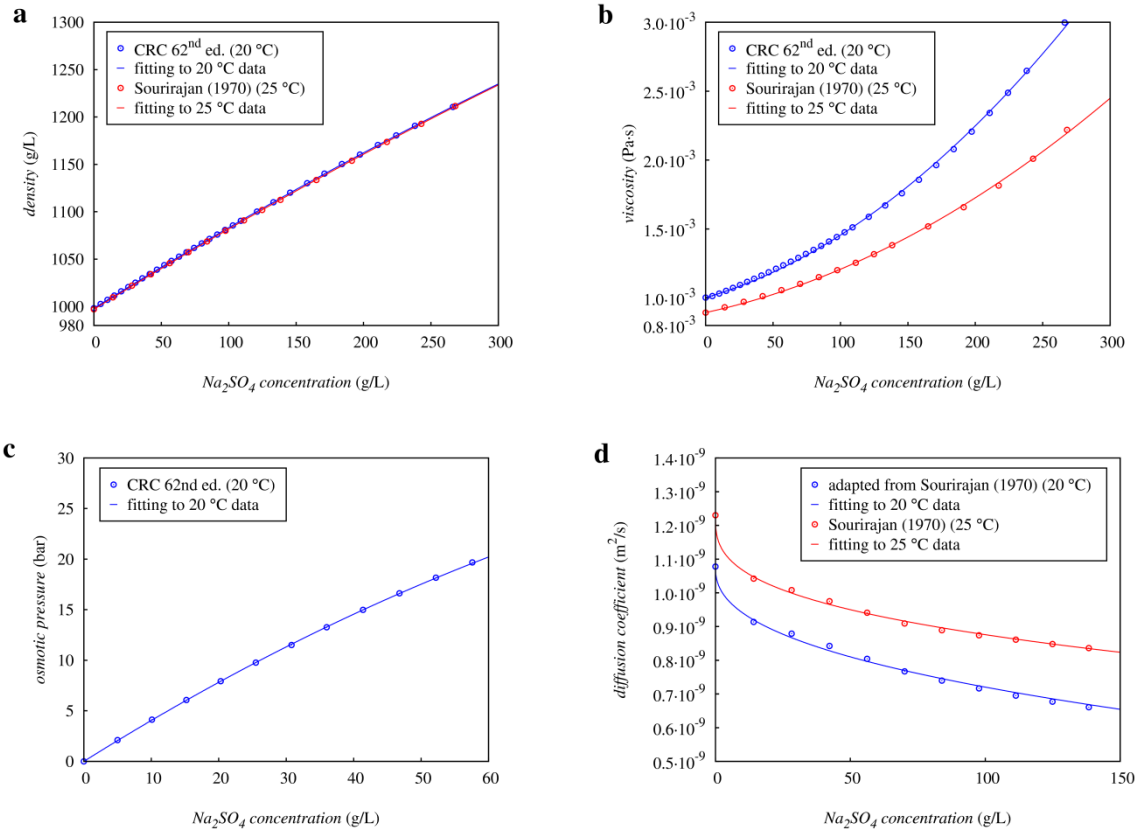


Figure A-4 – Properties of $Na_2SO_4$ aqueous solutions as function of $Na_2SO_4$ concentration: a) density; b) viscosity; c) osmotic pressure; d) diffusion coefficient.

Table A-5 – Expressions for the fittings of the density, viscosity, osmotic pressure and diffusion coefficient data of $Na_2SO_4$ aqueous solutions as function of $Na_2SO_4$ concentration.

| Property | Temperature | Expression | Condition |
|---|---|---|---|
| density | 20 °C | $\rho$ (g/L) = $-3.091\times10^{-4} \cdot c^2 + 8.818\times10^{-1} \cdot c + 998.2$ | $c$ < 250 g/L |
| | 25 °C | $\rho$ (g/L) = $-2.903\times10^{-4} \cdot c^2 + 8.763\times10^{-1} \cdot c + 997.1$ | $c$ < 250 g/L |
| viscosity | 20 °C | $\mu$ (Pa·s) = $1.695\times10^{-8} \cdot c^2 + 2.840\times10^{-6} \cdot c + 1.002\times10^{-3}$ | $c$ < 250 g/L |
| | 25 °C | $\mu$ (Pa·s) = $1.020\times10^{-8} \cdot c^2 + 2.121\times10^{-6} \cdot c + 0.894\times10^{-3}$ | $c$ < 250 g/L |
| osmotic pressure | 20 °C | $\pi$ (bar) = $-1.350\times10^{-3} \cdot c^2 + 4.178\times10^{-1} \cdot c$ | $c$ < 50 g/L |
| diffusion coefficient | 20 °C | $D$ ($m^2$/s) = $1.078\times10^{-9} \cdot (1 - 0.049 \cdot c^{0.417})$ | $c \leq$ 150 g/L |
| | 25 °C | $D$ ($m^2$/s) = $1.230\times10^{-9} \cdot (1 - 0.060 \cdot c^{0.339})$ | $c \leq$ 150 g/L |

### A.1.5 $K_2SO_4$

$K_2SO_4$ has a molecular weight of 174.27 g/mol. The relationships between some of the properties of the binary $K_2SO_4$-water solutions (density, viscosity, osmotic pressure and diffusion coefficient) as function of $K_2SO_4$ concentration are shown in Figure A-5. The expressions for the data fittings of Figure A-5 are shown in Table A-6.

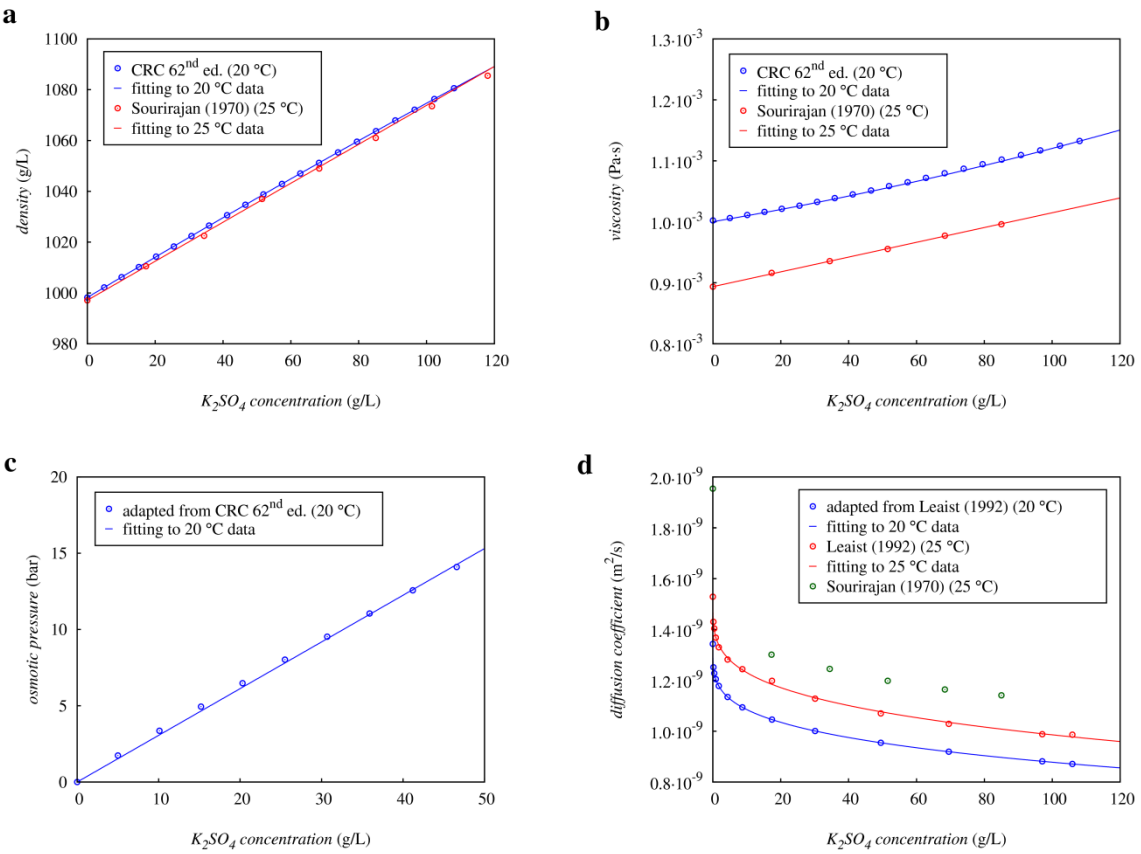


Figure A-5 – Properties of $K_2SO_4$ aqueous solutions as function of $K_2SO_4$ concentration: a) density; b) viscosity; c) osmotic pressure; d) diffusion coefficient.

Table A-6 – Expressions for the fittings of the density, viscosity, osmotic pressure and diffusion coefficient data of $K_2SO_4$ aqueous solutions as function of $K_2SO_4$ concentration.

| Property | Temperature | Expression | Condition |
|---|---|---|---|
| density | 20 °C | $\rho$ (g/L) = $-3.453\times10^{-4} \cdot c^2 + 7.991\times10^{-1} \cdot c + 998.2$ | $c < 100$ g/L |
| | 25 °C | $\rho$ (g/L) = $-1.686\times10^{-4} \cdot c^2 + 7.688\times10^{-1} \cdot c + 997.1$ | $c < 100$ g/L |
| viscosity | 20 °C | $\mu$ (Pa·s) = $2.512\times10^{-9} \cdot c^2 + 9.503\times10^{-7} \cdot c + 1.002\times10^{-3}$ | $c < 100$ g/L |
| | 25 °C | $\mu$ (Pa·s) = $1.211\times10^{-6} \cdot c + 0.894\times10^{-3}$ | $c < 100$ g/L |
| osmotic pressure | 20 °C | $\pi$ (bar) = $3.061\times10^{-1} \cdot c$ | $c < 50$ g/L |
| diffusion coefficient | 20 °C | $D$ ($m^2$/s) = $1.343\times10^{-9} \cdot (1 - 0.107 \cdot c^{0.256})$ | $c \leq 100$ g/L |
| | 25 °C | $D$ ($m^2$/s) = $1.529\times10^{-9} \cdot (1 - 0.107 \cdot c^{0.260})$ | $c \leq 100$ g/L |

## A.2 Non-ionic solutes

### A.2.1 Fructose

Fructose has a molecular weight of 180.16 g/mol. The relationships between some of the properties of the binary fructose-water solutions (density, viscosity, osmotic pressure and diffusion coefficient) as function of fructose concentration are depicted in Figure A-6. The expressions for the data fittings of Figure A-6 are shown in Table A-7.

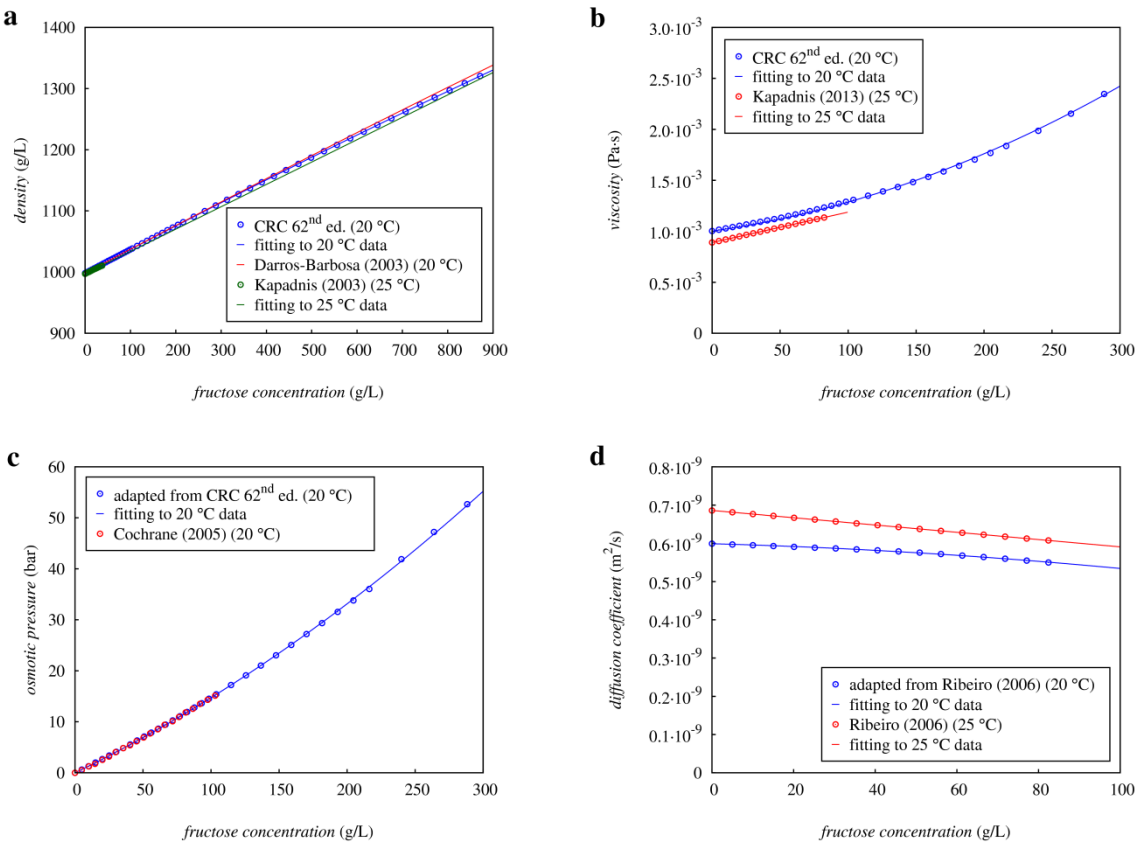


Figure A-6 – Properties of fructose aqueous solutions as function of fructose concentration: a) density; b) viscosity; c) osmotic pressure; d) diffusion coefficient.

Table A-7 – Expressions for the fittings of the density, viscosity, osmotic pressure and diffusion coefficient data of fructose aqueous solutions as function of fructose concentration.

| Property | Temperature | Expression | Condition |
|---|---|---|---|
| density | 20 °C | $\rho$ (g/L) = $-2.447\times10^{-5} \cdot c^2 + 3.911\times10^{-1} \cdot c + 998.2$ | $c$ < 900 g/L |
| | 25 °C | $\rho$ (g/L) = $3.657\times10^{-1} \cdot c + 997.1$ | $c$ < 900 g/L |
| viscosity | 20 °C | $\mu$ (Pa·s) = $9.472\times10^{-9} \cdot c^2 + 1.898\times10^{-6} \cdot c + 1.002\times10^{-3}$ | $c$ < 300 g/L |
| | 25 °C | $\mu$ (Pa·s) = $1.717\times10^{-9} \cdot c^2 + 2.804\times10^{-6} \cdot c + 0.894\times10^{-3}$ | $c$ < 80 g/L |
| osmotic pressure | 20 °C | $\pi$ (bar) = $1.837\times10^{-4} \cdot c^2 + 1.289\times10^{-1} \cdot c$ | $c$ < 300 g/L |
| diffusion coefficient | 20 °C | $D$ (m²/s) = $-3.545\times10^{-15} \cdot c^2 + 2.804\times10^{-13} \cdot c + 0.599\times10^{-9}$ | $c \leq$ 80 g/L |
| | 25 °C | $D$ (m²/s) = $-9.519\times10^{-13} \cdot c + 0.686\times10^{-9}$ | $c \leq$ 80 g/L |

### A.2.2 Sucrose

Sucrose has a molecular weight of 342.30 g/mol. The relationships between some of the properties of the binary sucrose-water solutions (density, viscosity, osmotic pressure and diffusion coefficient) as function of sucrose concentration are depicted in Figure A-7. The expressions for the data fittings of Figure A-7 are shown in Table A-8.

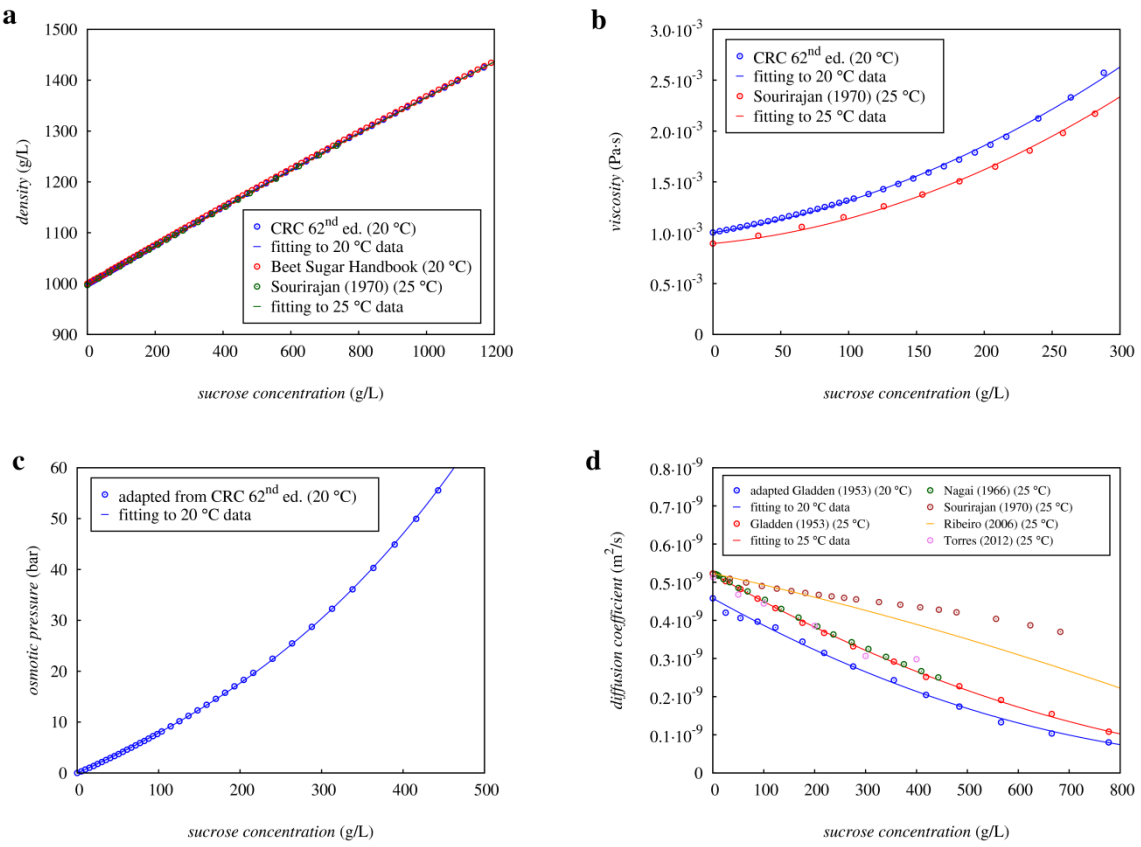


Figure A-7 – Properties of sucrose aqueous solutions as function of sucrose concentration: a) density; b) viscosity; c) osmotic pressure; d) diffusion coefficient.

Table A-8 – Expressions for the fittings of the density, viscosity, osmotic pressure and diffusion coefficient data of sucrose aqueous solutions as function of sucrose concentration.

| Property | Temperature | Expression | Condition |
|---|---|---|---|
| density | 20 °C | $\rho$ (g/L) = $-1.913\times10^{-5} \cdot c^2 + 3.879\times10^{-1} \cdot c + 998.2$ | $c$ < 1200 g/L |
| | 25 °C | $\rho$ (g/L) = $-1.595\times10^{-5} \cdot c^2 + 3.849\times10^{-1} \cdot c + 997.1$ | $c$ < 1200 g/L |
| viscosity | 20 °C | $\mu$ (Pa·s) = $1.152\times10^{-8} \cdot c^2 + 1.968\times10^{-6} \cdot c + 1.002\times10^{-3}$ | $c$ < 300 g/L |
| | 25 °C | $\mu$ (Pa·s) = $1.176\times10^{-8} \cdot c^2 + 1.281\times10^{-6} \cdot c + 0.894\times10^{-3}$ | $c$ < 300 g/L |
| osmotic pressure | 20 °C | $\pi$ (bar) = $1.740\times10^{-7} \cdot c^3 + 4.222\times10^{-5} \cdot c^2 + 7.287\times10^{-2} \cdot c$ | $c$ < 500 g/L |
| diffusion coefficient | 20 °C | $D$ (m²/s) = $3.260\times10^{-16} \cdot c^2 + 7.402\times10^{-13} \cdot c + 0.458\times10^{-9}$ | $c \leq$ 800 g/L |
| | 25 °C | $D$ (m²/s) = $2.878\times10^{-16} \cdot c^2 + 7.545\times10^{-13} \cdot c + 0.522\times10^{-9}$ | $c \leq$ 800 g/L |

### A.2.3 Polyethylene glycol (PEG-1000)

In this work, it was used polyethylene glycol polymer with weight average molecular weight of 1000 g/mol, which was herein in called as PEG-1000. The relationships between some of the properties of the binary PEG-1000-water solutions (density, viscosity, osmotic pressure and diffusion coefficient) as function of its concentration are depicted in Figure A-8. The expressions for the data fittings of Figure A-8 are shown in Table A-9.

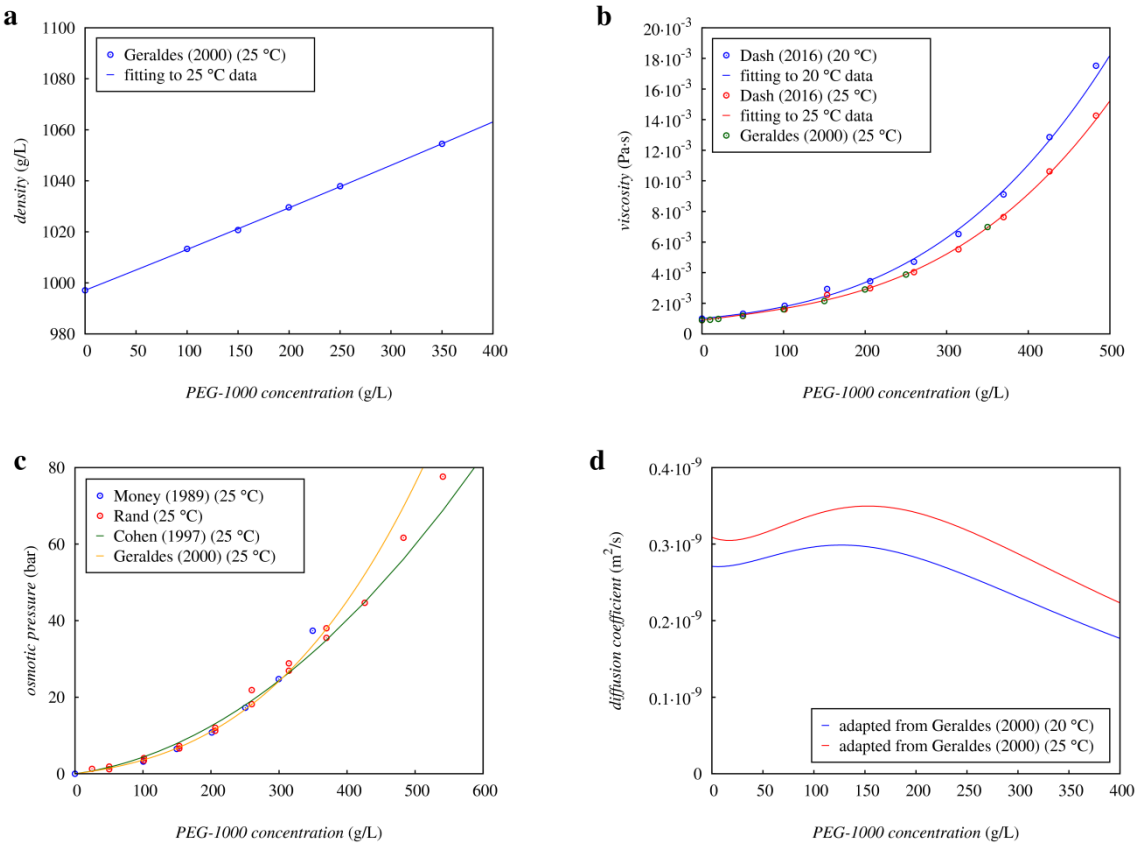


Figure A-8 – Properties of PEG-1000 aqueous solutions as function of PEG-1000 concentration: a) density; b) viscosity; c) osmotic pressure; d) diffusion coefficient.

Table A-9 – Expressions for the fittings of the density, viscosity, osmotic pressure and diffusion coefficient data of PEG-1000 aqueous solutions as function of PEG-1000 concentration.

| Property | Temperature | Expression | Condition |
|---|---|---|---|
| density | 25 °C | $\rho$ (g/L) = $1.695\times10^{-5} \cdot c^2 + 1.582\times10^{-1} \cdot c + 997.1$ | $c$ < 350 g/L |
| viscosity | 20 °C | $\mu$ (Pa·s) = $8.640\times10^{-11} \cdot c^3 + 1.484\times10^{-8} \cdot c^2 + 5.358\times10^{-6} \cdot c + 1.002\times10^{-3}$ | $c$ < 500 g/L |
| | 25 °C | $\mu$ (Pa·s) = $9.215\times10^{-11} \cdot c^3 - 2.526\times10^{-9} \cdot c^2 + 6.880\times10^{-6} \cdot c + 0.894\times10^{-3}$ | $c$ < 500 g/L |
| osmotic pressure | 25 °C | $\pi$ (bar) = $3.245\times10^{-7} \cdot c^3 + 9.429\times10^{-5} \cdot c^2 + 2.318\times10^{-2} \cdot c$ | $c$ < 400 g/L |
| diffusion coefficient | 25 °C | see (Geraldes 2000) | $c \leq$ 400 g/L |

## A.3 Comparison of the properties of the solutions for all the solutes

In Figure A-9 it is shown the comparison of density, viscosity, osmotic pressure and diffusion coefficient, as function of the solute concentration, for the several model solutes used in this work.

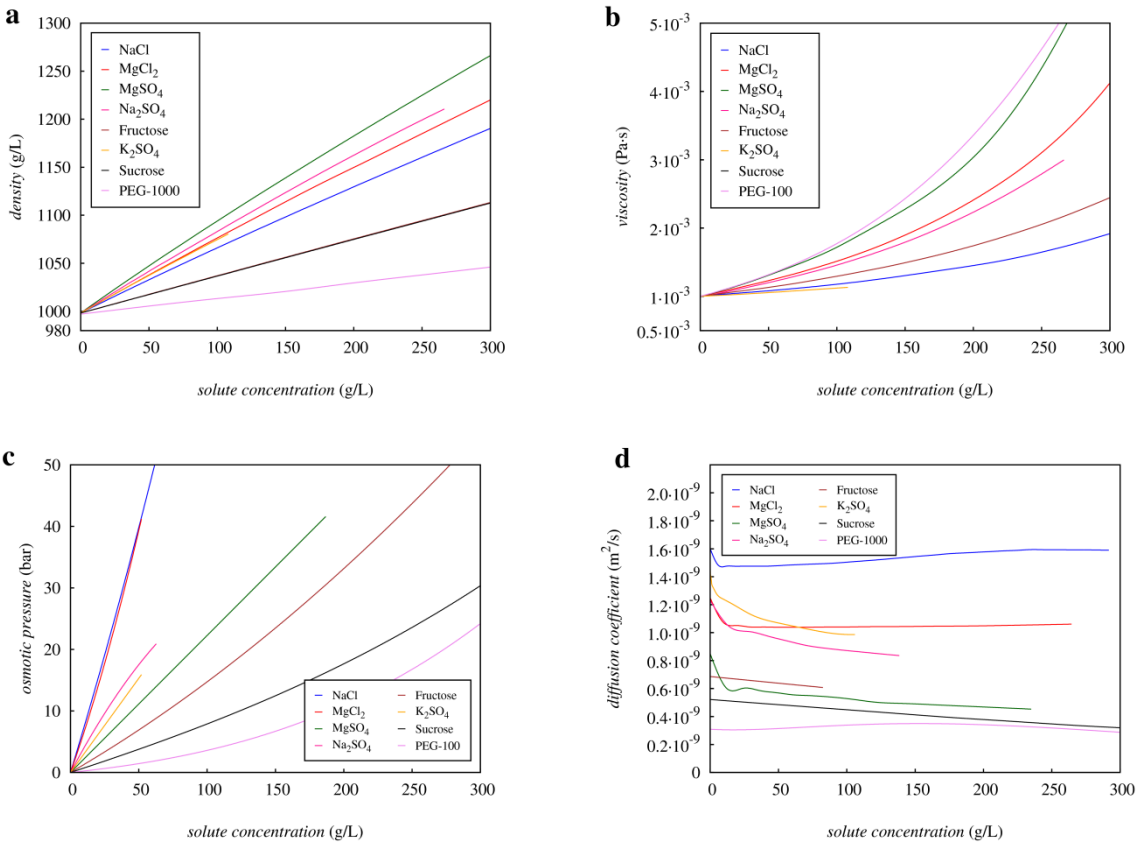


Figure A-9 – Properties of binary solute-water solutions as function of the solute concentration: a) density; b) viscosity; c) osmotic pressure; d) diffusion coefficient. With the exception of the osmotic pressure of NaCl and PEG-1000, which were determined for 25 °C, all the other data refers to 20 °C .

# Appendix B Calibration of the differential refractometer and of the conductivity meter

The differential refractive index curves obtained at room temperature for fructose, sucrose and PEG-1000, as function of solute concentration, are shown in Figure B-1. The differential refractive index was determined using the differential refractometer DD5 (Atago, Japan) and deionized water as the liquid reference. For all the curves the coefficient of determination, $R^2$, is higher than 0.998.

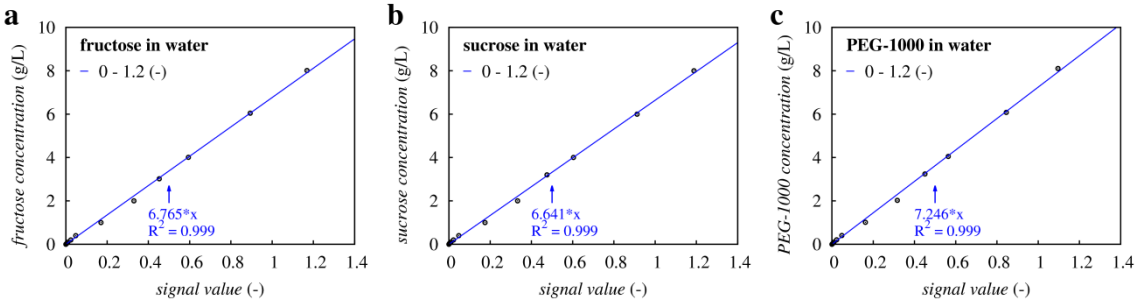


Figure B-1 – Differential refractive index (at room temperature) as function of the solute concentration for fructose, sucrose and PEG-1000 aqueous solutions.

The conductivity curves, at 25 °C, for binary salt-water solutions, as function of salt concentration, are shown in Figure B-2. To measure the conductivity of the solutions it was used the conductivity probe 980-K19/120 (Metler-Toledo, USA) coupled to the conductivity meter GLP32 (Crison, Spain). The conductivity meter was calibrated using standard solutions of known concentration and conductivity, namely potassium chloride 0.01 mol/L and the potassium chloride 0.1 mol/L, both supplied by BDH Prolabo (Belgium), which conductivities are 1.41 mS/cm and 12.8 mS/cm, respectively. The measurements of the conductivity were performed at room temperature but the conductivity meter automatically converts the acquired value to the conductivity value at 25 °C. For all the curves the coefficient of determination, $R^2$, is higher than 0.997.

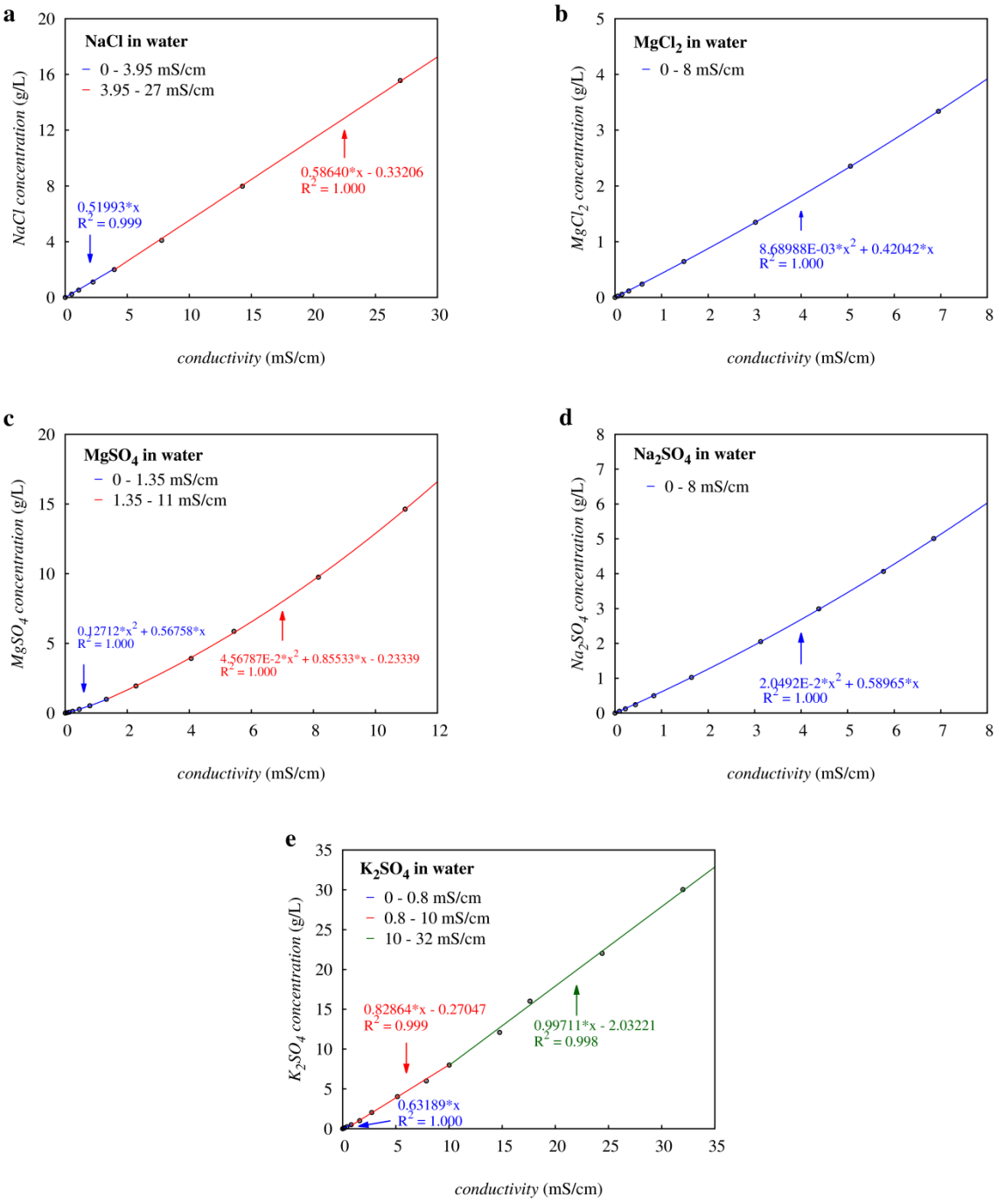


Figure B-2 – Conductivity at $T$ = 25 °C as function of the salt concentration for binary salt-water solutions.

# Appendix C Apparatus used in the micro-TFF system

This section is devoted to describe some of the equipment used in the micro-TFF nanofiltration system.

## C.1 Calibration of the pump

The correct functioning of the used pump (model 2150, LKB, Sweden) was accessed obtaining the relationship between the flow rate set on the pump controller and the measured flow rate delivered by the pump, using water as test fluid. The pump that feeds the system is a dual piston pump used to inject liquids into HPLC systems. The relationships for the non-pressurized system and for the pressurized systems, using the 100 psi (7 bar), 250 psi (17 bar) and 500 psi (34 bar) back-pressure valves, are depicted in Figure C-1.

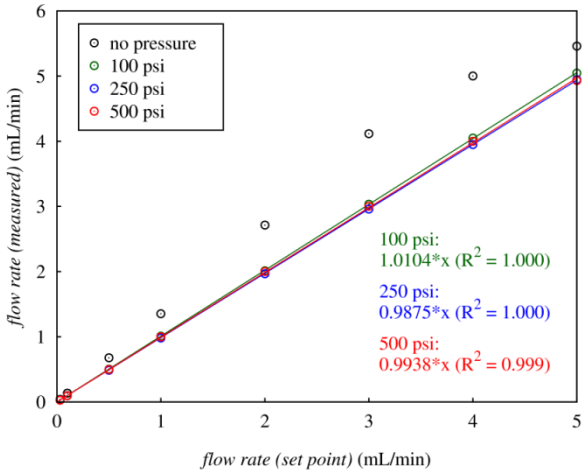


Figure C-1 – Relationship between the flow rate set on the HPLC pump, $Q_p$, and the measured flow rate, $Q$, for pressurized and non-pressurized systems.

If the system is pressurized, and for flow rates set equal or higher than 1 mL/min, the relative deviation between the set flow rate and the measured flow rate was less than 3%, but it can go up to 12 % when the flow rate is set as low as 0.03 mL/min. A reason for the higher relative deviations observed at low flow rates may be water evaporation from the collecting reservoir. In fact, at low flow rates the amount of water delivered by the pump is so small that a significant portion of it may evaporate during the time it is collected, resulting in a loss of water that was not weighted. In fact, for very low flow rates, the measured flow rate was always lower than the expected one. Thus, the real flow rate in the system may not differ, from the set flow rate as much as the measured flow rate shows. In addition, if the system is pressurized the

global relationship between the flow rate set on the pump controller and the measured flow rate delivered by the pump presents a coefficient of determination, $R^2$, close to the unity.

A different behaviour occurs when the system is not pressurized. In such circumstances, the flow rate delivered by the pump is unpredictable. Sometimes the measured flow rate is higher than the set flow rate (as depicted in the figure), while in other occasions it is lower. Thus, if flow control is needed, the HPLC pump 2150 should not be used in non-pressurized systems.

## C.2 Selection and calibration of the pressure sensors

### C.2.1 Introduction

Two types of pressure sensors were used to acquire pressure data on the micro-TFF system: gauge pressure sensors and differential pressure sensors. The gauge pressure sensors were connected to the micro-TFF system at upstream and downstream positions of the nanofiltration cell (Figure 3-1 and Figure 3-2) and were used to monitor the applied pressure inside the filtration channel. The differential pressure sensors were used to acquire the pressure drop on the filtration channels used within the micro-TFF system. The differential pressure sensors were connected to the nanofiltration cell by the ports near the inlet and outlet ports (Figure 3-1 and Figure 3-3). Since the overpressure of the differential pressure sensors can be as low as 20 psi, depending on the model, the pressure drop measurements were performed with the system depressurized.

The selected pressure sensors function based on the same principle: the sensors are transducers converting pressure differences into electrical voltage. Nevertheless, one must keep in mind several issues. First, each pressure sensor model has a well-defined pressure range where a linear pressure-to-voltage relationship should exist. Beyond that range the manufacturer of the pressure sensor does not guarantee linearity between pressure and voltage. Second, the electrical voltage span is also different among the pressure sensor models leading to distinct pressure sensibility. In addition, some models present a null output (voltage at differential pressure equal to zero) that is not zero volts. For these reasons the selected pressure sensors were calibrated using a pressure-to-voltage calibrator in order to check the data given by the manufacturer. Moreover, since the device that acquires the output of the pressure sensor (i.e. the acquisition board in Figure 3-1) has a discrete range for the input voltage, the pressure-to-voltage signal from the pressure sensor should be amplified to increase the sensibility of the results. To achieve this, the signal amplification was done in such way that the output voltage of the differential pressure sensors fall into the input voltage range of the acquiring device.

### C.2.2 Selection of the pressure sensors

The gauge pressure sensors were used to monitor the applied pressure in the micro-TFF system and they should cover the pressure range of the vast majority of the centrifugal nanofiltration experiments (most of them up to 35 bar). Thus, as gauge pressure sensors the 40PC500G2A model (Honeywell, USA) was selected, which is specified as a 500 psi (34.5 bar) pressure sensor. Two sensors of this model were purchased which were named as 40PC500G2A-64 and 40PC500G2A-74 (based on their serial numbers).

The differential pressure sensors were used to study the pressure drop along the channel of the nanofiltration cell. Estimation of the pressure drop, $\Delta p$, was calculated using a Hagen-Poiseuille-like equation (Fuerstman et al. 2007) for open channels with rectangular cross-section

$$\Delta p = \frac{a\mu LQ}{Wh^3} \tag{C-1}$$

where $a$ is given by

$$a = 12\left(1 - \left(192\frac{h}{\pi^5 W}\right)tanh\left(\frac{\pi W}{2h}\right)\right)^{-1} \tag{C-2}$$

The calculated pressure drops for three open channels with rectangular cross-section are shown in Table C-1. The estimates were determined based on the flow rate range of the used HPLC pump and on the design dimensions for the experimental channel: $h$ = 0.25 mm and $L$ = 69.1 mm for $W$ = 1 mm, 3.3 mm and 10 mm.

Table C-1 – Calculated pressure drop for three open channels with rectangular cross-section and $h$ = 0.25 mm, $L$ = 69.1 mm and widths of 1 mm. 3.3 mm and 10 mm.

| Q (mL/min) | Pressure drop (Pa) | | |
|---|---|---|---|
| | $W$ = 1 mm | $W$ = 3.3 mm | $W$ = 10 mm |
| 0.05 | 52.4 | 14.1 | 4.5 |
| 0.10 | 104.9 | 28.1 | 9.0 |
| 1.00 | 1048.7 | 281.3 | 89.8 |
| 2.00 | 2097.4 | 562.6 | 179.7 |
| 5.00 | 5243.6 | 1406.6 | 449.2 |

It is expected that the highest pressure drop (≈ 5250 Pa) occurs for the flow at maximum flow rate ($Q$ = 5 mL/min) inside the channel of smallest width ($W$ = 1 mm). Due to the entrance and exit sections of the channels, somewhat larger pressure drops, than the calculated ones, are

expected. Thus, three differential pressure sensors where selected for purchase: one for the range 0 – 0.5 psi (0 – 3450 Pa), one for the range 0 – 1 psi (0 – 6895 Pa) and another for the range 0 – 15 psi (0 – 103.4 kPa), the models 24PCEFA6D, 26PCAFA6D and 26PCCFA6D (Honeywell, USA), respectively.

### C.2.3 Calibration of the pressure sensors

The five selected pressure sensors (40PC500G2A-64, 40PC500G2A-74, 26PCAFA6D, 26PCCFA6D and 24PCEFA6D) were evaluated using a pressure-to-voltage calibrator DPI 610 (Druck, USA). The full scale of the used calibrator is limited to 15 psi (near 1 bar) and, for this reason, the evaluation in the whole range of the pressure sensors was only possible for the differential ones. The gauge pressure sensors were also evaluated but only up to the limit of the pressure-to-voltage calibrator (15 psi).

#### Non-amplified pressure-to-voltage signal

The non-amplified pressure-to-voltage data was obtained using the internal voltmeter of the pressure-to-voltage calibrator and the obtained curves are displayed in Figure C-2. Four main conclusions can be stated from the calibration of the non-amplified pressure-to-voltage signal of the pressure sensors. First, it was verified that the output voltage signal is stable and that for an equal applied pressure the output voltage remains the same at distinct runs (with minor deviations). Second, it was verified that the relationship between output voltage and the pressure is linear in the studied pressure range, as can be seen by the very high value of the coefficient of determination, $R^2$. Third, the null offsets of the sensors are in accordance with the ones referred by the manufacturer. Finally, the sensor sensibility, in terms of unit of voltage per unit of pressure, is also in good accordance with the ones referred by the manufacturer. These conclusions are easily accessed comparing the sensors specifications (Honeywell International Incorporated 2011; Honeywell International Incorporated 2015a; Honeywell International Incorporated 2015b) versus the experimental data of the sensor calibration, as shown in Table C-2.

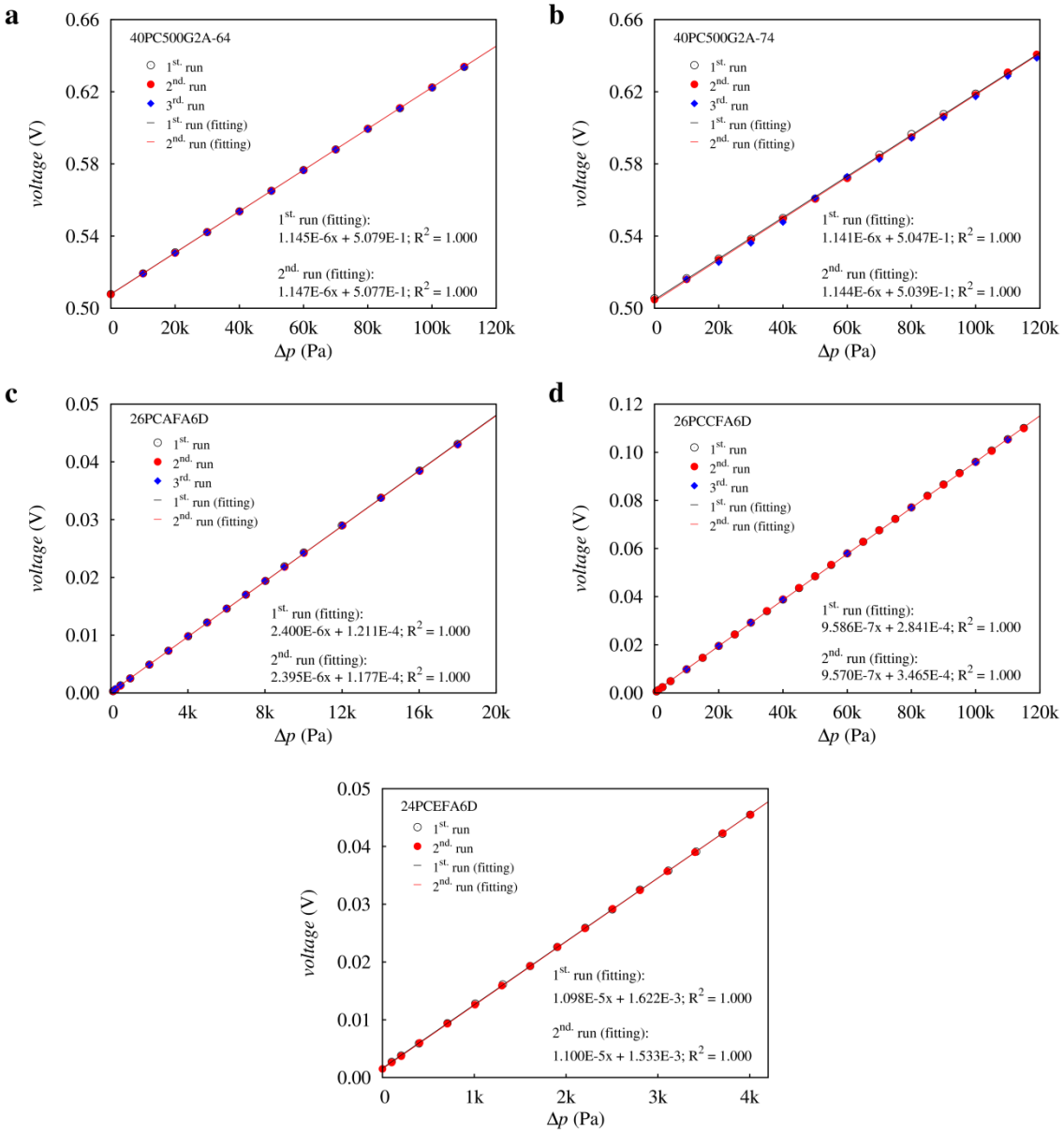


Figure C-2 – Relationship between the applied pressure and the non-amplified difference voltage output for the used pressure sensors: a) 40PC500G2A-64; b) 40PC500G2A-74; c) 26PCAFA6D; d) 26PCCFA6D; e) 24PCEFA6D.

Table C-2 – Comparison between specifications of the pressure sensors and experimental calibration.

| | Sensor | | | | | | | |
|---|---|---|---|---|---|---|---|---|
| | 24PCEF1D | | 26PCAFA6D | | 26PCCFA6D | | 40PC500G2A | |
| | Specific. | Exp. | Specific. | Exp. | Specific. | Exp. | Specific. | Exp. |
| Pressure range (psi) | 0 – 0.5 | 0 – 0.6 | 0 – 1 | 0 – 2.6 | 0 – 15 | 0 – 16.7 | 0 – 500 | 0 – 17.2 |
| Input voltage (V) | 10 (typical) | 10 ± 0.1 | 10 (typical) | 10 ± 0.1 | 10 (typical) | 10 ± 0.1 | 5 ± 0.25 | 5 ± 0.1 |
| Null offset (mV) | 0 ± 30 | < 5 | 0 ± 1.5 | < 1 | 0 ± 1.5 | < 1 | 500 ± 40 | 500 ± 30 |
| Sensibility (mV/psi) | 70 ± 20 | 75.6 | 16.7 ± 2 | 16.6 | 6.7 ± 0.2 | 6.6 | 8 (typical) | 7.7 – 7.9 |
| Voltage span (V) | 35 ± 10 | 39 | 16.7 ± 2 | 16.6 | 100 ± 3 | 99 | 4000 ± 90 | nd |
| Overpressure (psi) | 20 | nd | 20 | nd | 45 | nd | 1000 | nd |

nd: not determined

**Amplified pressure-to-voltage signal**

From the non-amplified pressure-to-voltage data one can be seen that the sensibility of the differential pressure sensors varies from 8.8 Pa / 0.1 mV, for the 24PCEF1D sensor, to 105 Pa / 0.1 mV, for the 26PCCFA6D. Comparing these values with the expected pressure drop for channels similar to those to be used experimentally (Table C-1), it is clear that it is advantageous to increase the overall sensibility by amplifying their pressure-to-voltage output signal.

The purpose of signal amplification is twofold. First, the raw pressure-to-voltage output signal of the pressure sensors can have sensibility as low as 6 mV/psi, so it would be interesting to increase it. Second, if we intend to acquire and store pressure data we have to use an acquisition board. However, the available apparatus in the laboratory (models NI USB-6008 and NI USB-6211, National Instruments, USA) gather the signal in a discrete range. This behaviour can be problematic if the voltage span of the sensor is small and for this reason signal amplification is necessary. Moreover, it would be impractical to use of handheld voltmeters during the experimental runs, being the use of an acquisition board much more convenient.

Signal amplification was performed using electronic integrated operational amplifiers LM324N (ST Microelectronics, Switzerland). In Figure C-3 are shown the electric connections made on the electronic board to create the signal amplification for each of the used pressure sensors. The resistors ($R_1$ and $R_2$) have different resistance values in order to obtain distinct amplifying gains and, thus, achieve a correct voltage span similar to the input voltage range of the acquisition board. In Figure C-3, GND stands for the ground connection, while VCC is the connection to a +16 V source to power the amplifier. In the same figure the AIxx lines connect the voltage signal, generated by the amplifier, to the input ports on the acquisition board.

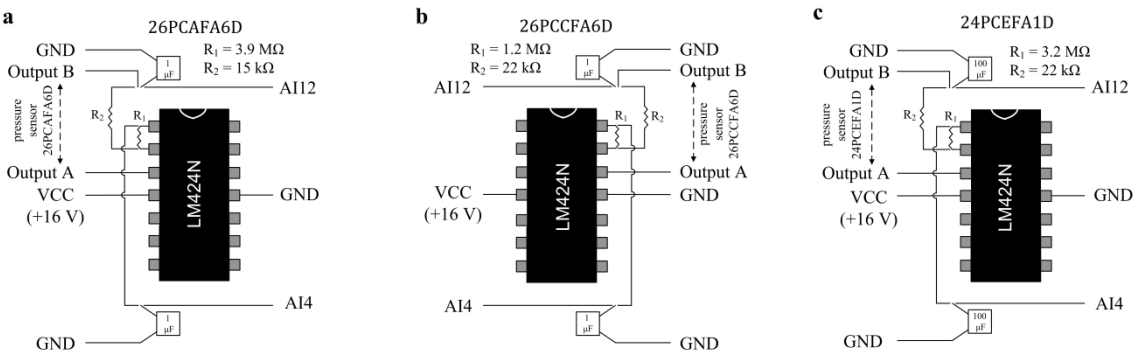


Figure C-3 – Schemes of the electric wiring connected between the pressure sensor and the op-amp and the electric wiring connected between the op-amp and the acquisition board for the pressure sensors: a) 26PCAFA6D; b) 26PCCFA6D; c) 24PCEFA1D.

Plotting the amplified output voltage signal versus the applied differential pressure on the sensor, linear relationships were obtained for the five pressure sensors, as can be seen in Figure C-4, also with correlation coefficients very close the unity.

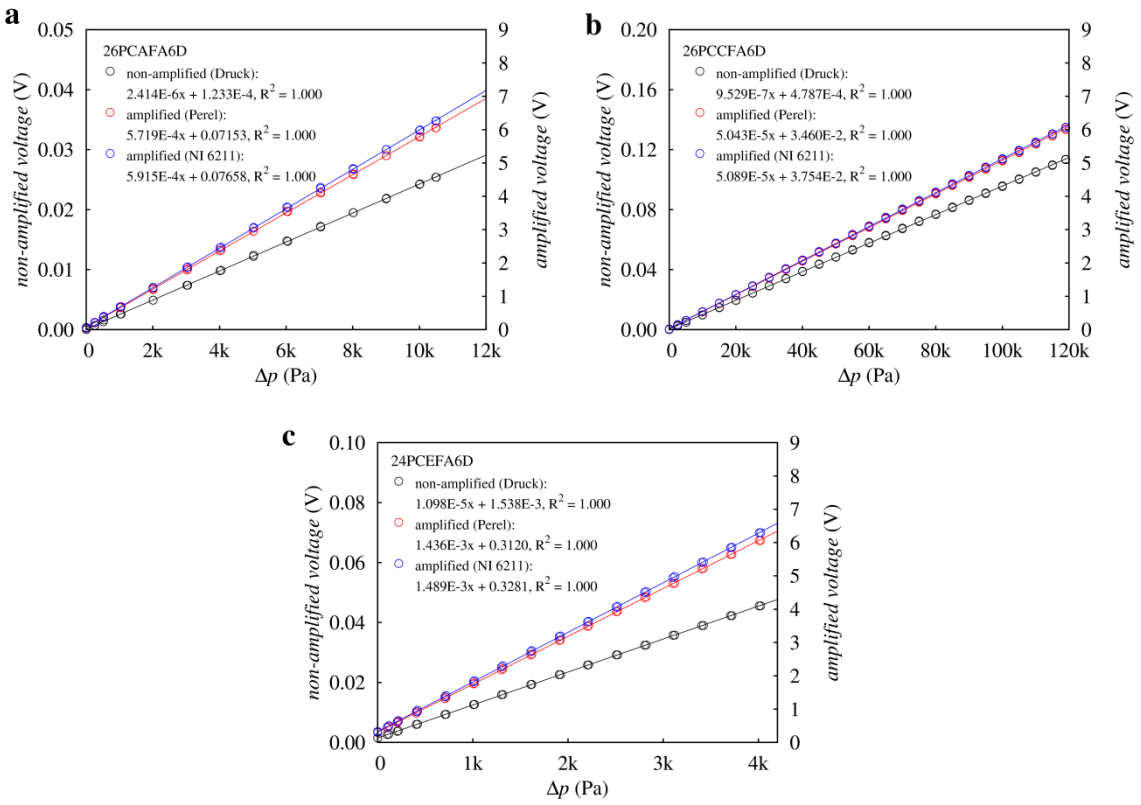


Figure C-4 –Relationships between the applied pressure and the amplified and non-amplified difference voltage output for the used pressure sensors: a) 26PCAFA6D; b) 26PCCFA6D; c) 24PCEFA6D.

# Appendix D Boundary conditions used in the numerical simulations

In section 4.4.2 two boundary conditions were presented for the used model of the nanofiltration in the NF cell: the equations (4-15) and (4-16).

The equation (4-15) is derived from the equation (2-26), the osmotic model, and based on three assumptions. First, it is assumed that all the streams are diluted and, thus, have the same density. Then, from equation (2-6), one obtains that the permeate quality is the same along the channel and equal to

$$w_p = w_f(1 - R_a) \tag{D-1}$$

Second, it is assumed that there is a linear relationship between the osmotic pressure and the solute concentration, which is valid for diluted solutions. Again, admitting constant density, the osmotic pressures at the membrane surface and in the permeate are, respectively,

$$\pi_m = Cw_m \tag{D-2}$$

$$\pi_p = Cw_p \tag{D-3}$$

where $C$ is a proportionally constant between the solute mass fraction and the osmotic pressure of the solution. Finally, the hydraulic permeability of the membrane is substituted by the right side of equation (2-3), but using the actual viscosity instead of the water viscosity. This results in the already presented expression, in equation (4-15), for the permeate flux

$$J_v = \frac{1}{\mu R_m}\left(\Delta p_m - C\left(w_m - w_f(1 - R_a)\right)\right) \tag{4-15}$$

The equation (4-16) can be derived in similar manner to that in which the equation (2-12) was obtained. Making a solute mass balance around the membrane, as sketched in Figure D-1, one has three components of the solute transport: the term $j_{s,c}$, which corresponds to the solute mass flux by convection from the bulk of the solution to the membrane, the term $j_{s,d}$, which corresponds to the solute mass flux by diffusion from the membrane to the bulk of the solution, and the term $j_s$, which corresponds to the solute mass flux that exits to the permeate stream. At steady-state there is no accumulation in the membrane and the balance is given by

$$j_s = J_v c_p = j_{s,c} - j_{s,d} \tag{D-4}$$

as already defined for the film theory model in equation (2-11). Equation (D-4) can be modified to

$$\rho_p J_v w_p = \rho_m J_m w_m - \rho_m D_{AB} \frac{dw_m}{dz} \tag{D-5}$$

where $\rho_m$ and $\rho_p$ are the liquid density at the membrane surface in the feed side and in the permeate sides, respectively, and $J_m$ and $J_v$ are volumetric solution flux that goes towards the membrane in the feed side and the permeate flux that permeates through the membrane, respectively, then by solving for $\frac{dw_m}{dz}$ and considering dilute solutions ($\rho_p \approx \rho_m$)

$$\frac{dw_m}{dz} = \frac{J_m w_m - J_v w_p}{D_{AB}} \tag{D-6}$$

Since $J_v = J_m$, and substituting $w_p$ by equation (D-1), one finally obtains equation (4-16)

$$\frac{dw_m}{dz} = \frac{J_v\left[w_m - (1 - R_a) w_f\right]}{D_{AB}} \tag{4-16}$$

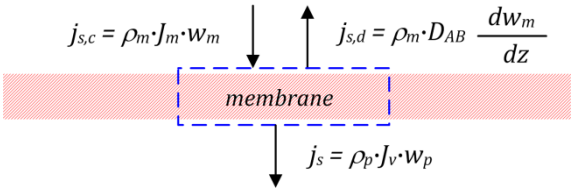


Figure D-1 – Balance of solute mass around the membrane.

# Appendix E Specifications of the used centrifuge and centrifuge rotors.

For the centrifugal nanofiltration experiments, it was used the superspeed RC6 centrifuge (Sorvall, USA). The RC6 centrifuge has temperature control and the angular speed can be set in 10 rpm intervals up to 10000 rpm and in 100 rpm intervals for rotor speed above 10000 rpm. Neither the temperature nor the angular speed was subject of verification, or calibration, and the apparatus were used as is.

The RC6 centrifuge can use any rotor that engages on its rotating shaft. During this work, several fixed-angle rotors were used, namely the rotors F10-6x500y (Piramoon Technologies, USA), SS-34 (Sorvall, USA) and SA-300 (Thermo Scientific, USA). The principal specifications of each of these rotors are shown in Table E-1.

Table E-1 – Specifications of the used centrifuge rotors. †

| Model (manufacturer) | Material | Maximum mass per bucket (g) | Maximum radius (mm) | Maximum speed in RC6 (rpm) | Angle $\beta$ (degrees) | Nr of buckets | Volume per bucket (mL) | Bucket (∅ × L) (mm) |
|---|---|---|---|---|---|---|---|---|
| F10-6x500y (Piramoon) | Composite | 780 ‡ | 158.0 | 10000 | 23 | 6 | 500 | 70 × 160 |
| SS-34 (Sorvall) | Aluminum | 115 | 107.0 | 20000 | 34 | 8 | 50 | 29 × 108 |
| SA-300 (Thermo) | Aluminum | 115 | 96.7 | 21000 | 34 | 6 | 50 | 29 × 108 |

† From references (Kendro Laboratory Products 2005; Thermo Fisher Scientific Incorporated 2007; Thermo Fisher Scientific Incorporated 2010; Thermo Fisher Scientific Incorporated 2014b; Thermo Fisher Scientific Incorporated 2014c). ‡ assumed the same of the rotor SLA-3000.

# Appendix F Experimental procedures and data treatment

## F.1 Assembly of the micro-TFF cell and experimental methods

In order to perform the assembly of the micro-TFF nanofiltration cell always in the same and systematic manner, the method described in Procedure F-1 was adopted. The main steps of the cell assembly method are also depicted in Figure F-1.

Procedure F-1 – Method to assembly the micro-TFF cell.

1. The parts of the cell should be kept and stored clean (Figure F-1a).
2. Prepare the plastic sheets that form the channel. In the Figure F-1b it is visible the permeate mesh glued in the depression of the bottom plate. A single O-ring is shown, in the bottom plate, but a similar one must also be present in the top plate.
3. Pieces of membrane and filter paper are cut with appropriate shapes (Figure F-1c).
4. A plastic piece with the desired channel design is placed in the depression of the top plate (Figure F-1d). The surface of this plastic piece that is to be in contact with the membrane is coated with a thin layer of silicone. To keep the plastic piece in place, a small drop of silicone is also spread between the plastic piece and the surface of the top plate depression.
5. Maintaining the top plate inverted, the screws are inserted in the holes (Figure F-1e).
6. The membrane piece is gently inserted along the screws, with the active layer of the membrane facing to the bottom face of the top plate (Figure F-1f). It is important to confirm that the O-ring do not slip from the groove where it is placed, otherwise it will change the channel height and may damage the membrane.
7. The filter paper piece is placed over the membrane, soaked with water, and flattened to avoid wrinkles on the membrane surface (Figure F-1g).
8. The bottom plate of the cell is placed over the filter paper (Figure F-1h) and the supports and nuts are tightened slightly just to keep the parts in place (Figure F-1i).
9. After inverting back the cell, placing it on its final orientation, the screws are firmly tightened in several steps (Figure F-1j)
10. Finally, the cell is connected to the tubing of the Static Nanofiltration System B (Figure F-1k).

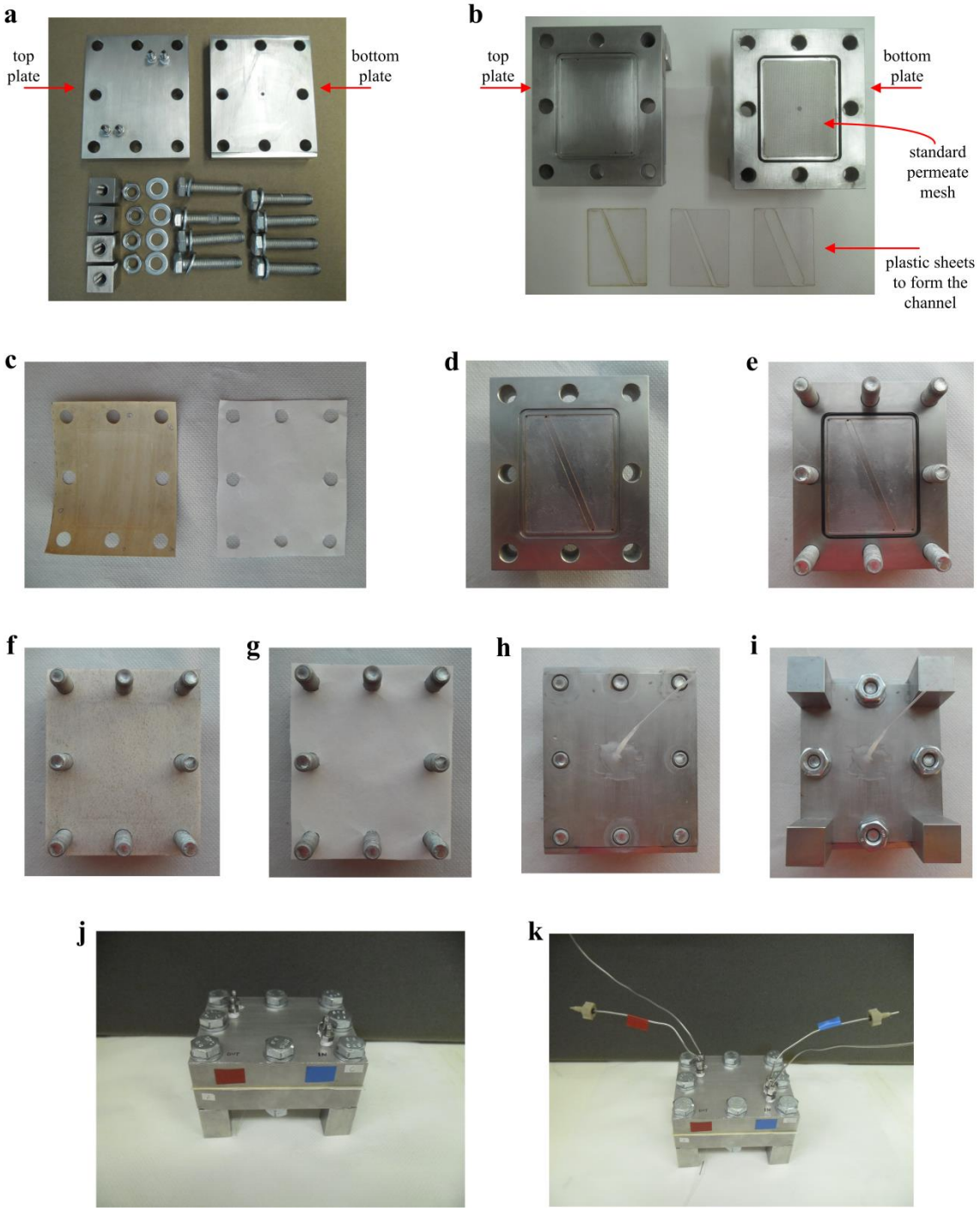


Figure F-1 – Method to assembly the micro-TFF nanofiltration cell. For details on each image see Procedure F-1.

The used method to measure the hydraulic permeability of a membrane is described in Procedure F-2.

Procedure F-2 – Method to measure the hydraulic permeability of a membrane.

1. After assembling a compacted membrane into the micro-TFF nanofiltration cell, rinse the cell with deionized water for at least 30 min at $p$ = 250 psi.

2. Select the desired pressure by inserting the corresponding back-pressure valve or by adjusting the micrometering valve.
3. Select the desired flow rate (it was selected the maximum flow rate that the HPLC pump can deliver: $Q_p$ = 5.00 mL/min)
4. For permeate flux stabilization, perform the filtration using deionized water at the desired pressure during 10 minutes
5. After doing the previous step, collect the permeate liquid at the desired pressure and register the corresponding elapsed time.
6. To perform experiments at different pressures repeat the steps 2 to 4.

The methodology adopted for the experiments to measure solute rejection is described in Procedure F-3.

Procedure F-3 – Method to measure the solute rejection of a membrane.

1. After assembling a compacted membrane into the micro-TFF nanofiltration cell, rinse the cell with deionized water for at least 30 min at $p$ = 250 psi.
2. To remove the water from the permeate chamber and from the permeate channel, perform nanofiltration of the solution under study, feeding it to the filtration chamber, for at least 30 min at $p$ = 250 psi and $Q_p$ = 5.00 mL/min.
3. To detach the CP layer (that was formed during the previous 30 min) from the membrane surface and to remove it from the filtration chamber, depressurize the system and rinse during at least 1 minute, feeding the solution under study at the maximum flow rate.
4. To achieve steady state conditions, pressurize the system at $p$ = 250 psi and perform nanofiltration of the solution under study for 15 min.
5. After those 15 min, start collecting the concentrate and permeate liquids until at least 1 mL of each are collected.
6. To perform experiments for different solutions repeat the steps 1 to 5.
7. Rinse the cell with deionized water for at least 30 min at $p$ = 250 psi.

The methodology adopted for the concentration of samples is described in Procedure F-4. The necessary time to process the sample depends on its volume and on the flow rate. The necessary time to process 9.6 mL (the volume of sample used in the present work) was presented before in Table 3-4.

Procedure F-4 – Method to concentrate small-volume samples using the micro-TFF nanofiltration cell.

1. After assembling a compacted membrane into the micro-TFF nanofiltration cell, rinse the cell with deionized water for at least 30 min at $p$ = 500 psi.
2. Rinse the cell with deionized water for at least 10 min at the selected pressure to be used in the concentration run.
3. To remove the water from the permeate chamber, perform nanofiltration with the solution under study, at the selected pressure, for a time period of at least 15 to 30 min (depending on the permeate flow rate).

4. To remove the CP layer from the membrane surface and from the filtration chamber, depressurize the system and rinse during at least 1 minute with the solution under study at the maximum feed flow rate.
5. Pressurize the system at the selected pressure, and perform the first experiment at the maximum feed flow rate ($Q_p$ = 5.00 mL/min) during the necessary time period to inject the selected volume (9.6 mL) from the sample reservoir.
6. Select a different, and smaller, feed flow rate and perform nanofiltration for a time period of at least 5 to 15 min (depending on the permeate flow rate), to remove the previous permeate from the permeate chamber and from the permeate channel.
7. To remove the CP layer from the membrane surface and from the filtration chamber, depressurize the system and rinse during at least 1 minute with the solution under study at the maximum feed flow rate ($Q_p$ = 5.00 mL/min).
8. Pressurize the system again and perform the nanofiltration experiment at the selected flow rate during the necessary time period to inject the selected volume (9.6 mL) from the sample reservoir.
9. To perform experiments at different flow rates repeat the steps 6 to 8.
10. To perform experiments at different pressure start from the step 1.
11. Rinse the cell with deionized water for at least 15 min at $p$ = 500 psi.

## F.2 Assembly of the TFF device and experimental methods for HI

The silicone used to fix a membrane to the NF cell must not cover any area of the membrane in the region of the porous support of the bottom part of the NF cell, especially in the region corresponding to the optical window. Otherwise, it would obstruct the laser beam and, thus, hinder the visualization of the interferometric fringes. For this reason, the membrane must be folded towards the lateral walls of the bottom part of the cell. Since thin-film composite NF membrane is too stiff to be folded, the active layer of the membrane was peeled from its support layer and then fixed to the bottom part of the cell, as shown in Figure F-2. The full method to fix a piece of membrane to the cell is described in Procedure F-5.

Procedure F-5 – Method to fix a piece of membrane to the nanofiltration TFF cell.

1. Clean and remove, from the bottom part of the cell any residues of the previous gluing process (Figure F-2a).
2. Cut a piece of membrane, with appropriate shape and size, from a pristine membrane sheet.
3. Peel the active layer of membrane from the membrane support layer (Figure F-2b).
4. Spread a thin layer of silicone around the porous support of the bottom part of the cell.
5. Place the peeled membrane over porous support the cell, fold it to the lateral sides (Figure F-2c) and press it against the silicone.
6. Apply vacuum on the permeate tubing during at least 10 minutes to ensure that the membrane gets flat and stuck to the silicone.
7. Cure the silicone overnight by immersing the bottom part of the cell (already attached to the membrane) into a tank filled with water.

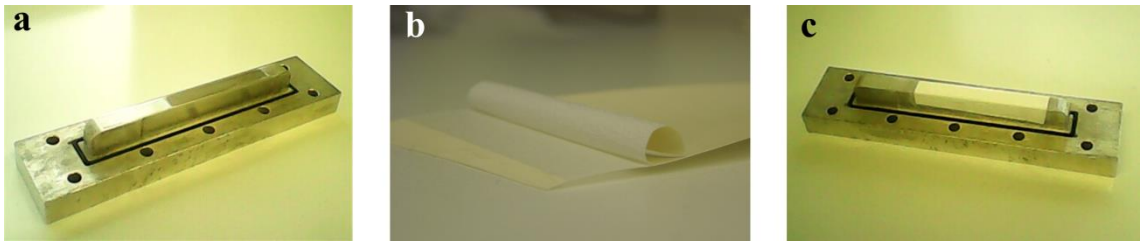


Figure F-2 – Some of the steps to fix a membrane piece into the TFF nanofiltration cell: a) cleaned bottom part of the cell; b) peeling of the active layer of the membrane; c) membrane glued to the bottom part of the cell.

The methodology described herein was used either in the studies of temporal evolution of CP layer and in the studies ate steady-state (to evaluate several operating conditions). The only difference is that while for temporal evolution experiments the interferograms were acquired at several well-defined time points, for steady-state experiments a single interferogram (for each $Re_h$) was acquired at a single time point: 30 min for $Re_h < 5$ and 10 min for $Re_h \geq 5$. The method performed to acquire holographic interferograms at different time instants for the study of the temporal evolution of the CP phenomena is described in Procedure F-6. In this procedure it is admitted that the reference state was already recorded in holographic plate and that the holographic plate is placed in the corrected position. Detailed information about the recording of the reference state in the holographic plate is available elsewhere (Rodrigues et al. 2013).

Procedure F-6 – Methodology to acquire holographic interferograms in the study of temporal evolution of concentration polarization in a filtration process using the TFF nanofiltration cell.

1. Place the TFF nanofiltration cell with the open channel over the support on the optical table and connect it to the hydraulic system.
2. Start the pump, increase the pressure of the system to trigger concentration polarization and let the flow stabilize (near 10 min). Keep in mind that the pressurization and depressurization should be done gradually.
3. Adjust the glass filter so that the fringes stay parallel to the membrane.
4. If other channel geometry is to be used remove the TFF nanofiltration cell, change the channel, place the cell over the support and start the pump again.
5. If needed, adjust the focal plane so that the image is focused inside the filtration channel but near the glass window closer to the holographic plate.
6. Adjust the pressure to the intended value.
7. Fully open the needle valve to remove the CP layer
8. Rapidly adjust the needle valve to the desired flow rate and acquire the interferogram at $t$ = 0 s. Keep in mind that to know the real inlet flow rate it is need to measure the concentrate and permeate flow rates.
9. Acquire the interferograms at the defined time periods.
10. To acquire interferograms at different flow rate or at different pressure repeat steps 6 to 9.

Some minor modifications are needed in order to obtain interferograms at steady-state. The setting of the system is the same but there is not the step to remove the CP layer and only a single interferogram is acquired for each flow rate, as defined in Procedure F-7.

Procedure F-7 – Methodology to acquire holographic interferograms for the evaluation of feed rate effect on the concentration polarization in a filtration process using the TFF nanofiltration cell.

1. to 5. The same steps as in Procedure F-6.
6. Adjust the pressure to the intended value.
7. Fully open the needle valve to remove the CP layer
8. Adjust the needle valve to the desired flow rate.
9. Let the flow rate stabilize during the necessary time (10 min for $Re_h \geq 5$ and 30 min for $Re_h < 5$) and acquire the interferogram
10. To acquire interferograms at different flow rate or at different pressure repeat steps 6 to 9.

## F.3 Assembly of the CNF device and the experimental methods used in CNF

The method used to glue a piece of dry membrane on the membrane support part of the CNF device is described in Procedure F-8. Some of the steps of the gluing process method are also shown in Figure F-3.

Procedure F-8 – Method to glue a piece of dry membrane on the membrane support part of the CNF device.

1. Remove the membrane and all glue residues of the previous gluing process. Make some new scratches on the edge, rinse with water and 2-propanol and let dry (Figure F-3a).
2. Prepare a piece of pristine membrane with adequate shape to be glued on the top surface of the membrane support part of the CNF device.
3. Spread a thin string (1 mm thickness) of OB-101 OMEGABOND® glue on the top surface of the membrane support part and on the support layer of the membrane piece. The glue string should be spread 2 mm away from the edges of those surfaces, except on the edge near the permeate channel hole, which should be kept without glue.
4. Spread a thin string (1 mm thickness) of Araldite® Standard glue on the top surface of the membrane support part and on the support layer of the membrane piece. The glue string should be spread 1 mm away from the edges of those surfaces, except on the edge near the permeate channel hole, which should be kept without glue.
5. Put the support layer of the membrane piece into contact with the top surface of the membrane support part and press gently. In this step, do not let any glue over the membrane surface (Figure F-3b).
6. Let the glue to cure for at least 6 hours, placing the “membrane + membrane support” assembly in an inverted orientation over a flat surface, so that the weight of the support part compresses the glue against the membrane. Use a flat plastic sheet, or absorbent paper, to protect the membrane surface.

7. Spread a small amount of Araldite® Rápido on the vertical face of the membrane support part, the face that will function as part of the concentrate chamber (below the permeate channel hole), and on the membrane support layer extremity that extends from the membrane support part.
8. Cover the membrane with a soft plastic sheet, for instance Parafilm M®, and press gently during at least 15 minutes, for instance using the handle of a spatula (Figure F-3c).
9. Use Araldite® Standard glue to fill the gaps, between the membrane and the membrane support part, and to cover, with very thin layer, the membrane surface up to 3 mm from the edge. Let the glue to cure.
10. Spread a very thin layer of OB-101 OMEGABOND® glue over the Araldite® Standard glue layer. Let the glue to cure.
11. Remove the excess of glue from the lateral wall of the membrane support part so that it enters easily inside the top part of the CNF device.

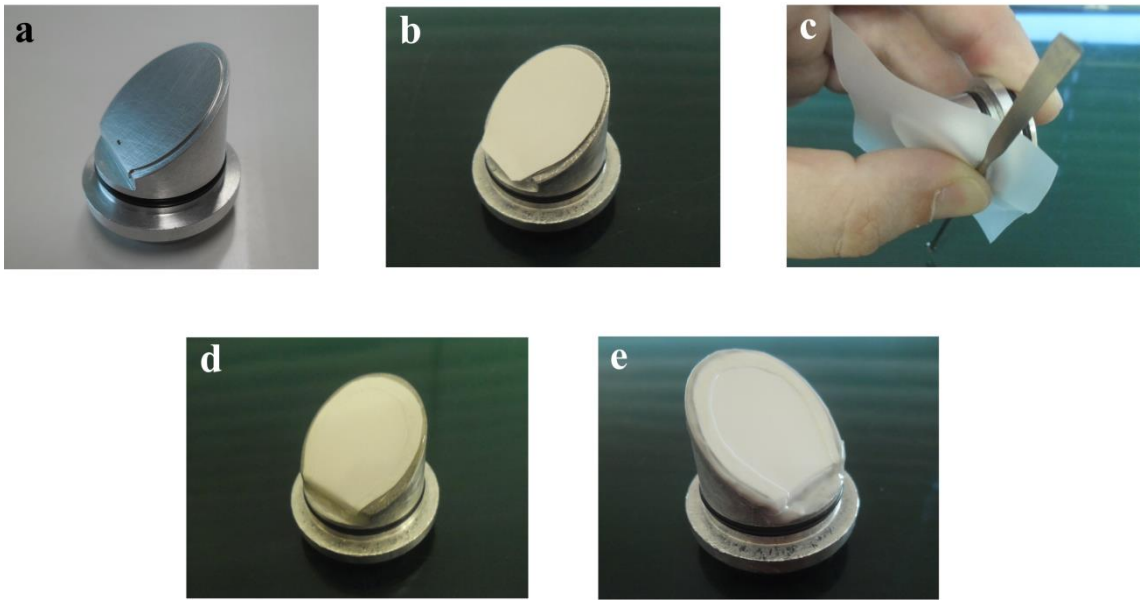


Figure F-3 – Some of the steps to fix a membrane piece on the membrane support part of the CNF device.

The assembly and filling of the CNF device with the liquid sample was executed as described in Procedure F- 9.

Procedure F- 9 – Method to assemble the CNF device and to inject liquid sample into it.

1. All the parts should be clean and dry, with the exception of the membrane that should be kept wet after the first usage.
2. Check that the O-rings are not damage, otherwise replace them.
3. Place the pretended internal block (if any) over the membrane support part in the correct orientation.
4. Insert those two parts (or just the membrane part if no internal block is to be used) inside the top part of the CNF device, maintaining the vent of the membrane support part aligned with the vent of the top part. The insertion movement should be made straight. Do not rotate the membrane support part in relation to the top part, otherwise the risk of damaging the gluing increases.
5. Insert the bottom part of the CNF device on the membrane support part.

6. Weight the empty CNF device.
7. Attach a thin and flexible tubing into a syringe (for instance a 1/16" PEEK tubing into a 5 mL syringe) and fill the syringe with the appropriate liquid sample.
8. Insert the tubing into the auxiliary channel of the CNF device and push it up to the concentrate chamber.
9. As you inject the liquid sample from the syringe start pulling the tubing.
10. Fill the sample chamber until shallow.
11. Close the CNF device placing the cap into the top part.
12. Clean the surplus liquid that overflows from the vent in the top part of the CNF device.
13. Weight the CNF device filled with liquid.

As referred in section 5.2 there are three methods that can be used to withdraw the liquid from the concentrate chamber, depending on the device design. Given the design of the developed CNF device, the concentrate was withdrawn by suction using a tube attached to a syringe. Therefore, the withdrawing of the liquids from the CNF device after the filtration cycle was executed as described in Procedure F-10.

Procedure F-10 – Method to withdraw the liquids from the CNF device after the filtration cycle.

1. Remove the CNF device from the centrifuge rotor and weight it.
2. Detach the bottom part of the CNF device, from the membrane support part.
3. Collect the permeate to a vial.
4. Detach the cap from the top part of the CNF device.
5. Collect any liquid remaining in the sample chamber, using a thin and flexible tubing attached to a syringe (for instance a 1/16" PEEK tubing into a 5 mL syringe).
6. Insert a thin and flexible tubing attached to a syringe (for instance a 1/16" PEEK tubing into a 5 mL syringe) into to the auxiliary channel of the CNF device and push it up to the concentrate chamber.
7. Collect the concentrate and store it in a vial.
8. Pull the tubing from the CNF device.
9. If you intend to collect separate fractions of the concentrate repeat steps 6 – 8 as many times as needed.
10. Detach all the parts of the CNF device, wash and dry them but keep the membrane wet for the following applications.

## F.4 Solute concentration estimation on the membrane surface

The solute concentration on the membrane surface, $c_m$, was estimated by two methodologies which are both based on the osmotic pressure model. The first method couples the osmotic pressure model, the film theory and experimental permeate fluxes. From the film theory model

$$\frac{c_m - c_p}{c_b - c_p} = exp\left(\frac{J_v}{k_c}\right) \quad (2\text{-}15)$$

Admitting that the relationship between the solute concentration and the osmotic pressure is linear (which is a good approximation only for diluted solutions) then equation (2-14) can be rearranged to

$$k_c = \frac{J_v}{ln\left(\frac{\pi_m - \pi_p}{\pi_b - \pi_p}\right)} \tag{F-1}$$

Coupling equations (2-2), (2-26) and (F-1) one obtains (Sutzkover et al. 2000)

$$k_c = \frac{J_v}{ln\left(\frac{\Delta p_m}{\pi_b - \pi_p}\left(1 - \frac{J_v}{J_w}\right)\right)} \tag{F-2}$$

Therefore, coupling equations (F-1) and (F-2) and solving for $\pi_m$ the $c_m$ value can be estimated.

Another way to estimate the solute concentration at the membrane surface is by using the osmotic pressure model only to and determine the $c_m$. Coupling equations (2-2), (2-3) and (2-26) one obtains

$$\Delta\pi = J_w \mu_w R_m - J_v \mu_w R_m \tag{F-3}$$

By equating equation (F-3) to equation (2-28) one can obtain $\pi_m$ and, therefore, $c_m$. This method allows to use non-linear relationships between $\pi_m$ and $c_m$ and, therefore is preferable to the first presented method.